

# AST Critical Propulsion and Noise Reduction Technologies for Future Commercial Subsonic Engines

Area of Interest 1.0: Reliable and Affordable Control Systems

*William Myers and Steve Winter  
General Electric Aircraft Engines, Cincinnati, Ohio*

## NASA STI Program . . . in Profile

Since its founding, NASA has been dedicated to the advancement of aeronautics and space science. The NASA Scientific and Technical Information (STI) program plays a key part in helping NASA maintain this important role.

The NASA STI Program operates under the auspices of the Agency Chief Information Officer. It collects, organizes, provides for archiving, and disseminates NASA's STI. The NASA STI program provides access to the NASA Aeronautics and Space Database and its public interface, the NASA Technical Reports Server, thus providing one of the largest collections of aeronautical and space science STI in the world. Results are published in both non-NASA channels and by NASA in the NASA STI Report Series, which includes the following report types:

- **TECHNICAL PUBLICATION.** Reports of completed research or a major significant phase of research that present the results of NASA programs and include extensive data or theoretical analysis. Includes compilations of significant scientific and technical data and information deemed to be of continuing reference value. NASA counterpart of peer-reviewed formal professional papers but has less stringent limitations on manuscript length and extent of graphic presentations.
- **TECHNICAL MEMORANDUM.** Scientific and technical findings that are preliminary or of specialized interest, e.g., quick release reports, working papers, and bibliographies that contain minimal annotation. Does not contain extensive analysis.
- **CONTRACTOR REPORT.** Scientific and technical findings by NASA-sponsored contractors and grantees.

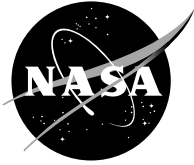
- **CONFERENCE PUBLICATION.** Collected papers from scientific and technical conferences, symposia, seminars, or other meetings sponsored or cosponsored by NASA.
- **SPECIAL PUBLICATION.** Scientific, technical, or historical information from NASA programs, projects, and missions, often concerned with subjects having substantial public interest.
- **TECHNICAL TRANSLATION.** English-language translations of foreign scientific and technical material pertinent to NASA's mission.

Specialized services also include creating custom thesauri, building customized databases, organizing and publishing research results.

For more information about the NASA STI program, see the following:

- Access the NASA STI program home page at <http://www.sti.nasa.gov>
- E-mail your question via the Internet to [help@sti.nasa.gov](mailto:help@sti.nasa.gov)
- Fax your question to the NASA STI Help Desk at 301-621-0134
- Telephone the NASA STI Help Desk at 301-621-0390
- Write to:  
NASA STI Help Desk  
NASA Center for AeroSpace Information  
7121 Standard Drive  
Hanover, MD 21076-1320





# AST Critical Propulsion and Noise Reduction Technologies for Future Commercial Subsonic Engines

Area of Interest 1.0: Reliable and Affordable Control Systems

*William Myers and Steve Winter  
General Electric Aircraft Engines, Cincinnati, Ohio*

Prepared under Contract NAS3-27720

National Aeronautics and  
Space Administration

Glenn Research Center  
Cleveland, Ohio 44135

## Document History

This research was originally published internally as AST037 in July 2000.

*Level of Review:* This material has been technically reviewed by NASA technical management.

Available from

NASA Center for Aerospace Information  
7121 Standard Drive  
Hanover, MD 21076-1320

National Technical Information Service  
5285 Port Royal Road  
Springfield, VA 22161

Available electronically at <http://gltrs.grc.nasa.gov>

## TABLE OF CONTENTS

	<u>Page</u>
Overview	1
AOI 1.2: Hydraulic Multiplexer	7
AOI 1.4: Active Combustor Control	53
AOI 1.4.1: Controlled Pressure Fuel Nozzle (CPFN) System	65
AOI 1.4.2: Fuel Multiplexer (FMUX) System	89
Attachment I: State and Parameter Estimation for a Jet Engine – Final Report	115
Attachment II: Control Design & Analysis for the CPFN System – Final Report	247
Attachment III: Neural Networks for NO <sub>x</sub> Emission Prediction – Final Report	291
Attachment IV: FMUX Dynamic Modeling – Summary Memorandum	339





*Aircraft Engines*

*Advanced Control Systems*

# **AOI 1 - Reliable & Affordable Controls Final Review October 5, 1999**

**GE Aircraft Engines  
Woodward Governor  
Parker Hannifin  
Analex  
Florida A&M  
GE CR&D  
PoleStar**

*NASA Critical Propulsion and Noise Technologies*

Participants in the Reliable and affordable controls program included GE Aircraft Engines (program lead), Woodward Governor (design/fabrication/test of hydraulic multiplexer & fuel multiplexer), Parker Hannifin (design/fabrication/test of controlled pressure fuel nozzles), Analex (fuel system dynamic analysis & neural network development), Florida A&M (tracking filter design), GE CR&D (neural network development), and Polestar (hydraulic multiplexer control system rig testing). In addition, CECO performed preliminary design work on a variable displacement vane pump prior to cancellation of this element.



## **Program Overview**

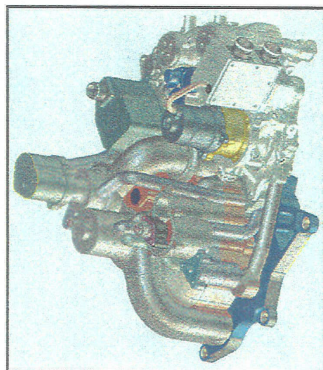
- Original program included 4 elements
  - variable displacement vane pump (VDVP)
  - hydraulic multiplexer (HMUX)
  - model-based intelligent engine control (IEC)
  - active combustor control
    - model-based combustor control logic
    - controlled pressure fuel nozzle (CPFN) system
    - individual fuel cup (IFC) control system
- Program scope was reduced due to funding constraints
  - VDVP element was eliminated
  - IEC element was eliminated
  - Engine and combustor rig tests were eliminated

The original contract award was for four separate elements: variable displacement vane pump, hydraulic multiplexer, intelligent engine control, and active combustor control. Two of these elements, variable displacement vane pump & intelligent engine control, were cancelled due to funding constraints. Because both of these elements were in the preliminary/conceptual design phases when cancelled, this report documents those elements only to the state at which they progressed to at the time of cancellation.

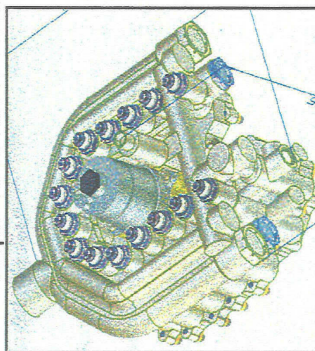
The objective of the hydraulic multiplexer element was to design, fabricate and test a component intended to replace the fuel metering and hydromechanical controllers used on current engines. The hydraulic multiplexer improves reliability by combining the functionality of up to 16 solenoids and servovalves into one component with a single electrically powered force motor. As the functional requirements of modern control systems increases, the hydraulic multiplexer is seen as a key technology for achieving reliability and commercial cost objectives.

The objective of the active combustor control element was to develop intelligent staging and control strategies for low emission combustors and to design, fabricate and test fuel metering and distribution systems for these combustors. This element consisted of three sub-elements: controlled pressure fuel nozzle system, individual fuel cup control system, and model-based combustor control logic.

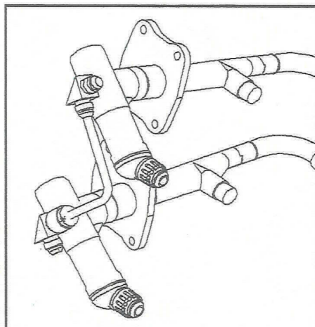




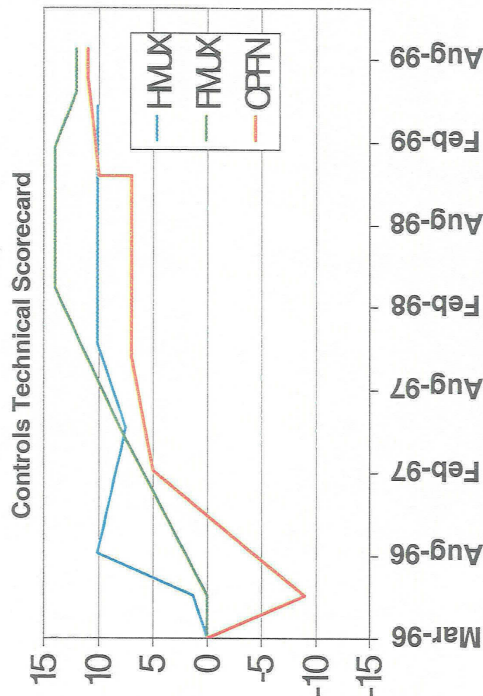
HMUX- Hydraulic Multiplexer  
1 hydraulic component replaces 7 components required to move actuators & valves



FMUX - Fuel Multiplexer  
1 hydraulic component replaces 15 valves required to meter fuel to independent zones



CPFN-Controlled Pressure Fuel Nozzle  
1 hydraulic component replaces 4 fuel staging valves required to sequence fuel.



## Goals / Targets / Objectives

- Develop Fuel/Actuation System with increased functional requirements in support of lower emissions while reducing acquisition cost by 10%, weight by 30 pounds, and removals by 42%.

## Key Accomplishments

- HMUX control/fuel system rig test complete
  - Engine clearance pending risk assessment
- CPFN system tests complete
  - Cleared for engine test
- FMUX system tests complete
  - Cleared for combustor rig test

Management of this program included the creation and maintenance of scorecards which tracked programmatic and technical progress. As shown above, the estimated recurring acquisition costs for each of three elements: hydraulic multiplexer, controlled pressure fuel nozzle system, and fuel multiplexer, were tracked as a percentage reduction relative to the technology in current engines. All three systems met the objective of achieving a 10% or greater cost reduction.

As a result of the effort performed under this contract, both the hydraulic multiplexer and controlled pressure fuel nozzle system were cleared for engine test which is the final step in the technology maturation process. The fuel multiplexer was cleared for combustor rig test which must be followed by an engine test to achieve full maturation.



*Aircraft Engines*

*Advanced Control Systems*

## **AOI 1.2: Hydraulic Multiplexer**

*NASA Critical Propulsion and Noise Technologies*





# HMUX - What Is It?

- HMUX – Hydraulic MUltipleXer
  - Single Force Motor drives Multiple 2<sup>nd</sup>-stage Valves
- Principle of Operation
  - Single Port in Rotating Sleeve is Positioned Sequentially, Serving Multiple Spool Valves
- Impact
  - Fewer Torque Motors, for Increased Reliability & Reduced Cost/Weight
  - Reduced FADEC I/O Requirements

*(HMUX is a product of Woodward Governor Co.)*



What is Hydraulic MultipleXer (HMUX) technology?

The HMUX system consists of a single, high-response force motor and rotating pilot valve that control the positions of multiple second-stage spool valves which, in turn, provide flow to control engine actuation functions such as variable geometry actuators and fuel staging. A single port in a rotating sleeve is positioned sequentially to allow the pilot valve to vary the position of up to 16 second-stage spool valves.

The HMUX system replaces multiple servovalves and their associated FADEC torque motor driver electronics with a single force motor/first-stage pilot valve and FADEC force motor driver circuit, resulting in weight and cost reductions as well as improved reliability due to fewer number of parts.



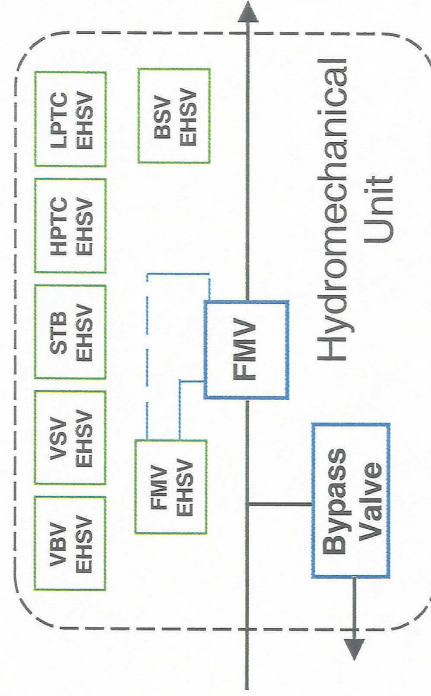
## Conventional Hydro-Mechanical Unit (HMU)

- HMU uses individual Electro-Hydraulic Servo Valves (EHSV's) to control:

- Metered flow (FMV)
- Variable stator vanes (VSV)
- Variable bleed valve (VBV)
- HP turbine clearance (HPTC)
- LP turbine clearance (LPTC)
- Start / transient bleed (STB)
- Burner staging (BSV)

- Each EHSV consists of:

- FADEC powered torque motor
- 1<sup>st</sup> stage valve (typically jet pipe design)
- 2<sup>nd</sup> stage spool valve (power amplification)
- Feedback spring so that EHSV flow is proportional to FADEC commanded torque motor current



Today's turbine engines utilize a complex "Hydro-Mechanical Unit" (HMU) containing many individual servovalves to control fuel flow to the combustor fuel manifolds and the position of engine variable-geometry actuators. A typical large commercial engine HMU incorporates electro-hydraulic servovalves for control of the internal HMU fuel metering, fuel staging and bypass functions as well as additional electro-hydraulic servovalves for the engine geometry actuation system, typically consisting of variable stator vane, variable bleed valve, start/transient bleed valve, high pressure turbine clearance control valve and low pressure turbine clearance control valve actuators.

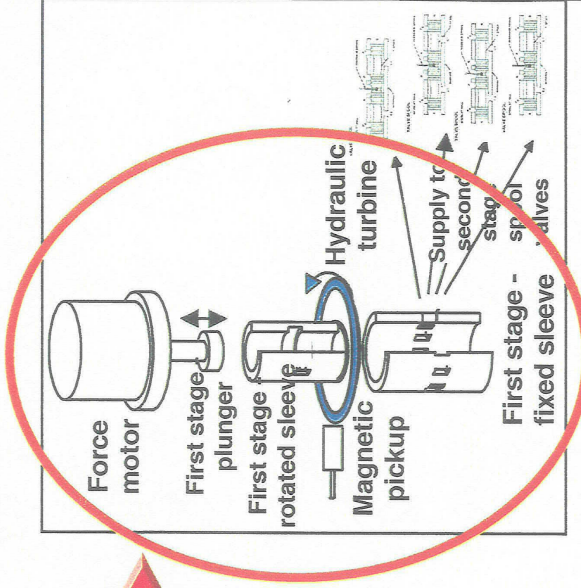
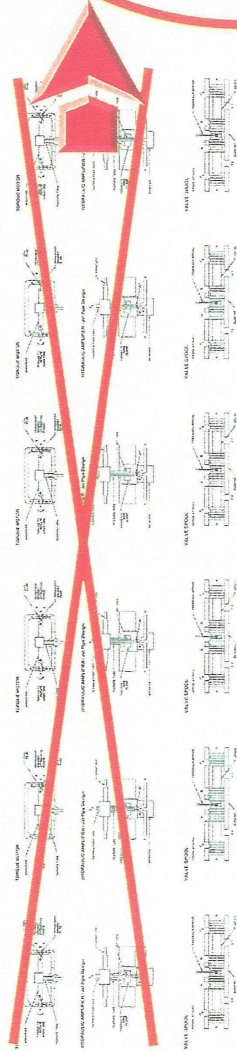
Each of these electro-hydraulic servovalves consists of a torque motor, first-stage valve and second-stage spool valve, and requires a dedicated torque motor driver circuit in the FADEC. In a typical design, the torque motor positions the first-stage valve which directs a low flow, high-energy fluid jet into small ports in order to provide pressure to position the second-stage spool valve. The second-stage spool valve provides the flow necessary to position the end actuation device (e.g. engine geometry actuator, fuel metering valve). A feedback spring is used to couple the second-stage spool valve to the first-stage in order to provide second-stage flow output that is proportional to the FADEC-commanded torque motor current.

While providing a reliable means for obtaining stable, accurate positioning of engine control functions, these servovalves are responsible for a significant portion of the weight and cost of the typical HMU, and each requires a dedicated torque motor driver electronics circuit in the FADEC.





# Hydraulic MULTiplexing (HMUX)



- HMUX feature incorporated into HMU
  - All the torque motors & 1<sup>st</sup> stage servo valves are replaced by a single force motor & a multiplexing type first stage which sequentially services all of the 2<sup>nd</sup> stage spool valves
  - HMU now receives commands to single HMUX force motor instead of multiple torque motors

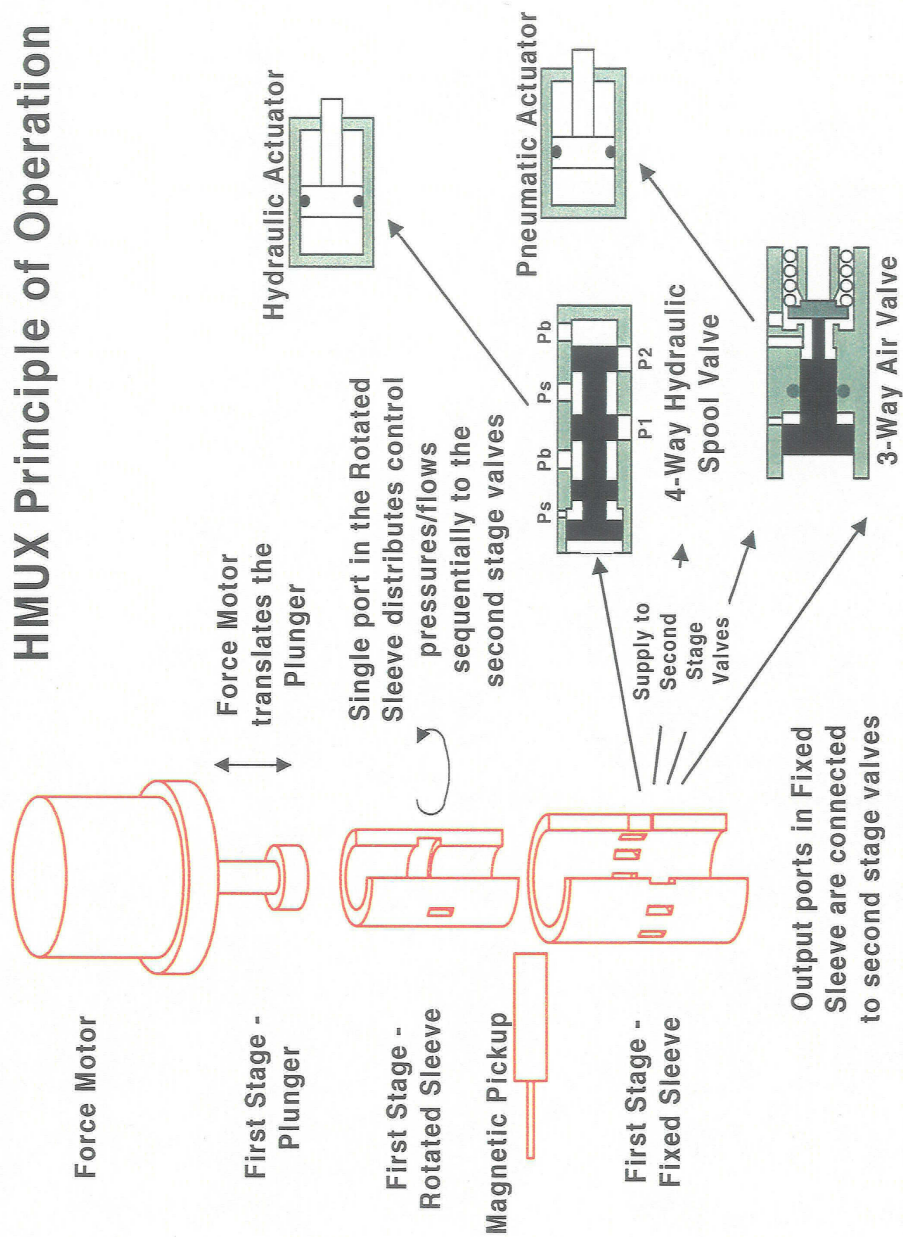
Incorporation of the HMUX system into the HMU results in the replacement of all the electro-hydraulic servovalve torque motors and first-stage valves with a single force motor and multiplexing type first-stage valve. Second-stage spool valves (similar to the electro-hydraulic servovalve second-stage valves), one for each actuation loop, are sequentially positioned by the multiplexing first-stage.

Elimination of the electro-hydraulic servovalves and associated FADEC torque motor driver circuit electronics for the fuel metering, fuel staging and external variable geometry actuation functions results in significant simplification of the HMU, resulting in weight and cost reductions, as well as improved reliability due to significantly fewer piece parts. An additional benefit is reduced FADEC I/O and the resulting reduction in engine electrical cable conductors needed for control of engine fuel and actuation functions.



# HMUX Principle of Operation

## HMUX Principle of Operation





The HMUX principle of operation is as follows:

- 1) The magnetic pickup senses the passing of a tooth on the first-stage rotated sleeve drive train, notifying the HMUX controller that the single port in the rotated sleeve is about to align with a fixed sleeve port. This signal is processed by the HMUX controller.
- 2) The HMUX controller performs the calculations necessary to determine the appropriate force motor current required to position the first-stage pilot valve (i.e. plunger) in order to provide the second-stage valve movement needed to close the actuator position control loop associated with the upcoming fixed sleeve port.
- 3) The FADEC force motor driver provides this electrical current to the force motor to position the first-stage pilot valve.
- 4) The single port in the rotated sleeve opens to the fixed sleeve port, and the appropriate flow is routed to its associated second-stage spool valve.
- 5) The second-stage spool valve moves left or right, as appropriate, to obtain the desired actuator position control loop response.
- 6) The single port in the rotated sleeve rotates past and closes off flow from the fixed sleeve port.
- 7) The magnetic pickup senses the passing of the next tooth on the first-stage rotated sleeve drive train, notifying the HMUX controller that the single port in the rotated sleeve is about to align with the next fixed sleeve port, and the cycle repeats.

Note that, in addition to typical “4-way” second-stage spool valves, the fixed sleeve ports can also be connected to “3-way” valves and discrete (on/off) valves.



# NASA AST Program Overview

- NASA-funded Hydraulic MultipleXer (HMUX) program launched 1Q96
- Original funded NASA AST scope: single-channel, bench-type HMUX to control actuation functions (only) using single-channel electronic controller
- In order to advance HMUX technology more rapidly, scope expanded to engine-mountable “drop-in” replacement for Dual Annular Combustor (DAC) HMU, with full dual-channel, FADEC-based HMUX controller
  - Woodward Aircraft Engine Systems (WAES) & Lockheed Martin Control Systems (LMCS) business agreement put in place to facilitate FADEC hardware & software mods.
  - WAES funded increased scope to develop dual channel, “product-like” HMUX HMU
  - control of Fuel Metering Valve added to HMUX functionality

The NASA-funded portion of the HMUX development program was formally launched in February, 1996. The funded scope of the HMUX program, as defined in the NASA contract statement of work, was to develop an HMUX system for the control of engine variable geometry actuators and combustor fuel manifold staging valves. This HMUX was to be a "bench" type device with a single-channel electronic controller box, all to be designed & fabricated by Woodward Aircraft Engine Systems (WAES).

However, during the subcontract negotiations with WAES, it was determined desirable by both GE and WAES to expand the scope of the HMUX system in order to more rapidly advance and mature HMUX technology, to better position the technology for near-term new engine development programs. To achieve that end, WAES teamed with Lockheed Martin Engine Controls Systems (LMCS), and both companies committed significant additional resources in order to meet the goals of this expanded scope HMUX system development program. The resulting HMUX development program included the following additional features:

- 1) The HMUX would be designed & fabricated to be a "product-like" engine mountable "drop-in" replacement unit for a current large engine dual annular combustor HMU. The GE90 engine HMU was selected as the target application for the HMUX system design.
- 2) The HMUX would have full dual electrical channel capability.
- 3) The HMUX controller would be full dual-channel, incorporated into an engine FADEC, fully integrated with the other engine control functions.
- 4) All of the GE90 HMU control functions, including the fuel metering valve, were to be included in the HMUX system design requirements.





# NASA AST Program Overview

- HMUX system completed 350 hours integrated fuel system rig testing at WAES using engine actuators, fuel pump, modified FADEC & engine model (3/98 - 10/98)
- HMUX system testing commenced on GE control system wet rig (11/98)
  - basic system checkout testing uncovered several FADEC hardware & software problems (i.e. sensor inputs)
  - cold (-65°F) fuel start testing successfully completed

Summary of HMUX system testing:

- 1) Fabrication of the first Actuation Control Module (ACM) completed in September 1997, and successful acceptance test performed.
- 2) Basic HMUX system testing using GE90 engine actuators & control law “tuning” continued at WAES until March 1998.
- 3) The first Fuel Metering Module (FMM) was completed, assembled to the ACM, and successfully passed GE90 HMU acceptance test in April 1998.
- 4) Functional testing of the complete HMUX (i.e. ACM/FMM assembly) commenced in April 1998 using a single-channel lab type electronic controller.
- 5) Full integrated HMUX system testing commenced in May 1998 on WAES’ system test rig using the FADEC-based HMUX controller. This system test rig allows the HMUX control system to run “closed loop” with a GE90 engine model, and utilized the actual GE90 fuel pump & variable geometry actuators to accurately simulate the engine control system behavior.
- 6) System testing and troubleshooting of numerous FADEC hardware & software problems continued through mid-1998. A second HMUX assembly and FADEC were integrated into the test program, and the complete system integration test was completed at WAES in October 1998. (Total of 350 hours system testing at WAES.)
- 7) The HMUX system was shipped to GE Aircraft Engines, and system rig testing at GE commenced in November 1998. Initial GE testing uncovered additional FADEC hardware & software problems with processing of sensor input signals.
- 8) Cold fuel (-65°F) startup testing successfully completed at GE in December 1998.





# NASA AST Program Overview

- HMUX system testing at GEAE completed 5/5/99
  - accels/decelers (large step & stair-step)
  - fuel & actuation control loop stability testing
  - stopcock; power off; power interrupt
  - overspeed governor
  - numerous simulated mission cycles
- 125 hours HMUX operation completed at GEAE with no HMUX mechanical or control problems observed
- Planned on-engine HMUX test dropped due to program funding reduction

Summary of HMUX system testing (cont.):

- 9) Following completion of cold fuel startup testing, FADEC returned to LMCS to correct several I/O problems identified in testing at GE. Both hardware & software modifications were required.
- 10) FADEC returned to GE and HMUX system rig testing resumed in March 1999.
- 11) HMUX system rig testing at GE completed in May 1999. Following tests successfully completed:
  - engine (i.e. system test rig) accelerations & decelerations, both “large” step and “stair-step” throttle inputs
  - stability testing of each primary fuel & actuation control loop (i.e. VSV, VB, fuel metering)
  - engine “stopcock” (i.e. fuel shutoff)
  - 100 msec. power interrupt & power off
  - overspeed governor engagement
  - numerous one-hour simulated mission cycles (i.e. “C-cycles”)
- 12) 125 hours of HMUX closed-loop system rig testing completed at GEAE with no significant HMUX mechanical or control loop problems noted.
- 13) Planned on-engine HMUX test under NASA AST funded program was cancelled due to program funding reductions.



# HMUX System Overview

- Designed to meet DAC HMU functional requirements
- Replaces:
  - 6 HMU TM's & solenoids with 1 HMUX
  - 6 FADEC electrical drivers with one driver
- Controls FMV, VSV, VBV, STB, HPTACC, BSV functions
- Consists of Actuation Control Module (ACM) and Fuel Metering Module (FMM)
  - ACM includes HMUX force motor, 1<sup>st</sup> & 2<sup>nd</sup> stage valves, fuel turbine & flow distribution manifold
  - FMM includes FMV, O/SG, press./shutoff, B/P & staging valves
- Fuel turbine provides HMUX rotation
- Separate gearshaft input for O/SG



As stated previously, the HMUX system was designed as a functional replacement for the GE90 dual annular combustor HMU. To this end, the HMUX HMU eliminates all six torque motors and solenoids of the conventional HMU, and replaces these with one force motor, one first-stage pilot valve with rotated sleeve (with single port) & a fixed sleeve (with 16 ports), and five second-stage spool valves. The HMUX controls the following engine functions:

- Fuel Metering Valve (FMV) [*controlled directly by HMUX first-stage*]
- Variable Stator Vane actuators (VSV)
- Variable Bypass Valve actuators (VBV)
- Start/Transient Bleed actuator (STB)
- High Pressure Turbine Active Clearance Control actuator (HPTACC)
- Burner Staging Valve (BSV)

The HMUX HMU consists of two modules: Actuation Control Module (ACM) and Fuel Metering Module (FMM). The ACM consists of the HMUX force motor, first- and second-stage valves, fuel-driven turbine to spin the rotated sleeve, and a flow distribution manifold to route the first-stage flow from each of the 16 ports to the appropriate second-stage spool valve (or directly to the FMV). Note that second-stage spool valves for selected functions (e.g. FMV, VSV & VBV) are serviced by more than one of the 16 first-stage ports in order to improve dynamic response for critical control loops. The FMM consists of the FMV, overspeed governor, pressurizing/shutoff valve, bypass valve and combustor staging valve. These FMM functions are essentially the same as those found in the conventional HMU. A gearshaft input driven by the engine gearbox is used to provide rotation for the overspeed governor, but is not used by the HMUX.



## HMUX System Overview

- FMV directly controlled by 1<sup>st</sup>-stage (no 2<sup>nd</sup>-stage valve)
- Dual-coil linear force motor drives 1<sup>st</sup>-stage valve
- Dual-coil magnetic pickup
- Dual-channel LVDT for FMV position feedback
- 68332 processor on modified FADEC IOP board controls HMUX operation
  - magnetic pickup signal input; force motor current output
- Fail-safe features (power loss):
  - VSV, VB, STB & HPTACC actuators driven in preferred direction @ desired rate
  - force motor null bias drives FMV closed @ desired rate
  - fail fixed BSV

Note that there are only five second-stage spool valves in the HMUX ACM even though the six torque motors & solenoids of the conventional HMU were eliminated. This is accomplished by directly controlling FMV position with HMUX first-stage flow, with no second-stage spool valve needed. (This is possible because the FMV control piston is much smaller than the pistons for the other actuators, so requires less flow to modulate.) However, in order to provide sufficient FMV control flow to meet its engine response requirements, five of the 16 first-stage ports are used for FMV control, resulting in an FMV position update rate of  $5 \times \text{HMUX rotational speed}$  (that is, approximately  $5 \times 1200 \text{ RPM}$ , for an update rate of 100 Hz).

Other features of the HMUX include a dual-coil linear force motor to drive the first-stage pilot valve, dual coil magnetic position pickup and dual-coil FMV position feedback LVDT, matching the dual-channel GE90 FADEC architecture and providing full electrical redundancy for the HMUX. The HMUX controller utilizes two dedicated Motorola® 68332 microprocessors (one per FADEC channel) installed on modified FADEC I/O boards (designated "IOP" boards). These microprocessors process the magnetic pickup position input signals, perform the control loop calculations, and provide the appropriate force motor current output for each HMUX port update.

Additional design features were incorporated to meet baseline GE90 engine HMU failsafe characteristics. These include second-stage spool valve features to drive engine actuators in the preferred direction at a controlled velocity upon total power loss to the FADEC and HMUX controller. A null bias (i.e. controlled flow with zero input current) is designed into the force motor in order to drive the FMV closed at a specified rate upon loss of electrical power. The BSV function is designed to fail fixed (i.e. "as is").

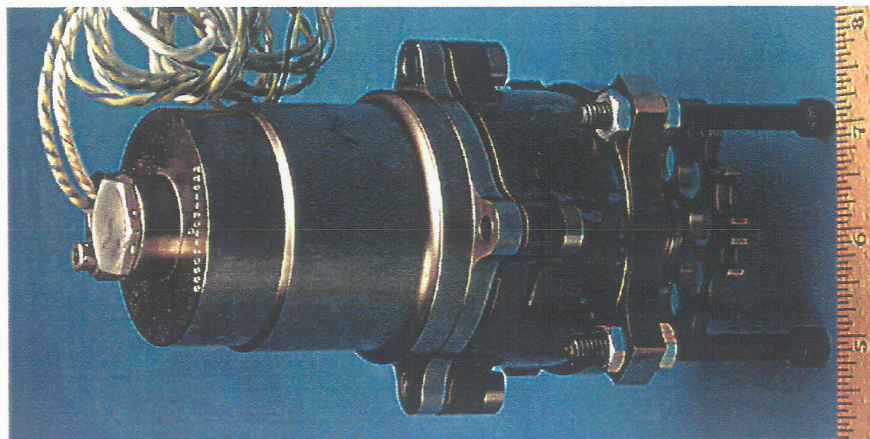




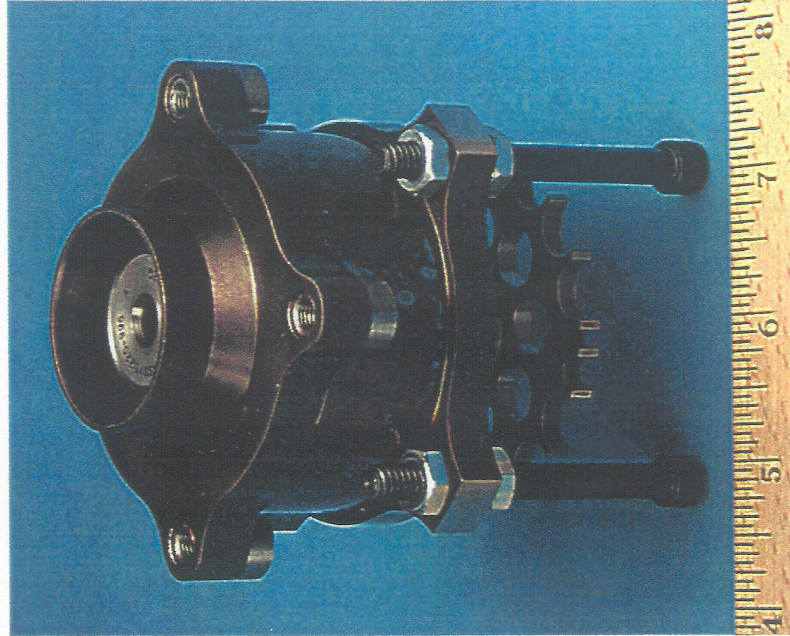
*Aircraft Engines*

*Advanced Control Systems*

## HMUX First-Stage Assembly



**Complete First-Stage  
Assembly**



**First-Stage Rotated  
Valve Assembly**

*NASA Critical Propulsion and Noise Technologies*

A view of the complete HMUX first-stage assembly is shown in the left-hand photograph, above. The linear force motor with its attached electrical leads is visible at the top, with the rotated valve assembly and toothed position wheel below.

A close-up view of the first-stage rotated valve assembly is shown in the right-hand photograph, above. Visible at the top is the end of the first-stage pilot valve (which is coupled to and driven by the force motor). The rotated sleeve containing the single port for updating each of the 16 fixed ports is contained within the central portion of the assembly and is coupled to the toothed wheel visible at the bottom. The toothed wheel has one tooth for each of the 16 fixed ports. The magnetic pickup detects the passing of each tooth in order to synchronize positioning of the first-stage pilot valve with the appropriate fixed port. Note, however, that there is a double tooth visible in the photograph – this double tooth is used to provide a “one per revolution” double pulse, as it is critical to HMUX operation that each position loop update be calculated and the correct first-stage flow delivered for the appropriate control loop. The double tooth provides a synchronizing pulse that is detected by the HMUX controller to ensure that each cycle of position loop updates is correctly synchronized. In the event that synchronization is lost, the HMUX controller provides zero force motor current (i.e. positions the first-stage valve at null) until the double pulse is unambiguously detected and synchronization is established. This feature is utilized on every engine startup and following any HMUX controller or FADEC electrical power interruption.

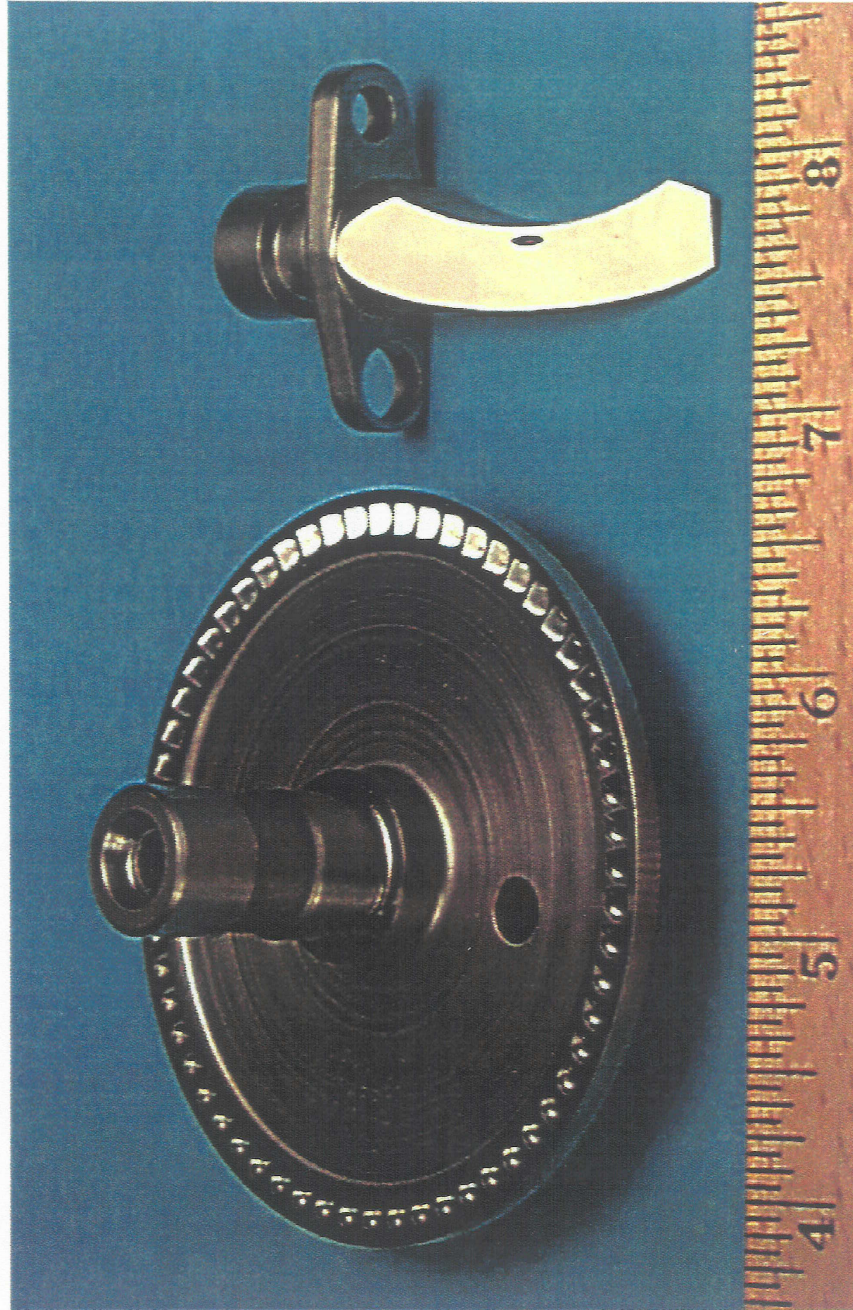




*Aircraft Engines*

*Advanced Control Systems*

## HMUX 1<sup>st</sup>-Stage Fuel Impulse Turbine



*NASA Critical Propulsion and Noise Technologies*

The fuel-driven turbine wheel is shown on the left, with the fuel nozzle shown on the right. The impulse turbine contains numerous "buckets" (visible on the top of the wheel near the outer edge). The flat portion of the fuel nozzle is installed over the turbine buckets with a small clearance gap, and a high velocity fuel jet exits the nozzle and impinges on the turbine buckets, spinning the turbine at several thousand RPM.

This design allows HMUX operation without an engine gearbox drive input. For the HMUX HMU designed and fabricated under the AST program, this feature provided complete drive train independence between the gearbox driven overspeed governor and the HMUX, a desirable safety enhancement. For a HMU application without a hydro-mechanical overspeed governor, use of the turbine drive provides the freedom to mount the HMUX HMU in locations other than on the gearbox, a potential weight and cost advantage. (Gearbox weight and cost are reduced because a gearbox drive pad is eliminated.)

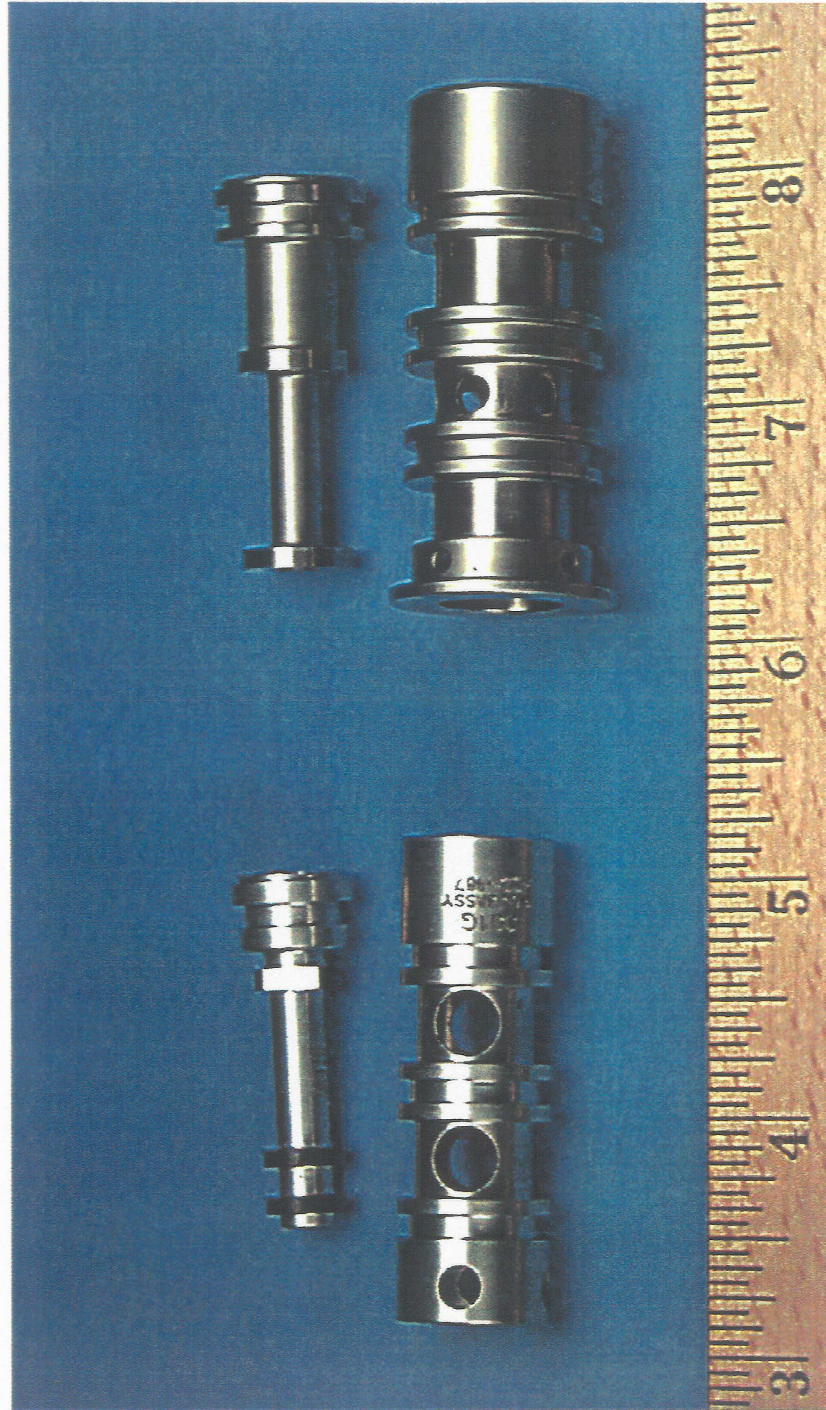




Aircraft Engines

Advanced Control Systems

# HMUX 2<sup>nd</sup>-Stage Control Valves



NASA Critical Propulsion and Noise Technologies

Two typical second-stage spool valves are shown in the above photograph.

The spool valve shown on the left is a 3-way valve used to control “discrete” (i.e. on/off) functions. For the GE90 HMUX design completed under the AST program, this valve was used to control the BSV position which is either “open” or “closed”. This spool valve “latches” in the last commanded position, so therefore does not require additional position updates from the HMUX first-stage in order to maintain a fixed BSV position.

The spool valve shown on the right is a 4-way valve used to control modulated functions, such as the HPTACC and STB actuators. This spool valve, as do all the spool valves controlling modulated functions, receives position updates from the HMUX first-stage each time the rotated sleeve aligns with the appropriate fixed sleeve port, at least once per revolution.

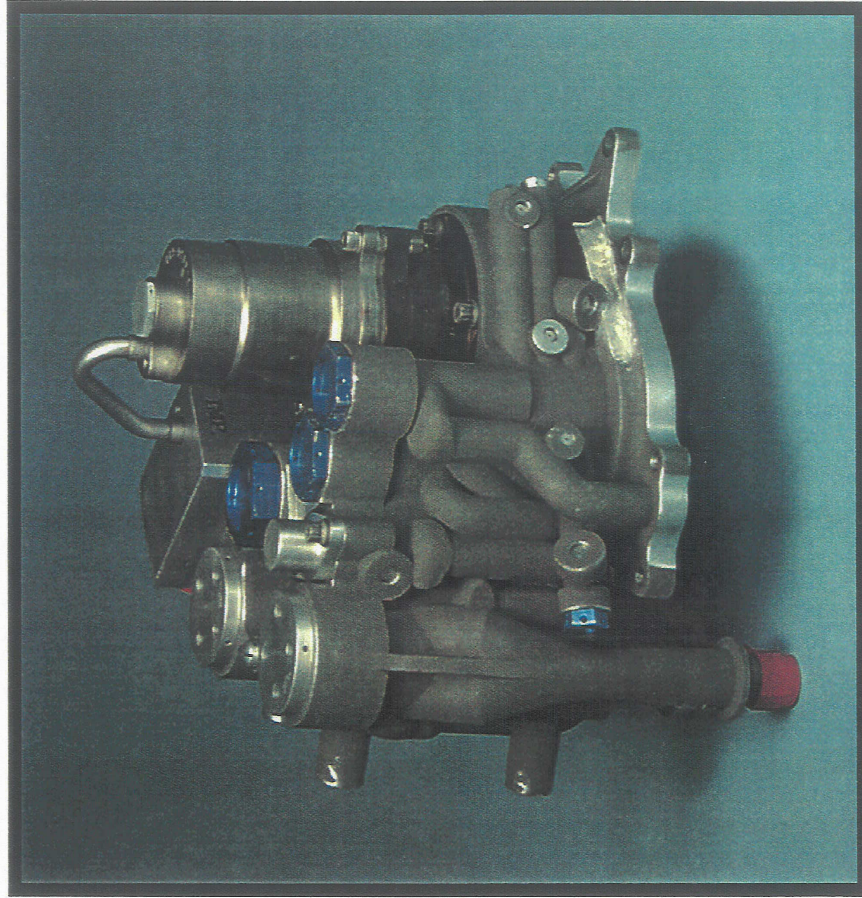




*Aircraft Engines*

*Advanced Control Systems*

## NASA/AST HMUX Actuation Control Module:



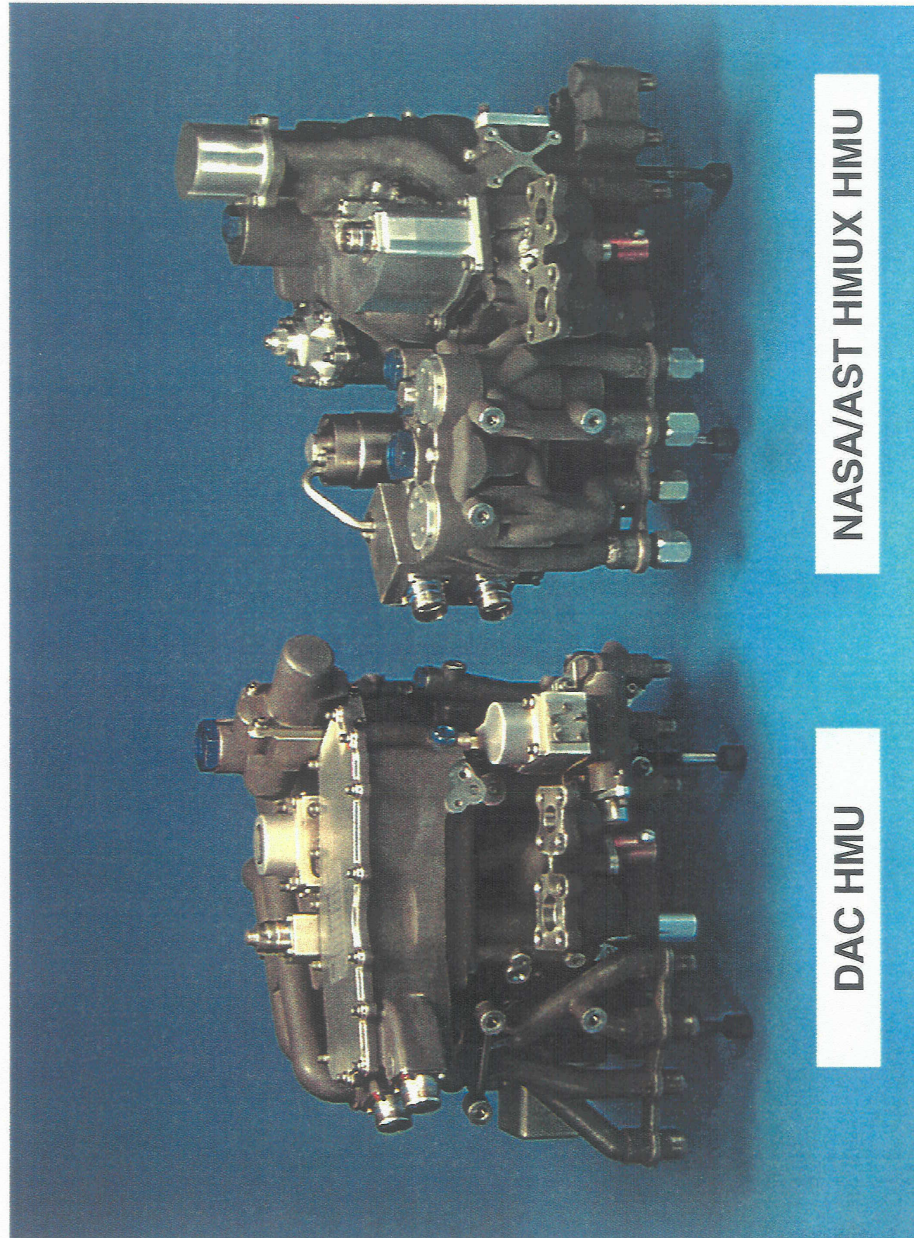
*NASA Critical Propulsion and Noise Technologies*

The above photograph shows the complete Actuation Control Module (ACM) portion of the HMUX HMU, which contains all the HMUX subassemblies. The ACM bolts to the Fuel Metering Module (FMM) to form the complete HMUX HMU assembly. The linear force motor is visible as the cylindrical object in the upper right-hand portion of the photograph. The two silvery colored objects on the left are the end caps for the large VSV and VB V second-stage spool valves. The three blue colored end caps mark the locations of the two discrete and one modulated second-stage spool valves (see photograph on previous page). The contoured flow passages visible in the ACM housing provide the routing of second-stage valve control flows from the ACM to the FMM, from which piping connections are made to the engine actuators.





## HMU Comparison:



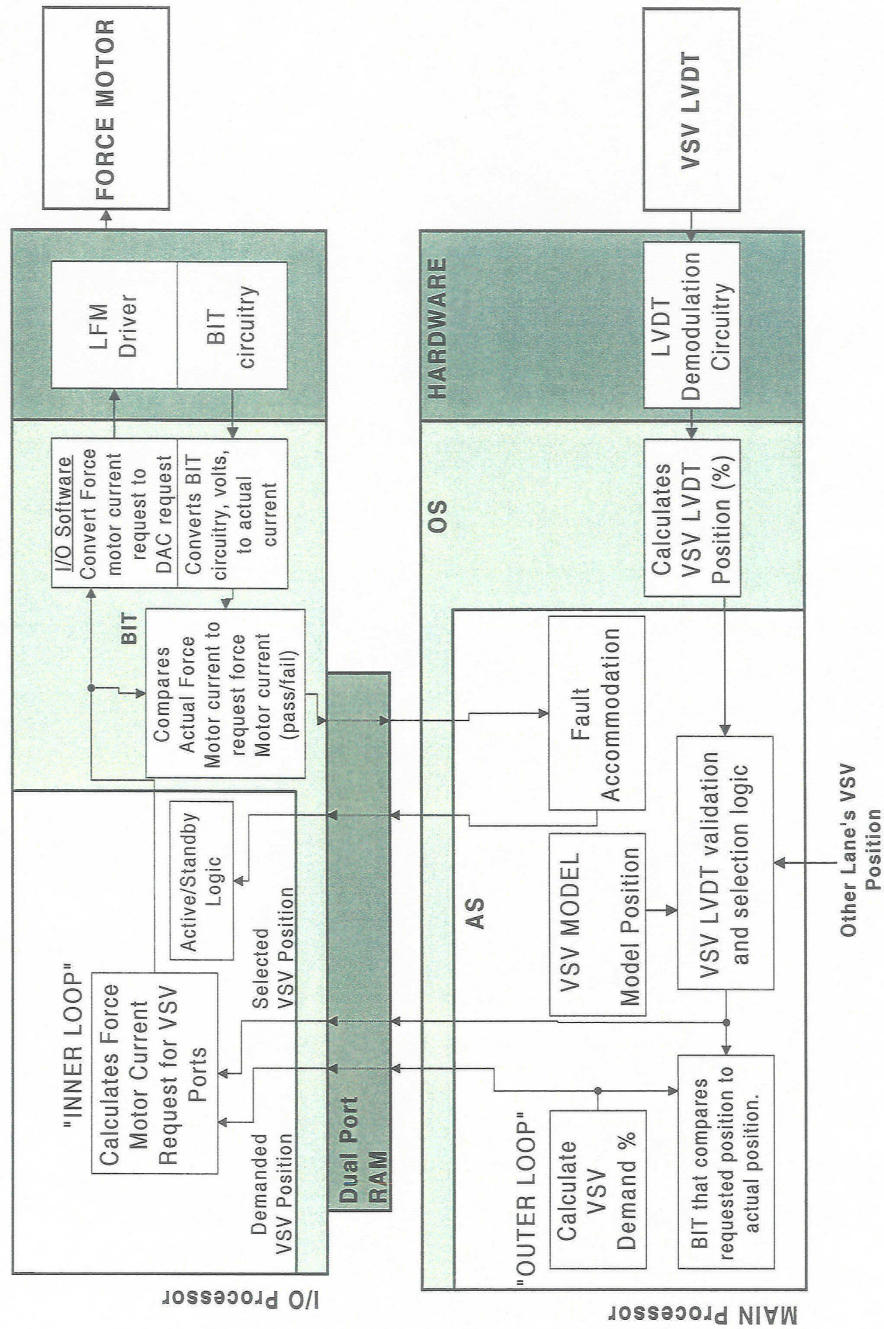
The above photograph shows the GE90 conventional DAC hydro-mechanical unit (HMU) on the left and the complete NASA AST HMUX HMU assembly on the right, which is functionally equivalent. This photograph shows how the ACM (from previous page) is mounted onto the FMM to form the complete HMUX HMU assembly.

It can be seen from the photograph that the HMUX HMU is physically smaller than the DAC HMU, but it retains the same fluid interfaces in order to meet the same engine interface requirements. The two metered fuel exit ports are visible in the center of each view. The FMV LVDT for the HMUX HMU is under the silvery colored cover visible at the upper right. The fuel shutoff valve is under the silvery cover with the electrical connector mounted on top. The top of the bypass valve cavity is visible slightly to the left & below of the FMV LVDT cover. The top of the overspeed governor assembly is visible slightly to the left & below of the bypass valve.





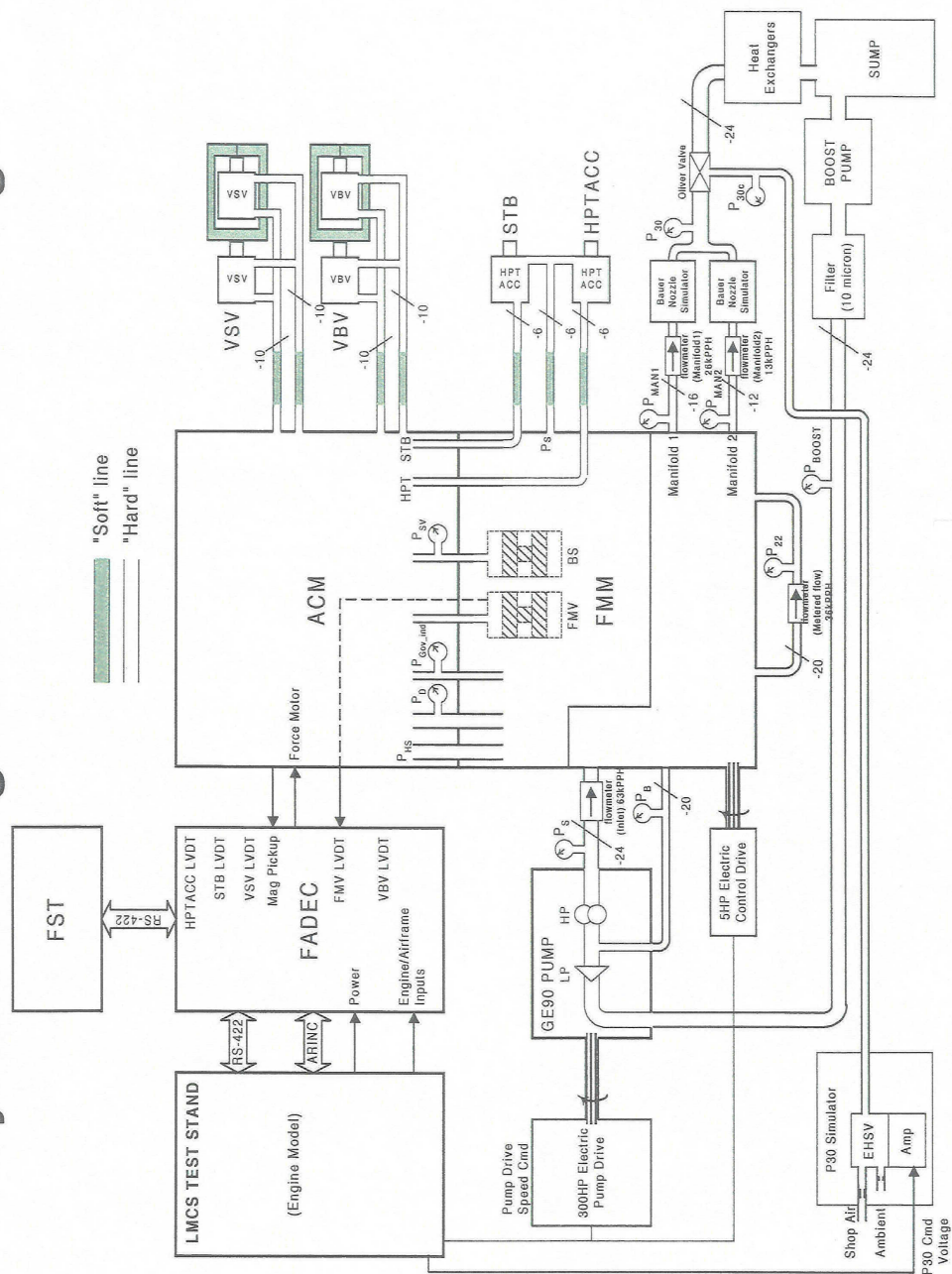
# HMUX Control Law Block Diagram



The HMUX control law block diagram shown above shows the functional path for the execution of the control laws for a typical actuator position control loop such as VSV:

- 1) The VSV L VDT position feedback signal enters the main processor board and is demodulated and converted to digital (refer to lower, right-hand portion of diagram).
- 2) The Operating System (OS) uses the demodulated, digitized values to calculate VSV position and converts this position to engineering units (%). This value is passed to the Application Software (AS) for comparison to values from other FADEC channel and from internal analytical model, and a “select” VSV position value determined.
- 3) The selected VSV position is passed through dual-port RAM (DPRAM) to the HMUX I/O Processor (IOP) board. The main processor performs the VSV “outer loop” calculation which generates a VSV Demand position based on current engine state & control schedules which is also passed through DPRAM to the IOP.
- 4) The IOP software uses the VSV Demand and actual (i.e. L VDT) positions to perform the “inner loop” calculation to determine the appropriate force motor current request needed to move the VSVs toward the Demand position (i.e. to “zero-out” the position error).
- 5) The IOP-based linear force motor (LFM) current driver is commanded by the IOP software to generate the desired current to the LFM. A built-in test (BIT) loop constantly monitors actual LFM current and compares to demanded current.
- 6) The LFM responds to the driver current to position the first-stage pilot valve to the appropriate position to provide flow to the VSV second-stage spool valve in order to obtain the desired VSV actuator response.

# System Integration Test Wet Rig





The above schematic shows the functional layout of the test rig used for system integration testing of the HMUX system. This rig is called a “wet” rig since it utilizes an engine fuel pump, heat exchangers, fuel nozzle simulators, variable geometry actuators and other components which operate using real fuel to simulate the engine fuel delivery system. An analytical engine model is used to simulate the response of the engine in the system rig. The fuel pump is driven by an electric drive stand which is controlled by the engine model computer to run at the appropriate speed, based on the model-calculated engine core speed (i.e. N2). The engine FADEC monitors some physical inputs such as actuator position & N2, and provides the appropriate control outputs to the various control loops (e.g. FMV, VSV) based on throttle request input. Other FADEC inputs (e.g. engine cycle pressures, temperatures & fan speed, NI) are calculated by the engine model and supplied to the FADEC as external simulated inputs or across a data bus.

Testing the HMUX system in this integrated test rig provides a comprehensive test of the control system (within the limitations of engine model fidelity) but at much lower cost and without the risk associated with actual on-engine testing. In fact, even when engine testing is planned, wet system rig testing is often performed in advance, to gain confidence in the capabilities of a new control system.

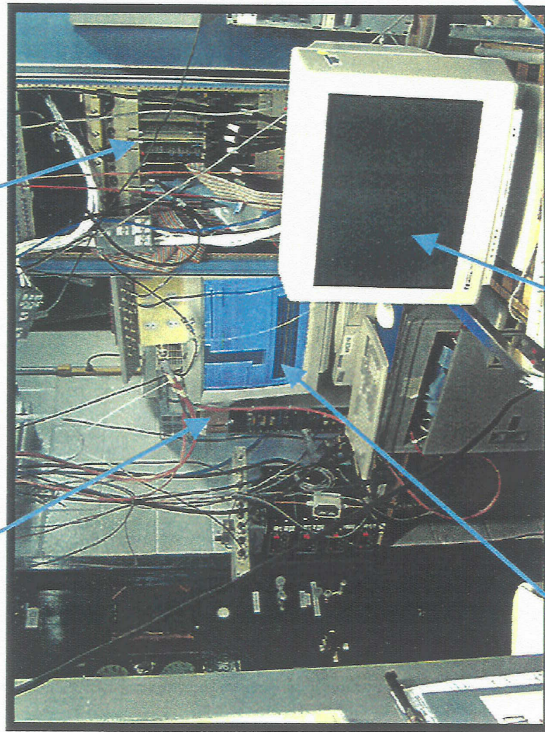


## HMUX System Rig Test at WAES

FADEC  
w/ HMUX Control

Engine Model Host

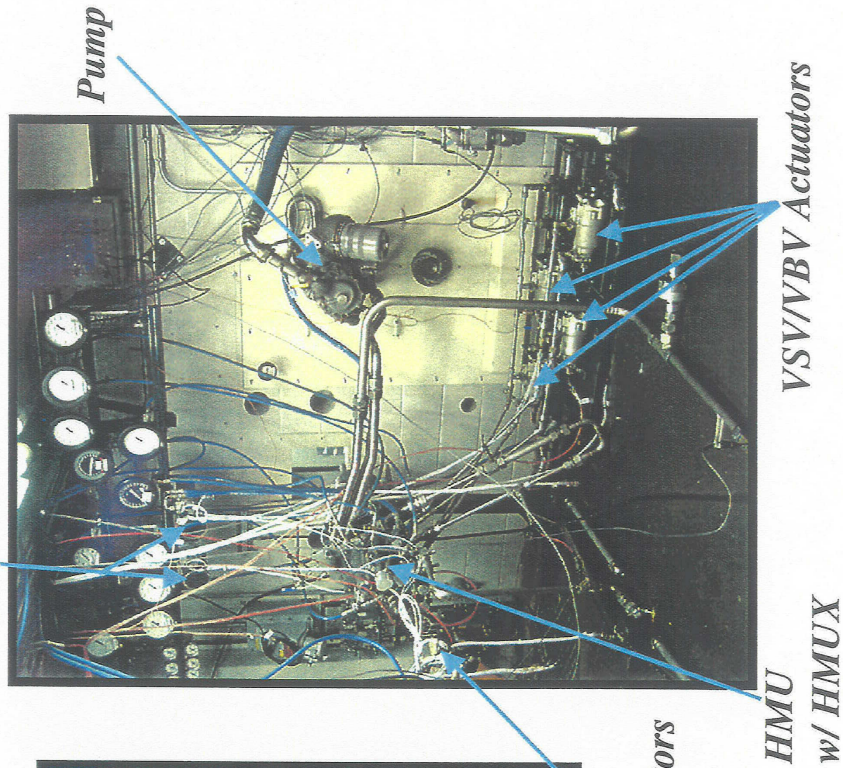
HPTACC/STB  
Air valves



HMUX  
controller  
interface

Nozzle Simulators

FADEC/Engine-model  
interface



Pump

HMU  
w/ HMUX

VSV/VBV Actuators

The above photograph shows portions of the system integration test rig at WAES.

The system test rig control room computer interfaces are shown in the left-hand photograph, with the HMUX controller interface computer shown on the left and the FADEC interface computer on the right. A portion of the FADEC is barely visible to the left of the HMUX controller interface computer. The rack visible above the FADEC interface computer contains the computer on which the analytical engine model is resident. This rack also contains the various I/O boards used to provide engine model simulated values to the FADEC.

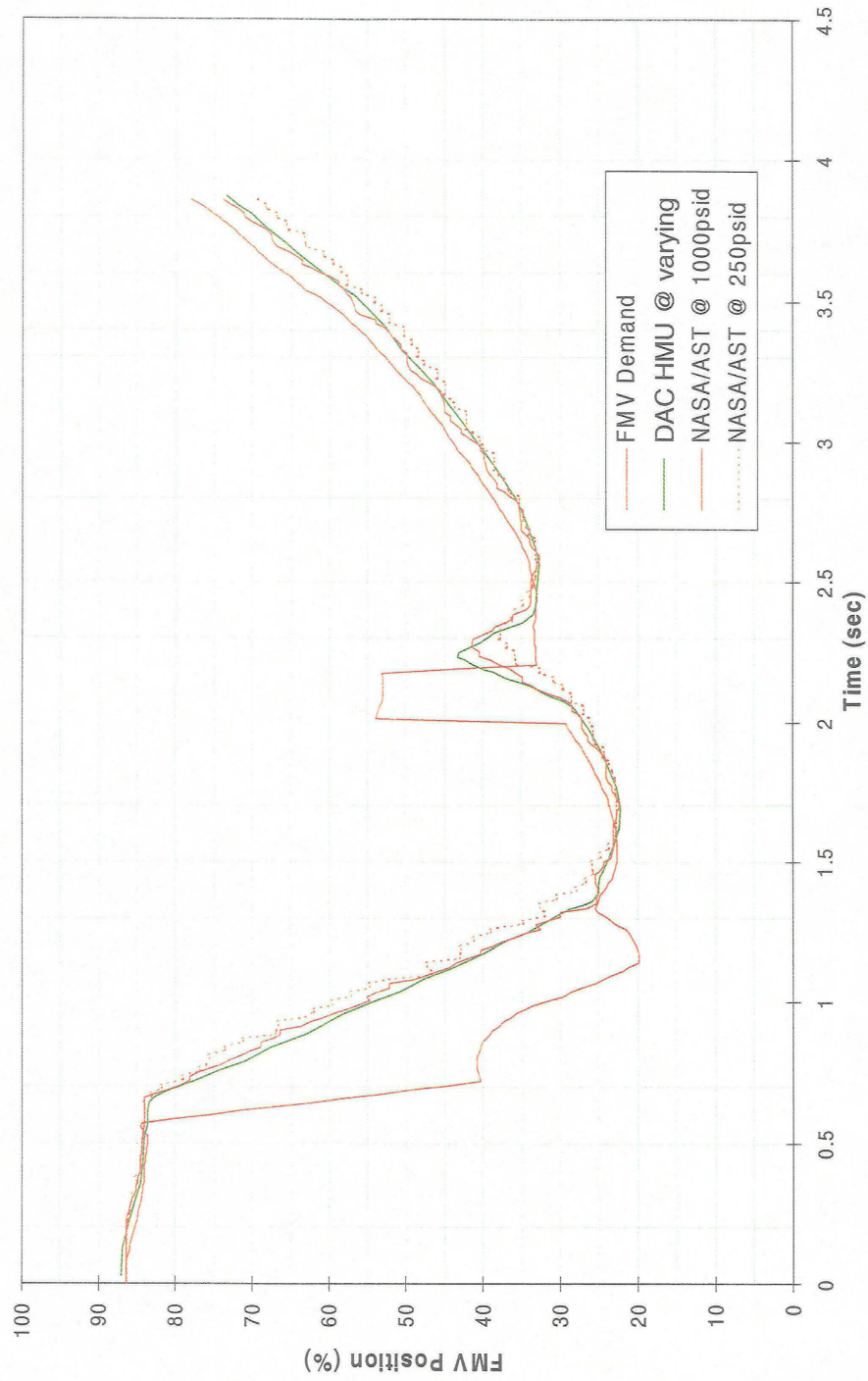
The system rig test cell is shown in the right-hand photograph, with the HMUX HMU and GE90 engine fuel pump clearly visible. Also shown are the GE90 engine VSV & VB V actuators (on floor, at lower right) and the STB and HPTACC air valves (mounted on rig structure, at upper left). The fuel nozzle simulators which provide a backpressure on the fuel system are shown in the middle left region of the photograph. The fuel nozzle simulators are controlled by the engine analytical model computer to provide a fuel system backpressure equivalent to the nozzle pressure drop + combustor discharge pressure.





## HMUX FMV Performance:

FMV Rapid Decel Response

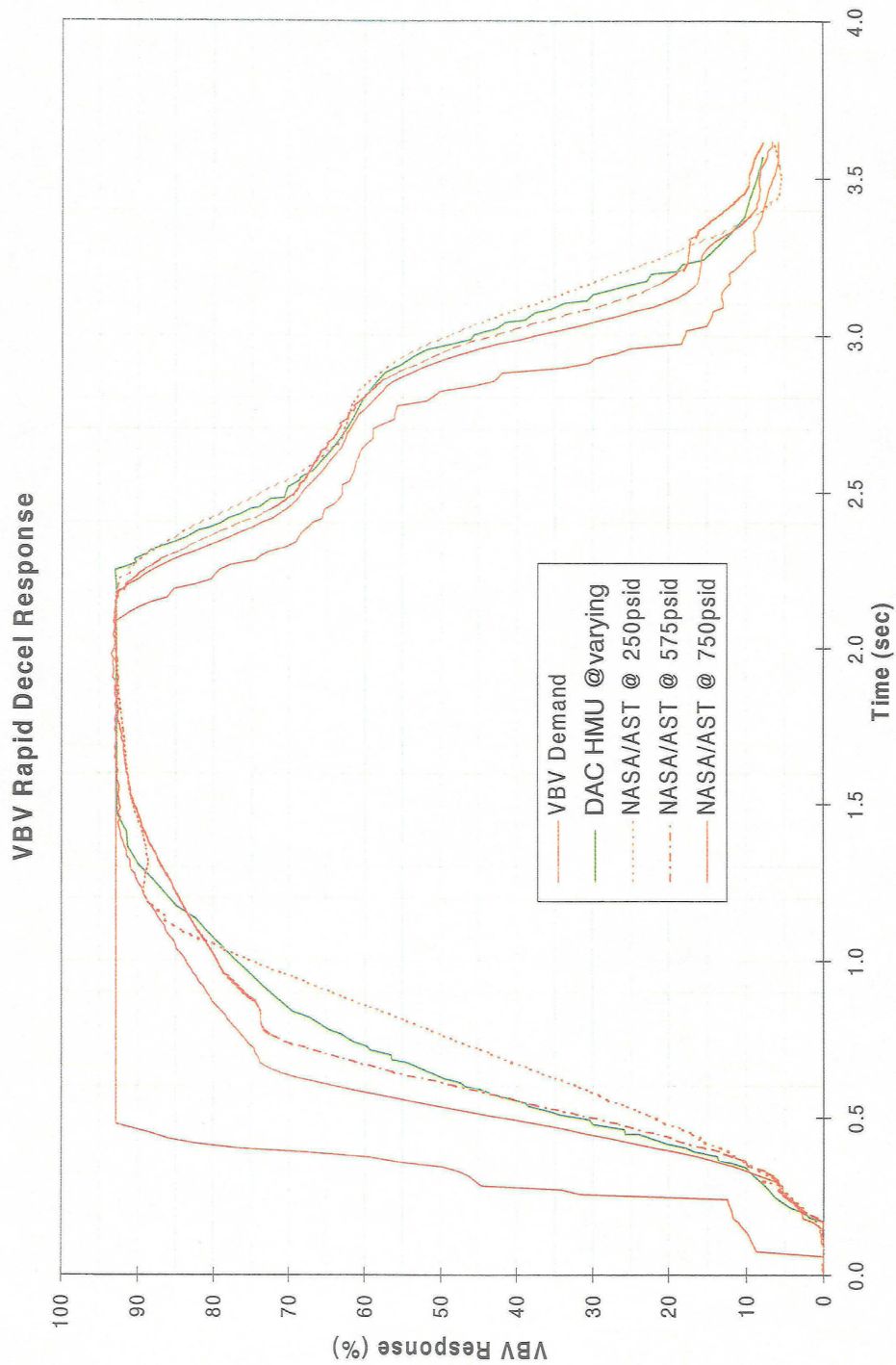




The above curves show Fuel Metering Valve (FMV) response for both the HMUX and conventional DAC HMUs to a rapid decrease followed by a more gradual increase in fuel flow demand, typical of a rapid engine deceleration transient. Note that the HMUX FMV response tracks the DAC FMV very well, although with more discrete steps visible in the rapidly changing portion of the transient, reflecting the pulsed nature of the HMUX as it updates FMV position. Note that the lag of the FMV response to demand is similar for both HMUX and DAC FMVs, a design goal. Some degradation in HMUX FMV response at a fuel system pressure of 250 psid relative to the 1000 psid response is also evident from the curves. The actual fuel system pressure varies during the transient, so the actual HMUX FMV response over the transient varies between the 1000 psid and 250 psid curves.



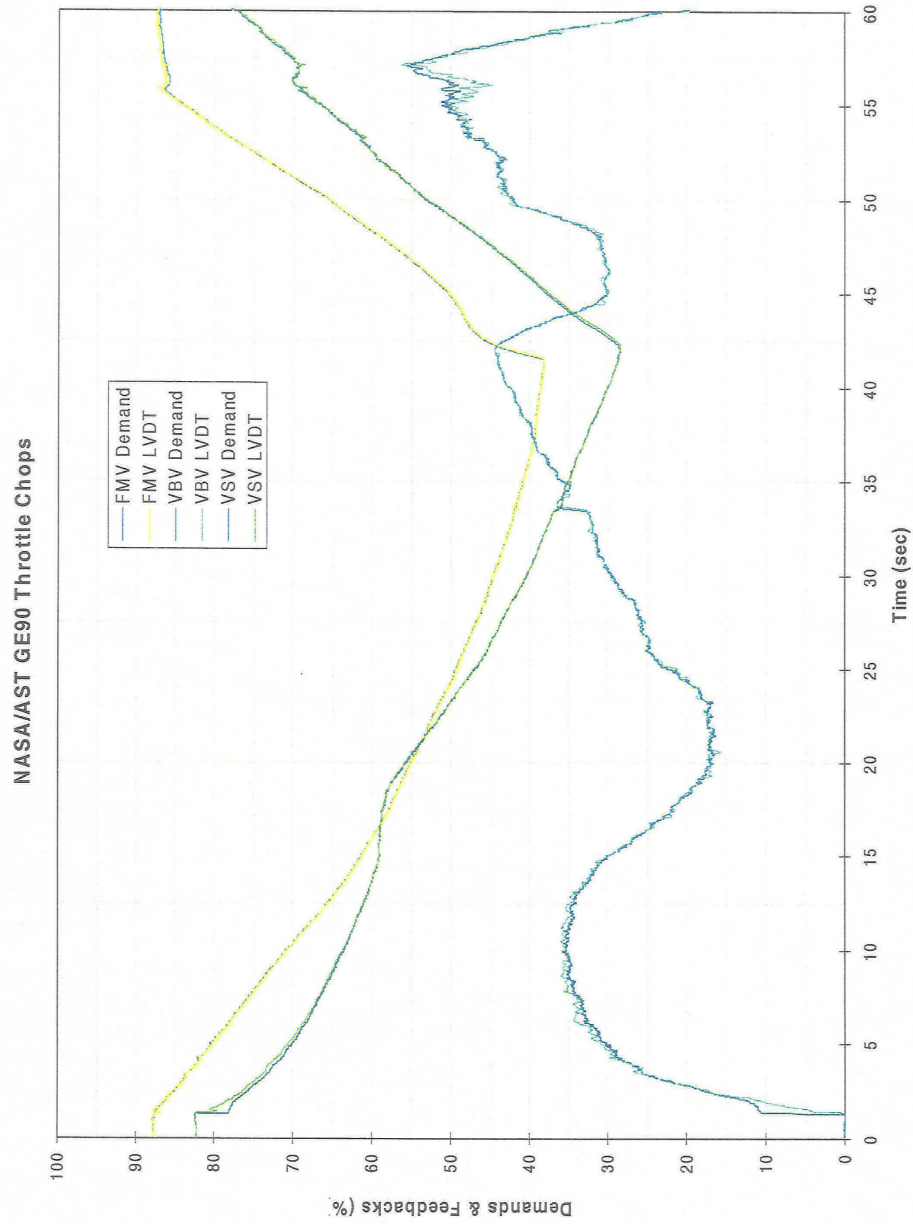
## HMUX VBV Performance:



The above curves show Variable Bypass Valve (VBV) response for both the HMUX and conventional DAC HMUs to a step increase followed by a rapid decrease in VBV position demand, typical of a rapid engine deceleration transient. For this transient, the HMUX VBV response is actually faster than that of the DAC VBV at higher fuel system pressures, but otherwise follows the shape of the DAC VBV response curve very closely. The HMUX VBV response at 250 psid lags the DAC VBV response somewhat, but, as in the case of the FMV response, the actual fuel system pressure varies during the transient, so the actual VBV response over the transient varies between the 750 psid and 250 psid curves.



## Performance During Throttle Chop





The above curves show the HMUX system FMV, VBV and VSV responses to an engine throttle chop from high power followed by an acceleration. As can be seen from these response curves, all three actuation control loops track their demand curves very closely. This type of engine throttle transient provides a good picture of overall control system response capabilities. The above curves are evidence that the HMUX control system is capable of meeting the response requirements of multiple position control loops simultaneously, even during a rapid transient.



## NASA/AST HMUX Program Conclusions

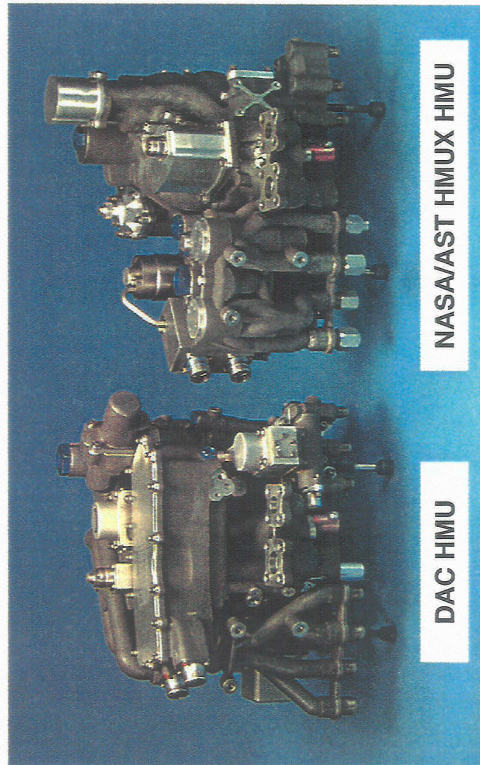
- Hydraulic MULTipleXing has advantages over existing control systems which use servovalves and solenoid valves
  - Cost
  - Parts Count
  - Weight
  - Reliability
  - Maintainability
  - Electrical Power Consumption (FADEC)
- Comprehensive component-level and system rig testing demonstrated performance functionally equivalent to conventional control systems
- HMUX has been shown to be a viable alternative for engine control systems

The Hydraulic MUltipleXer (HMUX) system designed, fabricated and demonstrated under the AST program has proven the viability of utilizing HMUX technology in the control systems of large complex turbofan engines. The comprehensive component-level testing performed at WAES, and system integration testing performed both at WAES and GE using a system rig running closed loop with an analytical engine model have demonstrated HMUX control system performance that is functionally equivalent to that of a conventional control system.

In addition, by fabricating a fully functional dual-channel HMUX system under the AST program, a valid basis was established for estimating the advantages of HMUX technology in production applications. These HMUX advantages include reductions in cost, overall parts count, weight & FADEC power consumption, and improvements in reliability and maintainability. Estimates of the specific benefits for the large turbofan engine application targeted by this program are shown on the next page.



## GE90 DAC-II HMU Vs. HMUX Comparison



DAC HMU

NASA/AST HMUX HMU

NASA AST HMUX	
Cost savings	22.5 % (HMU)
Weight savings	14.4 % (HMU - while maintaining existing interfaces)
IFSD improvement	14.3 %
Reliability improvement	30.6 %
Parts count reduction	44.7 % (HMU), 19.4 % (ECU)
Fault isolation	improved
Maintainability	improved



The above table contains estimates of quantified benefits of the HMUX control system as compared to a conventional control system for a large commercial turbofan engine. These estimates for the HMUX HMU system are based on a comparison to the baseline DAC HMU used on the GE90 engine application.

The cost savings are primarily due to the elimination of the relatively costly electro-hydraulic servovalve torque motors and solenoids used in the conventional HMU.

The weight savings are primarily achieved by improvements in packaging that are possible due to elimination of torque motors & solenoids. The heaviest portion of the conventional electro-hydraulic servovalves & solenoids are the metal bodies containing the second-stage spool valves which are functionally replaced by second-stage valves in the HMUX ACM subassembly. Since the HMUX does not require the mechanical coupling of second-stage valves to the first-stage, these spool valves can be packaged very efficiently and compactly in the HMUX, resulting in substantial weight savings.

The improvements in in-flight shutdown (IFSD) & reliability are directly related to the total parts count reduction achieved by the HMUX system. Total reliability is based on a rollup of individual part failure rates, so it is improved. Since several of the eliminated parts (such as certain torque motors) can each cause an IFSD upon failure, by combining these functions into a single multiplexed first-stage the overall IFSD rate is reduced.

The two benefits of improved fault isolation and maintainability are the result of the on-board diagnostics capability of the HMUX with its dedicated microprocessor. A significant element of the HMUX software development was in the area of fault monitoring and accommodation, resulting in the improved diagnostics capabilities.

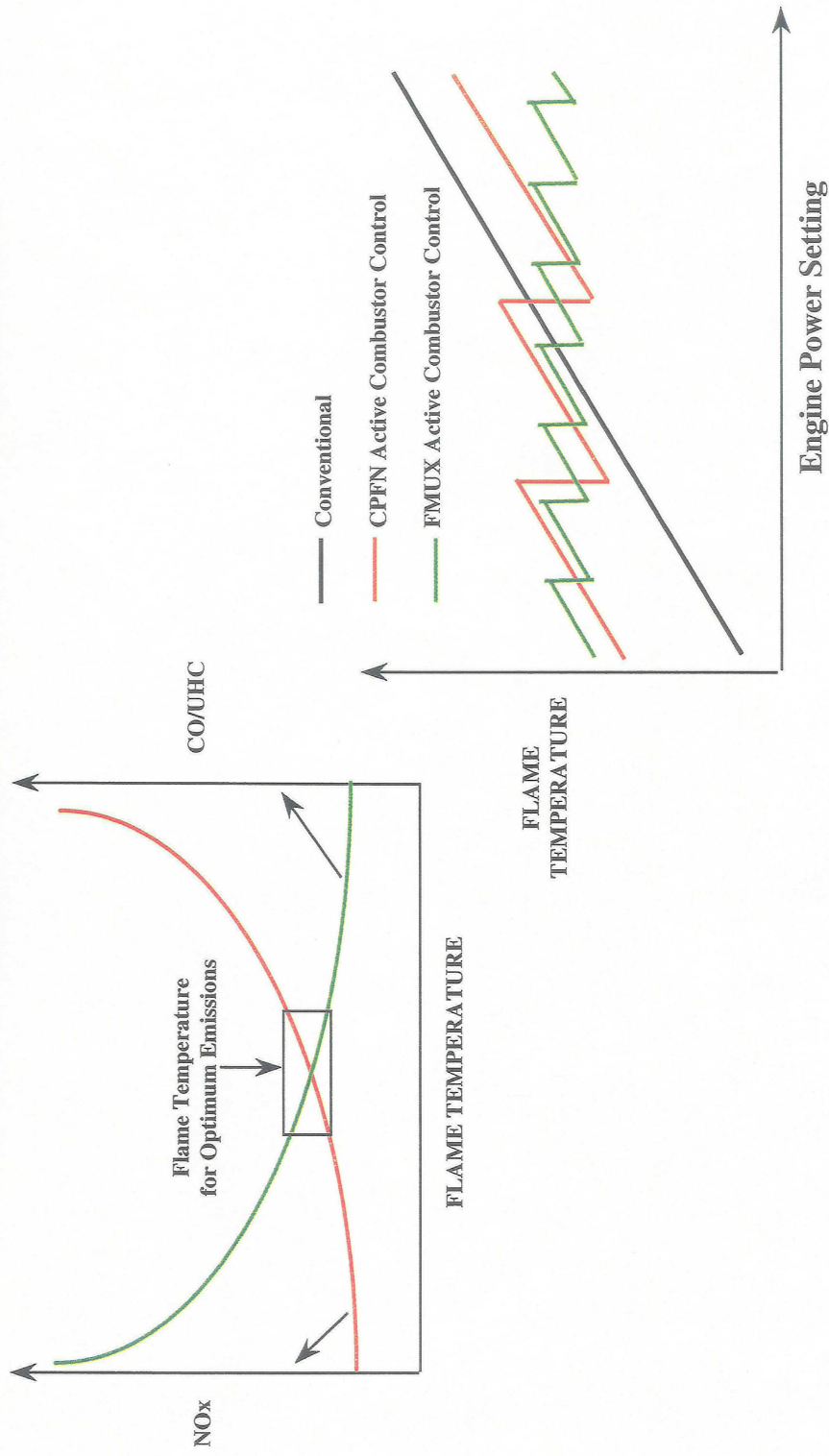


## **AOI 1.4: Active Combustor Control**





## Active Combustor Control - CPFN & FMUX



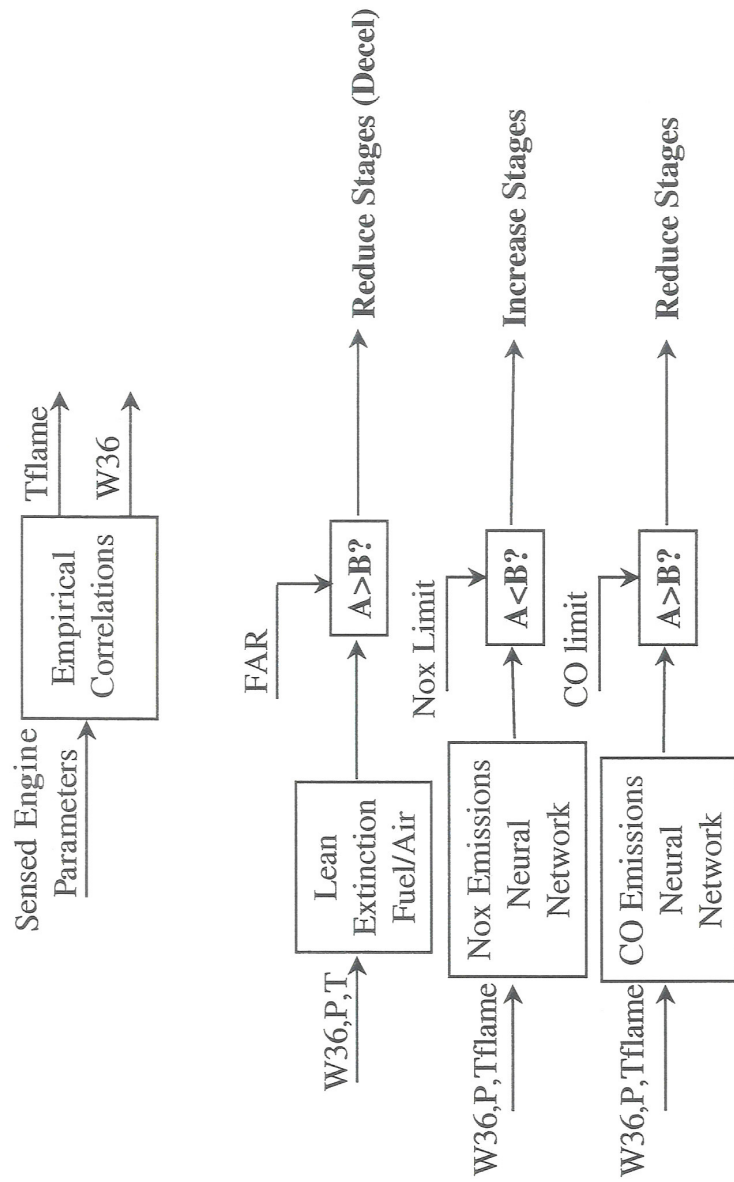


Progressive fueling of aerodynamically isolated zones of the combustor is one way to manage the production of harmful emissions. This approach is called fuel staging. In general, NOx increases as flame temperature increases. CO and UHC, on the other hand, decrease as flame temperature increases. In order to effectively manage all three emissions, flame temperature must be constrained to a narrow range. Fuel staging effectively limits the range of flame temperature, and the range is reduced as the number of stages is increased.

The Active Combustor Control Program developed two distinct fuel systems to manage the staging of fuel to the combustion zones. The Controlled Pressure Fuel Nozzle (CPFN) system was designed to meet the requirements of the Twin Annular Pre-mixing Swirler (TAPS) combustor developed separately by GE as part of the AST program. The CPFN system utilizes hydraulically synchronized staging valves within the fuel nozzles to turn flow on and off to each of the fueling zones within the inner and outer swirler cups. The fuel multiplexing (FMUX) system was designed to anticipate the potential requirements of an advanced combustor such as the Affordable Multi-point Injection (AMI) concept also developed separately by GE as part of the AST program. The FMUX utilizes the basic technology of the HMUX with some modifications to modulate and stage fuel flow to 30 independent fuel zones.



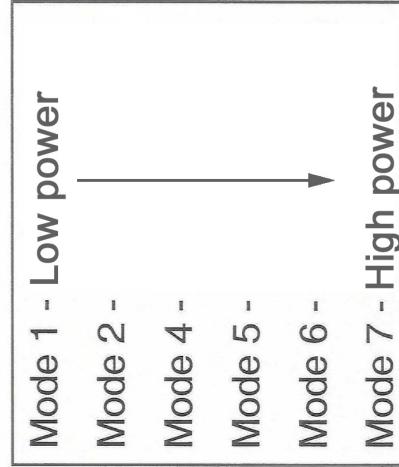
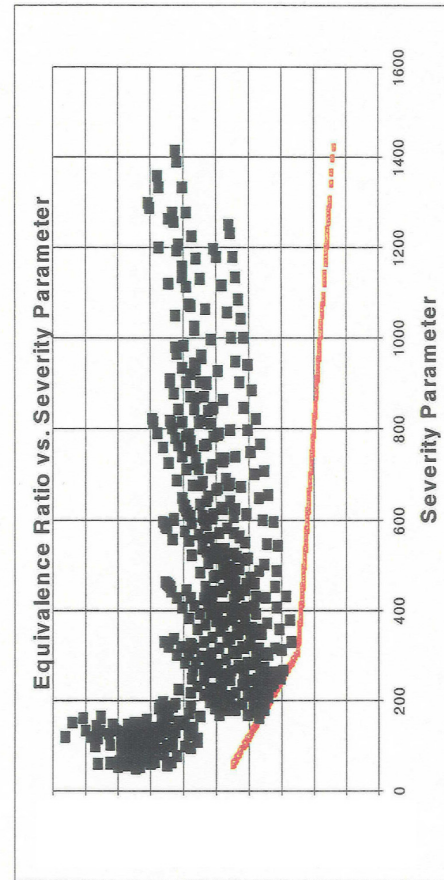
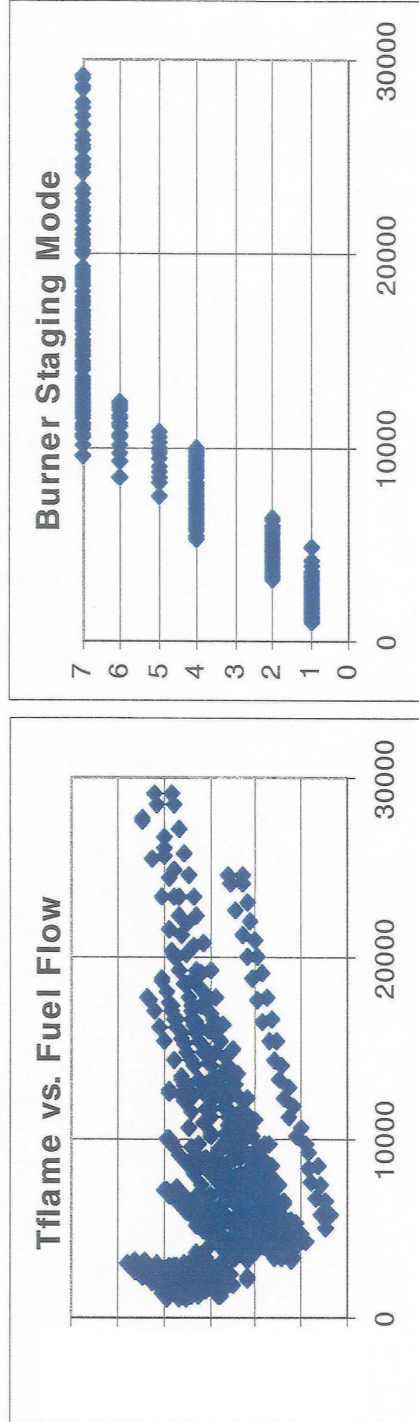
## Staging Logic



The control logic architecture developed as part of this program utilizes a hybrid model-based approach. Model-based techniques are used to calculate combustor air flow and fuel air ratio. Empirical correlation's are used to estimate flame temperature and lean extinction fuel/air ratio. Neural networks are used to estimate Nox and CO emissions. If the fuel/air ratio drops below the required lean extinction margin, the control logic demands a switch to fewer stages. This part of the logic has precedence over all others. If the predicted Nox emissions exceed the limit, the logic demands a switch to more stages. Finally, if the predicted CO emissions exceed the limit, the logic demands a switch to fewer stages. By controlling in this manner, the logic ensures that the engine will operate with acceptable stability and minimum emissions.



## Staging Logic - Parametric Studies

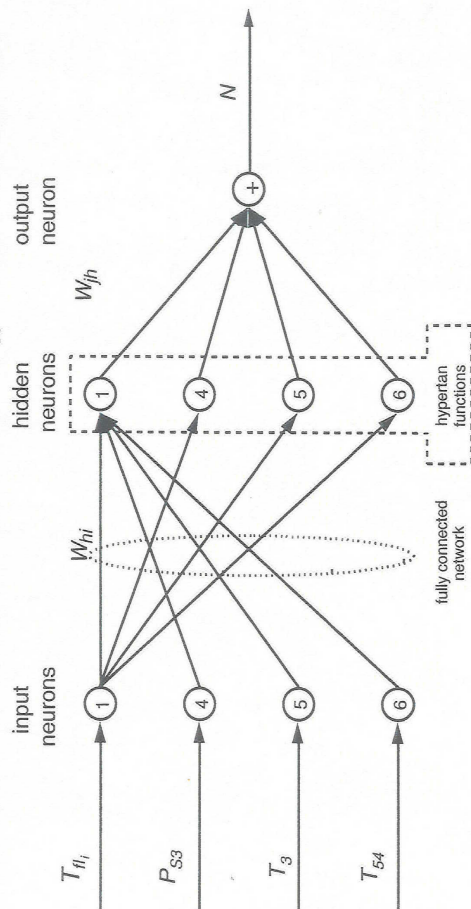




Parametric studies were done in order to map the operation of the control system. The TAPS combustor configuration utilized 6 modes of operation or stages from low power to high power. The figures above show flame temperature and equivalence ratio for engine operation throughout the flight envelope. Notice that the equivalence ratio reaches the blowout line but never drops below it. Also, discrete power hooks at individual flight conditions form the family of lines in the flame temperature plot. Without staging, the flame temperature at a given flight condition would have much steeper slope and cover a wider range.



### An Alternate Estimator for $\text{NO}_x$ : Neural Network



#### Advantages:

- More robust
- Adaptable to all operating modes
- Can use additional parameters (e.g. Staging Mode)

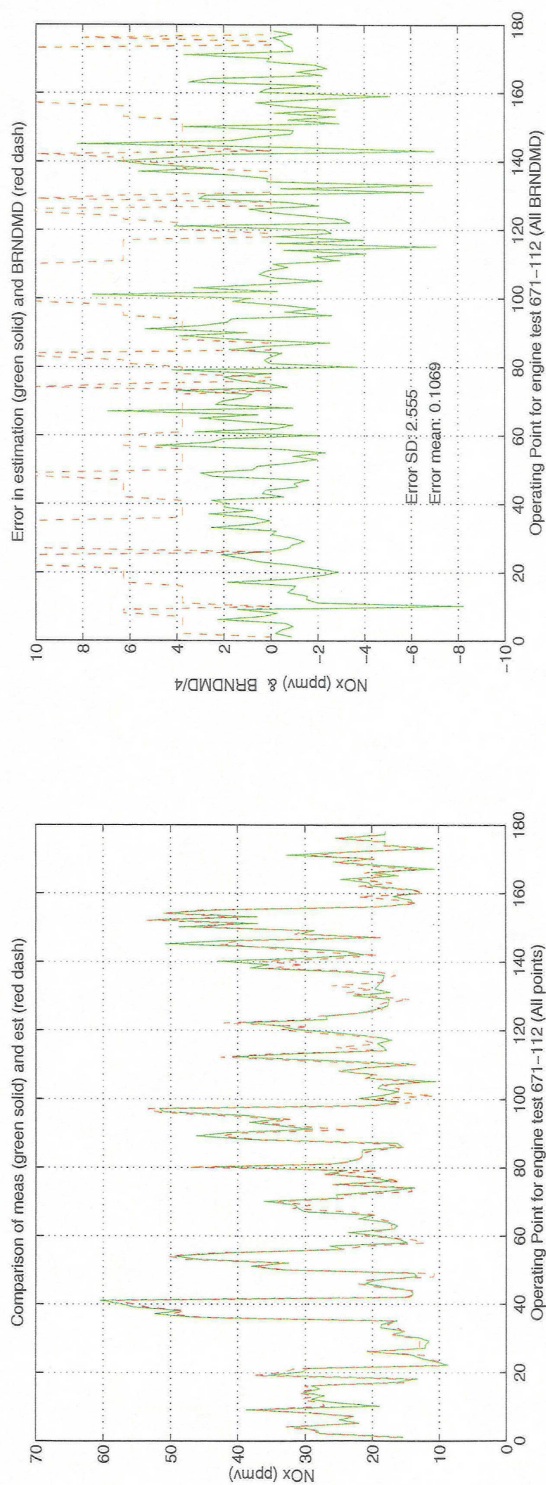
#### Disadvantages:

- Unpredictable when out of range

GE CR&D investigated various architectures for a neural network emissions predictor. The architecture which produced the most accurate results utilizes a hybrid approach with direct inputs from sensors for PS3, T3, and T54 as well as flame temperature determined through a combination of model-based and empirical techniques. The advantage of this neural network compared to an empirical correlation is better accuracy, more robustness and better adaptability to all operating modes and regimes. On the other hand, the neural network yields unpredictable results when used in operating regimes outside of the training set.



## Estimation Results Using Neural Networks



Network trained on half the data and tested on total

Preliminary Results Indicate Neural Network Significantly more Accurate than “Classic” Empirical Correlations



As shown in the plots above, when trained on half of the data and tested against the other half of the data, the neural network predicted Nox within an accuracy of  $\pm 8\%$  based on a  $\pm 3$  sigma process capability. This compares quite favorably to empirical correlation's which typically yield an accuracy of  $\pm 20\%$  or greater.



*Aircraft Engines*

*Advanced Control Systems*

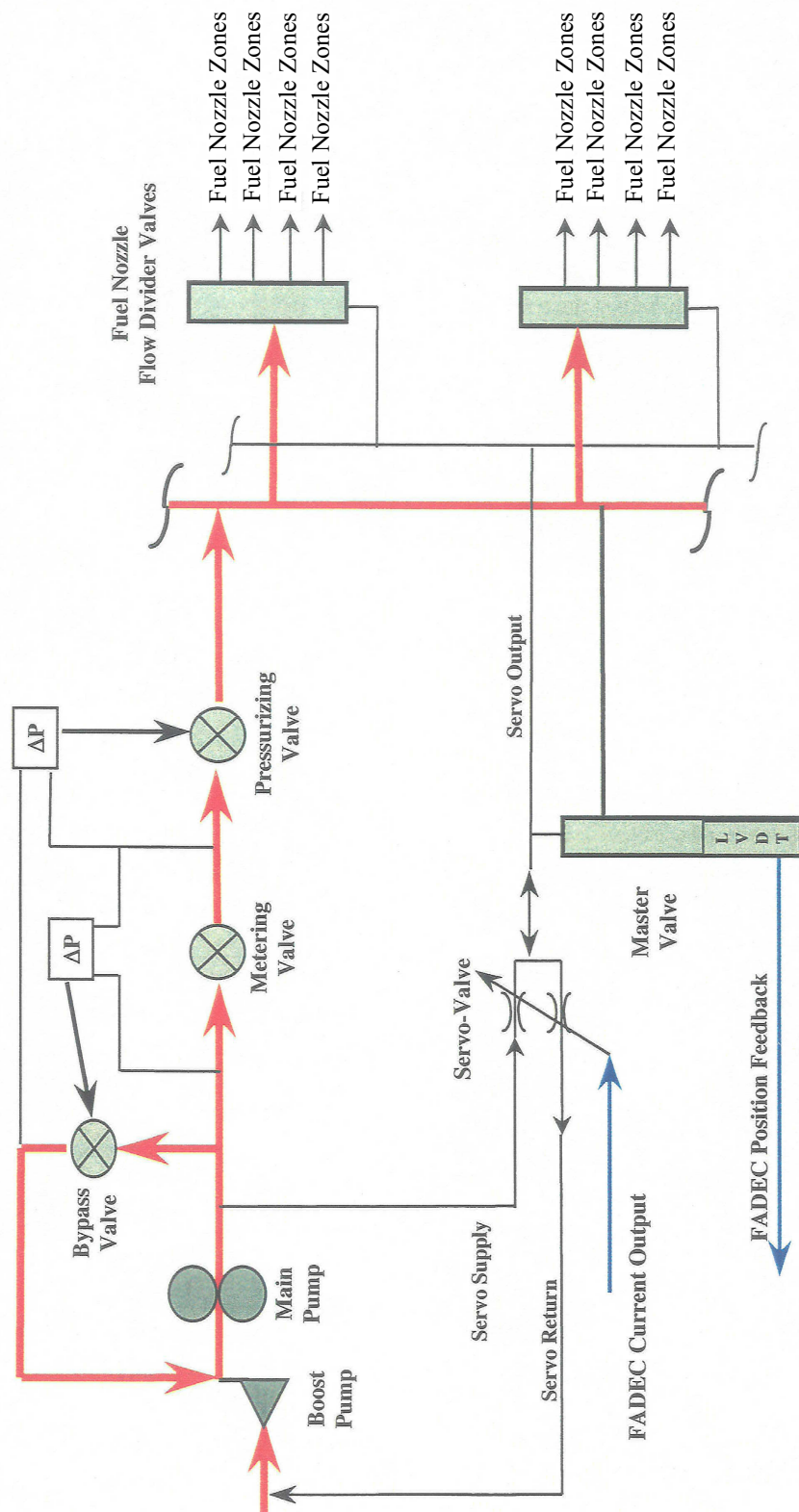
## **Sub-AOI 1.4.1: Controlled Pressure Fuel Nozzle**

*NASA Critical Propulsion and Noise Technologies*





## CONFIGURATION OVERVIEW - CPFN CONTROL SYSTEM

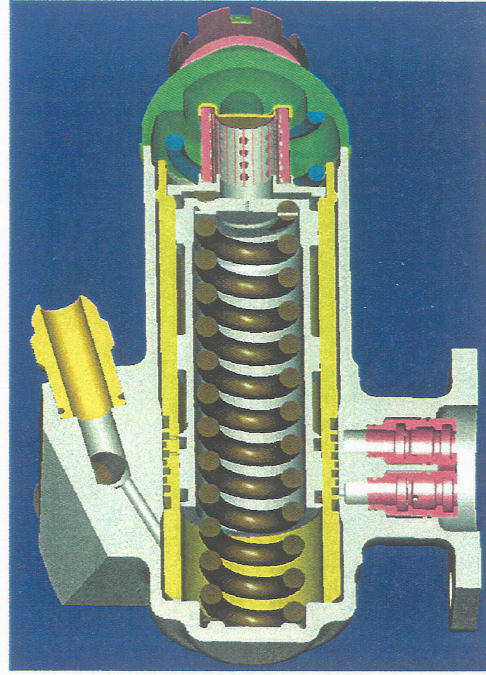
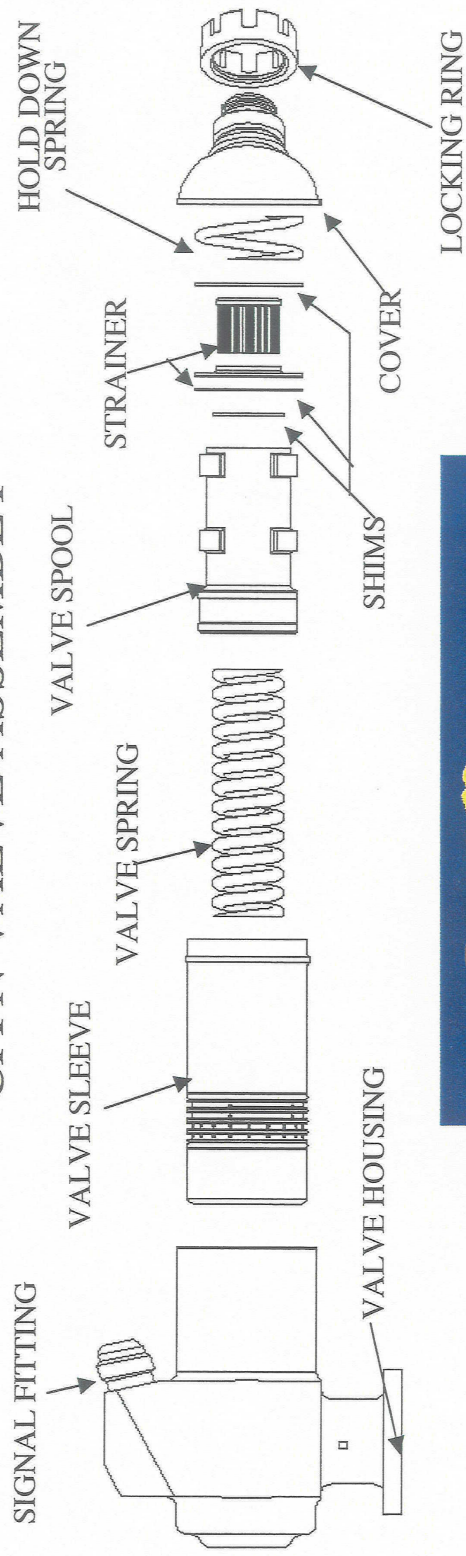




The fuel system architecture for the CPFN system is shown in the above figure. This system replaces the fuel nozzle flow divider valves on each nozzle with a CPFN valve. The position of the CPFN valves is modulated by a single servovalve which controls the reference pressure. Feedback to the control system is provided by a single master CPFN valve with a dual LVDT providing an electrical signal proportional to the position of the master valve. Within tolerances, the position of each CPFN fuel nozzle valve will be the same as the master valve.



## CPFV VALVE ASSEMBLY

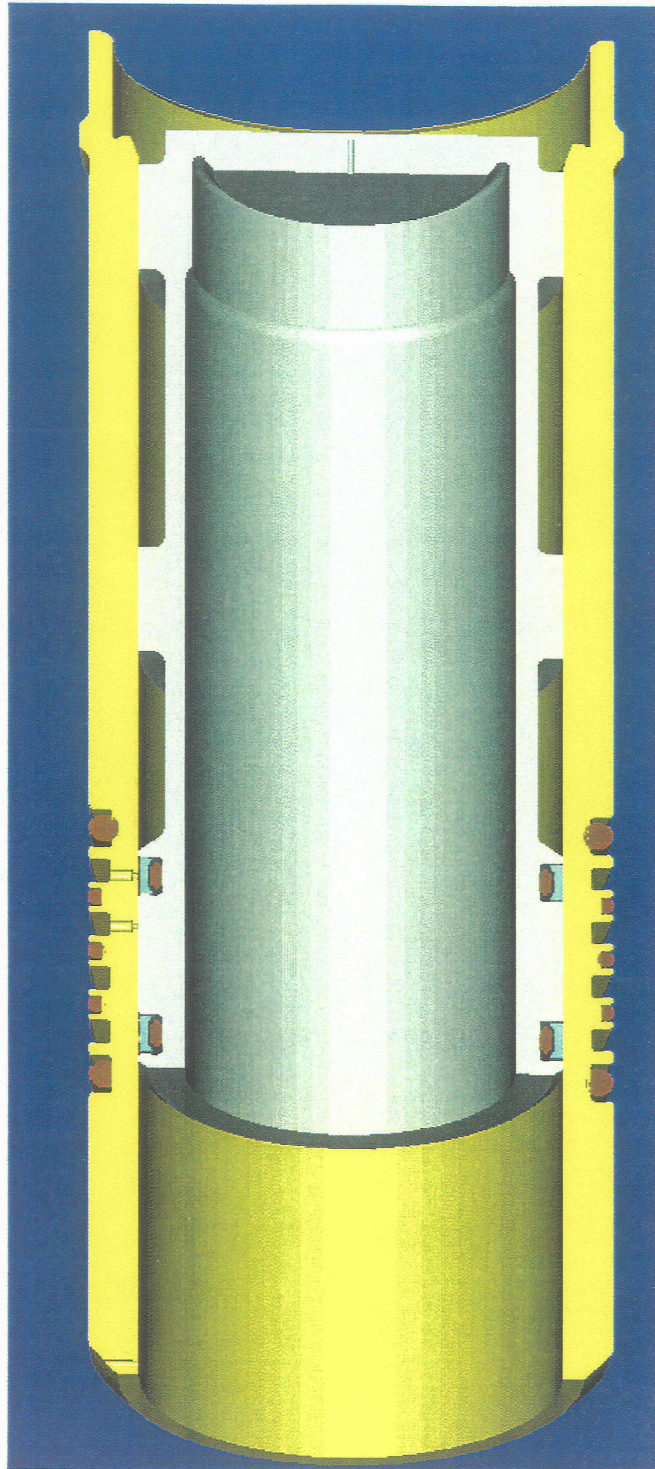


Each CFPN valve consists of a sleeve, spool, and spring. As the spool translates, ports for the four fuel zones are progressively uncovered. There is sufficient stroke between stages to ensure that all the valves will be staged correctly when the master valve is positioned at the nominal stroke. Two dynamic seals are utilized to prevent fuel leakage into the unstaged zones. If an unstaged zone gets leakage, fuel coking and high UHC emissions will result. A series of endurance tests were performed on various seal designs to select one with the best combination of low repeatable friction and low leakage.





- DESIGN RISK - SLIDING TEFLON SEALS OVER PORT HOLES



**SOLUTIONS:**

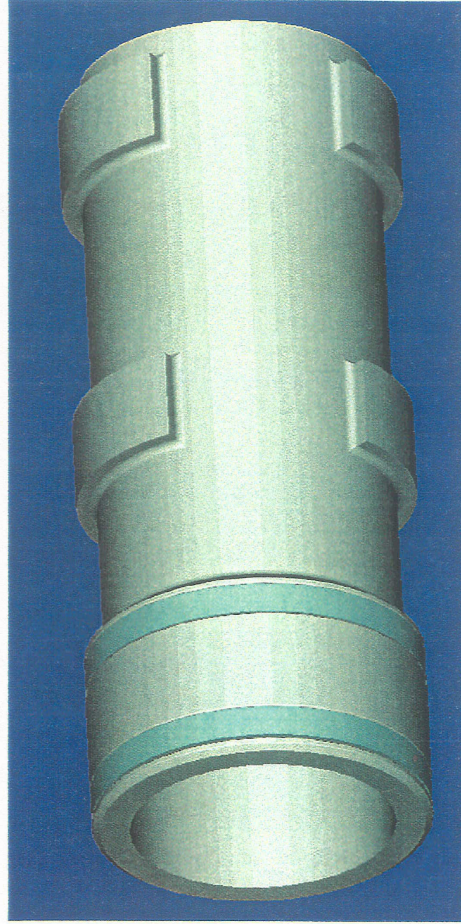
- ROLLER BURNISH I.D. OF SLEEVE TO REMOVE HIGH SPOTS AND SMOOTH FINISH
- EXTRUDE HONE I.D. OF SLEEVE TO BREAK EDGES OF ORIFICE HOLES



As a result of the preliminary design review, a risk of premature wear of the dynamic seals due to sliding contact with the ports was identified. Prior experience with this type of design led to changes in the manufacturing processes. In particular, the inner diameter of the sleeve was roller burnished to remove high spots and produce a smooth finish. In addition, the ports were extruded honed to break the edges of the holes. Endurance rig testing followed by inspection of the seals validated these process changes.



DESIGN RISK:  
•ENDURANCE,  
FRICTION LEVELS AND  
SEALING ABILITY OF  
TEFLON SEALS



A second risk leading to changes in the design assurance testing was identified in the preliminary design review. Because this system relies heavily on the assumption that the friction levels in the valves will remain consistent and repeatable, additional testing was done to quantify the variances in friction and leakage for three different seals provided by different suppliers.



## DYNAMIC SEAL TESTS

	PARKER SEAL	GREENE TWEED ENERCAP	SHAMBAN GLYD RING
<u>ZERO CYCLE TIME</u>			
BREAK-IN CYCLE	APPROX. 3-4 FULL STROKES	FRICION DECREASE THROUGHOUT TESTING	FRICION DECREASE THROUGHOUT TESTING
BREAKAWAY FRICTION	+6.0/-9.7 LBS	+3.2/-7.0 LBS	+2.2/-5.2 LBS
PEAK BREAKAWAY FRICTION	+9.0/-12.0 LBS	+5.0/-8.0 LBS	+3.9/-6.3 LBS
RUNNING FRICTION	+5.2/-9.0 LBS	+2.5/-6.2 LBS	+1.0/-5.2 LBS
<u>10,000 CYCLES</u>			
SEAL LEAKAGE	NO DETECTABLE LEAKAGE	NO DETECTABLE LEAKAGE	APPROX 14.8g LEAKAGE AFTER 80 HRS
BREAKAWAY FRICTION	NO DISCERNABLE BREAKAWAY FRICTION	PEAK ONLY	PEAK ONLY
PEAK BREAKAWAY FRICTION	N/A	+8.0/-8.0 LBS	+2.2/-5.2 LBS
RUNNING FRICTION	+11.5/-13.0	+5.5/-6.0 LBS	+1.9/-3.0 LBS
(+) VALVE OPENING			
(-) VALVE CLOSING			



As shown above, seals supplied by Parker, Green-tweed, and Sham-ban were run through a series of endurance tests. All three types of seals produced friction variations within the specification tolerances. However, the Green-tweed seals were selected based on having the best combination of low, repeatable friction and low leakage.



## STAGE CRACKING PRESSURES

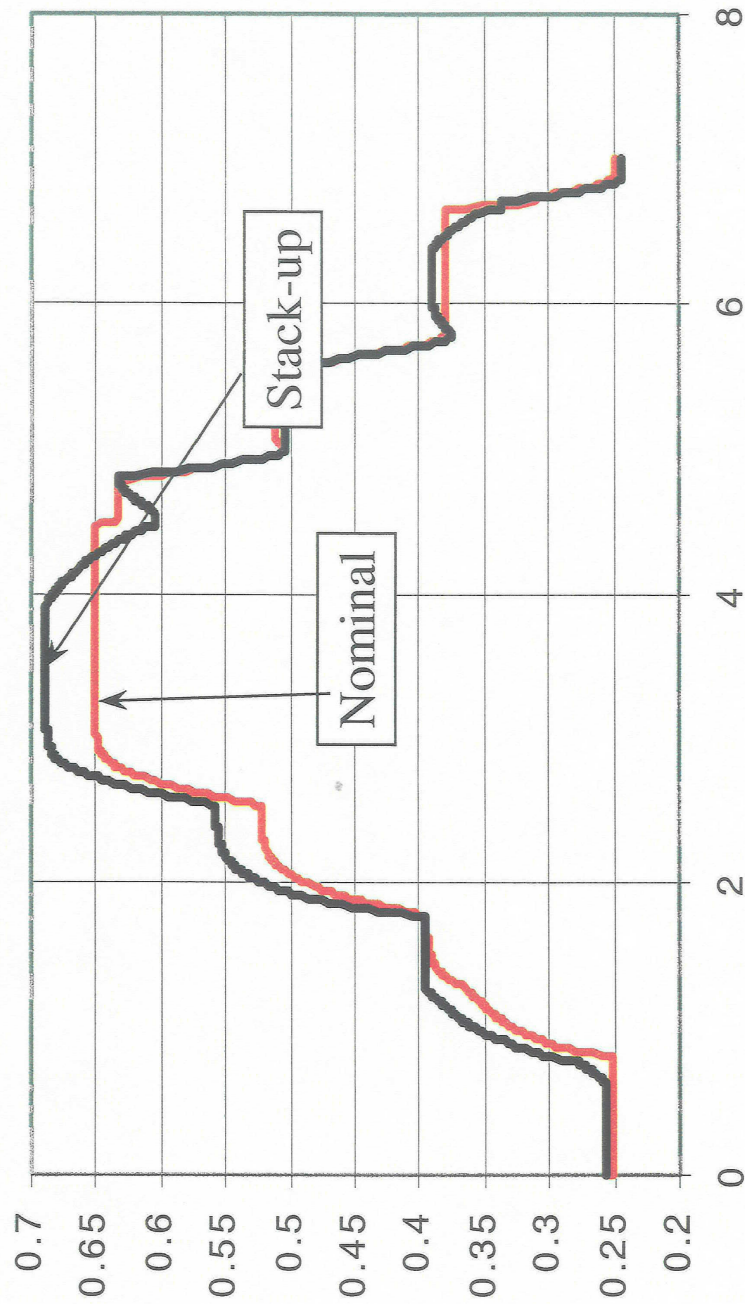
	<u>AVERAGE (PSIG)</u>	<u>MAXIMUM (PSIG)</u>	<u>MINIMUM (PSIG)</u>
STAGE 1 TURN ON	53.5	56	46
TURN OFF	42.4	46	32
STAGE 2 TURN ON	90.7	94	87
TURN OFF	79.8	88	74
STAGE 3 TURN ON	127.6	134	124
TURN OFF	114.8	118	109
STAGE 4 TURN ON	165.8	177	162
TURN OFF	150.9	162	145

To further validate the valve design, each valve was tested for cracking pressure after they were assembled. The test procedure was also used to quantify friction based on the on and off hysteresis levels. In the production batch of 15 valves, 12 met the specification tolerances and were delivered to GE for rig testing. For eventual production, the manufacturing yield must be improved, and Parker has identified several process changes which should accomplish this:

- 1.) Hot and cold fuel soaks of the valves to allow the seal O-rings to settle.
- 2.) Run a minimum of 100 break-in cycles to put-down thin teflon layer on the sleeve.



## CPFN Position vs. Time



Port spacing designed to accommodate stack-up



The above plot illustrates how the tolerance stackup was used to determine the required port spacing on the CPFN valves. The stackup includes variation in spring constant and preload, seal friction forces, force diameter, pressure drops in lines and fittings, and control loop overshoot/undershoot. These variations were measured in a representative sample of 10 piece parts. A dynamic model of the fuel system was developed to represent the effect of the system tolerances on spool position. The plot above shows the position Vs. time for a perfect nominal valve compared to a valve with worst-case tolerances. This analysis validated that a minimum stroke of 0.08" between stages was required.



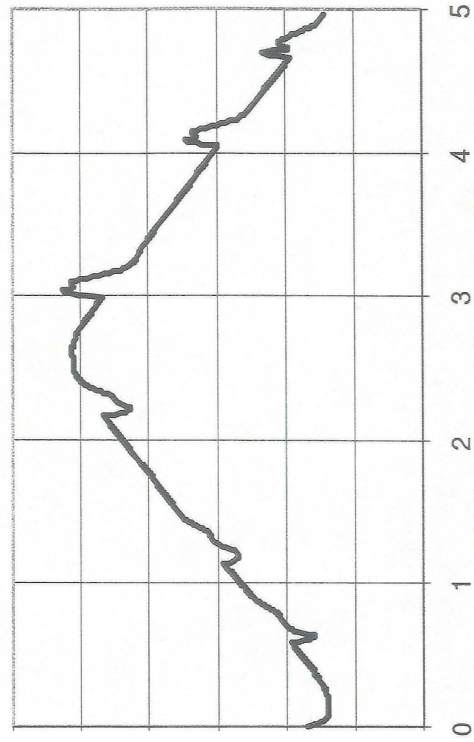
## Fuel System Dynamic Model

CPFN Position vs. Time



Analytical Model used to establish hardware requirements and to design regulator.

Combustor Fuel Flow vs. Time



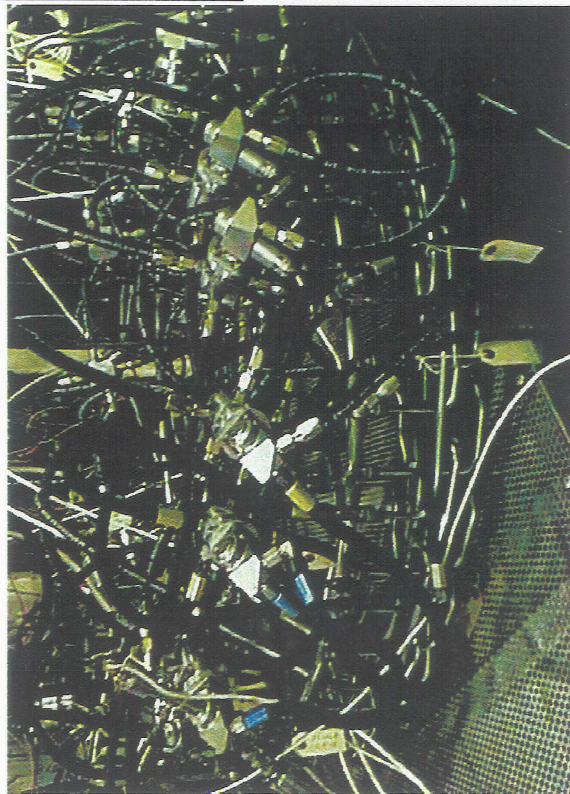
Analytical Model used to quantify system interactions and to design fuel flow compensation logic

The fuel system dynamic model was coupled to a transient engine model. This integrated model was used to identify potential fuel system/engine interactions. Of particular concern, was the potential for compressor stalls or combustor blowouts during staging transients. As shown above, fuel flow drops for a short time when the number of stages is increased. Conversely, fuel flow increases for a short time when the number of stages is reduced. The model was used to develop special fuel flow compensation logic to avoid blowouts and stalls.



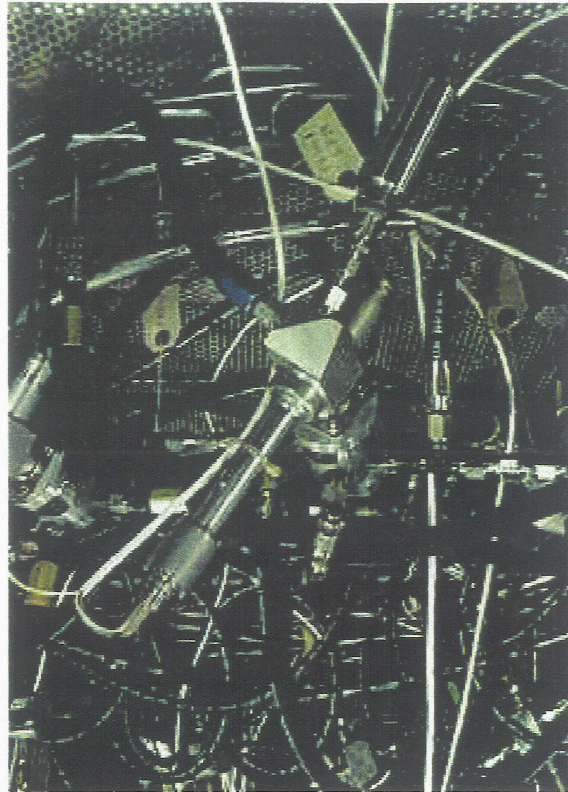


## Fuel System Test Rig



Valves, nozzle simulators, manifolds

- Production gearbox, pump, HMU, FADEC, and manifold
- Closed-loop on real-time engine model
- 10 slave CPFN valves, 2 master CPFN valves



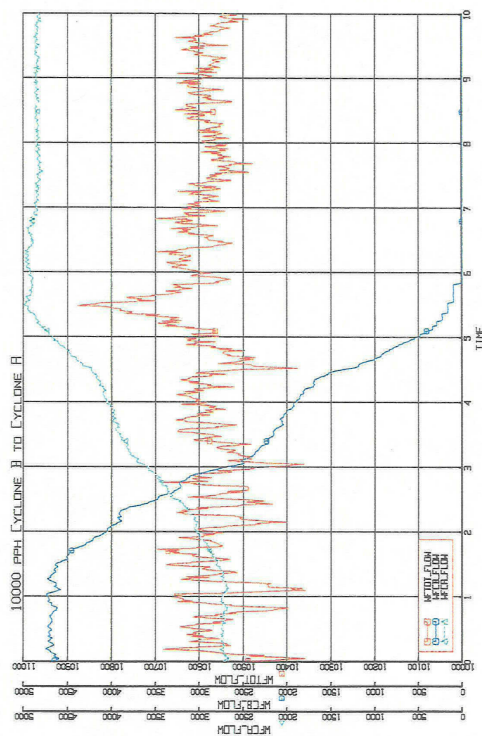
Close-up of master valve



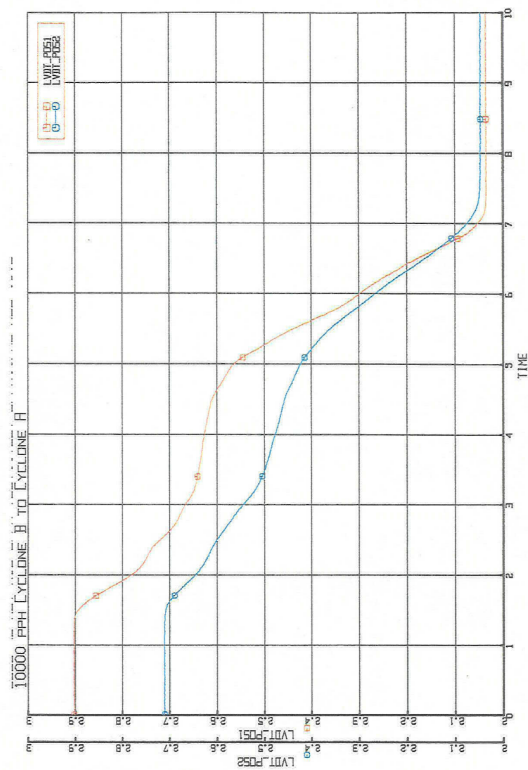
A comprehensive system rig test was performed in order to validate the operation of the CPFN fuel system. The test used a hardware-in-the-loop arrangement to simulate engine operation. A production gearbox, fuel pump, and fuel control were used in addition to the prototype CPFN hardware. The combustor was simulated by manifold together all of the CPFN outputs and controlling the back pressure to a simulated combustor pressure derived by a real-time engine model.



## Fuel System Test Results



Controlled and stable staging transients



Valve Position Error within Tolerance

The control rig test results validated the design of the CPFN fuel system. A key characteristic examined in this test was how the fuel metering system would respond to step changes in back pressure during staging transients. When an additional stage is opened, the back-pressure on the fuel metering valve goes down which drives the metered flow high until the bypass valve opens to cancel the effect. Conversely, when a stage is shut down, the back-pressure on the fuel metering valve goes up which drives the metered flow low until the bypass valve closes to cancel the effect. Design consideration was given to make the CPFN port flow numbers Vs. stroke characteristic gradual to reduce the severity of the transient. The plot at the upper left, shows a transition from cyclone B to cyclone A. The results indicate that the production bypass valve and head regulating system are capable of maintaining uniform and stable fuel flow during staging transients.

The CPFN valves were controlled closed-loop on the position feedback from the two master valves which housed LVDT's to measure the position of the spool. Due to the friction caused by the dynamic seals, a significant amount of test time was spent tuning the position loop regulator to minimize over/undershoot as well as steady-state error. The plot at the lower right, shows the position demand and position feedback for a staging transient from cyclone B to cyclone A. Undershoot is very small and the steady-state positioning error of the CPFN valves is within the specified tolerances used in the stack-up analysis.



## **Controlled Pressure Fuel Nozzle Conclusions**

- The controlled pressure fuel nozzle system has advantages over the current state-of-the-art in fuel staging controls.
  - Improved reliability
    - eliminates multiple solenoids, switches, and staging valves
  - Lower weight & cost
    - multiple fuel manifolds replaced by one manifold plus a signal line
- Through comprehensive component and rig testing the AST program has demonstrated that the CPFN system is suitable for engine application.
- Follow-on program to further develop the system in an engine test with the TAPS combustor is planned



The Controlled Pressure Fuel Nozzle System (CPFN) system designed, fabricated and demonstrated under the AST program has proven the viability of utilizing CPFN technology in the control systems of complex low emission combustors. The comprehensive component-level testing performed at Parker, and system integration testing performed at GE using a system rig running closed loop with an analytical engine model have demonstrated CPFN control system performance that is functionally equivalent to or better than that of a conventional fuel staging system which utilizes multiple solenoid controlled staging valves.

In addition, by fabricating a fully functional CPFN system under the AST program, a valid basis was established for estimating the advantages of CPFN technology in production applications. These CPFN advantages include reductions in cost & weight. Estimates of the specific benefits for the TAPS combustor application targeted by this program are shown below.

#### Typical Fuel Staging System for TAPS Combustor:

	<u>Cost (%)</u>	<u>Weight (lbs.)</u>
Three solenoid operated staging valves	17.6	15 lbs.
Three fuel manifolds	35.3	9 lbs.
<u>Fuel Nozzle flow divider valves (20)</u>	<u>47.1</u>	<u>16 lbs.</u>
Total	100%	40 lbs.

#### CPFN Fuel Staging System for TAPS Combustor:

	<u>Cost (%)</u>	<u>Weight (lbs.)</u>
One servovalve	7.8	2 lbs.
One fuel manifold	11.8	3 lbs.
One signal line	4.9	2 lbs.
Two CPFN Master Valves	7.1	3 lbs.
<u>Eighteen CPFN Slave Valves</u>	<u>28.2</u>	<u>18 lbs.</u>
Total	59.8%	28 lbs.



*Aircraft Engines*

*Advanced Control Systems*

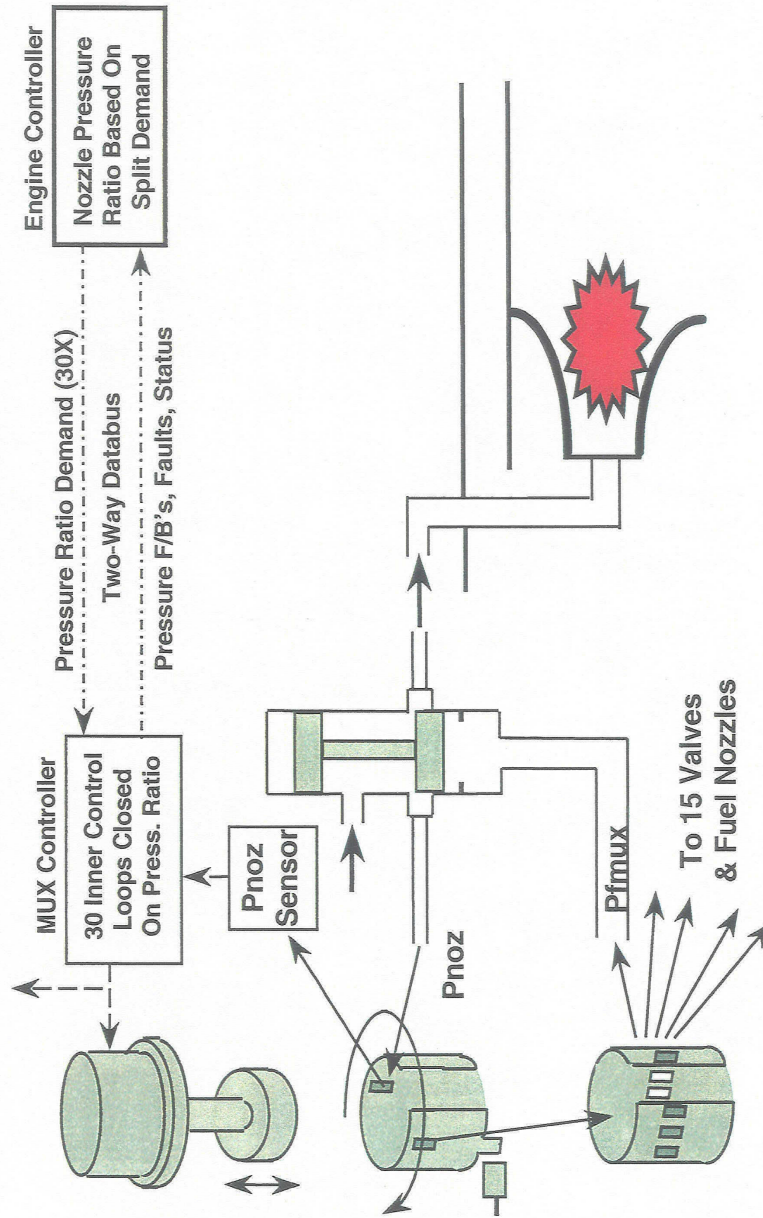
## **Sub-AOI 1.4.2: Fuel Multiplexer**

*NASA Critical Propulsion and Noise Technologies*





## Fuel Multiplexer - Principal of Operation NASA Active Control Research Configuration





The fuel multiplexer is a device which is designed to modulate fuel flow to multiple combustion zones. The system developed under AST utilizes two multiplexers each of which modulates 15 zones for a total of 30, one for each fuel cup in a large commercial engine such as the GE90. The device works by distributing total metered fuel flow from the main metering valve to multiple individually positioned throttling valves. The process which the FMUX system uses to control fuel flow is as follows:

- 1.) Based on a zone fuel ratio demand, the main engine control calculates a demanded pressure ratio for each zone referenced to the maximum flow zone according to the following relation:

$$(W_{\text{nozzle}}/W_{\text{max}}) = (P_{\text{nozzle-PS3}})/(P_{\text{max-PS3}})$$

- 2.) The main engine control passes the pressure ratio demands and PS3 measured value to the FMUX controller.
- 3.) Notice from the graphic that there are two ports on the FMUX's rotating spool. One port is used to send the individual fuel nozzle pressures to the pressure sensor. Therefore, as the spool completes one rotation, the 15 nozzle pressures are each sampled and measured one time by the pressure transducer. The function of the other port is identical to that of the rotating port on the HMUX. As the port is positioned on top of the transmission line to each of the second stage valves, the first stage force motor spool is positioned to port supply or return pressure in order to move the second stage valves open or closed.
- 4.) The FMUX electronic control receives the pressure signals from the transducer and calculates the pressure ratio feedback. The controller then processes the feedbacks and demands through closed-loop regulators to generate the signal demand for the first stage force motor.



## New Technology

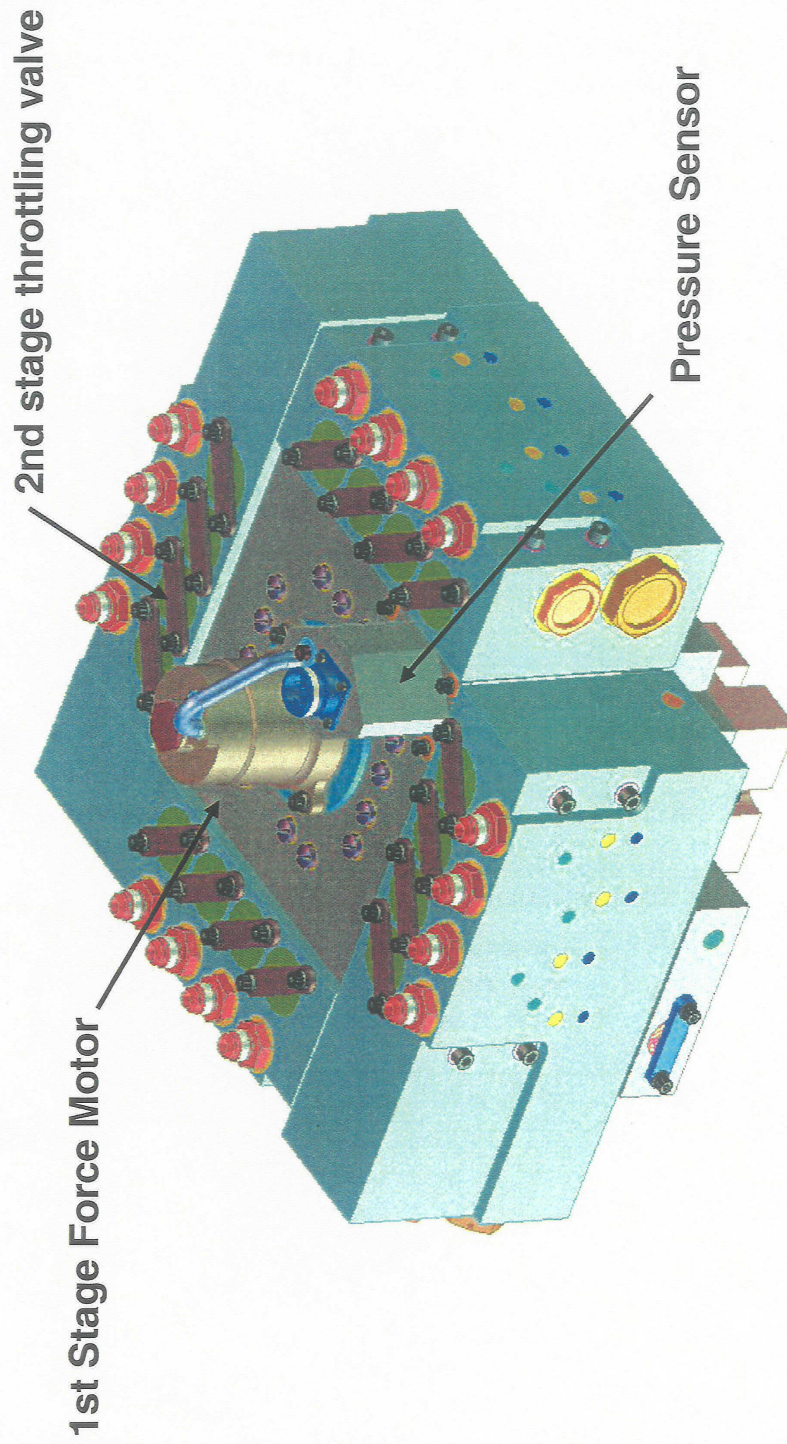
- **First Closed Loop Control of 30 Independent Valves (previous high was 20 -- 5 closed loop & 15 open loop)**
- **First Dual *Independent* HMUX Controller (only demonstrated dual gear linked units in the past)**
- **First Time Multiplexing both the Closed Loop Feedback and the Control Pressure Output at same time**
- **First Time using Dual Control Lands and Staggered Ports to Minimize Leakage**

The fuel multiplexer program advanced the state-of-the-art in generic multiplexing technology in several ways. This program includes the first time ever both the closed loop feedback and the control pressure output were multiplexed at the same time. In the basic multiplexer for actuation control for AOI 1.2, the multiplexer is used to port hydraulic flow to multiple individual actuators. However, each actuator has its own position sensor so that while the system reduces the number of torquemotors, the required number of sensors remains the same. The fuel multiplexer takes the concept a step forward by using a single sensor to provide feedback for all of the outputs. Therefore, with the fuel multiplexer, 15 individual torquemotors and 15 individual flow sensors are replaced by a single first stage force motor and a single pressure sensor.





## FMUX Solid Model





The solid model illustration above shows some of the individual parts of the multiplexer. The components developed for this program were prototypes and utilized machinings, rather than castings, for the housing. The eventual production design will utilize a cast housing and will be much more compact and lighter in weight. As the picture shows, the first stage assembly consisting of the force motor, rotating and fixed sleeves, and fuel turbine is located in the center of the assembly. The 15 second stage throttling valves are placed around the perimeter of the assembly.



## Simulink Modeling

- Modeled ACC Control System using Simulink
- Model demonstrated that final selected architecture would work and predicted its performance (accuracy, transient response, etc.)
  - System Time Constant: Predicted = 1 to 2 s, Actual = 2 s
  - Flow Split Accuracy: Predicted = +/- 5%, Actual = +/- 3%
- Model helped to predict and address potential problems before they occurred.
- Final control laws almost same as Simulink model
  - (saved a lot of time Vs. waiting for hardware to design control laws).

A high fidelity dynamic model of the fuel multiplexer was created in Simulink. The model was used to validate the feasibility of the concept and to predict the performance. In component tests, the multiplexer achieved a flow modulation accuracy of  $\pm 3\%$  and a system time constant of 2 seconds. Both of these parameters were within the limits of the specification. Please refer to attachment IV for a more detailed description of the Simulink model and the results of the analysis.



## Design of Experiments (DOE)

- Significant overshoot for 25% steps at high flow was discovered early during DAT testing.
- Tweaked control law gains using engineering judgment with little success.
- Decided to use DOE to optimize step response Performance (Rise time & Overshoot).
- Cause & Effect Diagram pointed to 11 potential factors that could be contributing to overshoot problem.
- Performed a Taguchi L12 “screening” design to filter out important factors from trivial ones.
- After screening, performed a 5 factor Central Composite Design (CCD)
- CCD model confirmed!
  - Able to optimize both Rise Time and Overshoot.



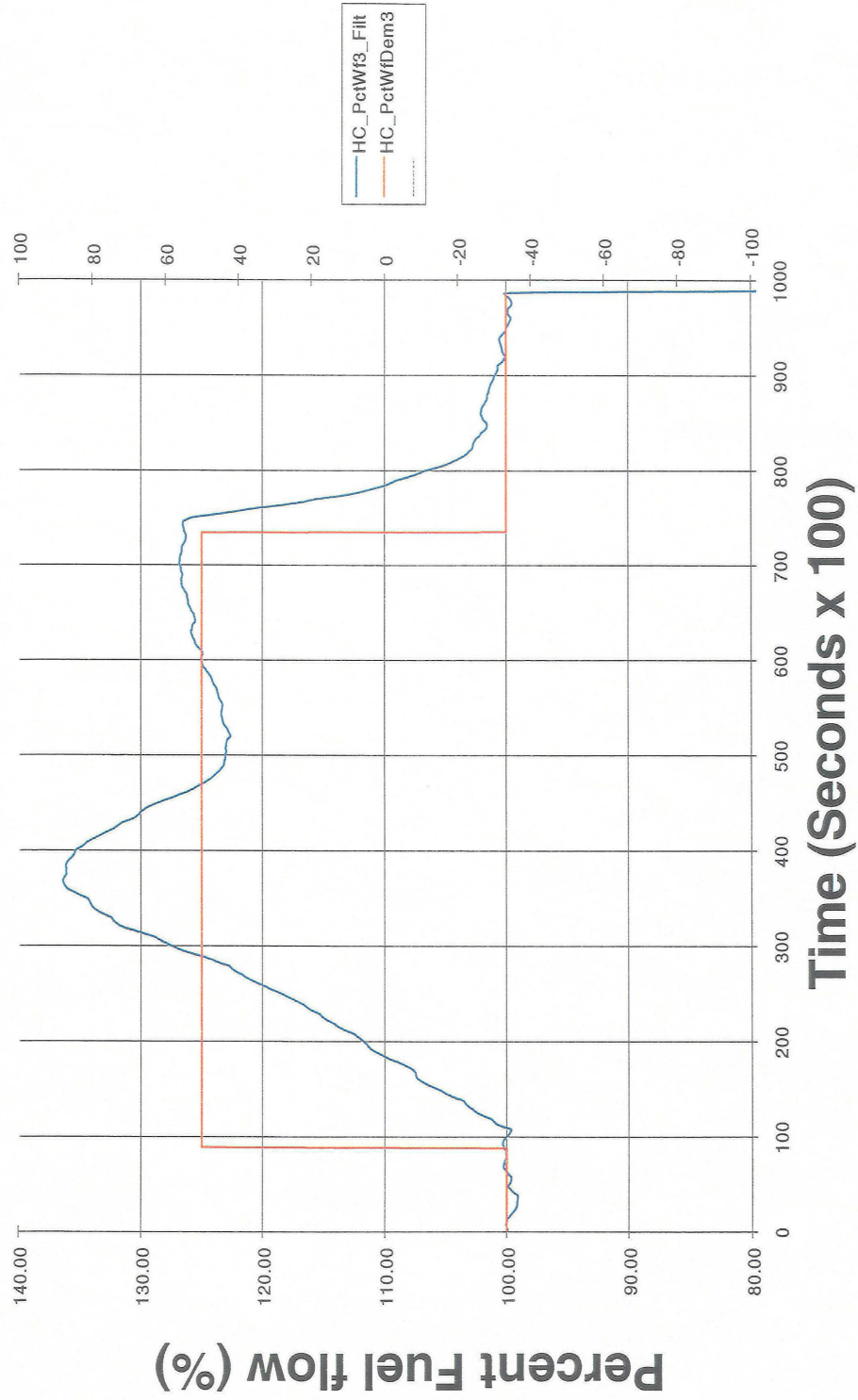
A design of experiments (DOE) project was executed to optimize the performance of the fuel multiplexer. This DOE identified 11 potential factors affecting the step response performance:

<b>Kp</b>	Proportional gain for Pn-P3 error
<b>KP_DP</b>	Proportional gain for the minimum P22 – Pn controller
<b>MDP_Schd_Hi</b>	Gain schedule based on P22-Pn when P22-Pn is greater than the set point
<b>MDP_Schd_Lo</b>	Gain schedule based on P22-Pn when P22-Pn is less than the set point
<b>P22mPn_dem</b>	Minimum throttle valve delta P set point
<b>Ki_P22</b>	Integral gain for the P22-Pn error
<b>Ki_Pn</b>	Integral gain for Pn-P3 error
<b>MWF_Schd_Hi</b>	Gain schedule based on Pn-P3 when Pn-P3 is greater than the set point
<b>MWF_Schd_Lo</b>	Gain schedule based on Pn-P3 when Pn-P3 is less than the set point
<b>Null_bias</b>	Null current set point
<b>Metered_Flow_setting</b>	Inlet flow level to the ACC

A Taguchi L12 screening design was used to eliminate second order variables and to identify 5 first order variables designated by the bold print in the above list.. A 5 factor Central Composite Design was then performed and used to effectively optimize both rise time and overshoot.



## Overshoot Before DOE



The plot above shows the rise time and overshoot prior to optimization. The rise time for a 25% step increase was about 2 seconds, and the overshoot approached 10%.

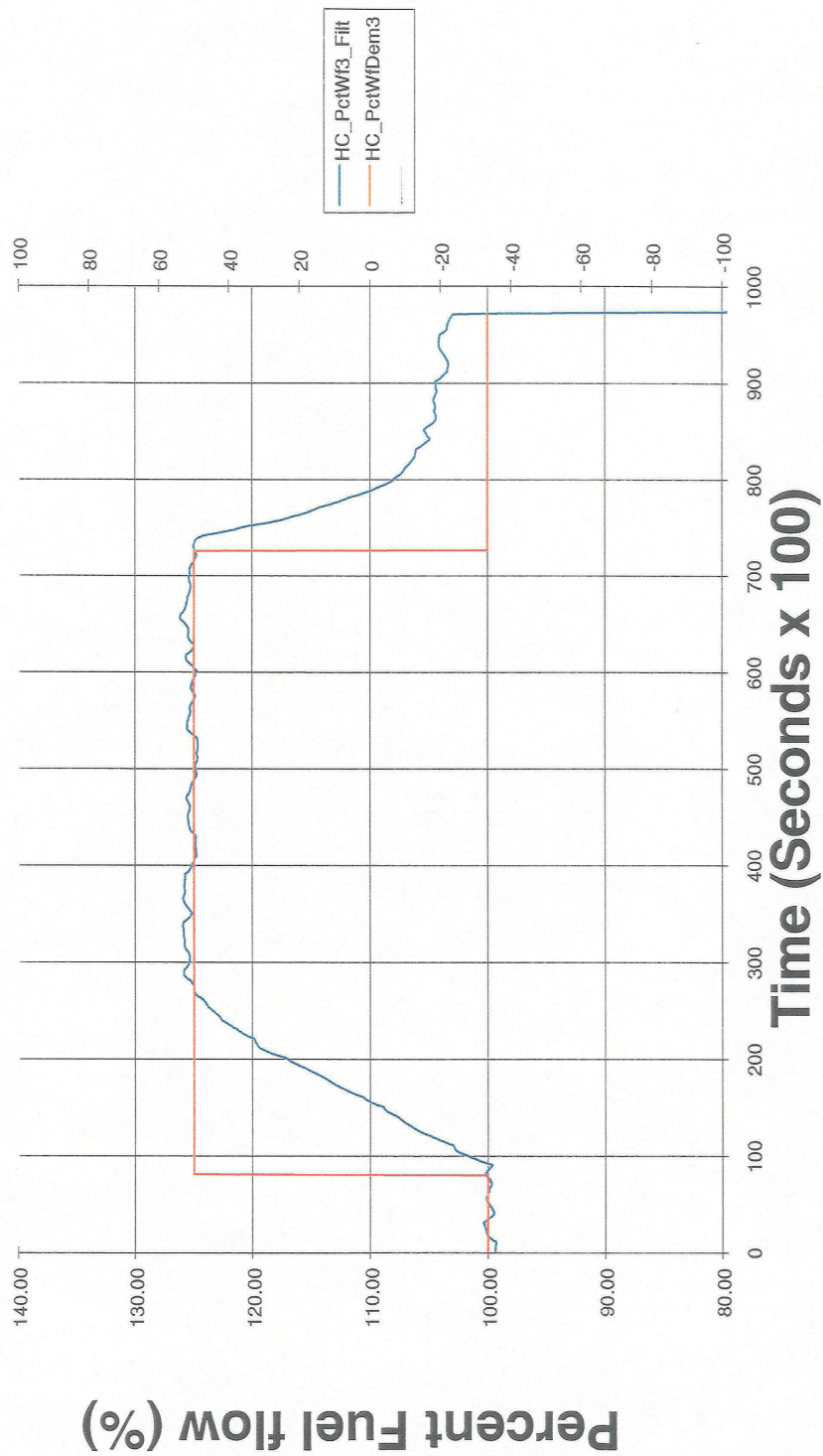


## Overshoot After DOE

CCD Confirmation run Kp at -5.125

Average Rise Time = 2.20 seconds

Overshoot = 4.15%





After optimization, the rise time remained slightly less than two seconds and the overshoot was negligible.



## Testing: FMUX

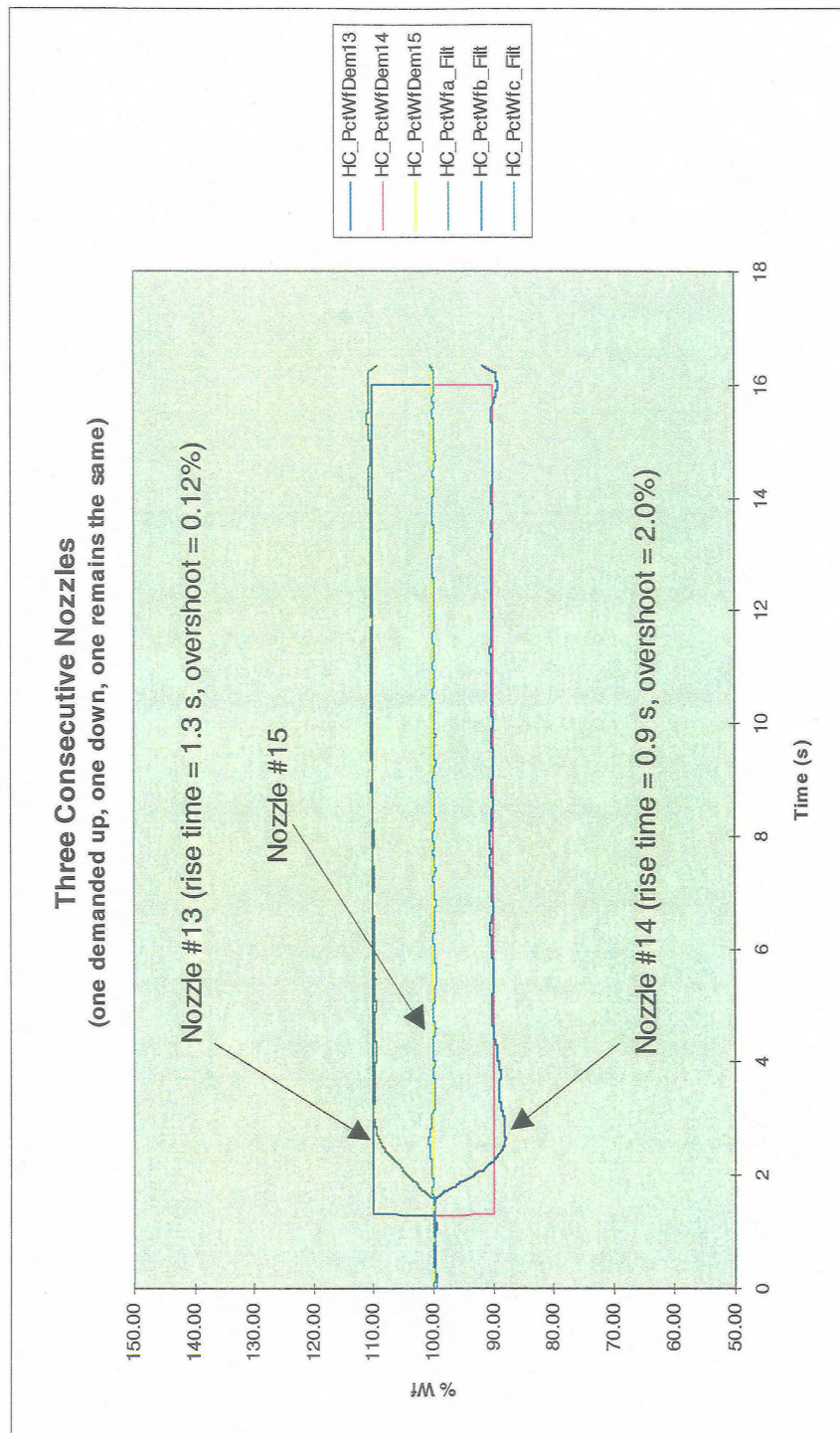
- Design Assurance Test (DAT):
  - Throttling Valve Friction
  - Throttling Valve Slew Rates
  - Positioning of Pressure Sampling Window
    - Evaluating effects of “manipulating” sample window (e.g., shift window left/right or enlarge/shrink window)
  - Controlling volume of pressure sense line
    - Evaluating effects of changing the fluid volume of the pressure sense line.
  - Fail-safe operation
    - Set fault condition (e.g., mag pickup open circuit) and verify that all throttling valves slew open
  - Closed Loop Testing
    - Steady-state flow split accuracy at low, intermediate, and high flow levels.
  - Dynamic (Step) Response Testing
    - Evaluate transient response at low, intermediate, and high flow levels for 10% and 25% steps:
      - Rise Time, Overshoot, Settling Time, Steady State Error at End of Step

A complete battery of design assurance and system integration tests were run on the FMUX system. Excess friction in the throttle valves can lead to undesired overshoot and undershoot in flow transients. Open loop testing to evaluate the mean value and variance in friction was conducted. The results indicated that the friction was within design limits required to achieve acceptable operation. Initial analysis with the dynamic model showed that the measured pressure could be significantly effected by the timing of the sampling window. As the window is opened there is some ringing or noise in the signal as the pressure reaches the steady-state value. Also, after the sampling port is closed, the pressure decays due to leakage. To optimize the sensing of pressure, the initiation and duration of the sampling window were varied to give the most accurate measurement. Another key factor in pressure sensing dynamics was the volume of the lines to the pressure sensor. Testing confirmed that reducing the line volumes reduced dynamic noise in the pressure measurement. System integration testing was aimed at quantifying fuel flow rates of change, overshoot and undershoot, and steady-state errors resulting from step changes in the input demand. Please refer to the FMUX Design Assurance Test Report, supplied under separate cover, for a detailed description of the testing and discussion of the results.





## Typical Step Response





The plot above shows the response when two adjacent streams were subjected to increasing and decreasing 10% step demand changes. For the increasing step, rise time was 1.3 seconds and overshoot was 0.12%. For the decreasing step, fall time was 0.9 seconds and undershoot was 2%. The other streams held stable for a constant input demand.



## Testing: Endurance

- 50 hours running C-Cycles
  - 10 hours hot (185 degF)
  - 10 hours cold (-10 degF)
  - 30 hours room (78 degF)
- During each test segment, demanded all nozzle flows up and down in a predetermined fashion.
- Nozzle flow data was then periodically logged for the entire 50 hours to ensure that the ACC control continued to operate correctly throughout the test cycles.

Endurance test run on the FMUX system included hot, cold and standard fuel temperature C cycles. No anomalies were found and the system performed acceptably throughout the testing.

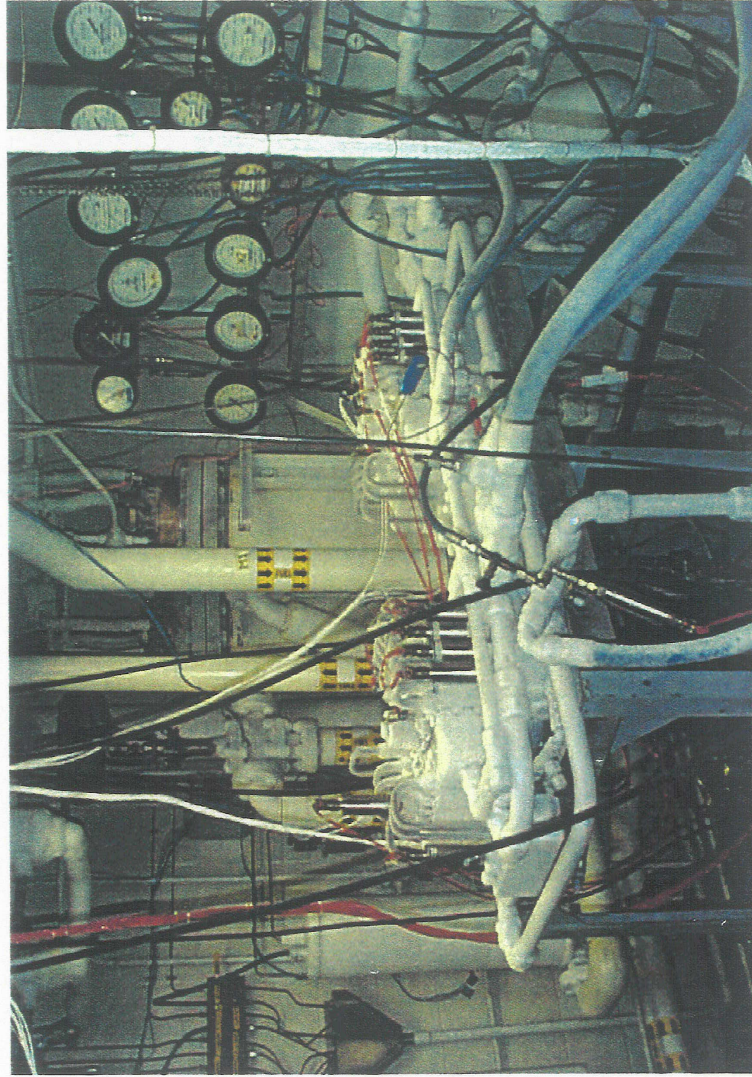




*Aircraft Engines*

*Advanced Control Systems*

# Endurance Test (Cold Setup)



*NASA Critical Propulsion and Noise Technologies*



The picture above shows the FMUX system being tested with cold fuel.



## Fuel Multiplexer Program Conclusions

- The fuel multiplexing system has significant advantages over the current state-of-the-art in controls for independent modulation of fuel flow to multiple combustion zones.
  - Improved reliability, cost, & weight
    - replaces multiple solenoids or servovalves with a single force motor
    - replaces multiple flow or position feedback devices with a single pressure sensor
- Through comprehensive component and rig testing the AST program has demonstrated that the FMUX system can meet required dynamic response and accuracy requirements.
- Benefits of potential applications must be quantified and system tests with combustor rigs must be performed.
  - Potential applications:
    - active pattern factor control
    - active acoustic control
    - active emission control

The Fuel Multiplexer (FMUX) system designed, fabricated and demonstrated under the AST program has proven the feasibility of utilizing a single force motor and single feedback transducer to modulate flow to multiple independent combustion zones. This technology makes proposed control schemes which require fuel flow control to many zones feasible for aircraft engines on the basis of cost, reliability, and weight. Several advanced control schemes with potential benefits are envisioned as candidates for this technology including the following:

- 1.) Active Pattern Factor Control enables less turbine cooling which results in improved cycle efficiencies
- 2.) Active Combustor Acoustic Control enables combustors to run at very lean fuel/air ratios which lowers NOx emissions.
- 3.) Active Emission Control enables combustor operation to be optimized for low emissions while maintaining good operability in terms of blowout margin.

The comprehensive component-level and system integration testing performed at Woodward using a system rig with the FMUX running in parallel with a typical production aircraft engine fuel metering system have demonstrated FMUX control system performance that meets the requirements of the above control schemes. Additional work needs to be undertaken to demonstrate the feasibility and benefits of one or more of the proposed control schemes. Having demonstrated the performance of the FMUX in a fuel system rig, the next logical step would be to conduct a combustor rig test program with the FMUX integrated into an active combustor control system.

**Attachment I: State and Parameter Estimation for a Jet  
Engine – Final Report**





# **State and Parameter Estimation for a General Electric Jet Engine (Final Report)**

by

**Emmanuel G. Collins, Jr., Rhashan B. Walker, and Arthur G. O. Mutambar**  
Department of Mechanical Engineering  
Florida A&M University - Florida State University  
2525 Pottsdamer Street  
Tallahassee, FL 32310-6046  
(850) 487-6373  
FAX: (850) 487-6337  
ecollins@eng.fsu.edu, rwalker@eng.fsu.edu, arthur@eng.fsu.edu

**Report prepared for:**  
General Electric Aircraft Engines  
1 Neumann Way  
Box 156301  
Cincinnati, Ohio 45215-6301  
Attn: Dr. Shrider Adibhatla

September 21, 1998

## Abstract

In order to enable higher performing feedback control and to better evaluate engine quality, it is desirable to be able to estimate both the state vector and key engine parameter variations and input biases throughout the flight envelope. This is a difficult problem in practice because there are less sensors than parameter variations and input biases, some of the sensors are very noisy, and some of the sensor measurements are biased. As shown in this report, due to the first difficulty, this estimation problem requires the simultaneous use of data from several operating points. Hence, a “stacked” system model, that can be used to incorporate data from several operating points, is proposed. The filtering is accomplished by using both the Kalman filter and its algebraic equivalent, the Information filter. As shown in simulation results, the Kalman filter sometimes diverged due to an ill-conditioned covariance matrix (i.e. the elements of the covariance matrix grew without bound) whereas the Information filter always converged. It was demonstrated that using the “stacked” configuration with data from three, appropriately chosen, operating points (from a list of 59 operating points) 15 parameter variations and input biases can be estimated accurately. The use of data from four operating points does not allow more parameter variations and input biases to be estimated while these 15 parameters variations and input biases cannot be estimated accurately with data from one or two operating points.

## 1. Introduction

Model-based control is expected to provide a significant improvement in the control performance for General Electric jet engines. One of the key uses of an aircraft engine model is online state estimation as a means of estimating the unmeasurable performance outputs of the engine such as thrust and stall margin. These estimates can then be used as the current values of these performance parameters in a gain-scheduled, servo control scheme. This type of control scheme can substantially decrease the conservatism inherent in current approaches that directly control measurable output variables which are only indirectly related to the real performance outputs.

In order to determine engine quality it is also desired to estimate certain engine parameter and input biases. (Note that “parameter *bias*” here refers to a parameter *variation*.) To accomplish both this objective and the objective discussed above, it is necessary to simultaneously estimate the state vector  $x$  and the vector of engine parameter and input biases which will be denoted by  $u_b$ . Note that some of the elements of  $u_b$  may actually vary at different operating points, but in this study we will assume that these parameters are constant over all operating conditions. Even then, the estimation problem is nontrivial because there are fewer elements of the sensor measurement vector  $y$  than elements of the vector of parameter and input biases  $u_b$ , some of the sensors are very noisy, and some of the sensor measurements are biased.

In this study it is initially assumed that we are interested in using steady-state data at various operating points to estimate both the steady-state, state vector  $x_{ss}$  and  $u_b$ . The estimation problem at one (generic) operating point is studied under the ideal conditions of no plant disturbance and no plant noise. It will be seen that this analysis indicates that data from one operating point is not sufficient to uniquely determine  $x_{ss}$  and  $u_b$ . Hence, the use of data from more than one operating point is considered. Guidelines are developed on the minimum number of operating points needed and a rank condition on a certain matrix is used



to determine appropriate combinations of operating points. A “stacked” model structure that utilizes data from several operating points is then proposed as the basis for the filter design.

A key issue in filtering is numerical robustness. It was observed that when the stacked structure was used the covariance matrix would occasionally become divergent (i.e. some of the elements grew without bound) causing the Kalman filter to diverge. Hence the Information (or inverse covariance) filter was used to increase the numerical robustness of the estimation process. To familiarize the reader with the Information filter it is described and compared with the Kalman filter.

This report is organized as follows. Section 2 discusses the steady-state estimation problem under the ideal conditions of no plant disturbances or sensor noise. It then proposes a filtering structure that uses data at several operating points simultaneously. Section 3 describes state and parameter estimation using the Kalman and Information filters. Section 4 illustrates the results with a simplified estimation problem. Section 5 presents results for a realistic set of parameters and sensors. Finally, Section 6 presents conclusions, including a brief discussion of how the results may be extended to estimation using transient data.

## 2. Fundamental Problem and Proposed Solution

To estimate the states and parameters at a particular operating point a linear model has to be constructed. Linear models with any combinations of outputs and inputs desired, are constructed by linearizing the nonlinear model provided by GE about specific operating points and nominal parameter values. If plant disturbances and sensor noise are ignored, then the resulting linear model (after discretization) is of the form

$$x(k+1) = Ax(k) + Bu(k) + B_b u_b \quad (2.1)$$

$$z(k) = Cx(k) + Du(k) + D_b u_b \quad (2.2)$$

where  $u$  denotes the system inputs and  $u_b$  denotes the parameter variations and input biases.

To consider the steady-state behavior of the system (2.1)-(2.2), define

$$x_{ss} = \lim_{k \rightarrow \infty} x(k), \quad z_{ss} = \lim_{k \rightarrow \infty} z(k), \quad u_{ss} = \lim_{k \rightarrow \infty} u(k). \quad (2.3)$$

Then, (2.1)-(2.2) yield the steady-state equations

$$x_{ss} = Ax_{ss} + Bu_{ss} + B_b u_b \quad (2.4)$$

$$z_{ss} = Cx_{ss} + Du_{ss} + D_b u_b \quad (2.5)$$

or equivalently

$$\mathcal{A}\mathcal{X} = \mathcal{Z} \quad (2.6)$$

where

$$\mathcal{A} = \begin{bmatrix} (A - I) & B_b \\ C & D_b \end{bmatrix}, \quad \mathcal{X} = \begin{bmatrix} x_{ss} \\ u_b \end{bmatrix}, \quad \mathcal{Z} = \begin{bmatrix} -Bu_{ss} \\ z_{ss} - Du_{ss} \end{bmatrix}. \quad (2.7)$$

Let us assume that  $x \in \mathbb{R}^3$ ,  $z \in \mathbb{R}^8$ ,  $u_b \in \mathbb{R}^{22}$  such that  $\mathcal{X} \in \mathbb{R}^{25}$ ,  $\mathcal{Z} \in \mathbb{R}^{11}$ , and  $\mathcal{A} \in \mathbb{R}^{11 \times 25}$ . (These dimensions are equal to the data given for the GE jet engine considered in this study.) Notice that if (2.6) has a solution, it is not unique. In fact, if a solution exists, then there are an infinite number of solutions. If a solution exist, a necessary condition for a unique solution is the satisfaction of the following condition.

**Condition 1.** (*A necessary condition.*)  $nrow(\mathcal{A}) \geq ncol(\mathcal{A})$  where  $nrow$  denotes the number of rows and  $ncol$  denotes the number of columns.

A necessary *and* sufficient condition is the satisfaction of the following.

**Condition 2.** (*A necessary and sufficient condition.*)  $rank(\mathcal{A}) = ncol(\mathcal{A})$  where  $rank$  denotes the rank of the matrix. (This condition requires  $\mathcal{A}$  to be full column rank.)

In theory it is possible to satisfy Condition 1 by adding more sensor outputs. For example, assume that as before  $x \in \mathbb{R}^3$  and  $u_b \in \mathbb{R}^{22}$  but now  $z \in \mathbb{R}^{22}$ . Then,  $\mathcal{X} \in \mathbb{R}^{25}$ ,  $\mathcal{Z} \in \mathbb{R}^{25}$ , and  $\mathcal{A} \in \mathbb{R}^{25 \times 25}$ . Since  $\mathcal{A}$  is square, Condition 1 is now satisfied. Condition 2 is satisfied (such that  $\mathcal{X}$  is unique) only *if*  $\mathcal{A}$  is also invertible. Unfortunately, due to engineering limitations in the jet

engine problem considered here, it is not possible to sufficiently increase the number of sensors such that  $\dim(y) \geq \dim(u_b)$  where  $\dim$  denotes vector dimension. Even if this were possible, Condition 2 may not be satisfied. Because in practice  $\dim(y) < \dim(u_b)$ , it is necessary to use data from several operating points to perform the estimation.

Consider  $N$  operating points and assume that the parameter and input bias vector  $u_b$  does not vary with respect to the operating point. Let  $(A_i, B_i, C_i, D_i)$  denote the linear system and  $x_{i,ss}$ ,  $y_{i,ss}$ , and  $u_{i,ss}$  respectively denote the steady-state, state, output, and input vectors at the  $i^{th}$  operating point. Then, the steady-state conditions at the  $N$  operating points are described by the following equations.

$$\begin{aligned}
 x_{1,ss} &= A_1 x_{1,ss} + B_1 u_{1,ss} + B_{b,1} u_{b,1} & : \\
 z_{1,ss} &= C_1 x_{1,ss} + D_1 u_{1,ss} + D_{b,1} u_{b,1}, \\
 x_{2,ss} &= A_2 x_{2,ss} + B_2 u_{2,ss} + D_{b,2} u_{b,2} \\
 z_{2,ss} &= C_2 x_{2,ss} + D_2 u_{2,ss} + D_{b,2} u_{b,2}, \\
 &\vdots \\
 x_{N,ss} &= A_N x_{N,ss} + B_N u_{N,ss} + D_{b,N} u_{b,N} \\
 z_{N,ss} &= C_N x_{N,ss} + D_N u_{N,ss} + D_{b,N} u_{b,N}.
 \end{aligned}$$

Concatenating the above equations yields the linear system

$$\mathcal{A}\mathcal{X} = \mathcal{Z} \tag{2.8}$$

where

$$\mathcal{A} = \begin{bmatrix} B_{b,1} & (A_1 - I) & 0 & \cdots & 0 \\ D_{b,1} & C_1 & 0 & \cdots & 0 \\ B_{b,2} & 0 & (A_2 - I) & \cdots & 0 \\ D_{b,2} & 0 & C_2 & \cdots & 0 \\ \vdots & \vdots & \vdots & \ddots & \vdots \\ B_{b,N} & 0 & 0 & \cdots & (A_N - I) \\ D_{b,N} & 0 & 0 & \cdots & C_N \end{bmatrix}, \tag{2.9}$$

$$\mathcal{X} = \begin{bmatrix} u_b \\ x_{1,ss} \\ x_{2,ss} \\ \vdots \\ x_{N,ss} \end{bmatrix}, \quad \mathcal{Z} = \begin{bmatrix} -B_1 u_{1,ss} \\ z_{1,ss} - D_1 u_{1,ss} \\ -B_2 u_{2,ss} \\ z_{2,ss} - D_2 u_{2,ss} \\ \vdots \\ -B_N u_{N,ss} \\ z_{N,ss} - D_N u_{2,ss} \end{bmatrix}. \quad (2.10)$$

Note that if  $u_b \in \mathbb{R}^{22}$  and  $x_i \in \mathbb{R}^3$ ,  $z_i \in \mathbb{R}^8$  for  $i \in \{1, 2, \dots, N\}$ , then  $\mathcal{X} \in \mathbb{R}^{22+3N}$ ,  $\mathcal{Z} \in \mathbb{R}^{11N}$ , and  $\mathcal{A} \in \mathbb{R}^{11N \times (22+3N)}$ . As seen by Table 1, for  $N \geq 3$  Condition 1 is satisfied. Condition 2 must be satisfied by choosing an appropriate combination of operating conditions. These combinations are dependent upon the physics of the problem and will have to be determined experimentally. In practice, given a set of  $N$  operating conditions where  $N$  is sufficiently large to satisfy Condition 1, it is necessary to actually construct the matrix  $\mathcal{A}$  defined in (2.9) to determine whether Condition 2 is satisfied.

If no noise is present, it would be possible to solve for the desired steady-state, state vectors  $x_{i,ss}$  and unknown bias vector  $u_b$  by simply solving the linear system (2.8). However, since noise is present in the real problem it is necessary to use a filtering technique such as Kalman or Information filtering. If  $N$  operating points are chosen, then the filtering should be based on the following “stacked” linear system structure.

$$\begin{bmatrix} x_1(k+1) \\ x_2(k+1) \\ \vdots \\ x_N(k+1) \end{bmatrix} = \begin{bmatrix} A_1 & 0 & \cdots & 0 \\ 0 & A_2 & \cdots & 0 \\ \vdots & \vdots & \ddots & \vdots \\ 0 & \cdots & 0 & A_N \end{bmatrix} \begin{bmatrix} x_1(k) \\ x_2(k) \\ \vdots \\ x_N(k) \end{bmatrix} + \begin{bmatrix} B_1 \\ B_2 \\ \vdots \\ B_N \end{bmatrix} u(k) + \begin{bmatrix} B_{b,1} \\ B_{b,2} \\ \vdots \\ B_{b,N} \end{bmatrix} u_b \quad (2.11)$$

$$\begin{bmatrix} z_1(k) \\ z_2(k) \\ \vdots \\ z_N(k) \end{bmatrix} = \begin{bmatrix} C_1 & 0 & \cdots & 0 \\ 0 & C_2 & \cdots & 0 \\ \vdots & \vdots & \ddots & \vdots \\ 0 & \cdots & 0 & C_N \end{bmatrix} \begin{bmatrix} x_1(k) \\ x_2(k) \\ \vdots \\ x_N(k) \end{bmatrix} + \begin{bmatrix} D_1 \\ D_2 \\ \vdots \\ D_N \end{bmatrix} u(k) + \begin{bmatrix} D_{b,1} \\ D_{b,2} \\ \vdots \\ D_{b,N} \end{bmatrix} u_b. \quad (2.12)$$

In practice this filter structure will require the storage of data at several operating points.



N	nrow( $\mathcal{A}$ )	ncol( $\mathcal{A}$ )
1	11	25
2	22	28
3	33	31
4	44	34
5	55	37
6	66	40
7	77	43
8	88	46
9	99	49
10	110	52
11	121	55
12	132	58

Table 1: Number of Rows and Columns of  $\mathcal{A}$

### 3. State and Parameter Estimation

This section begins by showing that the problem of simultaneous input and state estimation can be reformulated as a standard state estimation problem. State estimation by standard Kalman filtering is then briefly described. Next, state estimation by Information filtering is discussed and then compared with Kalman filtering.

#### 3.1. Input and State Estimation

It is desired to use Kalman or Information filtering to estimate the state vector  $x$  and the vector of parameter and input biases  $u_b$  using a model of the form

$$x(k+1) = Ax(k) + Bu(k) + B_b u_b \quad (3.1)$$

$$z(k) = Cx(k) + Du(k) + D_b u_b. \quad (3.2)$$

This may be approached by expressing (3.1)-(3.2) in a form in which  $u_b$  is part of an augmented state vector [5]. In particular, since  $u_b(k+1) = u_b(k)$ , (3.1)-(3.2) may be expressed as

$$x_{aug}(k+1) = A_{aug}x_{aug}(k) + B_{aug}u(k) \quad (3.3)$$

$$z(k) = C_{aug}x_{aug}(k) + D_{aug}u(k) \quad (3.4)$$

where

$$x_{aug}(k) = \begin{bmatrix} x(k) \\ u_b \end{bmatrix}, \quad A_{aug} = \begin{bmatrix} A & B_b \\ 0 & I \end{bmatrix}, \quad B_{aug} = \begin{bmatrix} B \\ 0 \end{bmatrix}, \quad C_{aug} = \begin{bmatrix} C & D_b \end{bmatrix}. \quad (3.5)$$

Hence, in what follows, without loss of generality, only state estimation will be considered.

### 3.2. The Kalman Filter

Consider the time-varying, discrete-time, linear stochastic system

$$x(k+1) = F(k)x(k) + G(k)u(k) + w(k) \quad (3.6)$$

$$z(k) = H(k)x(k) + J(k)u(k) + v(k) \quad (3.7)$$

where  $w(k)$  is white process noise with covariance  $Q(k)$  and  $v(k)$  is white sensor noise with covariance  $R(k)$ .

The Kalman filter is a recursive linear estimator which successively calculates a minimum variance estimate for the state  $x$  given the observations  $z$ . The Kalman filter minimizes the mean square estimation error and is optimal with respect to a variety of important criteria under specific assumptions about process and observation noise. The Kalman filter can be summarized in the following two stages.

#### Prediction

$$\hat{x}(k|k-1) = F(k)\hat{x}(k-1|k-1) + G(k)u(k) \quad (3.8)$$

$$P(k|k-1) = F(k)P(k-1|k-1)F^T(k) + Q(k) \quad (3.9)$$

### Estimation

$$\hat{x}(k|k) = [I - W(k)H(k)]\hat{x}(k|k-1) + W(k)[z(k) - J(k)u(k)] \quad (3.10)$$

$$P(k|k) = P(k|k-1) - W(k)S(k)W^T(k) \quad (3.11)$$

where the gain matrix is given by

$$W(k) = P(k|k-1)H^T(k)S^{-1}(k) \quad (3.12)$$

and the innovation covariance by

$$S(k) = H(k)P(k|k-1)H^T(k) + R(k). \quad (3.13)$$

From (3.10), the Kalman filter state estimate can be interpreted as a linear weighted sum of the state prediction and observation. The weights in this averaging process are  $I - W(k)H(k)$  associated with the prediction and  $W(k)$  associated with the observation. The values of the weights depend on the balance of confidence in prediction and observation as specified by the process and observation noise covariances.

### The Constant Gain Kalman Filter

For the jet engine problem considered here (and many other problems) the system matrices  $F$ ,  $G$ ,  $H$ ,  $K$  are constant. In addition, it is sensible to assume the noise covariances  $Q$  and  $R$  constant. In this case, to save processor throughout, it is advantageous to use the steady-state value of the Kalman gain  $W$  in the filter implementation. The Kalman filter algorithm then reduces to the following.

$$\hat{x}(k|k-1) = F\hat{x}(k-1|k-1) + Gu(k) \quad (3.14)$$

$$\hat{x}(k|k) = [I - WH]\hat{x}(k|k-1) + W[z(k) - Ju(k)] \quad (3.15)$$

where

$$W = PH^TS^{-1} \quad (3.16)$$

$$S = HPH^T + R \quad (3.17)$$

and  $P$  is the nonnegative definite solution of the algebraic Riccati equation,

$$P = FPF^T + P - FPH^T(R + HPH^T)^{-1}HPF^T. \quad (3.18)$$

### 3.3. The Information Filter

The *Information filter* is essentially a Kalman filter expressed in terms of measures of *information* about the parameters (states) of interest rather than direct state estimates and their associated covariances. This filter has also been called the *inverse covariance* form of the Kalman filter [3,6, 12]. In this section, the contextual meaning of the information filter is derived.

For the Information filter there are two key *information-analytic* variables required, the *information matrix* and *information state vector*. The information matrix is defined as the inverse of the covariance matrix,

$$Y(i|j) \triangleq P^{-1}(i|j). \quad (3.19)$$

The information state vector is a product of the inverse of the covariance matrix (information matrix) and the state estimate.

$$\hat{y}(i|j) \triangleq P^{-1}(i|j)\hat{x}(i|j). \quad (3.20)$$

The variables,  $Y(i|j)$  and  $\hat{y}(i|j)$ , form the basis of the information space ideas that are central to the estimation presented in this report. For a detail explanation of the derivation of the information filter refer to [7]. The Information filter algorithm is summarized as follows:



### Prediction

$$\hat{y}(k|k-1) = L(k|k-1)\hat{y}(k-1|k-1) \quad (3.21)$$

$$Y(k|k-1) = [F(k)Y^{-1}(k-1|k-1)F^T(k) + Q(k)]^{-1} \quad (3.22)$$

### Estimation

$$\hat{y}(k|k) = \hat{y}(k|k-1) + H^T(k)R^{-1}(k)[z(k) - Ju(k)] \quad (3.23)$$

$$Y(k)(k) = Y(k|k-1) + H^T(k)R^{-1}(k)H(k) \quad (3.24)$$

where the propagation coefficient is given by

$$L(k|k-1) = Y(k|k-1)F(k)Y^{-1}(k-1|k-1). \quad (3.25)$$

This is the information form of the Kalman filter, [4,8]. Despite its potential applications, it is not widely used and is thinly covered in literature. Barshalom [3] and Maybeck [6] briefly discuss the idea of information estimation, but do not explicitly derive the algorithm in terms of information as done above, nor do they use it as a principal filtering method.

### Constant Coefficient Information Filter

As for constant gain Kalman filtering assume that  $F$ ,  $G$ ,  $H$ ,  $K$ ,  $Q$ , and  $R$  are constant and that the steady-state propagation coefficient  $L$  is used. Information filter estimation then reduces to the following.

$$\hat{y}(k|k-1) = L\hat{y}(k-1|k-1) \quad (3.26)$$

$$\hat{y}(k|k) = \hat{y}(k|k-1) + H^T R^{-1}[z(k) - Ju(k)] \quad (3.27)$$

where

$$L = YFY^{-1} \quad (3.28)$$

and  $Y = P^{-1}$  where  $P$  is the solution of the algebraic Riccati equation (3.18).

### 3.4. Comparison of the Kalman and Information Filters

By comparing the implementation requirements and performance of the Kalman and Information filters, a number of attractive features of the latter are identified:

- The information estimation equations (3.23) and (3.24) are computationally simpler than the state estimation equations (3.10) and (3.11).
- Although the information prediction equations (3.21) and (3.22) are more complex than equations (3.8) and (3.9), prediction depends on a propagation coefficient which is independent of the observations. It is thus again easy to decouple and decentralize.
- There are no gain or innovation covariance matrices and the maximum dimension of a matrix to be inverted is the state dimension. In multisensor systems the state dimension is sometimes smaller than the observation dimension, in which case it is preferable to employ the Information filter and invert smaller information matrices than use the Kalman filter and invert larger innovation covariance matrices.
- Initializing the Information filter is much easier than for the Kalman filter. This is because information estimates (matrix and state) are easily initialized to zero information. However, in order to implement the Information filter a start up procedure is required, where the information matrix is set with small non-zero diagonal elements to make it invertible.

## 4. Preliminary Results

This section describes some results using a simplified version of the engine estimation (i.e., only a few sensors and parameters/input biases are considered). The results clearly demonstrate the utility of using the singular values of  $\mathcal{A}$  as a means of determining the conditioning of the corresponding filtering problem and show that the stacking technique can greatly increase the

quality of the estimation of the state and input and parameter biases. The models used at each operating point consist of 3 states ( $xnl, xnh, tmpc$ ) and the sample period used to generate the discrete-time models is  $T = 0.001sec$ . In each simulation, the sensor noise was chosen to have a very small covariance and no plant noise was simulated.

#### 4.1. Example 1

In the first example the operating point is given by (Altitude=0 ft, Mach No.=0, Power Code=40). The bias vector  $u_b$  was of dimension 4 and consisted of 2 input biases ( $za8_{bi}, zp2_{bi}$ ) and the variations of 2 parameters ( $sedm2, zsw7d$ ). The sensor vector  $z$  consisted of 8 measurements ( $xn2c, xn25c, t27c, t56c, ps15c, p27c, ps3c, ps56c$ ). “

Since  $\mathcal{A} \in \mathbb{R}^{11 \times 7}$  for this configuration, for  $rank(\mathcal{A}) = ncol(\mathcal{A})$ , the first 7 singular values must be nonzero. The first 7 singular values are given by

$$\begin{bmatrix} 6.77e+2 \\ 9.25e+1 \\ 6.99e+0 \\ 1.01e+0 \\ 1.00e+0 \\ 1.09e-1 \\ 8.99e-3 \end{bmatrix}. \quad (4.1)$$

Notice that not only are these singular values nonzero, the ratio of the minimum singular value to the maximum singular value is  $1.33E-5$ . This probably indicates that the filtering problem is well conditioned. This conjecture is clearly verified by Figures 1 thru 7 which show that each of the state, input biases and parameter variations converge to their actual values.

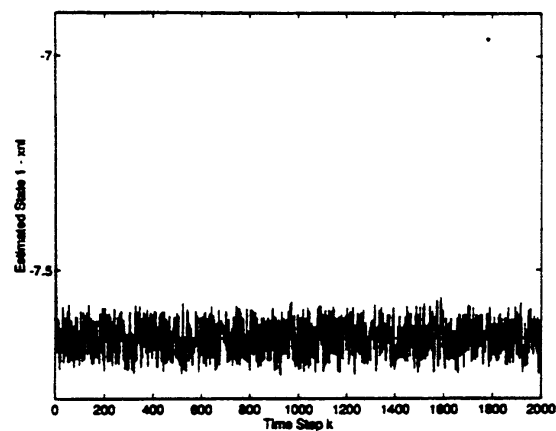


**Figure 1: 8 Measurement Estimation - State 1, XNL**

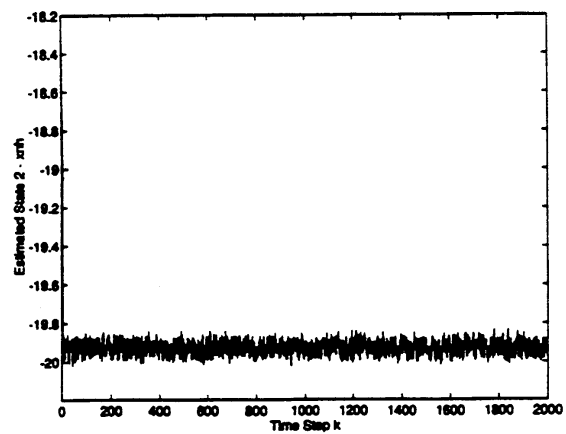


**Figure 2: 8 Measurement Estimation - State 2, XNH**



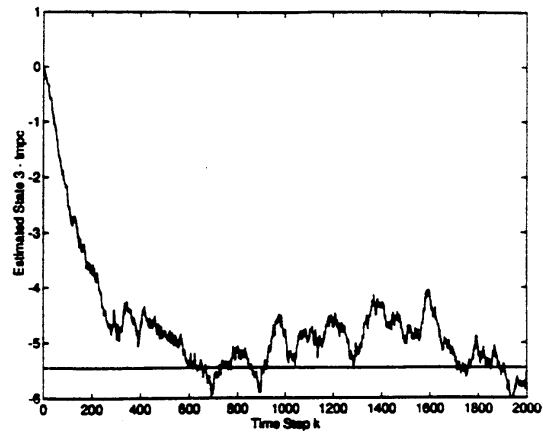


**Figure 3: 8 Measurement Estimation - State 3 TMPC**

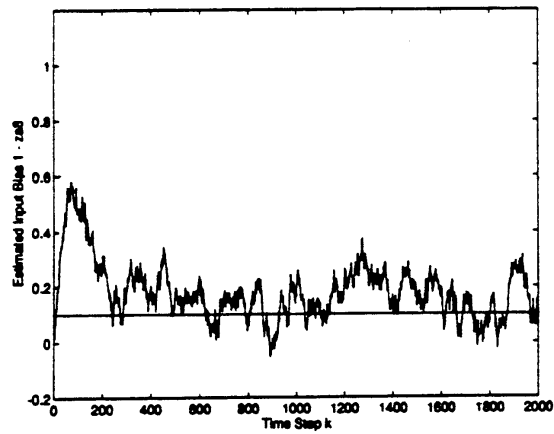


**Figure 4: 8 Measurement Estimation - Sensed Input 1, ZA8**

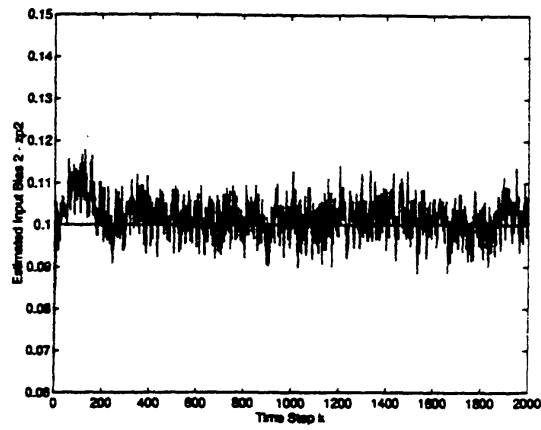


**Figure 5: 8 Measurement Estimation - Environmental Bias 2, ZP2**

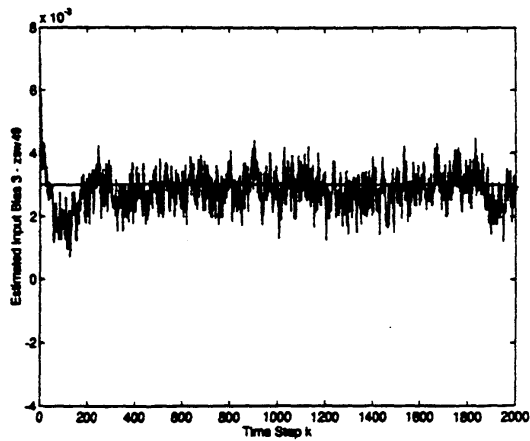


**Figure 6: 8 Measurement Estimation - Efficiency and Flow Scalar 3, ZSW49**

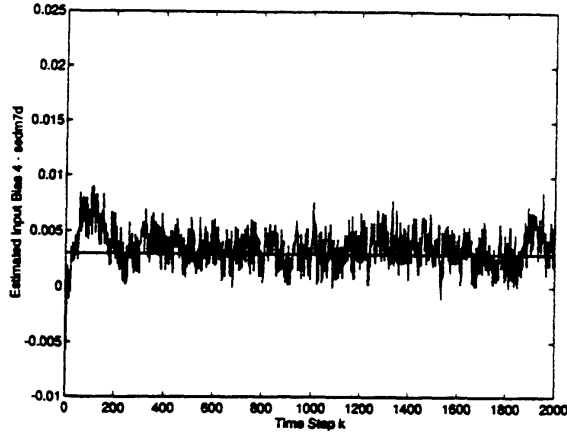


Figure 7: 8 Measurement Estimation - Efficiency and Flow Scalar 4, SEDM7D

#### 4.2. Examples 2 and 3

**Example 2.** As in Example 1, in this example the operating point is again given by (Altitude=0 ft, Mach No.=0, Power Code=40) and the bias vector  $u_b$  was of dimension 4 and consisted of 2 input biases ( $za8_{bi}$ ,  $zp2_{bi}$ ) and the variations of 2 parameters ( $sedm2$ ,  $zsw7d$ ). However, now the sensor vector  $z$  consisted of only 6 measurements ( $xn2c$ ,  $xn25c$ ,  $t27c$ ,  $t56c$ ,  $p27c$ ,  $ps56c$ ). (Example 1 measurements consisted of these 6 measurements plus  $ps15c$  and  $ps3c$ .)

Since  $\mathcal{A} \in \mathbb{R}^{9 \times 7}$  for this configuration, for  $rank(\mathcal{A}) = ncol(\mathcal{A})$ , the first 7 singular values must be nonzero. The first 7 singular values are given by

$$\begin{bmatrix} 6.73e+2 \\ 9.19e+1 \\ 3.22e+0 \\ 1.00e+0 \\ 1.00e+0 \\ 7.62e-3 \\ 3.06e-5 \end{bmatrix}. \quad (4.2)$$

Notice that each of these singular values is nonzero, but the ratio of the minimum singular value to the maximum singular value is  $4.55E-8$  which a factor of  $3.4E-3$  smaller than it

was for Example 1. This wider spread may indicate that the filtering problem is ill-conditioned. The “unstacked” curves in Figures 8 thru 14 clearly indicate that this is the case since several of the states, input biases and parameter variations fail to converge to their actual values.

**Example 3.** An attempted remedy to this filter failure is to use data from at least one additional operating point. Let us consider one additional operating point described by (Altitude=20,000ft,Mach No.=0.5,Power Code=40) with the same 6 sensors and 4 input biases and parameter variations as above.  $\mathcal{A}$  corresponding to the 2 operating points is  $18 \times 10$ . Hence, for  $\text{rank}(\mathcal{A}) = \text{ncol}(\mathcal{A})$ , the first 10 singular values must be nonzero. The first 10 singular values are given by

$$\begin{bmatrix} 9.78e+2 \\ 1.32e+2 \\ 3.55e+1 \\ 1.00e+0 \\ 1.00e+0 \\ 1.00e+0 \\ 1.00e+0 \\ 1.32e-1 \\ 4.96e-3 \\ 1.95e-3 \end{bmatrix} \quad (4.3)$$

Notice that each of these singular values is nonzero and the ratio of the minimum singular value to the maximum singular value is  $1.99E-6$  which is a factor of  $1.5E-1$  smaller than in Example 1 but a factor of  $4.39E+1$  larger than in Example 2. Since Example 1 converged to the correct states, input biases and parameter variations, it is logical to infer that this spread indicates that this filtering problem is well conditioned. The “stacked” curves in Figures 8 thru 14 clearly indicate that this is the case. With the exception of state 3 (see Figure 10) each of the states, input biases and parameter variations converged to their actual values.



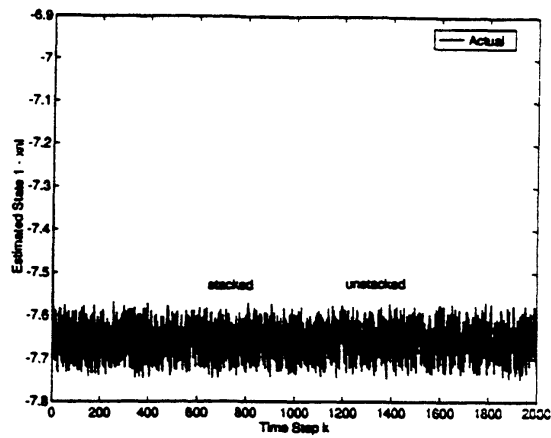


**Figure 8: 6 Measurement Estimation - State 1, XNL**

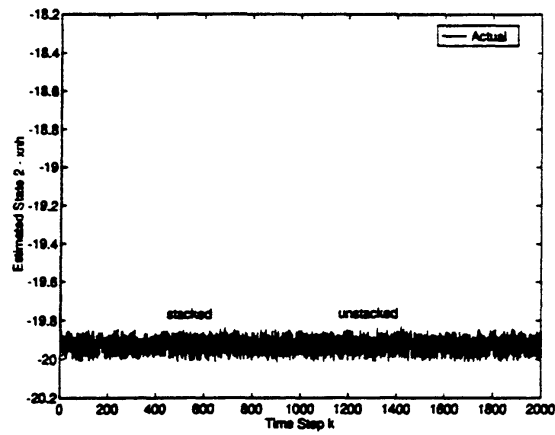


**Figure 9: 6 Measurement Estimation - State 2, XNH**

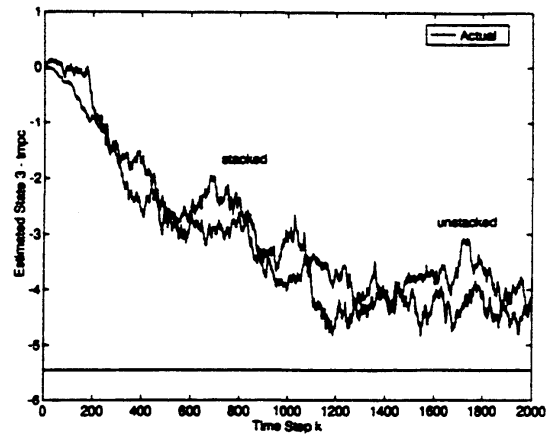


**Figure 10: 6 Measurement Estimation - State 3, TMPC**

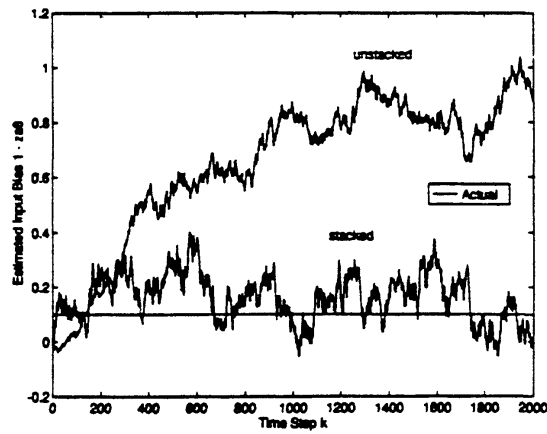


**Figure 11: 6 Measurement Estimation - Sensed Input 1, ZA8**

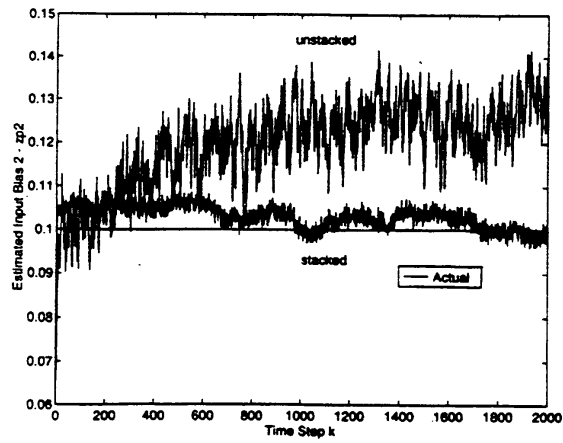


Figure 12: 6 Measurement Estimation - Environmental Bias 2, ZP2

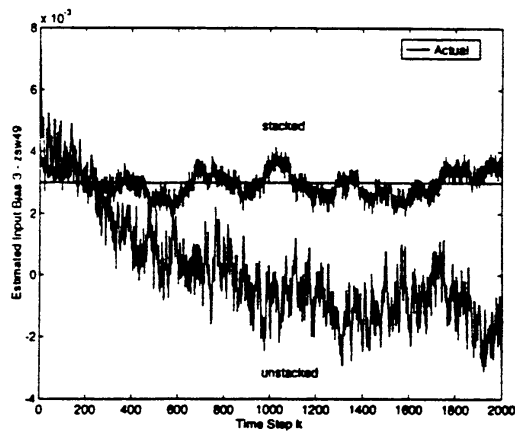


Figure 13: 6 Measurement Estimation - Efficiency and Flow Scalar 3, ZSW49

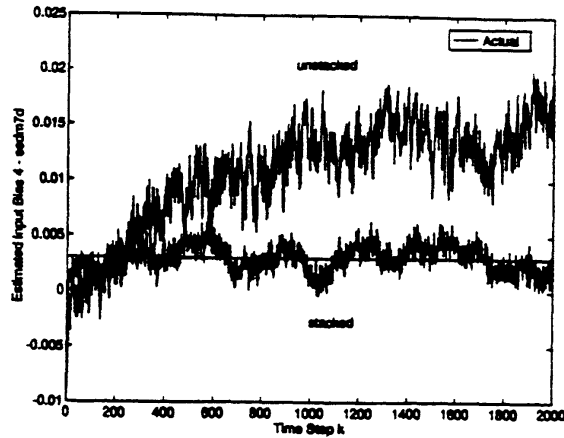


Figure 14: 6 Measurement Estimation - Efficiency and Flow Scalar 4, SEDM7D

## 5. Larger Scale Simulation

In this section we consider a parameter set more realistic than that considered in the previous section. As detailed in the tables of the next subsection, it was assumed that 8 sensors were available to estimate 3 states and 15 parameters. The Kalman and Information filters were not able to estimate the remaining 8 parameters no matter how many operating points were used. Hence, these 8 parameters are not considered in this simulation.

Linear models were constructed for 59 operating points in the flight envelope. These operating points are described in Appendix 1. A sampling period of  $T=0.2$  sec was used for the discretization of these linear models. In each simulation the actual values of the parameter set were calculated without white process noise,  $w(k)$ . The white sensor noise,  $v(k)$ , was simulated using the MATLAB function *RAND* to sample a uniform distribution between 0 and 1. In the Kalman filter algorithm the covariance,  $Q(k)$ , of the process noise and the covariance,  $R(k)$ , of the sensor noise were chosen to be diagonal. The diagonal elements of  $R(k)$  were chosen



to be equal to 0.1. The diagonal elements of  $Q(k)$  were chosen such that the three diagonal elements corresponding to the three plant states were 0.1, the variances of the 3 directly sensed inputs, ZWF36, ZA8, ZA16 (parameters 1,2,and 3 in Table 4) were 0.001, and the remaining diagonal elements were 0.0001.

Since 15 parameters were used in the simulation, the dimensions of  $\mathcal{A}$ , defined by (2.9) differed from those tabulated in Table 1. The dimensions for combinations of one, two, and three operating points are given in Table 2. For combinations of two and three operating points the inverse of the condition number of  $\mathcal{A}$ ,  $\text{cond}(\mathcal{A})$ , defined by

$$\text{cond}(\mathcal{A}) \triangleq \frac{\sigma_{\max}}{\sigma_{\min}} \geq 1,$$

was used to determine how well the matrix satisfied the full column rank condition. In particular the larger the value of  $\text{cond}(\mathcal{A})^{-1}$  the better a combination of two or three operating points. (Recognize that  $\text{cond}(\mathcal{A})^{-1} \leq 1$ .) All combinations of two and three operating points were created from the 59 available operating points and the corresponding  $\text{cond}(\mathcal{A})^{-1}$  were computed.

N	nrow( $\mathcal{A}$ )	ncol( $\mathcal{A}$ )
1	11	18
2	22	21
3	33	24

Table 2: Number of Rows and Columns of  $\mathcal{A}$

The largest 100  $\text{cond}(\mathcal{A})^{-1}$  for combinations of two and three operating points are listed in Appendix 1. Comparison of the largest  $\text{cond}(\mathcal{A})^{-1}$  for combinations of two operating points, 6.68E-07, to that of the largest  $\text{cond}(\mathcal{A})^{-1}$  using three operating points, 2.72E-06, reveals that the latter number is larger by a factor of 4. As seen in Appendix 1, the best combination of two operating points is (39, 40), while the best combination of three operating points is (7, 51, 58). Of the total 59 operating points considered only 43 were used in the top 100 combinations of three, while all were used in the top 100 combinations of two.

Except in the cases where the Kalman filter diverged, the estimates of the Kalman and Information filters was quite close. Hence, in the tabular results reported in this section (see Tables 5, 6 and 7), we report only the statistics associated with parameter estimation using the Information filter. The statistics for both the Kalman and Information filters are given in Tables 12 thru 18 of Appendices 2 thru 8.

## 5.1. Sensors and Parameters

Sensor Number	Sensor Name
1	XN2C - Low pressure rotor speed
2	XN25C - High pressure rotor speed
3	T27C - Core driven fan stage hub temperature
4	T56C - LP Turbine exit temperature
5	PS15C - Bypass duct static pressure
6	P27C - Core driven fan stage hub total pressure
7	PS3C - Compressor discharge static pressure
8	PS56C - LP Turbine frame static pressure

Table 3: Sensors Available for Simulation

Parameter Number	Parameter Name	Parameter Value
1	ZWF36 - Combustor fuel flow	3.00E-03
2	ZA8 - Nozzle area	0.00E+00
3	ZA16 - Rear VABI area	0.00E+00
4	ZSW2 - Fan flow scalar	3.00E-03
5	SEDM2 - Fan efficiency scalar	3.00E-03
6	ZSW7D - Compressor tip flow scalar	3.00E-03
7	SEDM7D - Compressor tip efficiency scalar	3.00E-03
8	ZSW27 - Compressor hub flow scalar	3.00E-03
9	SEDM27 - Compressor hub efficiency scalar	3.00E-03
10	ZSW41 - HP Turbine flow scalar	3.00E-03
11	ZSE41 - HP Turbine efficiency scalar	3.00E-03
12	ZSW49 - LP Turbine flow scalar	3.00E-03
13	ZSE49 - LP Turbine efficiency scalar	3.00E-03
14	ZWB3 - Compressor discharge bleed flow	0.00E+00
15	ZPWXH - Customer power extraction (core rotor)	0.00E+00

Table 4: Parameter Set to Be Estimated in Simulation

## 5.2. Simulation Results

Below several simulation and tabular results for nine cases are given. Complete sets of the simulation and tabular results are presented for the first seven cases in Appendices 2 thru 8. For the first four cases each of the parameters was initialized to zero in the filtering. These four cases respectively illustrate estimation using 1) the best combination of three operating points, 2) an arbitrary combination of three operating points, 3) the best combination of two operating points, and 4) a single operating point from the best combination of three. In each of these cases the parameter sets converge nicely, although some results do have better convergence than others.

In the next three cases each of the parameters was initialized to 0.5. Estimation results are given for the cases described above, with the exception of the arbitrary combination of three

operating points. When the parameters are initialized to 0.5, it is seen that the parameters do not converge to their true values using the best combination of two operating points. The results are even worse using the single operating point.

The final two cases illustrate that the Kalman filter sometimes diverged while the Information filter converged. Hence, the Information filter is seen to be more numerically robust.

#### 5.2.1. Case 1: Estimation Using The Best Combination of Three - Parameters Initialized to Zero

The first case considered was the combination of three operating points (7,51,58) with the largest  $\text{cond}(\mathcal{A})^{-1}$ . Table 5 and Figures 15 thru 17 show that the data from these three operating points are sufficient to estimate the parameter set successfully. A complete set of figures illustrating the estimation is given in Appendix 2.

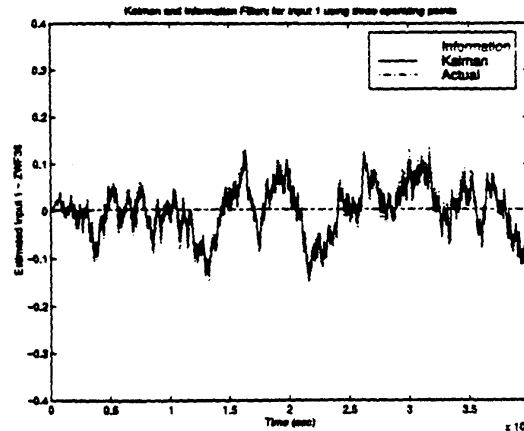
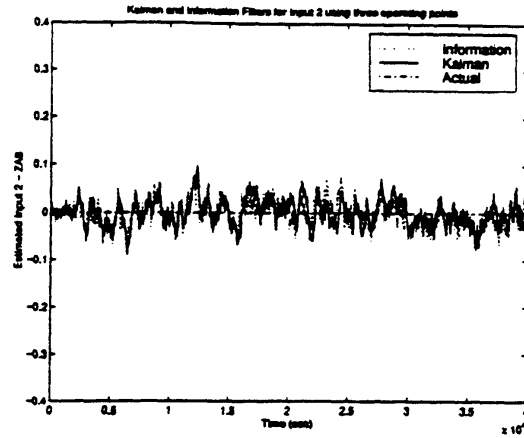
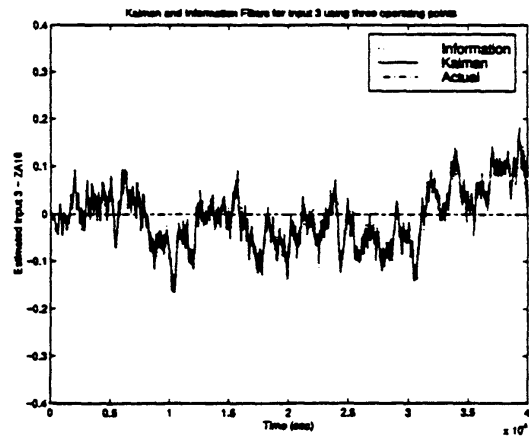


Figure 15: Measurement Estimation - Sensed Input 1, ZWF36 (Case 1)



**Figure 16:** Measurement Estimation - Sensed Input 2, ZA8 (Case 1)



**Figure 17:** Measurement Estimation - Sensed Input 3, ZA16 (Case 1)



### 5.2.2. Case 2: Estimation Using Arbitrary Combination of Three - Parameters Initialized to Zero

An arbitrary combination of three operating points was chosen (1,30,57) to be used to estimate the parameter set. For this case  $\text{cond}(\mathcal{A})^{-1} = 8.73\text{E-}7$ , which is a factor of 3 smaller than the previous case. Table 5 and Figures 18 thru 20 show that, as expected, the estimation process is not as accurate as for the best combination of three operating points. However, the results are still reasonable. A complete set of figures illustrating the estimation is given in Appendix 3.

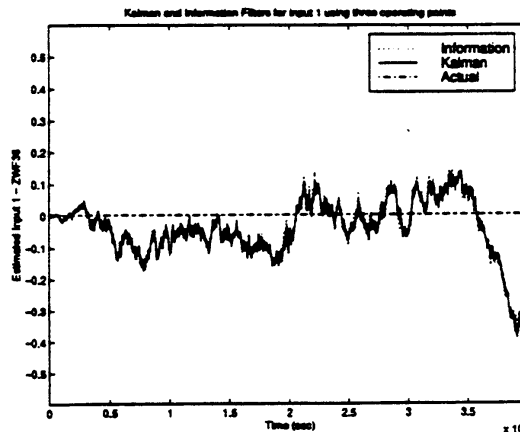


Figure 18: Measurement Estimation - Sensed Input 1, ZWF36 (Case 2)

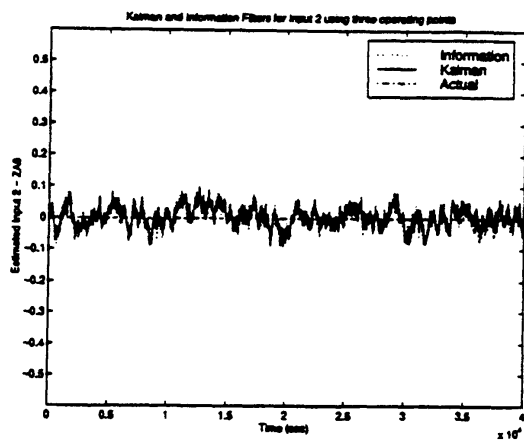


Figure 19: Measurement Estimation - Sensed Input 2, ZA8 (Case 2)

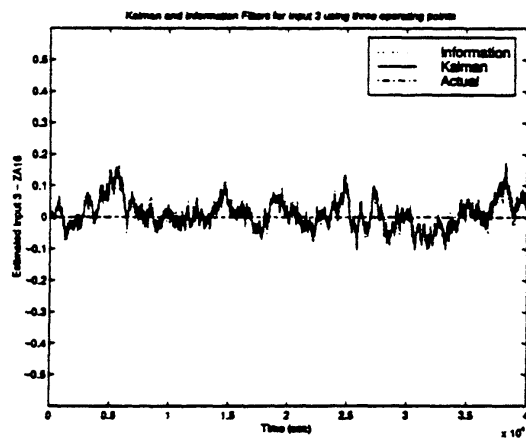


Figure 20: Measurement Estimation - Sensed Input 3, ZA16 (Case 2)

		Case 1		Case 2	
Parameter	Value	Mean	Variance	Mean	Variance
ZWF36	3.00E-03	3.24E-02	5.20E-03	3.24E-02	5.20E-03
ZA8	0.00E+00	5.20E-03	6.20E-04	-4.75E-04	6.20E-04
ZA16	0.00E+00	2.48E-02	2.97E-03	2.48E-02	2.97E-03
ZSW2	3.00E-03	2.99E-03	2.06E-07	2.99E-03	2.06E-07
SEDM2	3.00E-03	2.99E-03	1.06E-07	2.99E-03	1.06E-07
ZSW7D	3.00E-03	2.97E-03	6.46E-07	2.97E-03	6.46E-07
SEDM7D	3.00E-03	2.95E-03	1.29E-06	2.95E-03	1.29E-06
ZSW27	3.00E-03	3.02E-03	3.89E-08	3.02E-03	3.89E-08
SEDM27	3.00E-03	3.01E-03	7.10E-08	3.01E-03	7.10E-08
ZSW41	3.00E-03	3.01E-03	5.05E-08	3.01E-03	5.05E-08
ZSE41	3.00E-03	2.99E-03	1.62E-07	2.99E-03	1.62E-07
ZSW49	3.00E-03	3.02E-03	2.12E-07	3.02E-03	2.12E-07
ZSE49	3.00E-03	3.02E-03	2.00E-07	3.02E-03	2.00E-07
ZWB3	0.00E+00	1.56E-04	2.11E-05	1.56E-04	2.11E-05
ZPWXH	0.00E+00	-2.21E-02	6.81E-04	-2.21E-02	6.81E-04

Table 5: Means and Variances of Parameters Estimated Using the Information Filter - Cases 1 and 2

### 5.2.3. Case 3: Estimation Using Best Combination of Two - Parameters Initialized to Zero

Next consider the combination of two operating points (39,40) with the largest  $\text{cond}(\mathcal{A})^{-1}$  (6.68E-07) which is less than either of the combinations of three considered previously. Table 6 and Figures 21 thru 23 reveal that, as expected, the parameter estimation has worse convergence properties than the previous cases which used three operating points. A complete set of figures illustrating the estimation is given in Appendix 4.

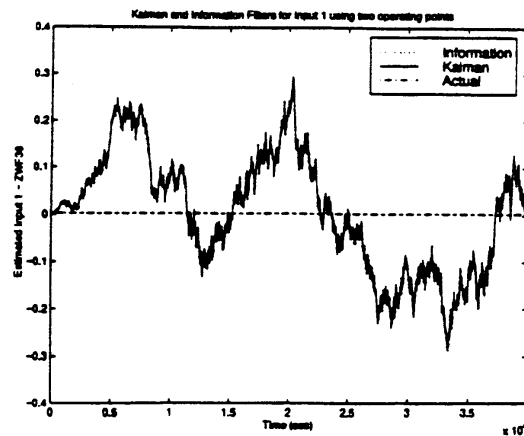


**Figure 21:** Measurement Estimation - Sensed Input 1, ZWF36 (Case 3)

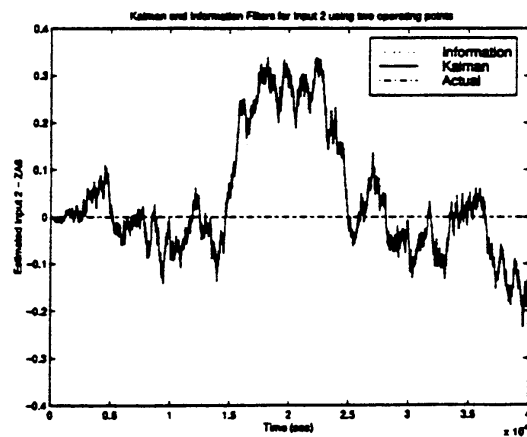


**Figure 22:** Measurement Estimation - Sensed Input 2, ZA8 (Case 3)

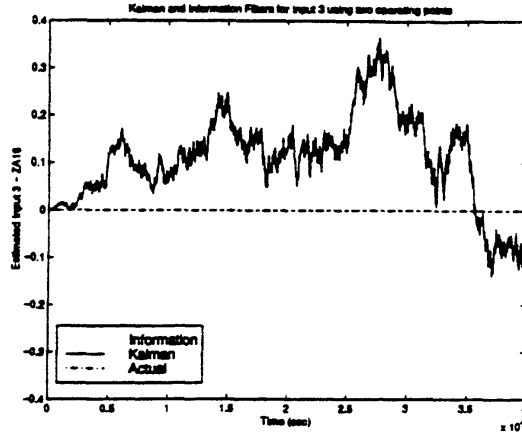


**Figure 23: Measurement Estimation - Sensed Input 3, ZA16 (Case 3)**

#### 5.2.4. Case 4: Estimation Using Single Operating Point - Parameters Initialized to Zero

It was determined by simulation that the single operating point from the best combination of three (7,51,58) that gives the best estimation results is 58. Since for one operating point  $\mathcal{A} \in \mathbb{R}^{11 \times 18}$  such that  $nrow(\mathcal{A}) < ncol(\mathcal{A})$ , it is possible for the estimation process to converge to the wrong parameter values. However, Table 6 and Figures 24 thru 26 illustrate that the estimation process with a single operating point can yield good results. This is because for this and all previous cases the parameter set was initialized to zero for the filtering, such that the initial parameter estimates were equal or close to their actual values. It will be shown below that the estimation process for a single operating point yields poor estimates with different initial parameters. A complete set of figures illustrating the estimation is given in Appendix 5.



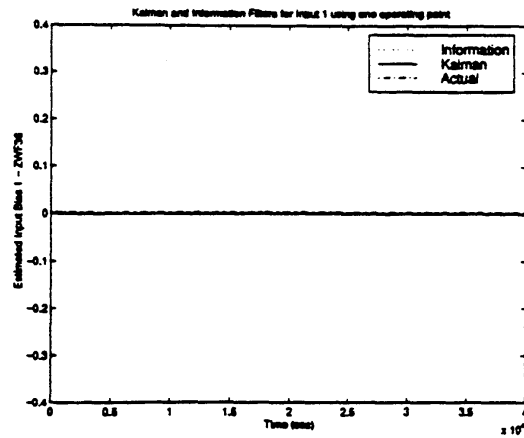


**Figure 24: Measurement Estimation - Sensed Input 1, ZWF36 (Case 4)**

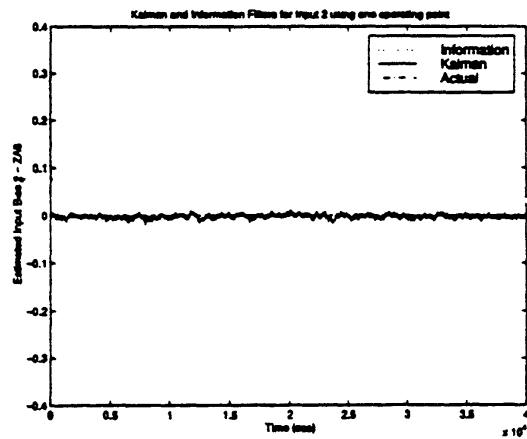


**Figure 25: Measurement Estimation - Sensed Input 2, ZA8 (Case 4)**

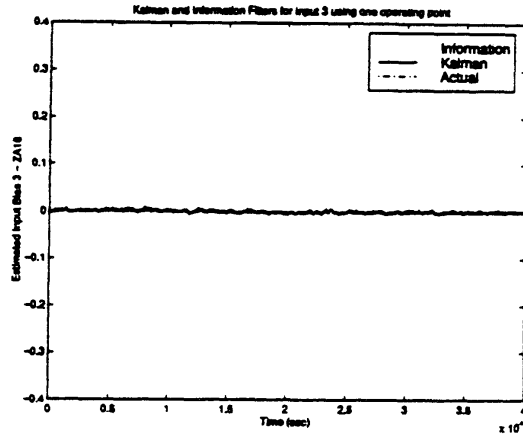


**Figure 26:** Measurement Estimation - Sensed Input 3, ZA16 (Case 4)

		Case 3		Case 4	
Parameter	Value	Mean	Variance	Mean	Variance
ZWF36	3.00E-03	6.57E-03	1.52E-02	7.26E-05	2.30E-08
ZA8	0.00E+00	3.90E-02	1.70E-02	-2.70E-03	2.00E-05
ZA16	0.00E+00	1.12E-01	9.10E-03	1.23E-03	6.11E-06
ZSW2	3.00E-03	2.94E-03	1.56E-05	2.95E-03	2.98E-06
SEDM2	3.00E-03	2.90E-03	6.52E-06	2.94E-03	4.05E-06
ZSW7D	3.00E-03	3.21E-03	4.56E-05	2.94E-03	6.33E-06
SEDM7D	3.00E-03	9.21E-04	9.42E-05	4.03E-03	5.05E-05
ZSW27	3.00E-03	2.92E-03	1.95E-06	3.15E-03	4.97E-06
SEDM27	3.00E-03	3.11E-03	2.38E-06	3.45E-03	4.67E-07
ZSW41	3.00E-03	2.98E-03	1.29E-06	3.05E-03	5.77E-07
ZSE41	3.00E-03	3.05E-03	1.29E-06	3.42E-03	1.94E-06
ZSW49	3.00E-03	3.01E-03	7.03E-06	1.83E-03	8.78E-07
ZSE49	3.00E-03	3.05E-03	1.48E-06	4.64E-04	5.59E-07
ZWB3	0.00E+00	-8.02E-04	5.18E-04	-5.57E-04	6.78E-07
ZPWXH	0.00E+00	1.08E-02	1.76E-04	-1.47E-06	6.14E-12

**Table 6:** Means and Variances of Parameters Estimated Using the Information Filter - Cases 3 and 4

#### 5.2.5. Case 5: Estimation Using Best Combination of Three - Parameters Initialized to 0.5

This case parallels that described in subsection 5.2.2 for the combination (7,51,58) with the exception that each of the parameters was initialized to 0.5. Table 7 and Figures 27 thru 29 show that the parameters converge to their actual values despite the poor initialization. A complete set of figures illustrating the estimation is given in Appendix 6.

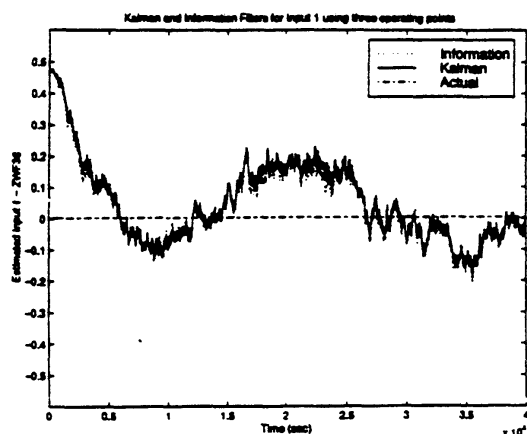


**Figure 27:** Measurement Estimation - Sensed Input 1, ZWF36 (Case 5)

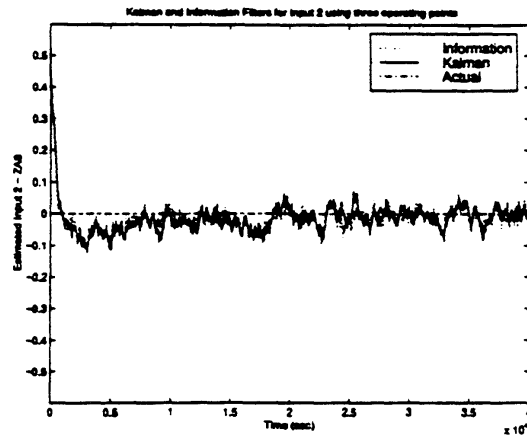


Figure 28: Measurement Estimation - Sensed Input 2, ZA8 (Case 5)

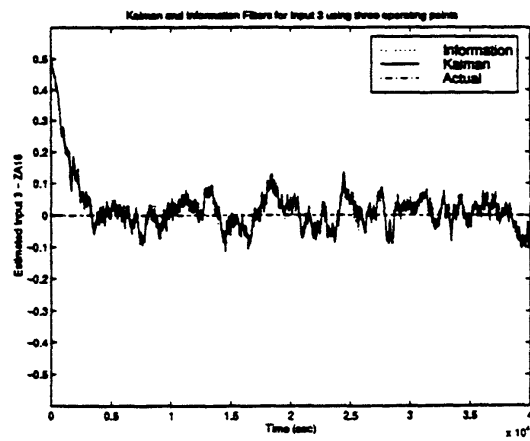
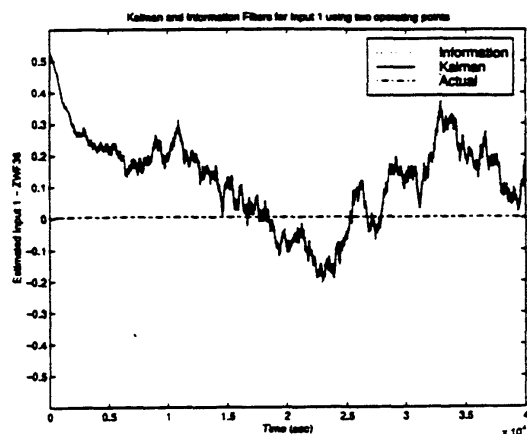


Figure 29: Measurement Estimation - Sensed Input 3, ZA16 (Case 5)

#### 5.2.6. Case 6: Estimation Using Best Combination of Two - Parameters Initialized to 0.5

This case parallels that described in subsection 5.2.3 for the combination (39,44) with the exception that each of the parameters was initialized to 0.5. Table 7 and Figures 30 thru 32 illustrate that the parameters converge slowly and do not always converge to their true values. A complete set of figures illustrating the estimation is given in Appendix 7.



**Figure 30:** Measurement Estimation - Sensed Input 1, ZWF36 (Case 6)



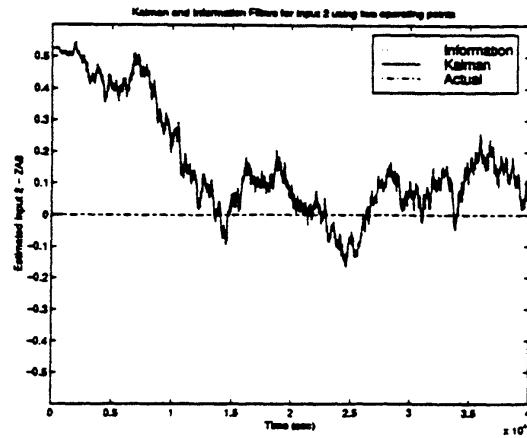


**Figure 31: Measurement Estimation - Sensed Input 2, ZA8 (Case 6)**

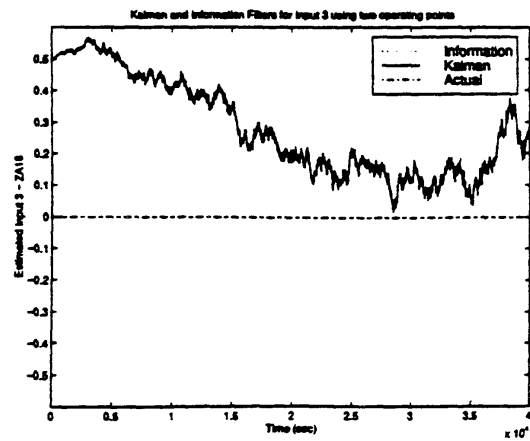


**Figure 32: Measurement Estimation - Sensed Input 3, ZA16 (Case 6)**

Parameter	Value	Case 5		Case 6	
		Mean	Variance	Mean	Variance
ZWF36	3.00E-03	4.34E-02	1.19E-02	1.15E-01	1.65E-02
ZA8	0.00E+00	-1.94E-02	7.97E-04	1.53E-01	2.83E-02
ZA16	0.00E+00	1.19E-02	2.51E-03	2.74E-01	2.25E-02
ZSW2	3.00E-03	2.95E-03	2.07E-07	3.93E-03	3.04E-05
SEDM2	3.00E-03	2.99E-03	1.07E-07	3.30E-03	9.50E-06
ZSW7D	3.00E-03	2.96E-03	6.49E-07	1.77E-03	5.16E-05
SEDM7D	3.00E-03	2.81E-03	1.33E-06	5.45E-03	9.73E-05
ZSW27	3.00E-03	3.01E-03	3.85E-08	3.39E-03	6.05E-06
SEDM27	3.00E-03	2.97E-03	7.22E-08	2.91E-03	2.60E-06
ZSW41	3.00E-03	3.00E-03	4.90E-08	3.15E-03	1.51E-06
ZSE41	3.00E-03	3.10E-03	1.68E-07	3.06E-03	3.64E-06
ZSW49	3.00E-03	3.00E-03	2.11E-07	2.82E-03	1.26E-05
ZSE49	3.00E-03	3.01E-03	1.93E-07	3.12E-03	1.93E-06
ZWB3	0.00E+00	1.49E-04	2.33E-05	3.17E-03	1.65E-03
ZPWXH	0.00E+00	1.72E-01	2.56E-02	4.67E-01	1.75E-03

Table 7: Means and Variances of Parameters Estimated Using the Information Filter - Cases 5 and 6

#### 5.2.7. Case 7: Estimation Using Single Operating Point from Best Combination of Three - Parameters Initialized to 0.5

This case parallels that described in subsection 5.2.4 with the exception that each of the parameters was initialized to 0.5. Table 7 and Figures 33 thru 35 show that the parameters do not converge to their true values. A complete set of figures illustrating the estimation is given in Appendix 8.

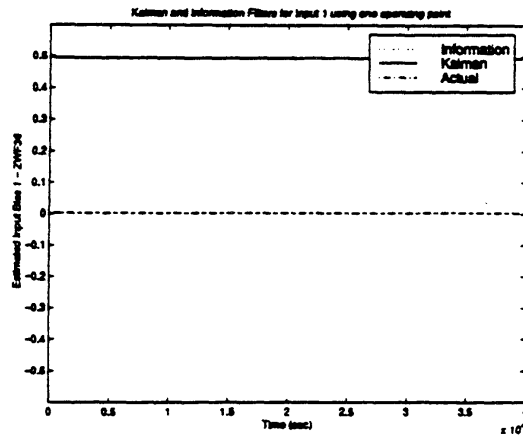


**Figure 33: Measurement Estimation - Sensed Input 1, ZWF36 (Case 7)**

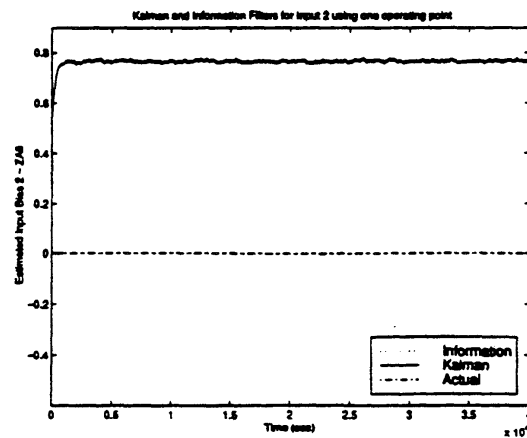


**Figure 34: Measurement Estimation - Sensed Input 2, ZAδ (Case 7)**

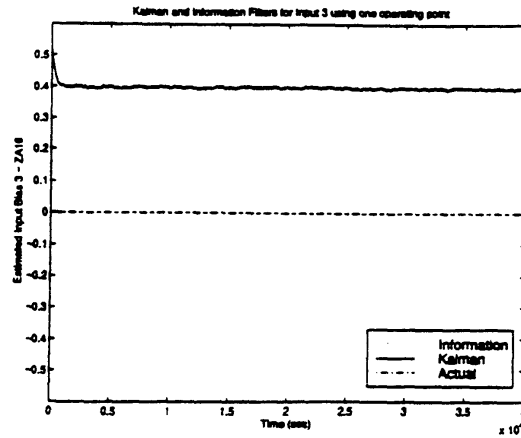


**Figure 35:** Measurement Estimation - Sensed Input 3, ZA16 (Case 7)

Parameter	Value	Case 7	
		Mean	Variance
ZWF36	3.00E-03	4.94E-01	2.13E-08
ZA8	0.00E+00	7.66E-01	1.86E-05
ZA16	0.00E+00	3.98E-01	5.70E-06
ZSW2	3.00E-03	2.09E-02	3.26E-06
SEDM2	3.00E-03	4.03E-03	4.61E-06
ZSW7D	3.00E-03	7.02E-03	6.83E-06
SEDM7D	3.00E-03	1.14E-01	4.68E-05
ZSW27	3.00E-03	4.42E-02	5.46E-06
SEDM27	3.00E-03	-1.55E-01	5.27E-07
ZSW41	3.00E-03	1.32E-02	5.64E-07
ZSE41	3.00E-03	-3.99E-02	1.91E-06
ZSW49	3.00E-03	2.22E-01	8.95E-07
ZSE49	3.00E-03	4.22E-01	5.66E-07
ZWB3	0.00E+00	5.61E-01	6.27E-07
ZPWXH	0.00E+00	5.00E-01	5.67E-12

**Table 8:** Means and Variances of Parameters Estimated Using the Information Filter - (

### 5.2.8. Estimation Illustrating Kalman Filter Divergence and Information Filter Convergence

One of the advantages of the Information filter over the Kalman filter (as discussed in Section 3.4) is the fact that there are no gain  $W(k)$  nor innovation covariance  $S(k)$  matrices involved in its algorithm, whereas these two matrices are central to the Kalman filter as shown in (3.10) - (3.12). From (3.11) it is clear that the gain  $W(k)$  depends on the predicted covariance  $P(k|k-1)$ , observation matrix  $H(k)$  and the innovation covariance  $S(k)$ . The innovation covariance in turns depends on  $H(k)$ ,  $P(k|k-1)$  and  $R(k)$ . This means the critical variable in both  $W(k)$  and  $S(k)$  is the predicted covariance  $P(k|k-1)$ . This predicted covariance is computed from the previous covariance  $P(k-1|k-1)$  given by (3.9). This means that any problems associated with an ill-conditioned covariance  $P(k|k)$ , such as singularity or divergence, will affect the Kalman filter.

On the other the hand, the Information filter does not involve  $W(k)$  nor  $S(k)$  at all. Although the definition of Fisher information given in (3.19) defines the Information matrix  $Y(k|k)$  as the inverse of the covariance  $P(k|k)$ , a careful inspection of the Information filter algorithm shows that it is not necessary to continuously compute and use  $P(k|k)$ . Consequently any problems associated with an ill-conditioned  $P(k|k)$ ,  $S(k)$  or  $W(k)$  won't affect the Information filter.

In particular, the concerns about the singularity of  $P(k|k)$  which are raised in the literature [12], are of no consequence to the Information filtering techniques discussed in this report. The only covariance required is the initial one, i.e  $P(0|0)$ , to obtain  $Y(0|0)$ . The Information filter algorithm avoids the singularity of  $P(0|0)$  by using a start-up procedure for initialization, where the initial covariance is equated to a product of a constant  $\alpha$  (a large positive number such as 100 or 1000) and the the process noise covariance  $Q(k)$  as follows:

$$P(0|0) = \alpha Q(0) \tag{5.1}$$



$$Y(0|0) = P(0|0)^{-1} \quad (5.2)$$

The idea is to have a start-up procedure where the initial information matrix is set with small non-zero diagonal elements [7]. This is in keeping with the fact that initializing the Information filter is much easier than initializing the Kalman filter, because the Information estimates (matrix and state) are easily initialized to zero information. From (3.21) - (3.25) it is clear that once the Information filter is started it does not require nor use  $P(k|k)$  and hence the singularity of  $P(k|k)$  is of no relevance.

Another form of an ill-conditioned  $P(k|k)$  is when the covariance matrix diverges, that is, its elements grow without bound towards infinity. It is seen from (3.13) that when  $P(k|k)$  diverges, (due to numerical ill-conditioning) the innovation covariance matrix  $S(k)$  also diverges. Consequently, from (3.10) the state estimate  $\hat{x}(k|k)$  similarly diverges, producing the divergence of the Kalman filter algorithm. On the other hand, since the terms  $P(k|k)$ ,  $W(k)$  and  $S(k)$  do not appear in the Information filter algorithm, it does not suffer from this divergence problem and hence successfully converges.

Figures 36 thru 41 show two cases in which the Kalman filter diverges due to the divergence of  $P(k|k)$  and  $S(k)$ , while the Information filter estimates successfully. Figures 36 thru 38 correspond to the combination (10,46,58) with  $\text{cond}(\mathcal{A})^{-1} = 1.45\text{E-}7$ , while Figures 39 thru 41 correspond to the combination (1,2,3) with  $\text{cond}(\mathcal{A})^{-1} = 9.43\text{E-}8$ . These results effectively illustrate the advantages of the Information filter over the Kalman filter in situations where combinations of operating points lead to ill-conditioned covariance matrices.

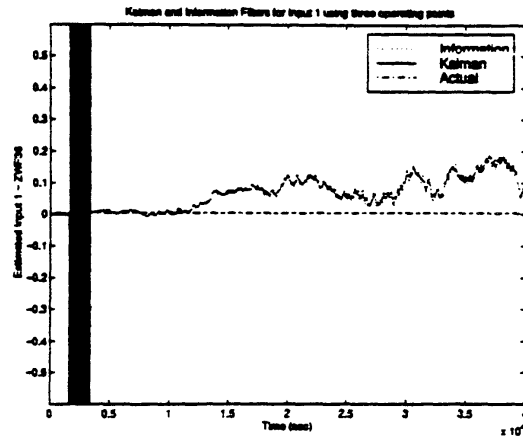


**Figure 36:** Measurement Estimation - Sensed Input 1, ZWF36 (Case 8)

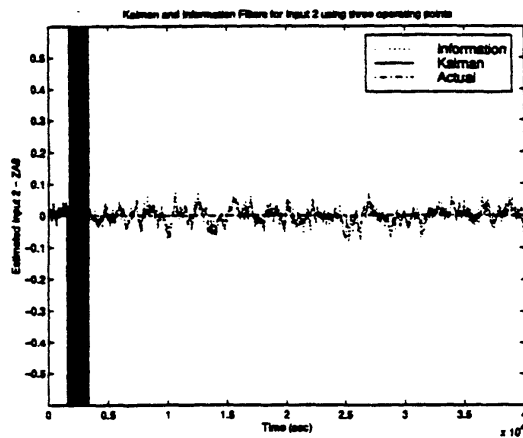


**Figure 37:** Measurement Estimation - Sensed Input 2, ZA8 (Case 8)

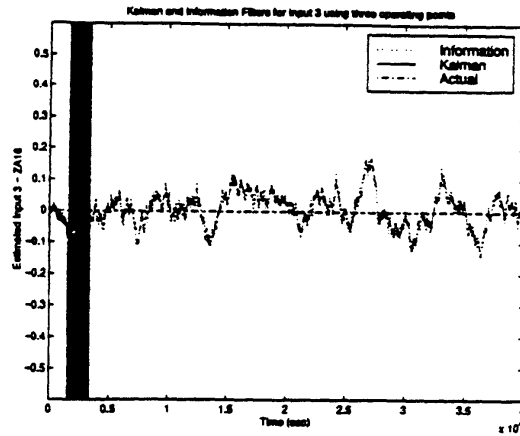


**Figure 38:** Measurement Estimation - Sensed Input 3, ZA16 (Case 8)

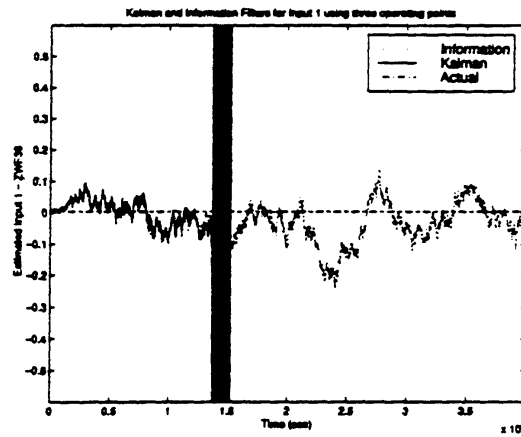


**Figure 39:** Measurement Estimation - Sensed Input 1, ZWF36 (Case 9)

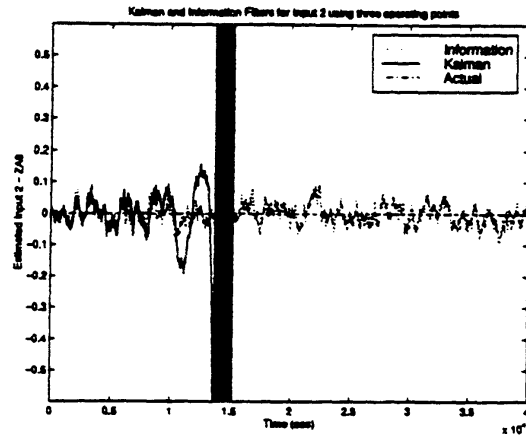


Figure 40: Measurement Estimation - Sensed Input 2, ZA8 (Case 9)

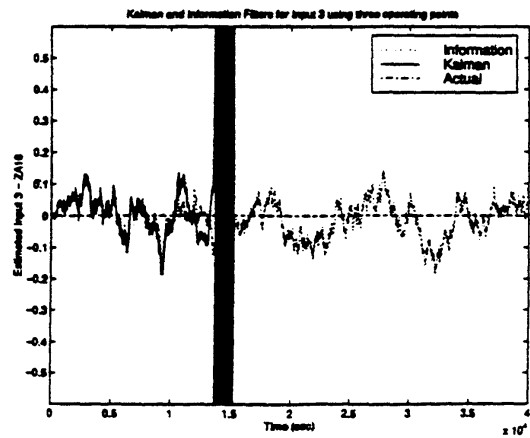


Figure 41: Measurement Estimation - Sensed Input 3, ZA16 (Case 9)

## 6. Conclusions

This report has studied the limitations of estimating the state *and* parameter and input biases at one operating point in the flight envelope. It was seen that if the number of sensors is less than the number of biases to be estimated, then it is essential to use data from more than one operating point to perform the estimation. A procedure for calculating the minimum number of operating points and for determining an appropriate combination of operating points was given in terms of a rank test of a matrix  $\mathcal{A}$  that is a function of the system matrices of each of the operating points. In addition, a “stacked” model structure was proposed as the basis of the estimation. Practical implementation of the estimation would then require storing data from several operating points and some preliminary results of that implementation have been given. The results in this report validate the use of the matrix  $\mathcal{A}$  in predicting estimation performance.

Given a realistic set of 59 operating points from the flight envelope, all combinations of three and two were computed as well as the condition numbers of  $\mathcal{A}$  for each case, which determines essentially how well  $\mathcal{A}$  meets the rank condition. It was shown that this number has a strong bearing on how well the parameter set is estimated. The data from three appropriately chosen operating points was shown both theoretically and via simulation to be adequate for estimating the parameter set.

The results reported here clearly indicate that with the “stacked” configuration the use of Information filter will be more numerically robust than Kalman filter. While the Kalman filter sometimes diverged in our simulation, the Information filter always converged.

Finally, it should be noted that although the results developed here assume that exclusively steady-state data is available for estimation. In practice, a combination of transient and steady-state data will be available. When transient data is used, the analysis involving  $\mathcal{A}$  is not strictly valid as presented here. This is because the problem becomes significantly more



complex. In particular, the plant matrices,  $A$ ,  $B$ ,  $C$ , etc..., vary with time and the steady-state assumptions do not hold. In this case, standard Kalman and Information filtering are also not adequate. Instead, it is necessary to use *Extended* Kalman and Information filtering. However, the “stacked” configuration should still be a useful paradigm for obtaining better estimates. Each level of the stack will now correspond to a particular set of transient and steady-state data where each of these data sets is of the same length. Unlike the assumptions in this report, the data sets will in general *not* represent data about one operating point. Extended Kalman or Information filtering must then be used to perform the estimation.

The question remains as to which data sets will be adequate? Although the analysis with  $\mathcal{A}$  is not strictly valid since it assumes steady-state data, it may still be useful. Using engineering judgment, it is possible to associate with each set of (transient and steady-state) data a finite number of plant matrix sets, representing the system at various points in the flight regimes represented by the data set. Hence, we can associate with each combination of data sets, finite sets of  $\mathcal{A}$  matrices. It is conjectured that evaluation of these sets of  $\mathcal{A}$  matrices, will provide valuable insight into which combinations of data sets will yield the most accurate estimates. However, the details of the exact procedures to use involving transient data must be developed and could be the subject of further research.

## References

1. S. Adibhatla, H. Brown, and Z. Gastineau. Intelligent engine control (iec). *28th Joint Propulsion Conference and Exhibit*, July 1992. AIAA 92-3484.
2. Y. Bar-Shalom and T.E. Fortman. *Tracking and Association*. Academic Press, 1988.
3. Y. Bar-Shalom and X. li. *Estimation and Tracking*. Artec House, 1993.
4. S. Grime, H.F. Durrant-Whyte, and P. Ho. Communication in decentralized sensing. *Proc. American Control Conference*, 1992.
5. K.L. Johnson. A constant gain extended kalman filter for turbofan performance tracking. Master's thesis, U. Cincinnati, 1992.
6. P. S. Maybeck. *Stochastic Models, Estimation and Control*, Vol. I. Academic Press, 1979.
7. A.G.O. Mutambara. *Decentralized Estimation and Control for Multisensor Systems*. CRC Press, 1998.
8. A.G.O. Mutambara and H.F. Durrant-Whyte. A formally verified modular decentralized robot control system. In *IEEE/RSJ Int. Conf. on Intelligent Robot and Systems (IROS)*, pp. 2023-2030, 1993.
9. F.J. Pineo. Adaptive update method for embedded real-time jet engine model. Master's thesis. M.I.T., February 1985.
10. J.A. Polley, S. Adibhatla, and P.J. Hoffman. Multivariable turbofan engine control for full flight envelope operation. *Trans. of the ASME*, 111:130-137, January 1989.
11. O.F. Qi and N.R.L. Maccullum. A model based approach to the control of an aircraft turbine engine. *Intl. Gas Turbine Aeroengine Congress and Expo.*, May 1993. ASME 93-GT-420.

12. M.S. Grewal and A.P. Andrews. *Kalman Filtering: Theory and Practice*. Prentice-Hall. 1993.



## Appendix 1: Tables of Operating Points and Combination Rankings

The first table lists each of the 59 operating points along with the corresponding altitude, mach number, ambient temperature and power code. The second table lists the top 100 combinations of two operating points, ranked according to  $cond(\mathcal{A})^{-1}$ . The third table lists the top 100 combinations of three operating points, ranked according to  $cond(\mathcal{A})^{-1}$ .

Operating Point	Altitude	Mach No	Amb. Temperature	Power Code
1	0	0	0	50
2	0	0	0	47.5
3	0	0	0	45
4	0	0	0	42.5
5	0	0	0	40
6	0	0	0	35
7	0	0	0	27.5
8	0	0	0	25
9	0	0	0	22.5
10	0	0	0	20
11	40000	0.4	0	50
12	40000	0.4	0	47.5
13	40000	0.4	0	45
14	40000	0.4	0	42.5
15	40000	0.4	0	40
16	40000	0.4	0	37.5
17	40000	0.4	0	32.5
18	40000	0.4	0	30
19	40000	0.4	0	27.5
20	40000	0.4	0	22.5
21	40000	0.4	0	21
22	0	0	-100	50
23	0	0	-50	50
24	45000	1.725	0	50
25	50000	1.725	0	50



Operating Point	Altitude	Mach No	Amb. Temperature	Power Code
26	55000	1.725	0	50
27	60000	1.725	0	50
28	70000	1.725	0	50
29	10000	0	0	50
30	10000	0	0	40
31	10000	0	0	20
32	20000	0.2	0	50
33	20000	0.2	0	40
34	20000	0.2	0	21
35	50000	0.6	0	50
36	50000	0.6	0	40
37	50000	0.6	0	35
38	50000	0.6	0	30
39	60000	0.8	0	40
40	60000	0.8	0	30
41	20000	1.7	0	50
42	36809	0.8	0	50
43	36809	0.8	0	40
44	36809	0.8	0	21
45	20000	0.5	0	50
46	20000	0.5	0	40
47	20000	0.5	0	21
48	40000	1.5	0	50
49	40000	1.5	0	45
50	0	0	-100	40
51	0	0	-100	20
52	0	0	-150	50
53	0	0	-150	40
54	0	0.7	130	50
55	0	0.7	130	40
56	0	0.7	130	30
57	0	0.7	130	25
58	30000	0.9	0	50
59	30000	0.9	0	40

Table 9: Operating Points Used From The Flight Envelope

Combination	Operating Points	$Cond(\mathcal{A})^{-1}$
1	39 44	6.6800E-07
2	18 47	3.0446E-07
3	39 51	2.8830E-07
4	39 47	2.7890E-07
5	7 39	2.5803E-07
6	13 50	2.5368E-07
7	39 57	2.3908E-07
8	34 40	2.2053E-07
9	33 39	2.2027E-07
10	37 49	2.1896E-07
11	4 39	2.1397E-07
12	24 37	2.1244E-07
13	33 37	2.1188E-07
14	21 39	2.0969E-07
15	13 44	2.0730E-07
16	30 39	2.0536E-07
17	40 47	2.0015E-07
18	13 18	1.9843E-07
19	21 40	1.9829E-07
20	31 39	1.9634E-07
21	13 41	1.8841E-07
22	39 46	1.8527E-07
23	19 47	1.8162E-07
24	18 34	1.7726E-07
25	3 39	1.7034E-07
26	38 47	1.6883E-07
27	37 43	1.6695E-07
28	27 39	1.6140E-07
29	28 55	1.5912E-07
30	6 51	1.5757E-07
31	48 57	1.5683E-07
32	21 56	1.5595E-07
33	13 21	1.5420E-07
34	13 59	1.5152E-07
35	25 37	1.5131E-07

Combination	Operating Points	$Cond(\mathcal{A})^{-1}$
36	26 39	1.5072E-07
37	21 27	1.4873E-07
38	37 46	1.4829E-07
39	39 43	1.4638E-07
40	8 39	1.4081E-07
41	32 39	1.4035E-07
42	39 54	1.3693E-07
43	25 39	1.3606E-07
44	12 39	1.3408E-07
45	24 39	1.3362E-07
46	2 39	1.3310E-07
47	11 39	1.3291E-07
48	39 59	1.3207E-07
49	1 39	1.3111E-07
50	29 39	1.2847E-07
51	39 48	1.2755E-07
52	13 39	1.2709E-07
53	35 44	1.2691E-07
54	39 49	1.2670E-07
55	15 55	1.2604E-07
56	18 53	1.2324E-07
57	7 55	1.2080E-07
58	30 37	1.1927E-07
59	13 25	1.1831E-07
60	20 47	1.1783E-07
61	14 39	1.1715E-07
62	13 24	1.1662E-07
63	35 39	1.1626E-07
64	7 19	1.1539E-07
65	18 58	1.1420E-07
66	36 55	1.1346E-07
67	34 38	1.1330E-07
68	32 37	1.1296E-07
69	16 55	1.1130E-07
70	39 42	1.1129E-07

Combination	Operating Points	$Cond(\mathcal{A})^{-1}$
71	39 50	1.1015E-07
72	5 37	1.0948E-07
73	7 57	1.0921E-07
74	13 52	1.0831E-07
75	6 28	1.0799E-07
76	8 18	1.0748E-07
77	4 37	1.0625E-07
78	27 50	1.0623E-07
79	10 40	1.0537E-07
80	27 35	1.0491E-07
81	20 39	1.0396E-07
82	17 40	1.0307E-07
83	36 49	1.0280E-07
84	9 18	1.0228E-07
85	27 44	9.9899E-08
86	17 57	9.9673E-08
87	37 59	9.9529E-08
88	13 45	9.9176E-08
89	31 40	9.9159E-08
90	13 48	9.8708E-08
91	30 38	9.8444E-08
92	19 33	9.7973E-08
93	13 53	9.7601E-08
94	19 30	9.7383E-08
95	6 10	9.7203E-08
96	38 51	9.6950E-08
97	18 42	9.6464E-08
98	39 58	9.4706E-08
99	12 37	9.4689E-08
100	17 51	9.4608E-08

Table 10: Largest 100 Singular Values and Corresponding Combinations of Two Operating Points

Combination	Operating Points	$Cond(\mathcal{A})^{-1}$
1	7 51 58	2.7247E-06
2	18 44 47	2.5709E-06
3	8 42 56	2.4606E-06
4	28 31 42	2.4603E-06
5	18 31 44	2.3981E-06
6	18 44 51	2.3901E-06
7	9 13 18	2.3594E-06
8	8 18 47	2.3505E-06
9	13 47 51	2.3488E-06
10	19 44 47	2.3435E-06
11	28 34 42	2.3365E-06
12	12 47 51	2.3321E-06
13	18 34 38	2.3309E-06
14	8 18 31	2.3271E-06
15	18 38 47	2.3223E-06
16	27 31 48	2.3223E-06
17	17 34 44	2.3213E-06
18	27 47 51	2.3137E-06
19	17 44 47	2.2952E-06
20	24 51 55	2.2924E-06
21	18 27 51	2.2833E-06
22	8 18 34	2.2825E-06
23	8 48 56	2.2803E-06
24	10 18 19	2.2799E-06
25	9 12 18	2.2755E-06
26	27 48 51	2.2672E-06
27	17 31 44	2.2557E-06
28	9 18 43	2.2544E-06
29	42 47 51	2.2536E-06
30	37 44 51	2.2509E-06
31	37 44 47	2.2498E-06
32	9 14 18	2.2447E-06
33	18 21 47	2.2338E-06
34	11 47 51	2.2319E-06
35	9 18 27	2.2230E-06



Combination	Operating Points	$Cond(\mathcal{A})^{-1}$
36	13 18 57	2.2194E-06
37	27 31 58	2.2168E-06
38	9 16 18	2.2041E-06
39	18 20 51	2.1990E-06
40	18 21 34	2.1975E-06
41	28 31 58	2.1954E-06
42	18 38 51	2.1945E-06
43	7 47 59	2.1933E-06
44	26 47 51	2.1873E-06
45	10 18 44	2.1829E-06
46	17 20 47	2.1824E-06
47	19 44 51	2.1822E-06
48	7 47 49	2.1821E-06
49	24 28 31	2.1793E-06
50	17 20 34	2.1779E-06
51	25 28 31	2.1746E-06
52	13 32 51	2.1728E-06
53	27 47 59	2.1701E-06
54	8 56 58	2.1681E-06
55	9 15 18	2.1668E-06
56	34 37 44	2.1643E-06
57	27 51 53	2.1629E-06
58	10 19 20	2.1628E-06
59	8 10 18	2.1624E-06
60	47 56 59	2.1619E-06
61	11 14 30	2.1612E-06
62	9 44 47	2.1562E-06
63	28 31 48	2.1559E-06
64	35 38 44	2.1542E-06
65	11 15 30	2.1522E-06
66	8 13 18	2.1515E-06
67	7 18 31	2.1502E-06
68	19 27 31	2.1456E-06
69	8 15 43	2.1454E-06
70	17 44 51	2.1448E-06

Combination	Operating Points	$Cond(\mathcal{A})^{-1}$
71	17 20 31	2.1422E-06
72	26 30 47	2.1338E-06
73	9 16 19	2.1335E-06
74	18 27 31	2.1321E-06
75	18 34 44	2.1317E-06
76	10 16 19	2.1284E-06
77	16 19 38	2.1259E-06
78	12 19 38	2.1254E-06
79	28 31 49	2.1236E-06
80	18 28 31	2.1225E-06
81	12 32 51	2.1212E-06
82	12 18 57	2.1173E-06
83	7 14 43	2.1167E-06
84	7 48 51	2.1150E-06
85	7 15 43	2.1126E-06
86	8 18 51	2.1120E-06
87	8 47 49	2.1113E-06
88	8 47 59	2.1111E-06
89	18 28 51	2.1050E-06
90	18 27 57	2.1020E-06
91	8 14 18	2.0995E-06
92	9 18 26	2.0993E-06
93	5 42 47	2.0989E-06
94	13 17 44	2.0949E-06
95	11 15 33	2.0947E-06
96	8 12 18	2.0929E-06
97	18 43 57	2.0919E-06
98	7 42 51	2.0900E-06
99	8 16 18	2.0896E-06
100	8 15 18	2.0881E-06

Table 11: Largest 100 Singular Values and Corresponding Combinations of Three Operating Points

## Appendix 2: Complete Data for Estimation Using the Best Combination of Three - Parameters Initialized to Zero (Case 1)

Below presents 1) a complete set of figures illustrating the estimation process, 2) a table describing the mean and variances of the parameter estimates of both the Kalman and Information filters, and 3) a complete list of the singular values of  $\mathcal{A}$ .

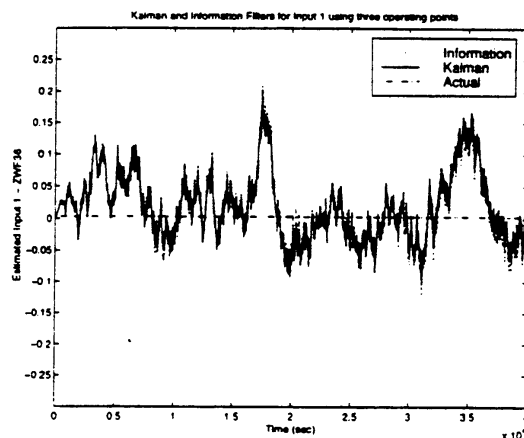


Figure 42: Measurement Estimation - Sensed Input 1, ZWF36 (Case 1)

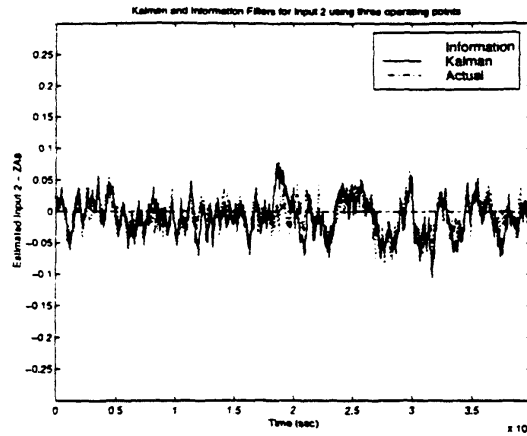


Figure 43: Measurement Estimation - Sensed Input 2, ZA8 (Case 1)

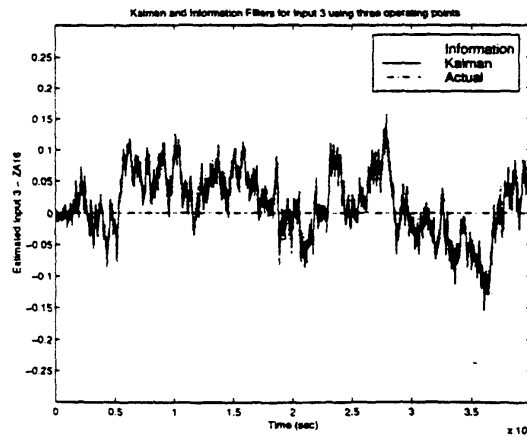


Figure 44: Measurement Estimation - Sensed Input 3, ZA16 (Case 1)

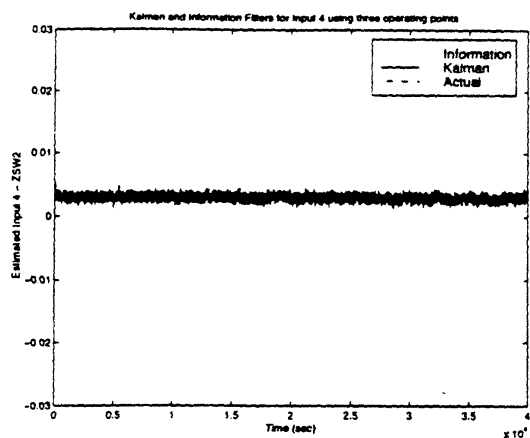


Figure 45: Measurement Estimation - Efficiency and Flow Scalar 1, ZSW2 (Case 1)

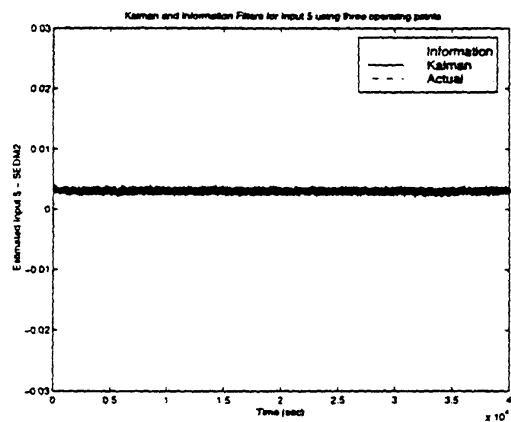
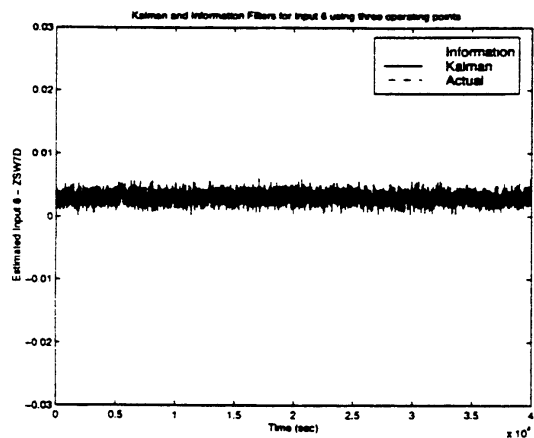
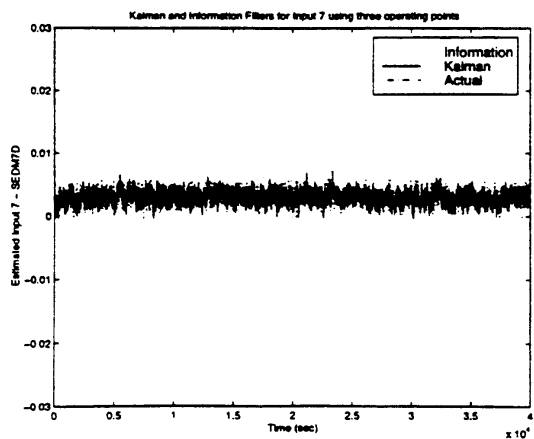


Figure 46: Measurement Estimation - Efficiency and Flow Scalar 2, SEDM2 (Case 1)



**Figure 47:** Measurement Estimation- Efficiency and Flow Scalar 3, ZSW7D (Case 1)



**Figure 48:** Measurement Estimation - Efficiency and Flow Scalar 4, SEDM7D (Case 1)



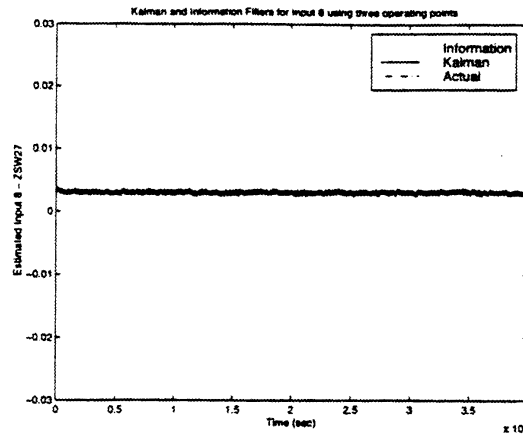


Figure 49: Measurement Estimation- Efficiency and Flow Scalar 5, ZSW27 (Case 1)

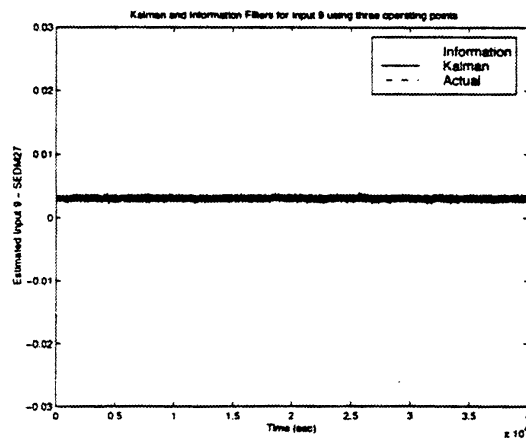
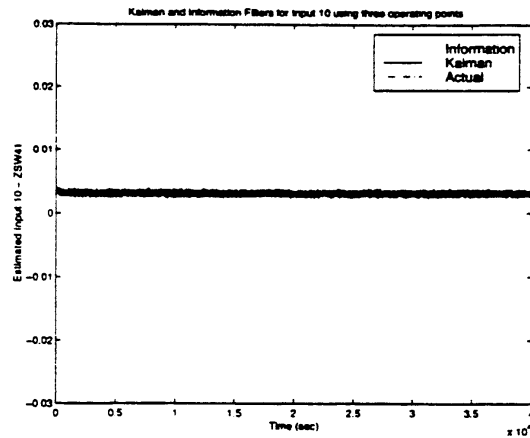
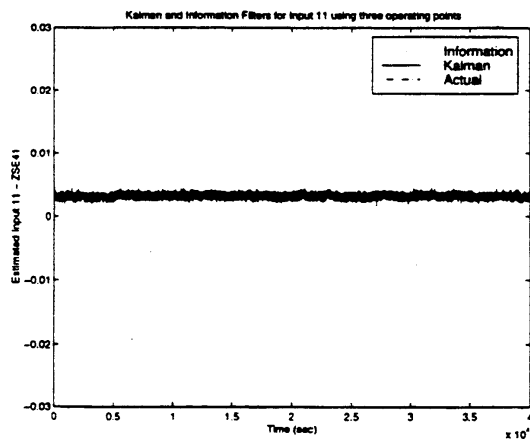


Figure 50: Measurement Estimation - Efficiency and Flow Scalar 6, SEDM27 (Case 1)



**Figure 51:** Measurement Estimation - Efficiency and Flow Scalar 7, ZSW41 (Case 1)



**Figure 52:** Measurement Estimation - Efficiency and Flow Scalar 8, ZSE41 (Case 1)

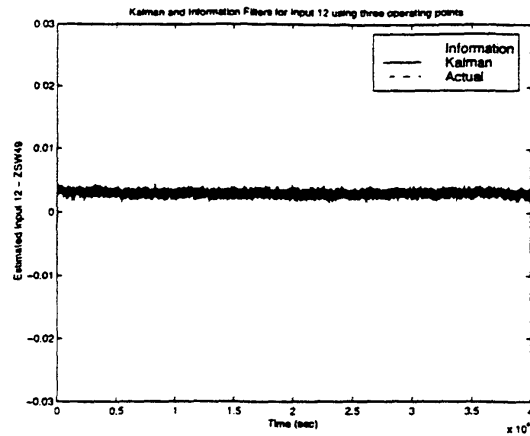


Figure 53: Measurement Estimation - Efficiency and Flow Scalar 9, ZSW49 (Case 1)

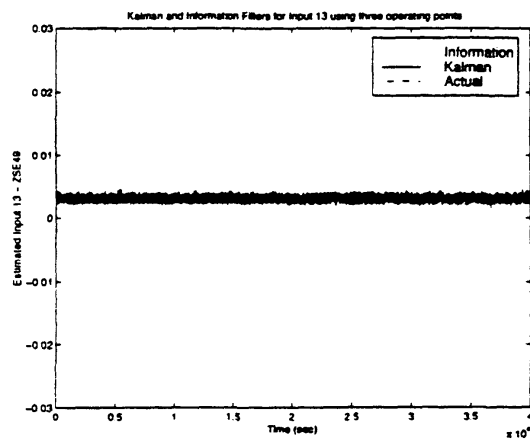


Figure 54: Measurement Estimation - Efficiency and Flow Scalar 10, ZSE49 (Case 1)

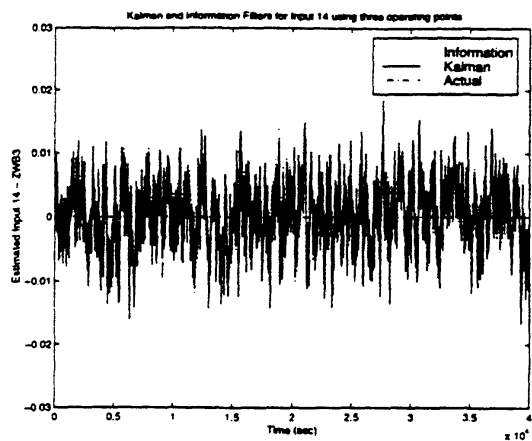


Figure 55: Measurement Estimation - Bleed 1, ZWB3 (Case 1)

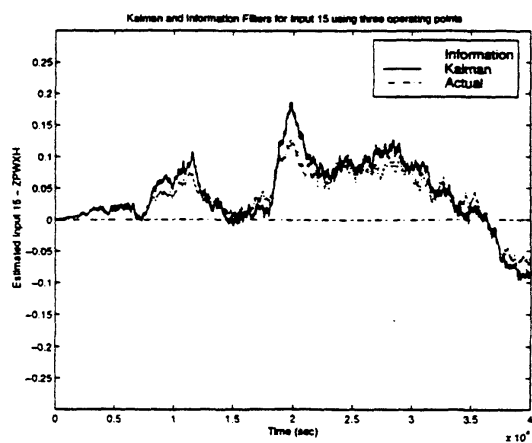


Figure 56: Measurement Estimation - Power Extraction 1, ZPWXH (Case 1)

Parameter	Actual Value	Mean:KF	Mean:IF	Variance:KF	Variance:IF
ZA8	0.00E+00	-1.74E-03	-4.75E-04	9.56E-04	6.20E-04
ZA16	0.00E+00	2.41E-02	2.48E-02	3.17E-03	2.97E-03
ZSW2	3.00E-03	2.99E-03	2.99E-03	2.34E-07	2.06E-07
SEDM2	3.00E-03	3.00E-03	2.99E-03	1.13E-07	1.06E-07
ZSW7D	3.00E-03	2.97E-03	2.97E-03	7.38E-07	6.46E-07
SEDM7D	3.00E-03	2.95E-03	2.95E-03	9.48E-07	1.29E-06
ZSW27	3.00E-03	3.02E-03	3.02E-03	4.64E-08	3.89E-08
SEDM27	3.00E-03	3.00E-03	3.01E-03	7.64E-08	7.10E-08
ZSW41	3.00E-03	3.01E-03	3.01E-03	8.32E-08	5.05E-08
ZSE41	3.00E-03	3.00E-03	2.99E-03	1.45E-07	1.62E-07
ZSW49	3.00E-03	3.01E-03	3.02E-03	1.80E-07	2.12E-07
ZSE49	3.00E-03	3.02E-03	3.02E-03	1.73E-07	2.00E-07
ZWB3	0.00E+00	2.04E-04	1.56E-04	2.11E-05	2.11E-05
ZPWXH	0.00E+00	-1.97E-02	-2.21E-02	1.21E-03	6.81E-04

Table 12: Mean and Variance of Parameter Estimates of Kalman and Information Filters (Case 1)

Here is the list of singular values:

$$\begin{bmatrix} 3.9709588e+03 \\ 2.8197357e+03 \\ 1.0810832e+03 \\ 7.1665676e+02 \\ 3.9900754e+02 \\ 3.1146032e+02 \\ 2.1304143e+02 \\ 1.6403454e+02 \\ 1.1763709e+02 \\ 2.8748288e+01 \\ 2.3572168e+00 \\ 1.0517054e+00 \\ 1.0381604e+00 \\ 1.0117562e+00 \\ 9.9682120e-01 \\ 9.5306144e-01 \\ 9.4553955e-01 \\ 3.1604635e-01 \\ 7.0784597e-02 \\ 3.2675650e-02 \\ 2.9271329e-02 \\ 1.9956495e-02 \\ 1.4331101e-02 \\ 1.0819510e-02 \end{bmatrix} \quad (6.1)$$



### Appendix 3: Complete Data for Estimation Using an Arbitrary Combination of Three - Parameters Initialized to Zero (Case 2)

Below presents 1) a complete set of figures illustrating the estimation process, 2) a table describing the mean and variances of the parameter estimates of both the Kalman and Information filters, and 3) a complete list of the singular values of  $\mathcal{A}$ .

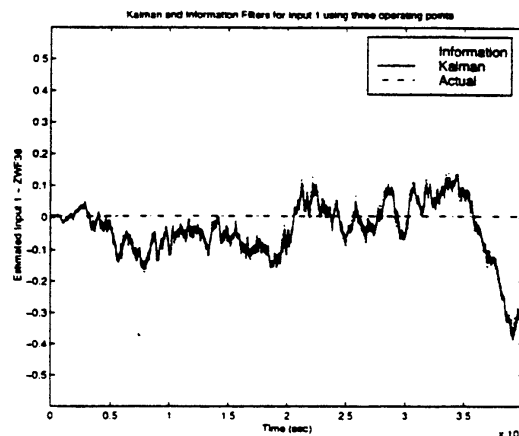


Figure 57: Measurement Estimation - Sensed Input 1, ZWF36 (Case 2)

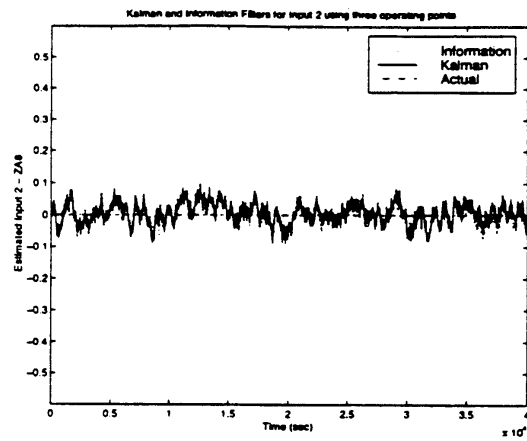


Figure 58: Measurement Estimation - Sensed Input 2, ZA8 (Case 2)

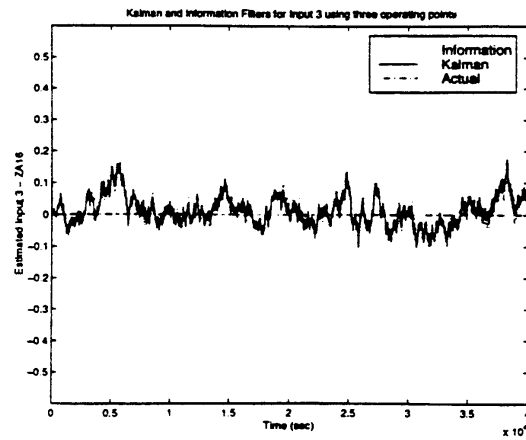


Figure 59: Measurement Estimation - Sensed Input 3, ZA16 (Case 2)

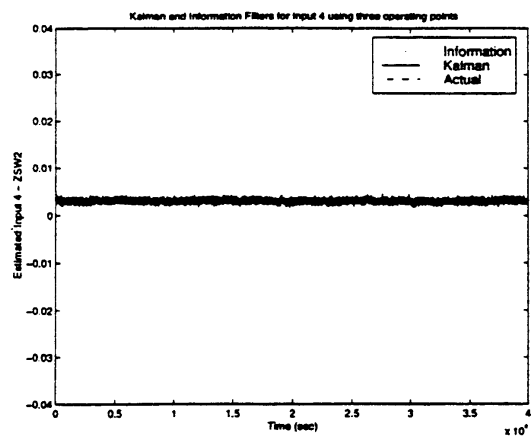


Figure 60: Measurement Estimation - Efficiency and Flow Scalar 1, ZSW2 (Case 2)

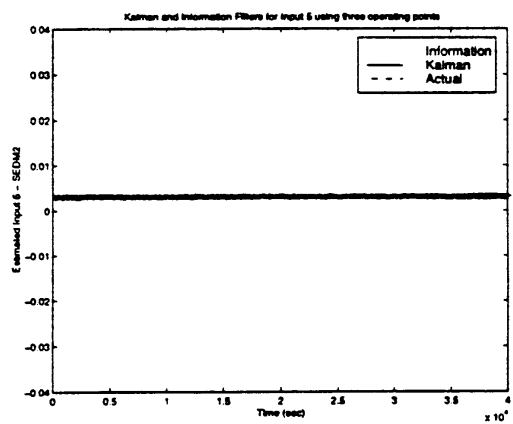
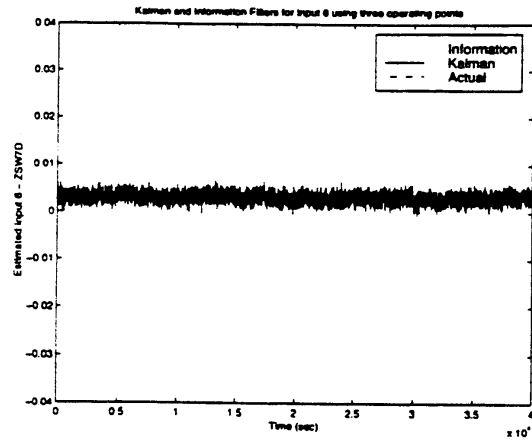
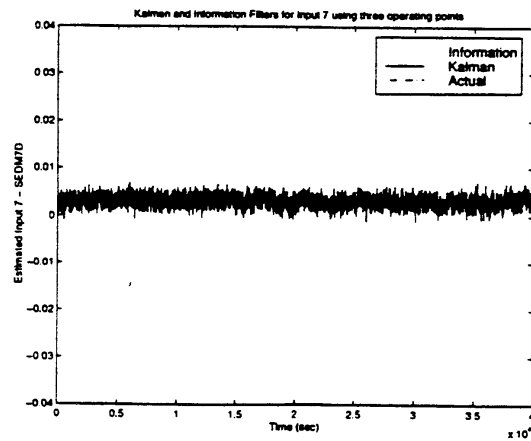


Figure 61: Measurement Estimation - Efficiency and Flow Scalar 2, SEDM2 (Case 2)



**Figure 62:** Measurement Estimation- Efficiency and Flow Scalar 3, ZSW7D (Case 2)



**Figure 63:** Measurement Estimation - Efficiency and Flow Scalar 4, SEDM7D (Case 2)

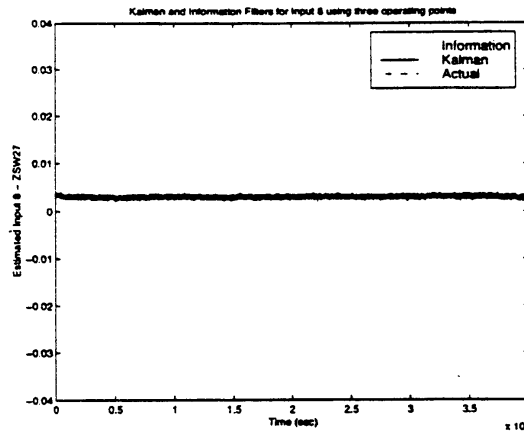


**Figure 64:** Measurement Estimation- Efficiency and Flow Scalar 5, ZSW27 (Case 2)

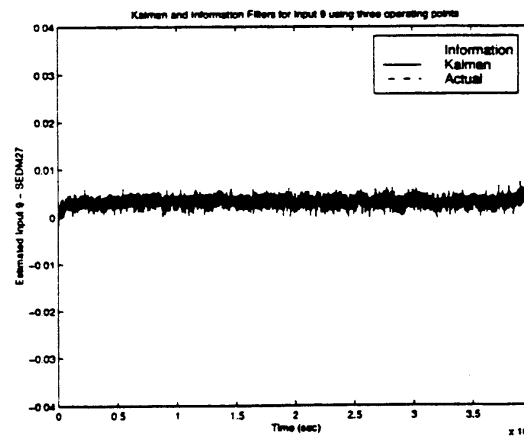


**Figure 65:** Measurement Estimation - Efficiency and Flow Scalar 6, SEDM27 (Case 2)

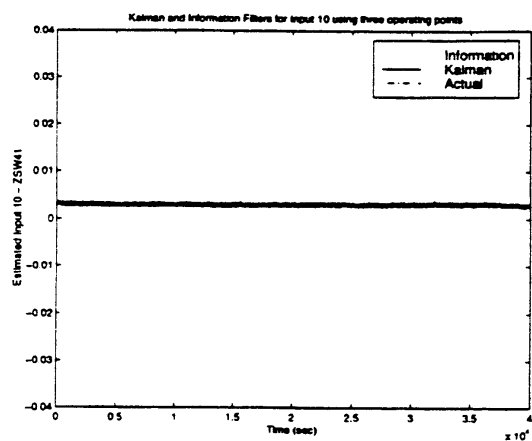


**Figure 66:** Measurement Estimation - Efficiency and Flow Scalar 7, ZSW41 (Case 2)

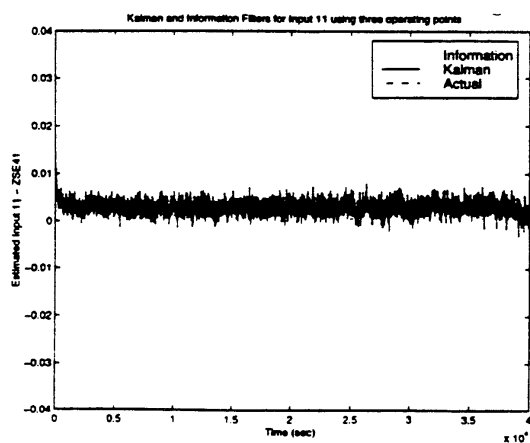


**Figure 67:** Measurement Estimation - Efficiency and Flow Scalar 8, ZSE41 (Case 2)



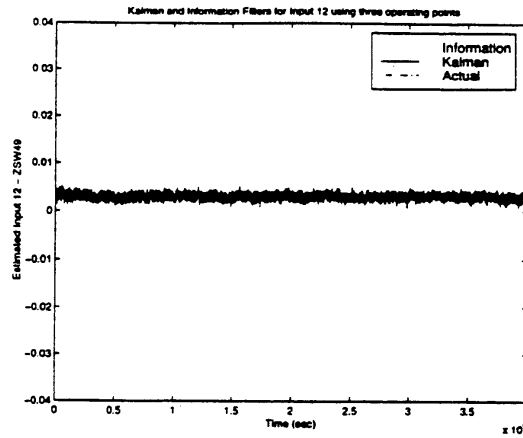


**Figure 68:** Measurement Estimation - Efficiency and Flow Scalar 9, ZSW49 (Case 2)

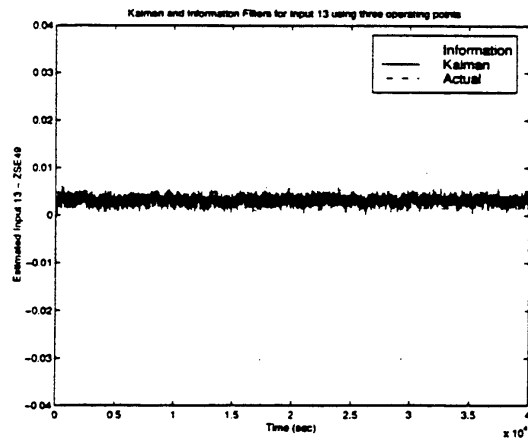


**Figure 69:** Measurement Estimation - Efficiency and Flow Scalar 10, ZSE49 (Case 2)

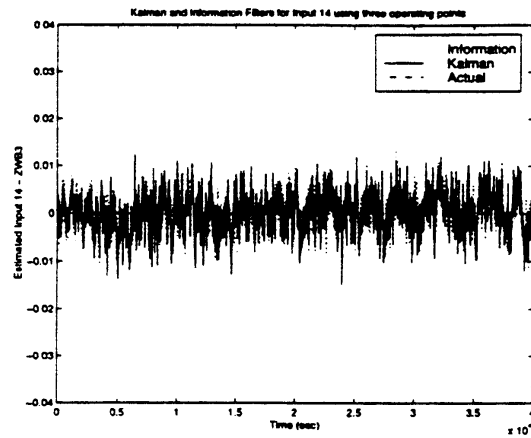


**Figure 70:** Measurement Estimation - Bleed 1, ZWB3 (Case 2)

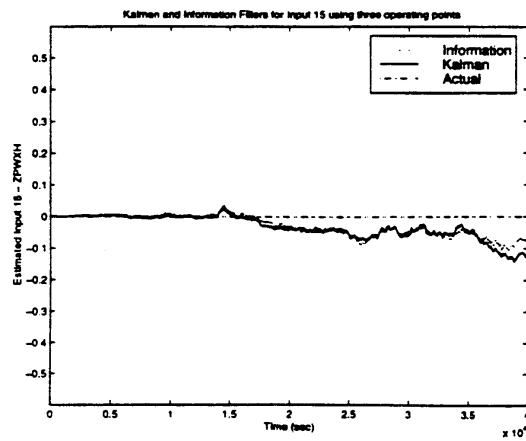


**Figure 71:** Measurement Estimation - Power Extraction 1, ZPWXH (Case 2)

Parameter	Actual Value	Mean:KF	Mean:IF	Variance:KF	Variance:IF
ZA8	0.00E+00	-1.74E-03	-4.75E-04	9.56E-04	6.20E-04
ZA16	0.00E+00	2.41E-02	2.48E-02	3.17E-03	2.97E-03
ZSW2	3.00E-03	2.99E-03	2.99E-03	2.34E-07	2.06E-07
SEDM2	3.00E-03	3.00E-03	2.99E-03	1.13E-07	1.06E-07
ZSW7D	3.00E-03	2.97E-03	2.97E-03	7.38E-07	6.46E-07
SEDM7D	3.00E-03	2.95E-03	2.95E-03	9.48E-07	1.29E-06
ZSW27	3.00E-03	3.02E-03	3.02E-03	4.64E-08	3.89E-08
SEDM27	3.00E-03	3.00E-03	3.01E-03	7.64E-08	7.10E-08
ZSW41	3.00E-03	3.01E-03	3.01E-03	8.32E-08	5.05E-08
ZSE41	3.00E-03	3.00E-03	2.99E-03	1.45E-07	1.62E-07
ZSW49	3.00E-03	3.01E-03	3.02E-03	1.80E-07	2.12E-07
ZSE49	3.00E-03	3.02E-03	3.02E-03	1.73E-07	2.00E-07
ZWB3	0.00E+00	2.04E-04	1.56E-04	2.11E-05	2.11E-05
ZPWXH	0.00E+00	-1.97E-02	-2.21E-02	1.21E-03	6.81E-04

Table 13: Mean and Variance of Parameter Estimates of Kalman and Information Filters (Case 2)

Here is the list of singular values:

$$\begin{bmatrix} 5.0854727e + 03 \\ 3.8351638e + 03 \\ 1.1897171e + 03 \\ 5.3147287e + 02 \\ 4.8395378e + 02 \\ 2.6610648e + 02 \\ 2.2399671e + 02 \\ 1.3298740e + 02 \\ 2.4897525e + 01 \\ 2.1671352e + 01 \\ 4.0442263e + 00 \\ 1.1685319e + 00 \\ 1.1162751e + 00 \\ 1.0360077e + 00 \\ 1.0219474e + 00 \\ 1.0204436e + 00 \\ 9.6435485e - 01 \\ 1.8047916e - 01 \\ 1.4189555e - 01 \\ 5.7273237e - 02 \\ 5.2015201e - 02 \\ 1.8247701e - 02 \\ 7.1876819e - 03 \\ 4.4370659e - 03 \end{bmatrix} \quad (6.2)$$

## Appendix 4: Complete Data for Estimation Using the Best Combination of Two - Parameters Initialized to Zero (Case 3)

Below presents 1) a complete set of figures illustrating the estimation process, 2) a table describing the mean and variances of the parameter estimates of both the Kalman and Information filters, and 3) a complete list of the singular values of  $\mathcal{A}$ .

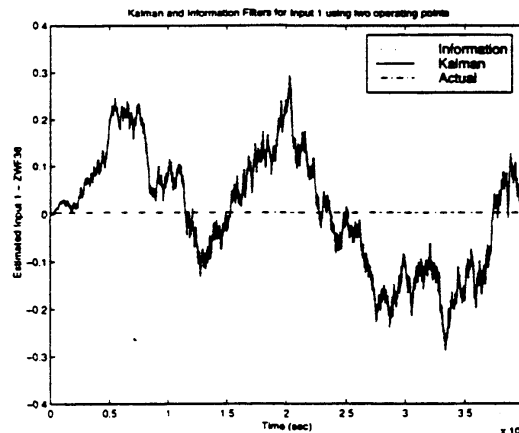


Figure 72: Measurement Estimation - Sensed Input 1, ZWF36 (Case 3)

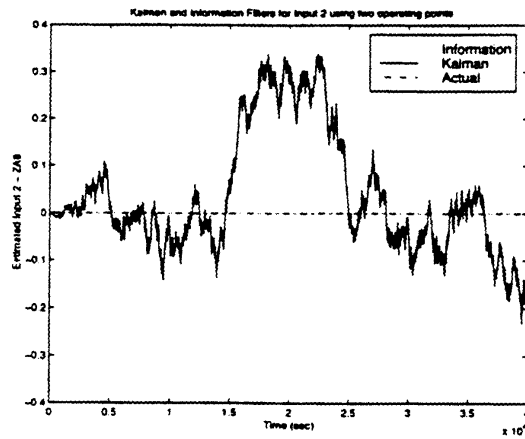


Figure 73: Measurement Estimation - Sensed Input 2, ZA8 (Case 3)

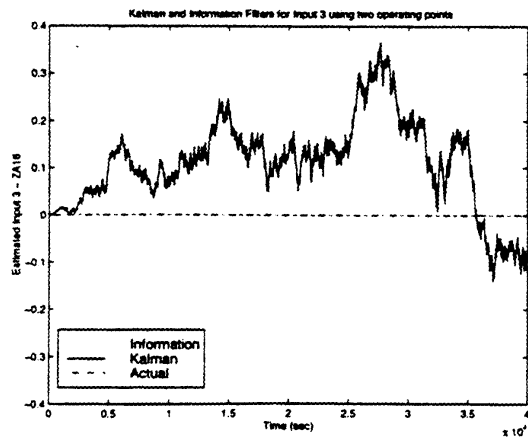
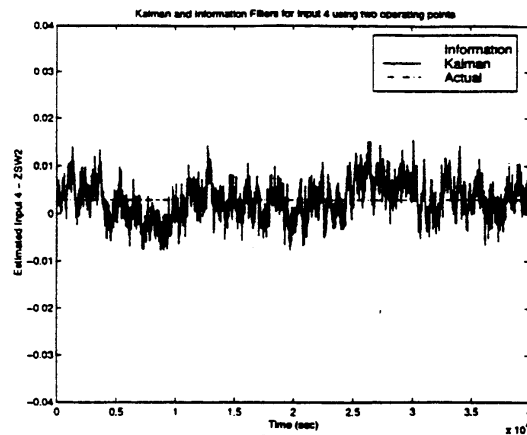
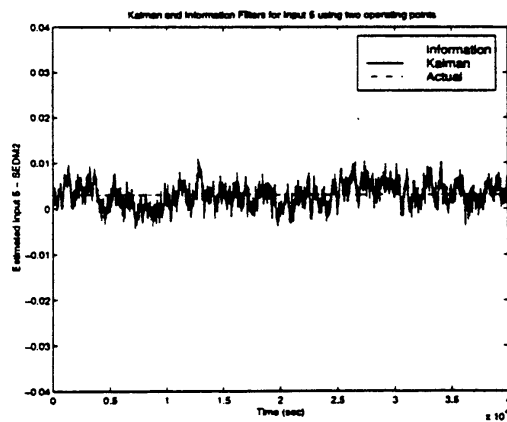


Figure 74: Measurement Estimation - Sensed Input 3, ZA16 (Case 3)





**Figure 75:** Measurement Estimation - Efficiency and Flow Scalar 1, ZSW2 (Case 3)



**Figure 76:** Measurement Estimation - Efficiency and Flow Scalar 2, SEDM2 (Case 3)

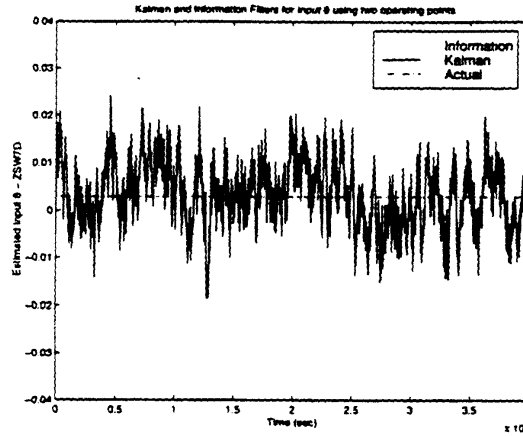


Figure 77: Measurement Estimation- Efficiency and Flow Scalar 3, ZSW7D (Case 3)

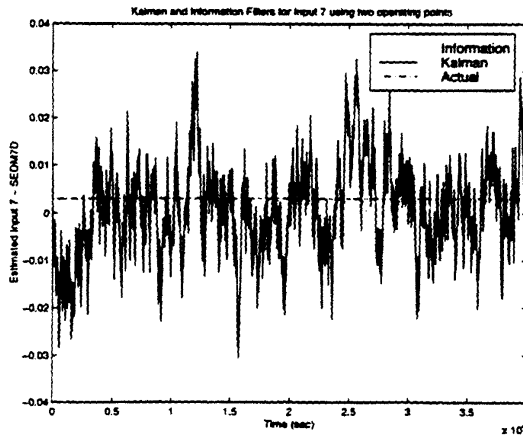


Figure 78: Measurement Estimation - Efficiency and Flow Scalar 4, SEDM7D (Case 3)

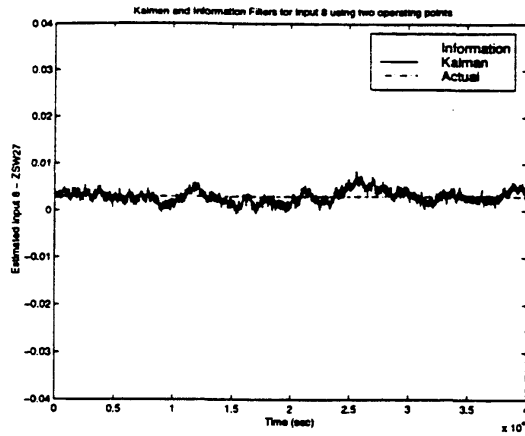


Figure 79: Measurement Estimation- Efficiency and Flow Scalar 5, ZSW27 (Case 3)

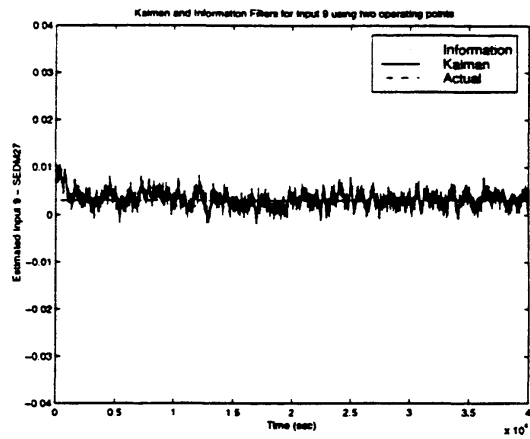


Figure 80: Measurement Estimation - Efficiency and Flow Scalar 6, SEDM27 (Case 3)

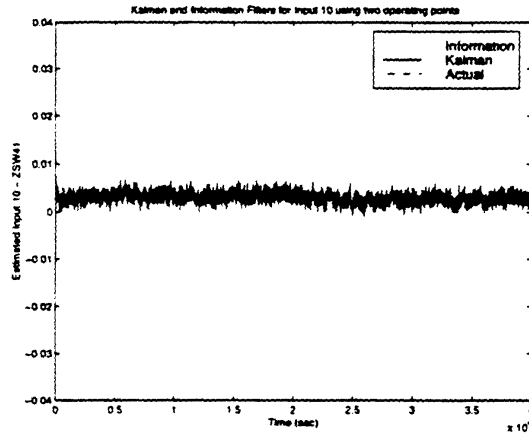


Figure 81: Measurement Estimation - Efficiency and Flow Scalar 7, ZSW41 (Case 3)

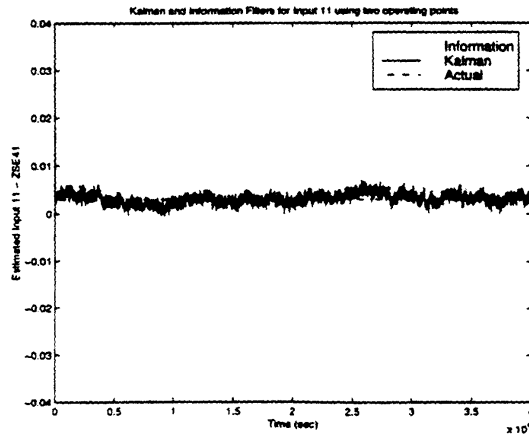


Figure 82: Measurement Estimation - Efficiency and Flow Scalar 7, ZSW41 (Case 3)

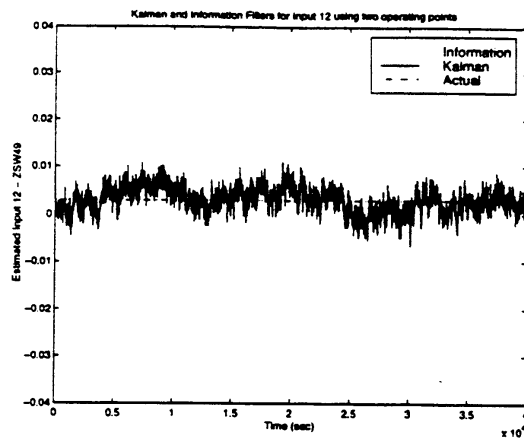


Figure 83: Measurement Estimation - Efficiency and Flow Scalar 9, ZSW49 (Case 3)

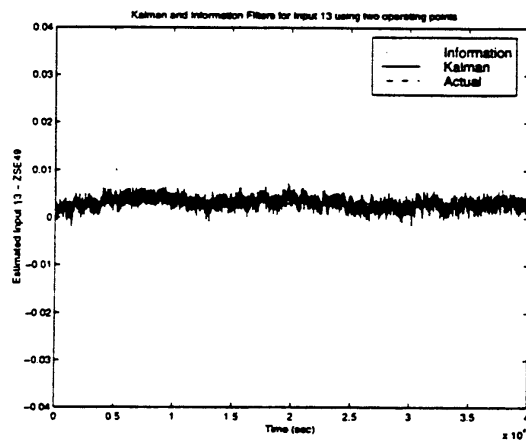
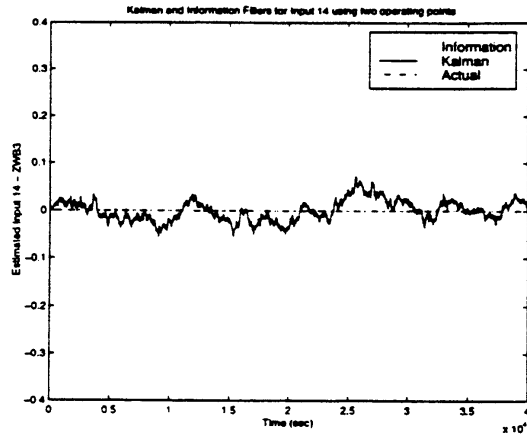
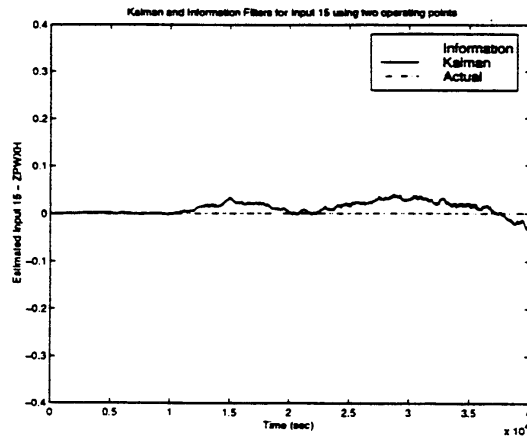


Figure 84: Measurement Estimation - Efficiency and Flow Scalar 10, ZSE49 (Case 3)



**Figure 85:** Measurement Estimation - Bleed 1, ZWB3 (Case 3)



**Figure 86:** Measurement Estimation - Power Extraction 1, ZPWXH (Case 3)



Parameter	Actual Value	Mean:KF	Mean:IF	Variance:KF	Variance:IF
ZWF36	3.00E-03	6.25E-03	6.57E-03	1.54E-02	1.52E-02
ZA8	0.00E+00	3.87E-02	3.90E-02	1.71E-02	1.70E-02
ZA16	0.00E+00	1.12E-01	1.12E-01	9.06E-03	9.10E-03
ZSW2	3.00E-03	2.94E-03	2.94E-03	1.56E-05	1.56E-05
SEDM2	3.00E-03	2.90E-03	2.90E-03	6.50E-06	6.52E-06
ZSW7D	3.00E-03	3.21E-03	3.21E-03	4.55E-05	4.56E-05
SEDM7D	3.00E-03	9.20E-04	9.21E-04	9.38E-05	9.42E-05
ZSW27	3.00E-03	2.92E-03	2.92E-03	1.94E-06	1.95E-06
SEDM27	3.00E-03	3.11E-03	3.11E-03	2.33E-06	2.38E-06
ZSW41	3.00E-03	2.98E-03	2.98E-03	1.30E-06	1.29E-06
ZSE41	3.00E-03	3.05E-03	3.05E-03	1.26E-06	1.29E-06
ZSW49	3.00E-03	3.01E-03	3.01E-03	6.80E-06	7.03E-06
ZSE49	3.00E-03	3.05E-03	3.05E-03	1.41E-06	1.48E-06
ZWB3	0.00E+00	-7.85E-04	-8.02E-04	5.15E-04	5.18E-04
ZPWXH	0.00E+00	1.08E-02	1.08E-02	1.75E-04	1.76E-04

Table 14: Mean and Variance of Parameter Estimates of Kalman and Information Filters (Case 3)

Singular values:

$$\begin{bmatrix} 1.8399722e + 03 \\ 1.0276994e + 03 \\ 5.6560175e + 02 \\ 3.3739302e + 02 \\ 1.3176407e + 02 \\ 1.0460710e + 02 \\ 6.1757593e + 01 \\ 6.5545381e + 00 \\ 1.4091978e + 00 \\ 9.3456088e - 01 \\ 9.2003604e - 01 \\ 9.0724849e - 01 \\ 9.0596324e - 01 \\ 6.0473198e - 01 \\ 2.1403897e - 01 \\ 1.4343693e - 02 \\ 7.0246684e - 03 \\ 3.9373848e - 03 \\ 3.0239887e - 03 \\ 2.6316146e - 03 \\ 1.2291035e - 03 \end{bmatrix} . \quad (6.3)$$

## Appendix 5: Complete Data for Estimation Using Single Operating Point - Parameters Initialized to Zero (Case 4)

Below presents 1) a complete set of figures illustrating the estimation process, 2) a table describing the mean and variances of the parameter estimates of both the Kalman and Information filters, and 3) a complete list of the singular values of  $A$ .

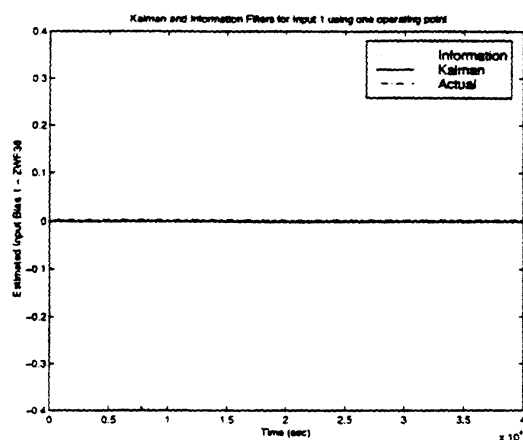


Figure 87: Measurement Estimation - Sensed Input 1, ZWF36 (Case 4)

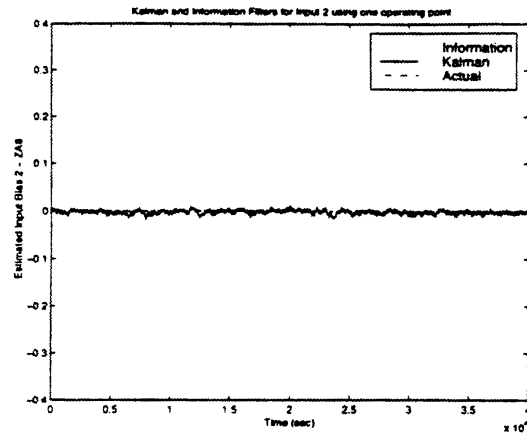


Figure 88: Measurement Estimation - Sensed Input 2, ZA8 (Case 4)

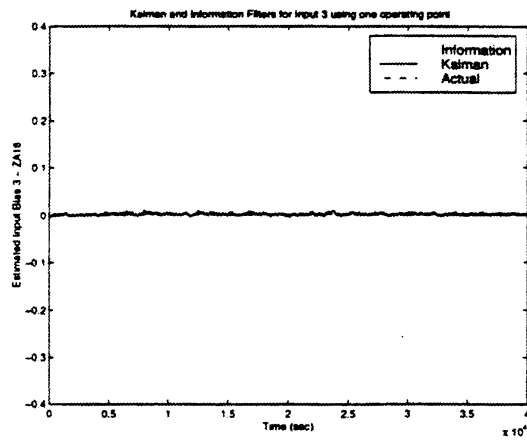


Figure 89: Measurement Estimation - Sensed Input 3, ZA16 (Case 4)

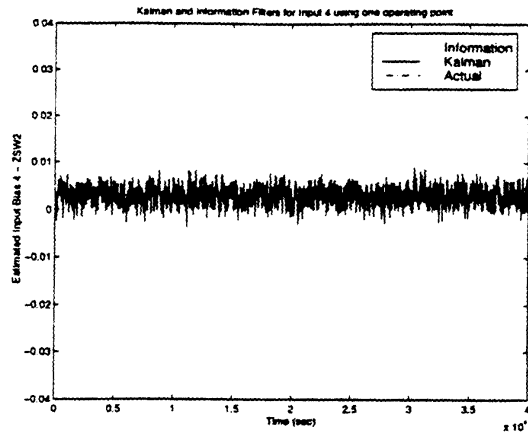


Figure 90: Measurement Estimation - Efficiency and Flow Scalar 1, ZSW2 (Case 4)

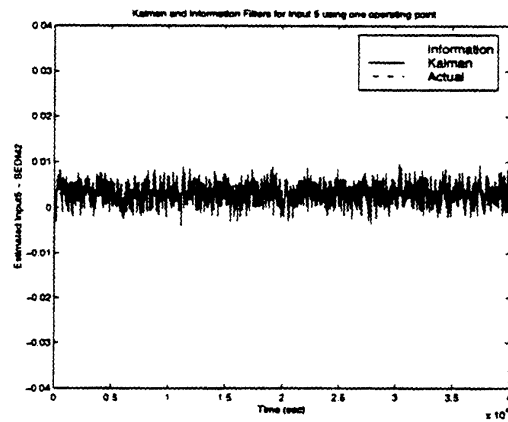


Figure 91: Measurement Estimation - Efficiency and Flow Scalar 2, SEDM2 (Case 4)

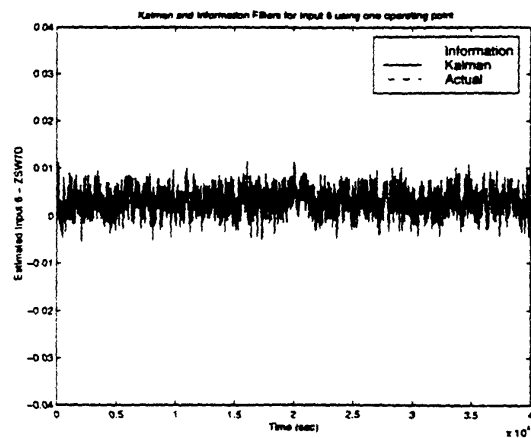


Figure 92: Measurement Estimation- Efficiency and Flow Scalar 3, ZSW7D (Case 4)

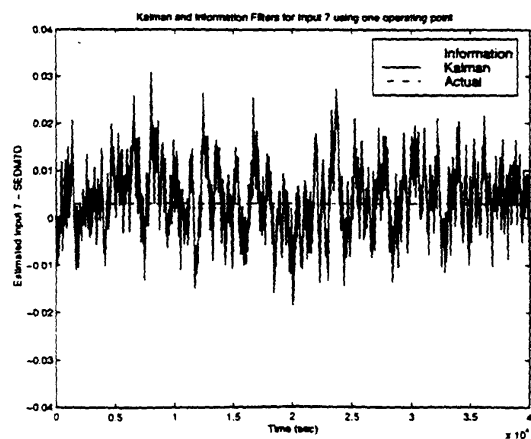


Figure 93: Measurement Estimation - Efficiency and Flow Scalar 4, SEDM7D (Case 4)



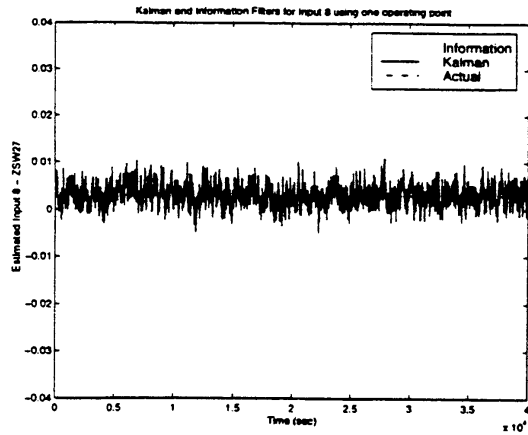


Figure 94: Measurement Estimation- Efficiency and Flow Scalar 5, ZSW27 (Case 4)

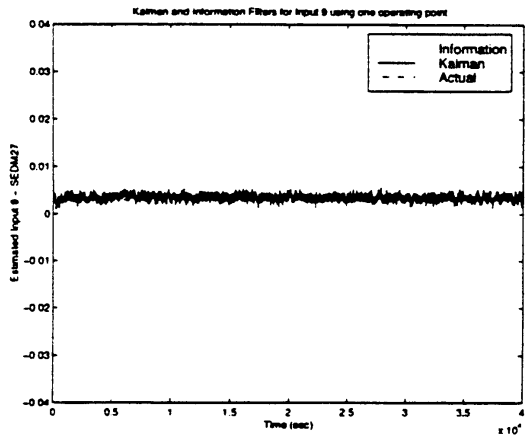
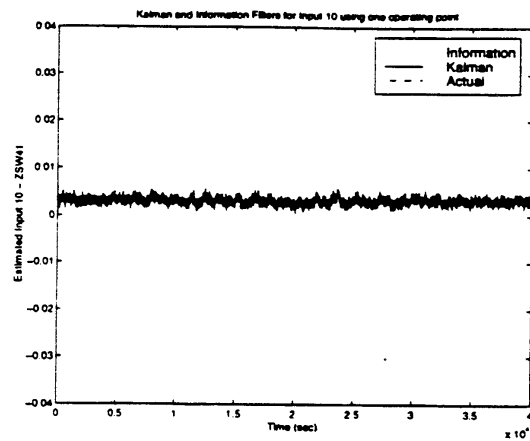
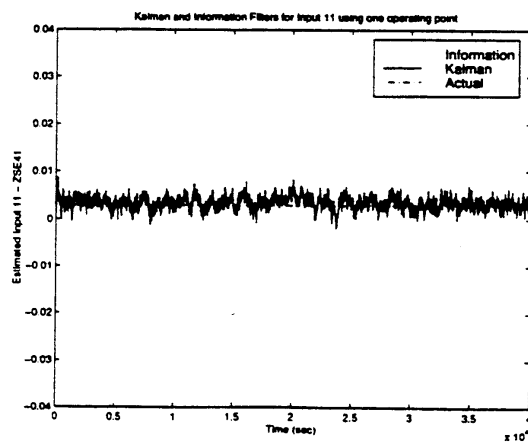


Figure 95: Measurement Estimation - Efficiency and Flow Scalar 6, SEDM27 (Case 4)



**Figure 96:** Measurement Estimation - Efficiency and Flow Scalar 7, ZSW41 (Case 4)



**Figure 97:** Measurement Estimation - Efficiency and Flow Scalar 7, ZSE41 (Case 4)

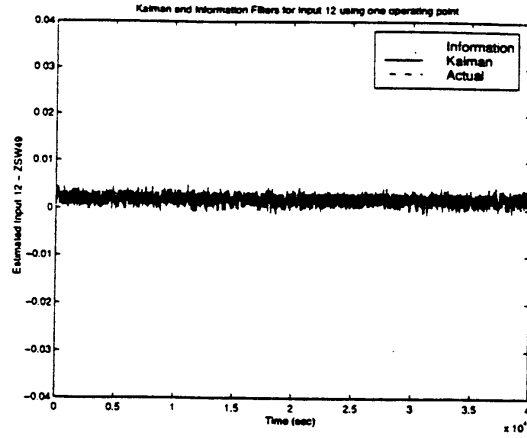


**Figure 98:** Measurement Estimation - Efficiency and Flow Scalar 9, ZSW49 (Case 4)

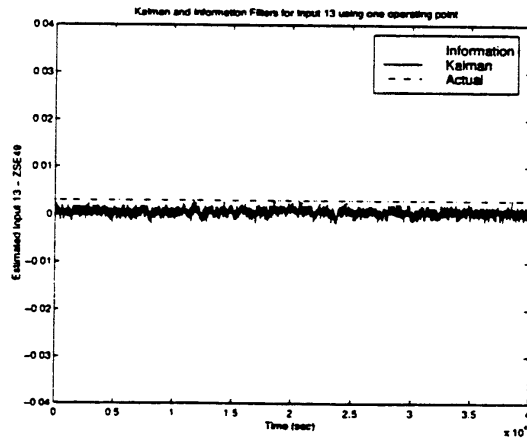


**Figure 99:** Measurement Estimation - Efficiency and Flow Scalar 10, ZSE49 (Case 4)

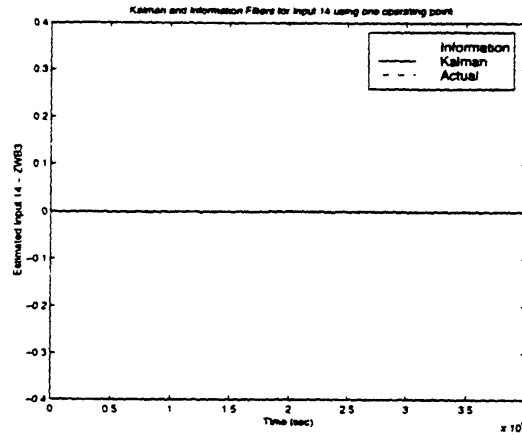


Figure 100: Measurement Estimation - Bleed 1, ZWB3 (Case 4)

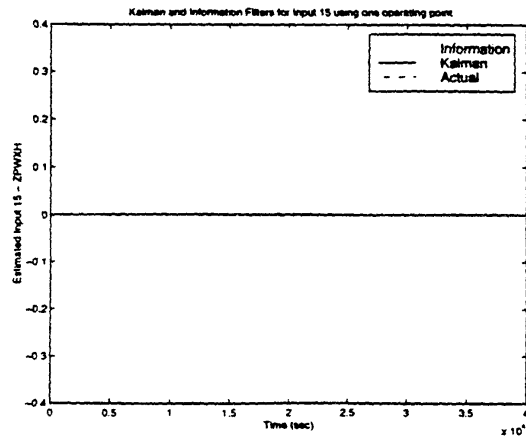


Figure 101: Measurement Estimation - Power Extraction 1, ZPWXH (Case 4)

Parameter	Actual Value	Mean:KF	Mean:IF	Variance:KF	Variance:IF
ZWF36	3.00E-03	7.26E-05	7.26E-05	2.28E-08	2.30E-08
ZA8	0.00E+00	-2.70E-03	-2.70E-03	1.99E-05	2.00E-05
ZA16	0.00E+00	1.23E-03	1.23E-03	6.08E-06	6.11E-06
ZSW2	3.00E-03	2.95E-03	2.95E-03	3.07E-06	2.98E-06
SEDM2	3.00E-03	2.94E-03	2.94E-03	4.06E-06	4.05E-06
ZSW7D	3.00E-03	2.94E-03	2.94E-03	6.32E-06	6.33E-06
SEDM7D	3.00E-03	4.03E-03	4.03E-03	5.02E-05	5.05E-05
ZSW27	3.00E-03	3.15E-03	3.15E-03	4.90E-06	4.97E-06
SEDM27	3.00E-03	3.45E-03	3.45E-03	4.64E-07	4.67E-07
ZSW41	3.00E-03	3.05E-03	3.05E-03	5.86E-07	5.77E-07
ZSE41	3.00E-03	3.42E-03	3.42E-03	1.92E-06	1.94E-06
ZSW49	3.00E-03	1.83E-03	1.83E-03	8.08E-07	8.78E-07
ZSE49	3.00E-03	4.65E-04	4.64E-04	5.23E-07	5.59E-07
ZWB3	0.00E+00	-5.57E-04	-5.57E-04	6.73E-07	6.78E-07
ZPWXH	0.00E+00	-1.47E-06	-1.47E-06	6.08E-12	6.14E-12

Table 15: Mean and Variance of Parameter Estimates of Kalman and Information Filters (Case 4)

Singular values:

$$\begin{bmatrix} 3.0135163e + 03 \\ 1.9332938e + 03 \\ 6.8244808e + 02 \\ 1.7598337e + 02 \\ 1.0068188e + 02 \\ 9.4230100e + 00 \\ 7.5684915e + 00 \\ 3.5334475e + 00 \\ 1.0320413e + 00 \\ 9.4464178e - 01 \\ 8.0679049e - 01 \end{bmatrix} \quad (6.4)$$



## Appendix 6: Complete Data for Estimation Using the Best Combination of Three - Parameters Initialized to 0.5 (Case 5)

Below presents 1) a complete set of figures illustrating the estimation process, and 2) a table describing the mean and variances of the parameter estimates of both the Kalman and Information filters.

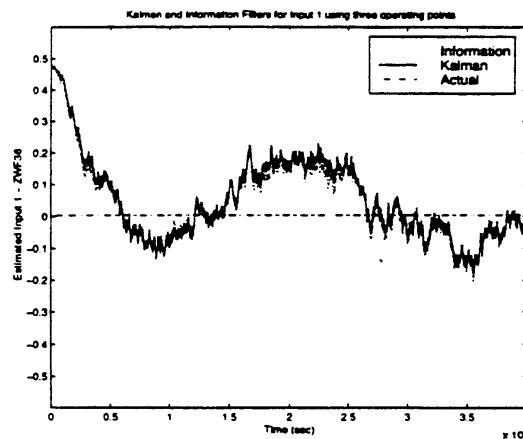
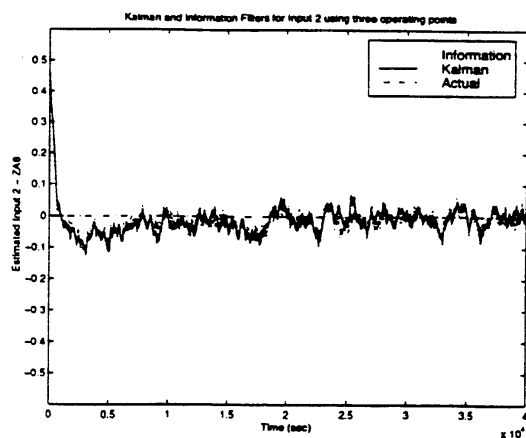
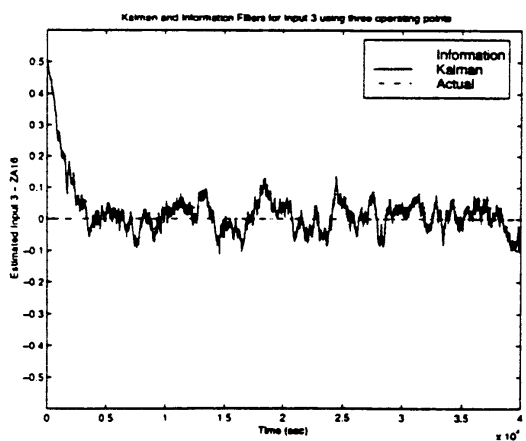


Figure 102: Measurement Estimation - Sensed Input 1, ZWF36 (Case 5)





**Figure 103:** Measurement Estimation - Sensed Input 2, ZA8 (Case 5)



**Figure 104:** Measurement Estimation - Sensed Input 3, ZA16 (Case 5)

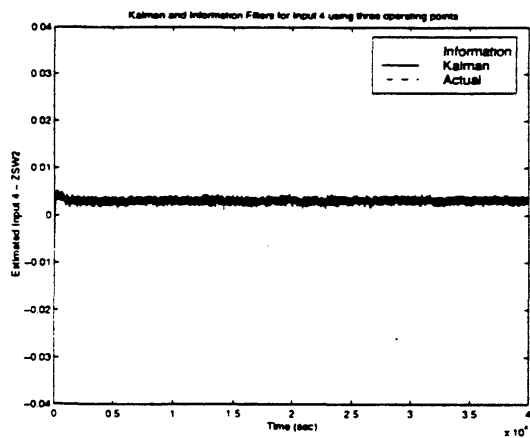


**Figure 105:** Measurement Estimation - Efficiency and Flow Scalar 1, ZSW2 (Case 5)

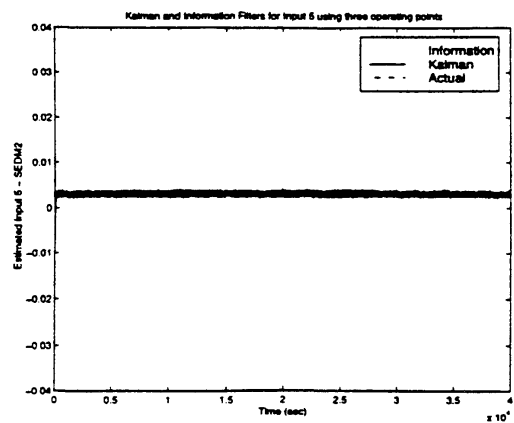


**Figure 106:** Measurement Estimation - Efficiency and Flow Scalar 2, SEDM2 (Case 5)

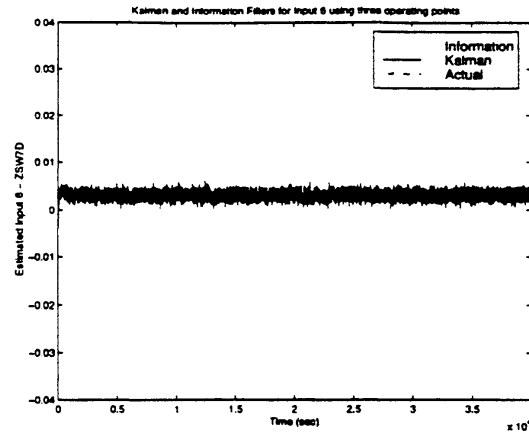


Figure 107: Measurement Estimation- Efficiency and Flow Scalar 3, ZSW7D (Case 5)

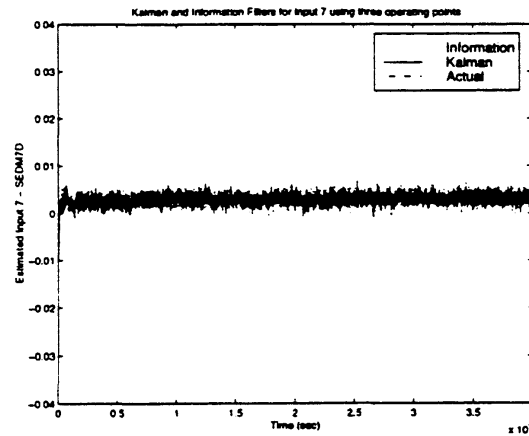


Figure 108: Measurement Estimation - Efficiency and Flow Scalar 4, SEDM7D (Case 5)

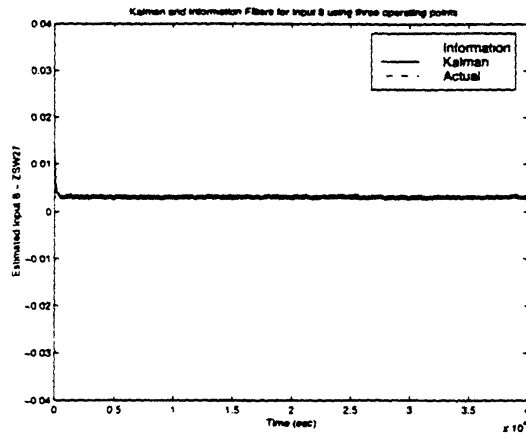


Figure 109: Measurement Estimation- Efficiency and Flow Scalar 5, ZSW27 (Case 5)

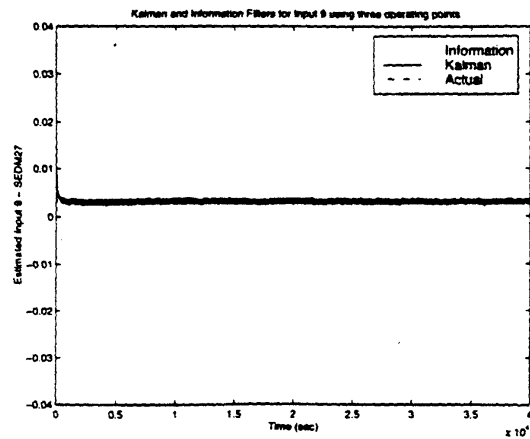


Figure 110: Measurement Estimation - Efficiency and Flow Scalar 6, SEDM27 (Case 5)

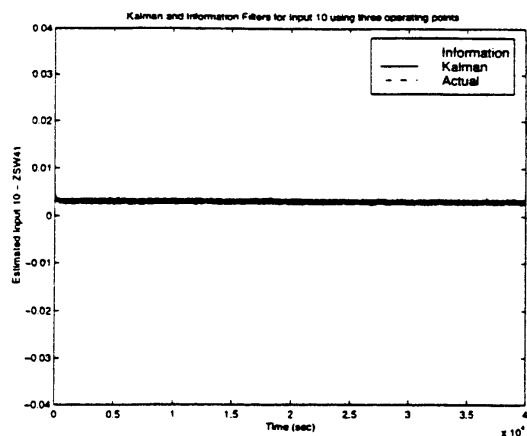


Figure 111: Measurement Estimation - Efficiency and Flow Scalar 7, ZSW41 (Case 5)

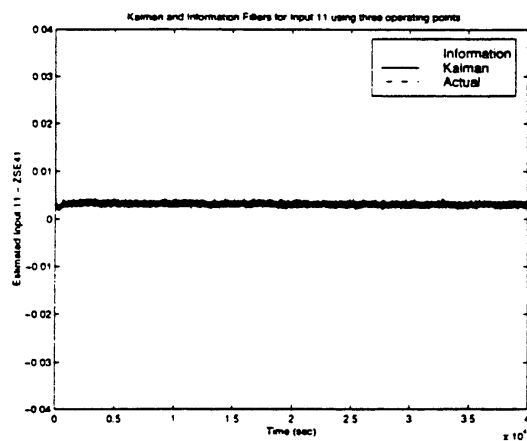


Figure 112: Measurement Estimation - Efficiency and Flow Scalar 8, ZSE41 (Case 5)

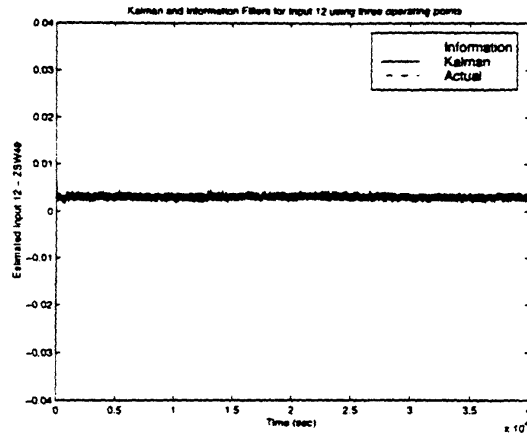


Figure 113: Measurement Estimation - Efficiency and Flow Scalar 9, ZSW49 (Case 5)

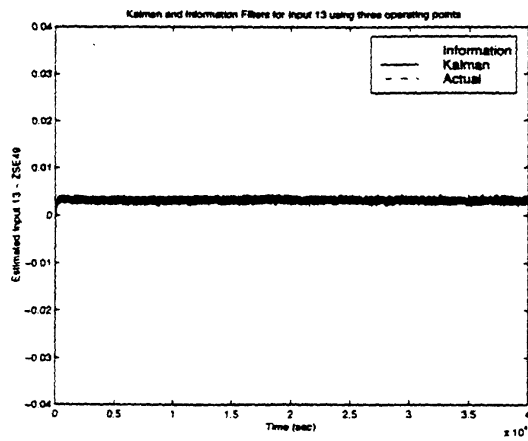
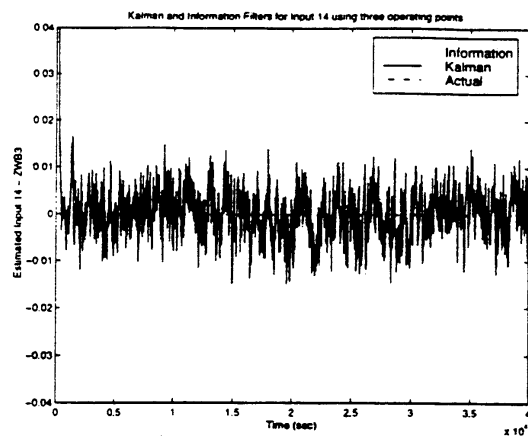
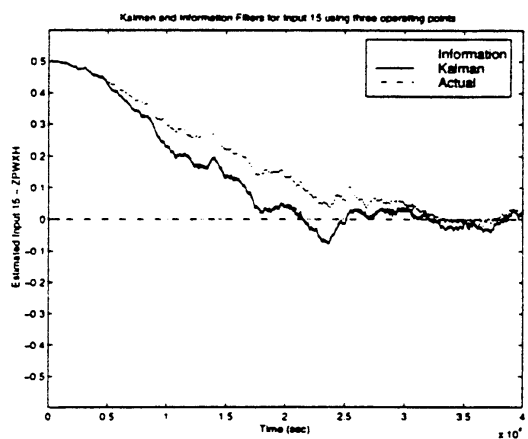


Figure 114: Measurement Estimation - Efficiency and Flow Scalar 10, ZSE49 (Case 5)



**Figure 115:** Measurement Estimation - Bleed 1, ZWB3 (Case 5)



**Figure 116:** Measurement Estimation - Power Extraction 1, ZPWXH (Case 5)



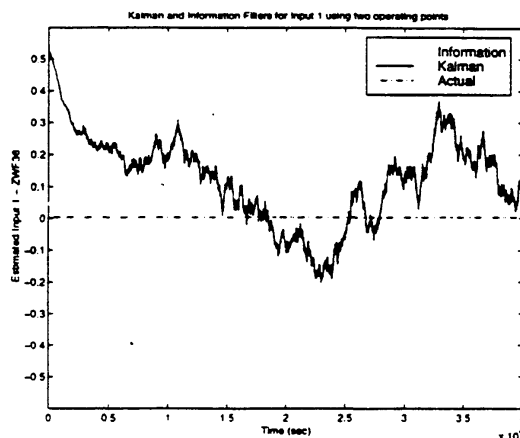
Parameter	Actual Value	Mean:KF	Mean:IF	Variance:KF	Variance:IF
ZWF36	3.00E-03	4.34E-02	3.26E-02	1.33E-02	1.19E-02
ZA8	0.00E+00	-1.98E-02	-1.94E-02	1.08E-03	7.97E-04
ZA16	0.00E+00	1.11E-02	1.19E-02	2.69E-03	2.51E-03
ZSW2	3.00E-03	2.95E-03	2.95E-03	2.36E-07	2.07E-07
SEDM2	3.00E-03	2.99E-03	2.99E-03	1.13E-07	1.07E-07
ZSW7D	3.00E-03	2.97E-03	2.96E-03	7.38E-07	6.49E-07
SEDM7D	3.00E-03	2.84E-03	2.81E-03	9.75E-07	1.33E-06
ZSW27	3.00E-03	3.00E-03	3.01E-03	4.37E-08	3.85E-08
SEDM27	3.00E-03	2.96E-03	2.97E-03	7.89E-08	7.22E-08
ZSW41	3.00E-03	3.00E-03	3.00E-03	8.18E-08	4.90E-08
ZSE41	3.00E-03	3.10E-03	3.10E-03	1.56E-07	1.68E-07
ZSW49	3.00E-03	2.99E-03	3.00E-03	1.80E-07	2.11E-07
ZSE49	3.00E-03	3.00E-03	3.01E-03	1.70E-07	1.93E-07
ZWB3	0.00E+00	1.64E-04	1.49E-04	2.36E-05	2.33E-05
ZPWXH	0.00E+00	1.22E-01	1.72E-01	2.85E-02	2.56E-02

Table 16: Mean and Variance of Parameter Estimates of Kalman and Information Filters (Case 5)



## Appendix 7: Complete Data for Estimation Using the Best Combination of Two - Parameters Initialized to 0.5 (Case 6)

Below presents 1) a complete set of figures illustrating the estimation process, and 2) a table describing the mean and variances of the parameter estimates of both the Kalman and Information filters.



**Figure 117:** Measurement Estimation - Sensed Input 1, ZWF36 (Case 5)

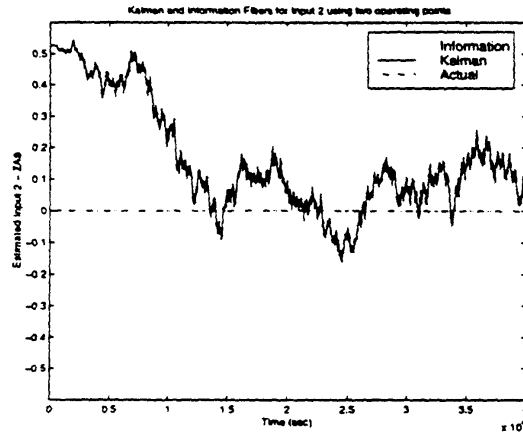


**Figure 118:** Measurement Estimation - Sensed Input 2, ZA8 (Case 6)

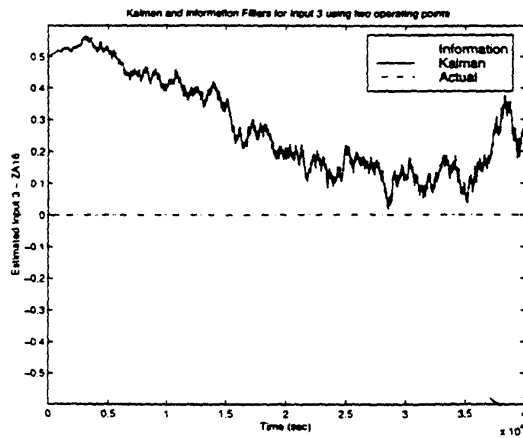


**Figure 119:** Measurement Estimation - Sensed Input 3, ZA16 (Case 6)

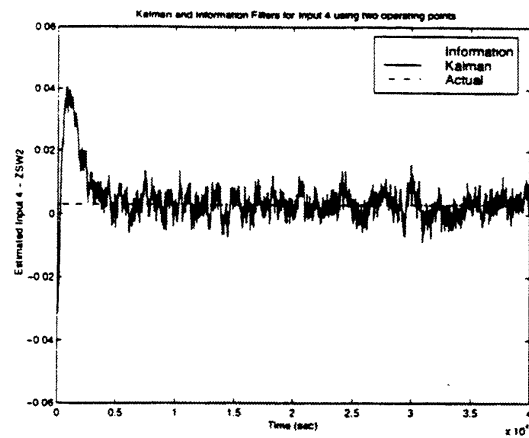


Figure 120: Measurement Estimation - Efficiency and Flow Scalar 1, ZSW2 (Case 6)

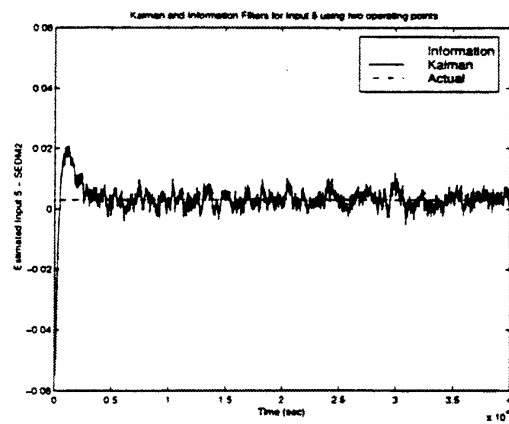


Figure 121: Measurement Estimation - Efficiency and Flow Scalar 2, SEDM2 (Case 6)

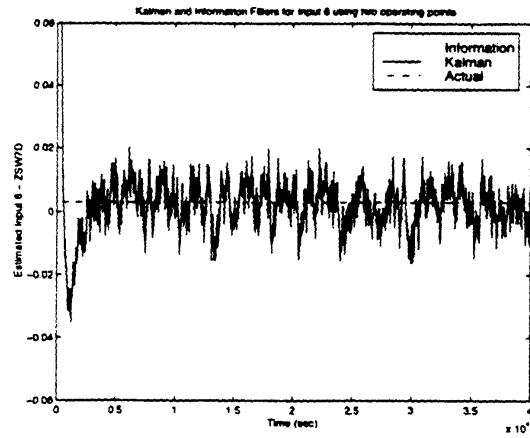


Figure 122: Measurement Estimation- Efficiency and Flow Scalar 3, ZSW7D (Case 6)

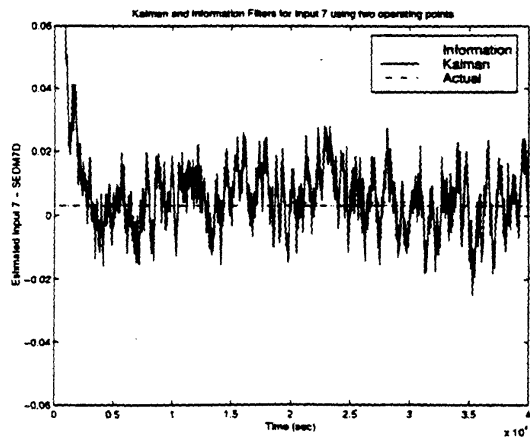


Figure 123: Measurement Estimation - Efficiency and Flow Scalar 4, SEDM7D (Case 6)

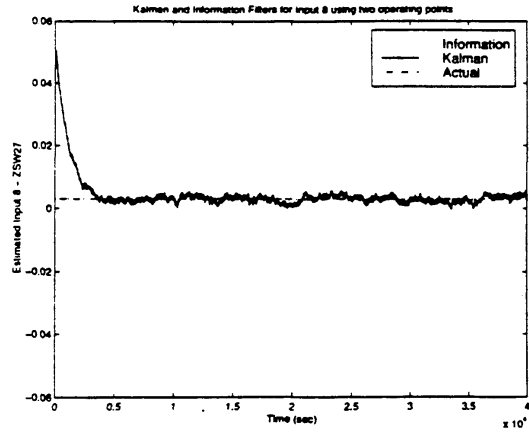


Figure 124: Measurement Estimation- Efficiency and Flow Scalar 5, ZSW27 (Case 6)

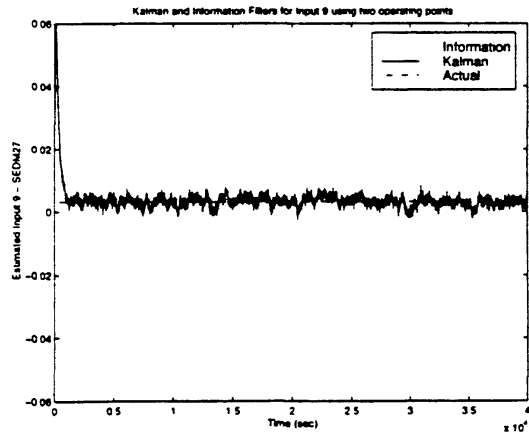


Figure 125: Measurement Estimation - Efficiency and Flow Scalar 6, SEDM27 (Case 6)



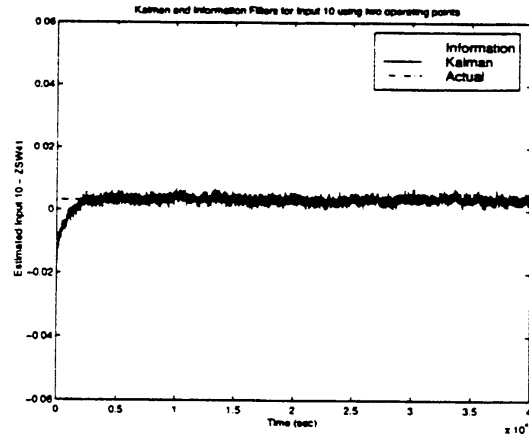


Figure 126: Measurement Estimation - Efficiency and Flow Scalar 7, ZSW41 (Case 6)

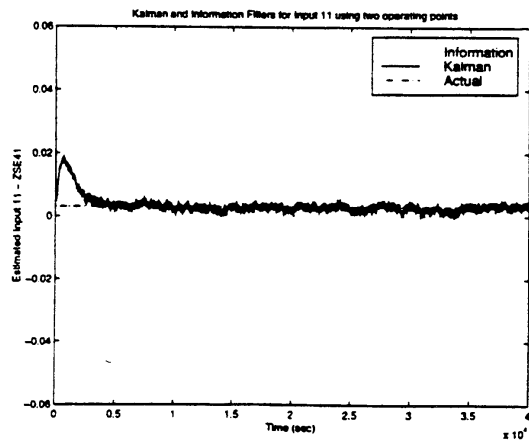


Figure 127: Measurement Estimation - Efficiency and Flow Scalar 8, ZSE41 (Case 6)

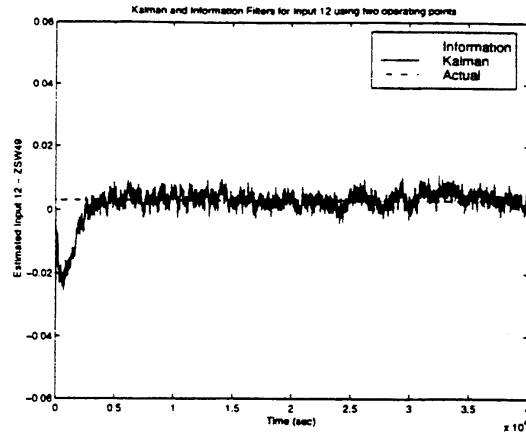


Figure 128: Measurement Estimation - Efficiency and Flow Scalar 9, ZSW49 (Case 6)

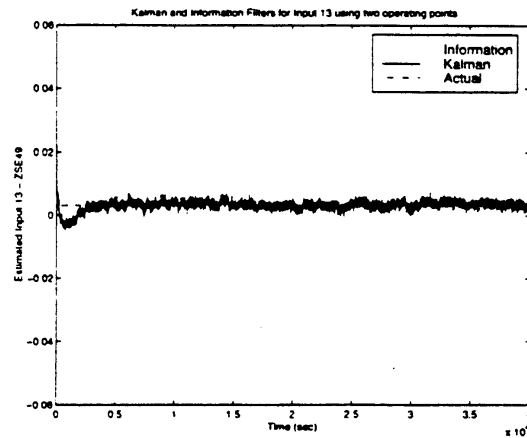


Figure 129: Measurement Estimation - Efficiency and Flow Scalar 10, ZSE49 (Case 6)

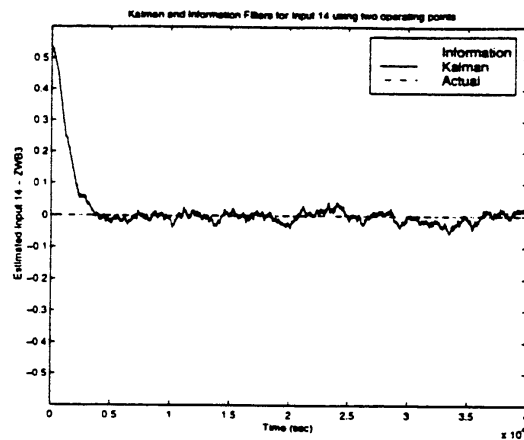


Figure 130: Measurement Estimation - Bleed 1, ZWB3 (Case 6)

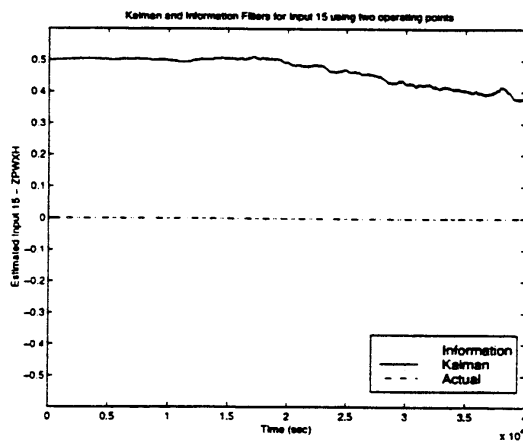


Figure 131: Measurement Estimation - Power Extraction 1, ZPWXH (Case 6)

Parameter	Actual Value	Mean:KF	Mean:IF	Variance:KF	Variance:IF
ZWF36	3.00E-03	1.15E-01	1.15E-01	1.67E-02	1.65E-02
ZA8	0.00E+00	1.53E-01	1.53E-01	2.82E-02	2.83E-02
ZA16	0.00E+00	2.74E-01	2.74E-01	2.24E-02	2.25E-02
ZSW2	3.00E-03	3.93E-03	3.93E-03	3.03E-05	3.04E-05
SEDM2	3.00E-03	3.30E-03	3.30E-03	9.47E-06	9.50E-06
ZSW7D	3.00E-03	1.78E-03	1.77E-03	5.12E-05	5.16E-05
SEDM7D	3.00E-03	5.41E-03	5.45E-03	9.66E-05	9.73E-05
ZSW27	3.00E-03	3.39E-03	3.39E-03	6.05E-06	6.05E-06
SEDM27	3.00E-03	2.92E-03	2.91E-03	2.55E-06	2.60E-06
ZSW41	3.00E-03	3.15E-03	3.15E-03	1.52E-06	1.51E-06
ZSE41	3.00E-03	3.06E-03	3.06E-03	3.59E-06	3.64E-06
ZSW49	3.00E-03	2.81E-03	2.82E-03	1.24E-05	1.26E-05
ZSE49	3.00E-03	3.12E-03	3.12E-03	1.87E-06	1.93E-06
ZWB3	0.00E+00	3.23E-03	3.17E-03	1.64E-03	1.65E-03
ZPWXH	0.00E+00	4.67E-01	4.67E-01	1.74E-03	1.75E-03

Table 17: Mean and Variance of Parameter Estimates of Kalman and Information Filters (Case 6)



## Appendix 8: Complete Data for Estimation Using Single Operating Point - Parameters Initialized to 0.5 (Case 7)

Below presents 1) a complete set of figures illustrating the estimation process, and 2) a table describing the mean and variances of the parameter estimates of both the Kalman and Information filters.

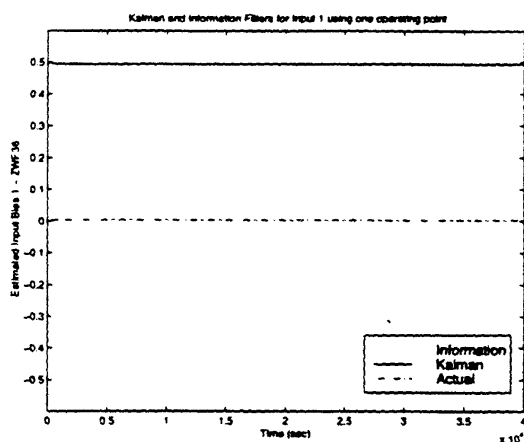
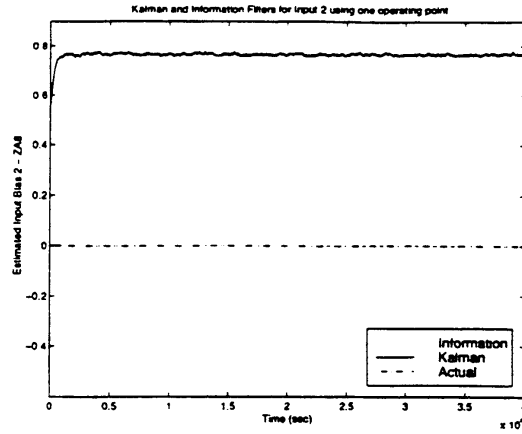
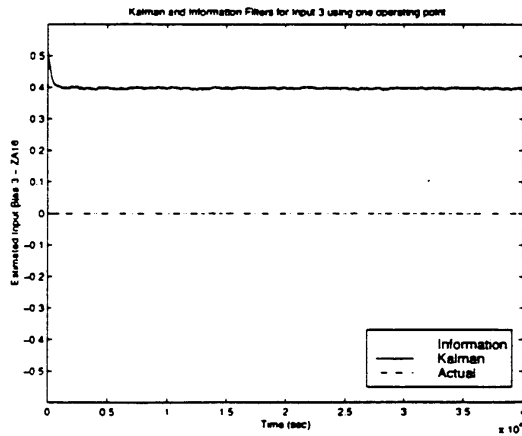


Figure 132: Measurement Estimation - Sensed Input 1, ZWF36 (Case 7)



**Figure 133:** Measurement Estimation - Sensed Input 2, ZA8 (Case 7)



**Figure 134:** Measurement Estimation - Sensed Input 3, ZA16 (Case 7)



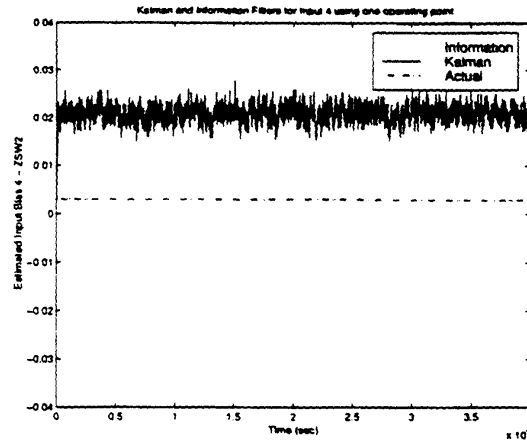


Figure 135: Measurement Estimation - Efficiency and Flow Scalar 1, ZSW2 (Case 7)

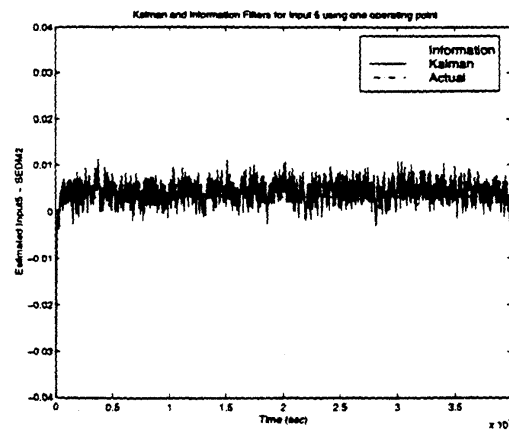
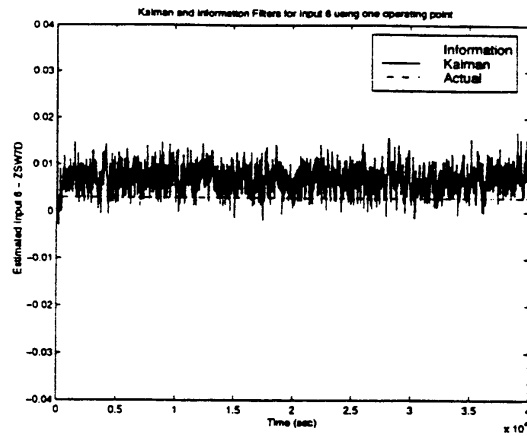
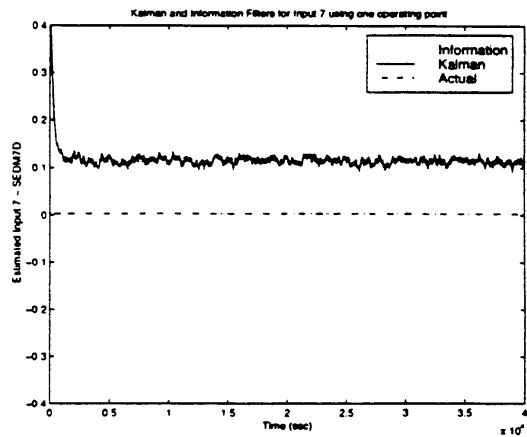


Figure 136: Measurement Estimation - Efficiency and Flow Scalar 2, SEDM2 (Case 7)



**Figure 137:** Measurement Estimation- Efficiency and Flow Scalar 3, ZSW7D (Case 7)



**Figure 138:** Measurement Estimation - Efficiency and Flow Scalar 4, SEDM7D (Case 7)

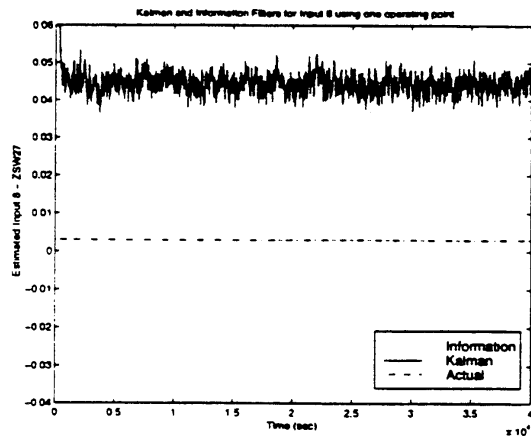


**Figure 139:** Measurement Estimation- Efficiency and Flow Scalar 5, ZSW27 (Case 7)

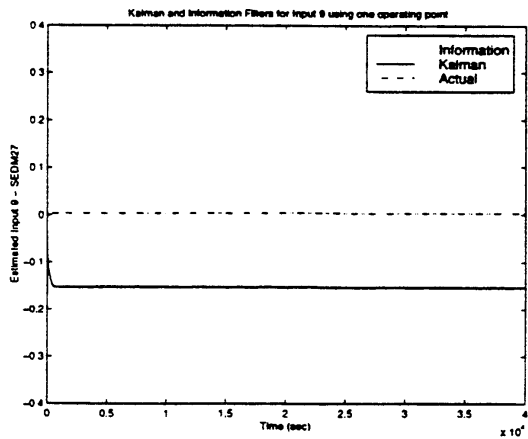


**Figure 140:** Measurement Estimation - Efficiency and Flow Scalar 6, SEDM27 (Case 7)

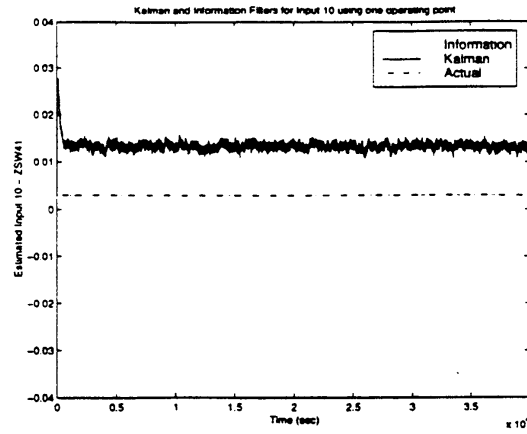


Figure 141: Measurement Estimation - Efficiency and Flow Scalar 7, ZSW41 (Case 7)

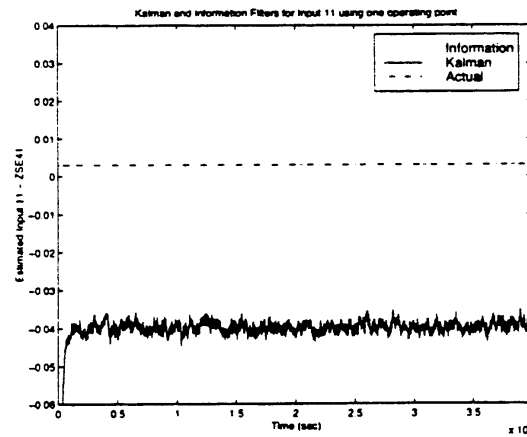


Figure 142: Measurement Estimation - Efficiency and Flow Scalar 8, ZSE41 (Case 7)

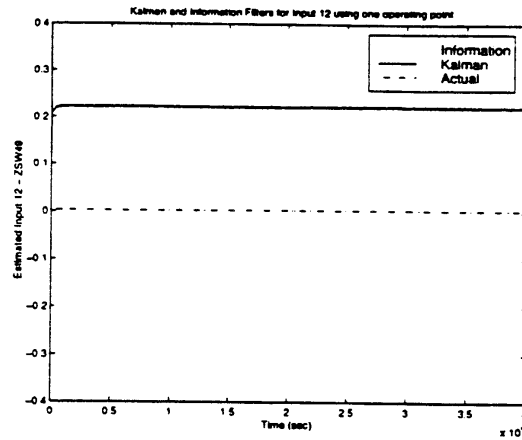


Figure 143: Measurement Estimation - Efficiency and Flow Scalar 9, ZSW49 (Case 7)

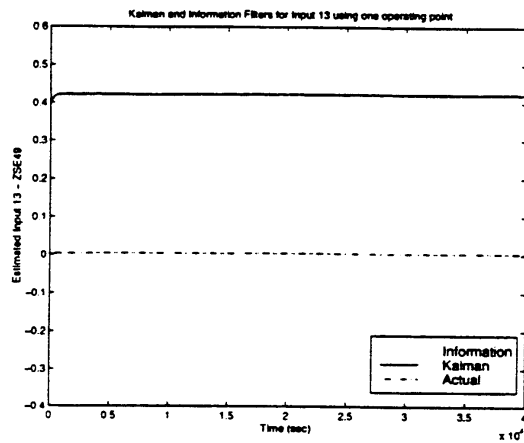
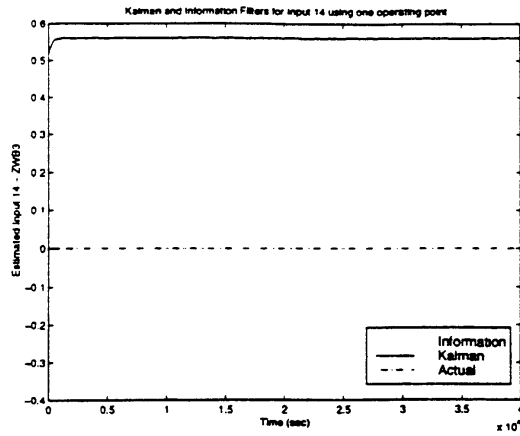
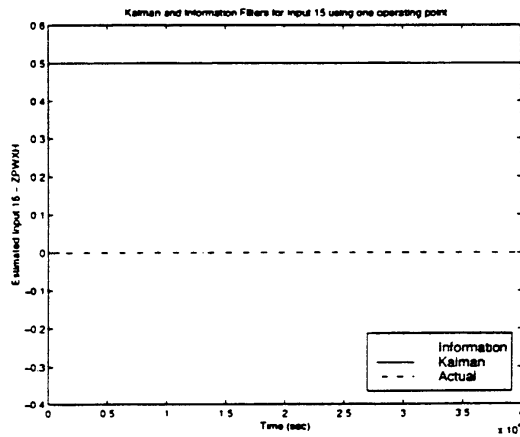


Figure 144: Measurement Estimation - Efficiency and Flow Scalar 10, ZSE49 (Case 7)



**Figure 145:** Measurement Estimation - Bleed 1, ZWB3 (Case 7)



**Figure 146:** Measurement Estimation - Power Extraction 1, ZPWXH (Case 7)

Parameter	Actual Value	Mean:KF	Mean:IF	Variance:KF	Variance:IF
ZWF36	3.00E-03	4.94E-01	4.94E-01	2.11E-08	2.13E-08
ZA8	0.00E+00	7.66E-01	7.66E-01	1.85E-05	1.86E-05
ZA16	0.00E+00	3.98E-01	3.98E-01	5.68E-06	5.70E-06
ZSW2	3.00E-03	2.09E-02	2.09E-02	3.34E-06	3.26E-06
SEDM2	3.00E-03	4.03E-03	4.03E-03	4.61E-06	4.61E-06
ZSW7D	3.00E-03	7.02E-03	7.02E-03	6.81E-06	6.83E-06
SEDM7D	3.00E-03	1.14E-01	1.14E-01	4.65E-05	4.68E-05
ZSW27	3.00E-03	4.42E-02	4.42E-02	5.40E-06	5.46E-06
SEDM27	3.00E-03	-1.55E-01	-1.55E-01	5.23E-07	5.27E-07
ZSW41	3.00E-03	1.32E-02	1.32E-02	5.78E-07	5.64E-07
ZSE41	3.00E-03	-3.99E-02	-3.99E-02	1.89E-06	1.91E-06
ZSW49	3.00E-03	2.22E-01	2.22E-01	8.28E-07	8.95E-07
ZSE49	3.00E-03	4.22E-01	4.22E-01	5.32E-07	5.66E-07
ZWB3	0.00E+00	5.61E-01	5.61E-01	6.24E-07	6.27E-07
ZPWXH	0.00E+00	5.00E-01	5.00E-01	5.63E-12	5.67E-12

Table 18: Mean and Variance of Parameter Estimates of Kalman and Information Filters (Case 7)





**Attachment II: Control Design & Analysis for the CPFN  
System – Final Report**



**PRELIMINARY  
CONTROL DESIGN AND  
ANALYSIS FOR THE  
CPFN VALVE**

**September 30, 1998**

**Prepared By:**

---

**Rick Lalonde  
Engineer  
Controls Group  
Analex Corporation**

## **Introduction**

The main purpose of the work reported here is to design a controller or tune a PID controller for the GE90 CPFN fuel system. The secondary purpose is to analyze the stability and performance of the controlled system.

The model for the fuel system that was used for this work was supplied by the Controls Center of Excellence Department of General Electric's Aircraft Engines Engineering Division. It is an Excel model and it contains some basic fluid compression and fluid momentum effects.

The fuel system model is partially described in the next section followed by a section listing the controller goals. The section after that discusses the basic controller that was included in the spreadsheet as well as a new controller that is proposed in this paper. The stability of the fuel system is then detailed, followed by simulation results showing the performance of the controlled system with the basic and proposed controllers.

## **Fuel System Model**

### **Components**

The components of the fuel system are the main pump, boost pump, bypass valve, fuel metering valve (FMV), pressurizing valve (PV), controlled pressure fuel nozzle (CPFN) pressurizing servovalve (PSV), and CPFN valves. The purposes of these are described below.

The main pump should be capable of delivering enough fuel for the combustor at maximum usage and also deliver fuel to the PV and CPFN PSV for control purposes. The goal of the bypass valve is to bypass pump flow back toward the pump inlet to maintain a constant prescribed pressure drop across the FMV. However, during transients, the pressure drop may deviate by about 5 psi. The flow through the FMV is simply proportional to the flow number of the FMV when the pressure drop is at the prescribed value. The purpose of the CPFN PSV is to supply the signal side of the CPFN valve with the proper pressure and flow to move the CPFN piston to follow a demanded position. The purpose of the PV is to keep the boost pressure at least 250 psi above the supply pressure.

### Equations in EXCEL

The following equations were extracted from the EXCEL model. They were included here mostly to document the model and can be skipped without losing the main focus of this paper.

#### Engine:

$$P_{36} = ((607-90.9) / (24639-2440)) * WF_{36} + 54$$

$$XN_2 = ((9197-6066)/(24639-2440)*WF_{36} + 4700)*64981/5722$$

#### PSV:

$$P_C = P_{BOOST} + 160$$

$$DP_{PV} = IF(MODE_{PSV} > 1, P_C - P_{IGUESS}, 0)$$

$$V_{PV} = IF(DP_{PV} > 0, 77 * K_{27} * SQRT(DP_{PV}) / K_{25}, -77 * K_{27} * SQRT(-DP_{PV}) / K_{25})$$

$$DVDT = (V_{PV} - V_{PV(k-1)}) / T$$

$$F_{NET} = DVDT * K_{28} / (32.12 * 12)$$

$$MODE = (1 \text{ for stuck, } 2 \text{ for forward, } 3 \text{ for backward})$$

$$FORCE = (P_2 - P_C + DP_{PV}) * K_{25} - K_{22} - K_{21} * X_{PV(k-1)}$$

$$\begin{aligned} \text{FRICTION} = & IF \text{ MODE}=1 \text{ THEN } \max(-K_{29}, (\min(K_{29}, \text{FORCE}))) \\ & IF \text{ MODE}=2 \text{ THEN } -K_{30} \\ & IF \text{ MODE}=3 \text{ THEN } +K_{30} \end{aligned}$$

$$ERRX_{PV} = FORCE + FRICTION - F_{NET}$$

$$V_{PV} = IF(MODE_{PSV} < 2, 0, V_{PV})$$

$$X_{PV} = \max(K_{24}, \min(K_{23}, X_{PV(k-1)} + V_{PV}^2 * .02)))^2 + P_{22}$$

$$FN_{PV} = (16689 * 0.6 * (2.14 * X_{PV}^2 - 0.02))$$

$$P_2 = P_{22} + (W_{FM} / FN_{PV})^2$$

CPFN:

$$F_{\text{SPRING}} = K * X_{\text{CPFN}} + \text{PRELOAD}$$

$$\begin{aligned} \text{FRICTION} &= \text{IF MODE}=1 \text{ THEN } \max(-\text{FST}, (\min(\text{FST}, \text{FORCE}))) \\ &\quad \text{IF MODE}=2 \text{ THEN } -\text{FSL} \\ &\quad \text{IF MODE}=3 \text{ THEN } +\text{FSL} \end{aligned}$$

$$F_{\text{NET}} = \text{FORCE} + \text{FRICTION} + F_{\text{SRPING}}$$

$$A = F_{\text{NET}} / \text{MASS}$$

$$V = V(k-1) + a * T$$

$$X_{\text{CPFN}} = X_{\text{CPFN}}(k-1) + V * T$$

$$X_{\text{DMD,CPFN}} = f(X_{\text{DMD,FMV}})$$

$$A5S4 = F_{19} * X_{\text{SENS,CPFN}}(k-1) + H_{19} * X_{\text{CPFN}}(k-1)$$

$$X_{\text{SENS}} = A5S4 + I_{19} * X_{\text{CPFN}}$$

$$\text{ERRX}_{\text{CPFN}} = X_{\text{SENS,CPFN}} - X_{\text{DMD,CPFN}}$$

$$\text{ERRX2}_{\text{CPFN}} = \text{ERRX}_{\text{CPFN}}(k-1) - \max(\min(\text{ERRX}_{\text{CPFN}}(k-1), 0.005, -0.005))$$

$$\text{ERRX3}_{\text{CPFN}} = \max(\min(\text{ERRX2}_{\text{CPFN}}, 0.01, -0.01))$$

$$\text{STB1}_{\text{CPFN}} = \text{STB1}_{\text{CPFN}}(k-1) + \text{KI}_{\text{CPFN}} * \text{ERRX3}_{\text{CPFN}}$$

$$\text{STB2}_{\text{CPFN}} = \text{STB1} - H_{11}$$

$$\text{INTPART} = \text{STB2}_{\text{CPFN}}$$

$$\text{KP}_{\text{PSV}} = \text{IF}(\text{TMC4} < 0, E_{25} * \sqrt{100 / (P_1(k-1) - 20)}, E_{25} * \sqrt{100 / (P_s(k-1) - P_1(k-1))})$$

$$\text{PROPPART} = \text{KP}_{\text{PSV}} * \text{ERRX}_{\text{CPFN}}$$

$$\text{TMC4} = \min(100, \max(-100, \text{PROPPART} + \text{INTPART}))$$

$$\text{TMC4N} = \text{TMC4} + H_{11}$$

$$\begin{aligned} \text{TMC4H} &= \text{TMC4H}(k-1) + \min(\text{TMC4N} - \text{TMC4H}(k-1) + 0.5 * \text{HYS}_{\text{CPFN}}, 0) \\ &\quad + \max(\text{TMC4N} - \text{TMC4H}(k-1) - 0.5 * \text{HYS}_{\text{CPFN}}, 0) \end{aligned}$$

$$P_1 = P_2 + 0.0278 * K_{14} * dQ_1/dt / ((386 * \pi * K_{15}^2)/4 + \text{sign}(Q_{PSV}) * 0.001892 * Q_{PSV}^2)$$

$$Q_{EXP1} = H_{13} * H_{14} * \text{SQRT}(\text{abs}((P_1 - 20)/100)) * TMC4H + (1 - H_{13}) * Q_{PSV}(K-1)$$

$$Q_{EXP2} = H_{13} * H_{14} * \text{SQRT}(\text{abs}((P_S - P_1)/100)) * TMC4H + (1 - H_{13}) * Q_{PSV}(K-1)$$

$$Q_{EXP3} = -H_{13} * H_{14} * \text{SQRT}(\text{abs}((P_1 - 20)/100)) * TMC4H + (1 - H_{13}) * Q_{PSV}(K-1)$$

$$Q_{EXP4} = -H_{13} * H_{14} * \text{SQRT}(\text{abs}((P_S - P_1)/100)) * TMC4H + (1 - H_{13}) * Q_{PSV}(K-1)$$

IF (P<sub>1</sub> > 20)

THEN

$$Q_{BIAS} = -0.0465 * \text{SQRT}(P_1 - 20)$$

IF Q<sub>EXP1</sub> < 0

THEN Q<sub>PSV</sub> = Q<sub>EXP1</sub>

ELSE Q<sub>PSV</sub> = Q<sub>EXP2</sub>

ELSE

$$Q_{BIAS} = 0.465 * \text{SQRT}(20 - P_1)$$

IF Q<sub>EXP3</sub> < 0

THEN Q<sub>PSV</sub> = Q<sub>EXP3</sub>

ELSE Q<sub>PSV</sub> = Q<sub>EXP4</sub>

END

$$Q_{PSV} = Q_{PSV} + Q_{BIAS}$$

q<sub>2v</sub> = from solver

$$Q_2 = 30 * q_{2v}$$

$$dP_2 / dt = (Q_{psv} - Q_2) * 75000 / (K_{14} * \pi * (K_{15}^2)/4)$$

$$P_2 = P_2(k-1) + T * dP_2/dt$$

$$dQ_1 / dt = (Q_{PSV} - Q_{PSV}(k-1)) / T$$

### Physical Equations for the CPFN Valve

The force balance equation for the piston position is

$$(P_T - P_B)A = F_F + (Kx + \text{preload}) + ma .$$

where:

P<sub>T</sub> = pressure at the top of the piston (manifold side)

P<sub>B</sub> = pressure at the bottom of the piston (signal side)



$A$  = area  
 $F_F$  = force of friction  
 $K$  = spring constant  
 $x$  = piston position  
 preload = spring force at  $x=0$   
 $m$  = mass  
 $a$  = acceleration

In the limit, as the mass of the piston goes to zero, the term “ $ma$ ” goes to zero. The equation then becomes

$$P_{DIFF}A = F_F + (Kx + \text{preload}) .$$

where:

$$P_{DIFF} = P_T - P_B$$

The flow through the hole in the piston is

$$Q_T = FN \cdot \sqrt{P_{DIFF}}$$

### Moving Piston

When the piston is moving, the velocity of the piston is related to the net flow in the bottom half of the cylinder. Since the bulk modulus of liquids, like jet fuel, is high, a good approximation can be obtained by neglecting fluid compression:

$$AV = Q_B - Q_T \quad \text{or}$$

$$AV = Q_B - FN \cdot \sqrt{(Kx + \text{preload} + F_F)/A} .$$

where:

$V$  = velocity

$Q_T$  = flow from the manifold side (TOP) of the CPFN valve to the signal side through the piston orifice

$Q_B$  = flow out of the signal side (BOTTOM) of the CPFN piston towards the CPFN PSV

When the piston has positive velocity,  $F_F = +F_{ST}$ , so the equation relating  $Q_B$  to velocity is

$$V = Q_B/A - FN/A \cdot \sqrt{(Kx + \text{preload} + F_{ST})/A} .$$

When the velocity is negative,

$$V = Q_B/A - FN/A \cdot \sqrt{(Kx + \text{preload} - F_{ST})/A} .$$

Therefore, velocity is proportional to the flow out of the bottom of the piston with a bias term that is a function of the position. When  $x$  is large enough, the orifice flow is not affected much by the direction of the velocity.

Plots of the above simplified equations were made in EXCEL and it was shown that they are very good approximations to the EXCEL equations with fluid compression and nonzero mass.

### Static Piston

When the piston is static,

$$Q_T = FN \cdot \sqrt{(F_F + Kx + \text{preload})/A}$$

where the frictional force in the force balance equation satisfies the inequality

$$-F_{ST} < F_F < F_{ST} .$$

From the equation for  $Q_T$ , it is seen that for a particular position, the range of  $F_F$  implies a range of allowable flows.

### CPFN Transfer Functions

A linear model of the CPFN loop was calculated to determine the linear stability. It was calculated using the physical equations for the CPFN piston (of the previous section), the Excel equations for the sensor and actuator, and the control laws that apply when the piston is moving.

To determine stability of a linear model, the external inputs to the loop are not relevant. The stability is just a function of the open loop gain. The transfer functions, by definition are the ratio of the transform of the output of a block divided by the transform of the input, neglecting effects of the output on external inputs.

The transfer function from CPFN velocity to position is

$$G_1(z) = X(z) / V(z) = T / (z-1) .$$

where:

$T$  = integration time step

The transfer function of the sensor is

$$G_2(z) = X_{\text{SENS}}(z) / X(z) = (1 - 0.6065) / (z - 0.6065) .$$

It therefore has a steady-state gain of unity. The transfer function of the controller when the piston is moving is

$$G_3(z) = \text{TMC4}(z) / X_{\text{SENS}}(z) = (K_P * K_{P,PSV} z + (K_I * T - K_P * K_{P,PSV})) / (z-1) .$$

where:

$K_P$  = proportional gain when piston is moving

$K_I$  = integral gain when piston is moving

$K_{P,PSV}$  = gain that is a function of  $P_1$  and  $P_S$

TMC4 = CPFN torque motor current

The input to the controller is the sensed position and the output is the torque motor current. The gain from the CPFN torque motor current, TMC4, to the flow,  $Q_{PSV}$  is

$$G_4(z) = Q_{PSV}(z) / \text{TMC4}(z) = g_{PSV} * 0.18 * (1 - 0.6065) / (z - 0.6065) .$$

where:

$g_{PSV}$  = gain for the torque motor current, this is a function of  $P_1$  and  $P_S$

The steady state gain of  $G_4(z)$  is  $g_{PSV} * 0.18$ . From the previous section, the equation relating velocity to flow (neglecting fluid compression) is  $AV = Q_B - Q_T$ . Since there are 30 CPFN valves

$$Q_B = -Q_{PSV}/30$$

and the equation becomes

$$AV = -Q_{PSV}/30 - Q_T.$$

For the linear model,  $Q_T$  is treated as a disturbance. Therefore, the transfer function from the flow to velocity is

$$G_5(z) = V(z) / Q_{PSV}(z) = -1 / (30 * A).$$

The factor  $K_{P,PSV}$  in the controller was designed to nearly cancel out the effect of the variable gain,  $g_{PSV}$ , from the TMC to the signal flow. If the TMC were not limited, and if the factor  $K_{P,PSV}$  multiplied both the proportional and integral terms,  $K_{P,PSV}$  would exactly cancel out the gain change from the TMC to the signal flow.

## Controller Goals And Issues

### Controller Goals

1. Control the CPFN piston to make single stage change within 0.5 seconds.
2. The steady-state error of the CPFN piston should be small.
3. When stage changes are not requested, the controller should keep the CPFN piston still, if possible. If it does not hold the piston still, the movements should either be small or driven back to the set point quickly. This applies particularly to movements due to changes in the fuel manifold pressure.
4. Keep dips in the combustor fuel flow due to CPFN piston flow small.
5. The controller should have good stability margins with the linear model of the fuel system.
6. The fuel nozzle pressure drop should be greater than 20 PSI.

### Uncommanded Piston Movements

When the commanded value of the CPFN piston is held constant, the piston, unfortunately can still move due to changes in the manifold pressure. This can occur when the demanded fuel flow is a ramp and the demanded CPFN piston position is a series of steps. The position sensor will not indicate the buildup of pressure because the position will not change until the static friction is exceeded. Therefore, advance notice of the movement, if desired, will have to come from pressures.

## Controllers

### Basic Controller

Analex received the spreadsheet with a proportional and integral controller with position error as input. The position error is the demanded position minus the sensed position. For the integral term, this error was put through a dead band of 0.005 inches, multiplied by the integral gain ( $K_I$ ), integrated, and then the output was rate limited to a change of  $\pm 0.01$  per integration time step ( $T$ ) of 0.01 seconds.

For the proportional part, the error was multiplied by a gain that is a function of  $P_1$  and  $P_3$ . This gain,  $K_{PSV}$ , was chosen to be the reciprocal of the gain from the torque motor current (TMC4) to the pressurizing servovalve current,  $Q_{PSV}$ .

## Proposed Controller

This report proposes to use the previously mention controller when the piston is moving and to use a controller based on the estimated value of the CPFN static friction when the piston is static. (The actual value of the friction is known in the simulation, but with the physical system, it must be estimated). The reason for this, is that a controller sensing only position, can not determine when the pressure difference across the cylinder is building up and is about to cause unwanted piston movement. By monitoring the estimated friction, it is possible to predict when the piston is going to break away from its position. If the direction of movement of the friction is not known, then it makes sense to attempt to keep the friction near zero because this will allow the largest deviation without breakaway. If the direction in which the friction is likely to move is known, then the target friction should be set to be near the static friction limit in the opposite direction.

According to a previous section, when the piston is static, the frictional force should be

$$F_{ST} = A*(P_{MAN} - P1) - (K*X - \text{pre-load}).$$

Therefore, driving the following error signal to zero should drive the static friction to zero also.

$$\text{error}_{DP} = P_{MAN,SENS} - P1_{SENS} - (K_{CONT}*X_{SENS} - \text{pre-load}_{CONT}) / A_{CONT}.$$

where:

$\text{error}_{DP}$  = error signal for the pressure feedback controller (delta pressure controller)

$P_{MAN,SENS}$  = sensed value of  $P_{MAN}$

$P1_{SENS}$  = sensed value of  $P1$

$K_{CONT}$  = value of the spring constant used by the controller

$\text{pre-load}_{CONT}$  = value of the pre-load used by the controller

$A_{CONT}$  = value of the area used by the controller

Since the position feedback controller works moderately well alone, i.e. for a dynamic and static piston, it is proposed that the pressure feedback controller be used only when the measurements provide a very high probability that the piston is in the static mode. The following criteria are recommended to be used to determine when to activate the pressure feedback controller (static controller):

- 1 position error below a given threshold
- 2 velocity has been below a threshold for “n” consecutive time periods or low passed filtered velocity signal is below a threshold

It is recommended that both of these be satisfied when using pressure feedback. The velocity criteria may introduce a small delay in the turning on the pressure feedback controller, but this will not cause problems. There will be no delay switching from the

static controller to the dynamic controller because even though criteria #2 may still be satisfied, criteria #1 will not be and the position feedback controller will be turned on.

To have the output of the integrator properly initialized when the pressure feedback controller is turned on, the same integrator can be used for both controllers. However, it is fine to use different dead bands and rate limiters.

Since the sensed pressures and the spring parameters will be slightly different than the actual values, the actual friction force will not be exactly zero when the feedback signal is zero. However, a full dispersion analysis is beyond the scope of the present task.

### Flow Control

Another method to drive the frictional force to zero is to control the flow out of the signal end of the cylinders. This could be accomplished as follows:

- 1 calculate a pressure drop across the piston, based on the position, to cancel out the spring force (i.e. no static friction)
- 2 calculate the flow through the orifice corresponding to this pressure drop, denote this as the demanded flow (this depends on an accurate value for the orifice flow number)
- 3 calculate the actual flow by measuring a pressure drop in the path
- 4 drive a simple controller with the error between demanded flow, #2, and the actual flow, #3

The method in the previous section was chosen over this method because this method relies on an accurate value for the orifice flow number and on measuring the flow.

### Fuel Demand Modification

When the CPFN piston changes stages a flow drop to the combustion chamber occurs which is equal to the area times the velocity. The FMV does not have the bandwidth to cancel out this disturbance. In fact, even if the demand is increased as an attempt cancel this disturbance, the disturbance is still not canceled, but it can be significantly reduced. The method that was employed for this work was to modify the fuel demand by adding half a period of a sine wave to the demanded fuel flow. To change the demand for a time interval of  $W$  seconds, the following equation was used.

$$WF_{DMD,ADD} = A \cdot \sin(\omega \cdot (t - (t_{stage} - W/2))) \quad \text{for} \quad (t_{stage} - W/2) < t < (t_{stage} + W/2)$$

where:

$t_{stage}$  = anticipated time for the CPFN piston to start a stage change

$T = 2 \cdot W$

$f = 1 / T$

$\omega = 2 \cdot \pi \cdot f$

Reasonable values for the parameters are  $A=800$  lbm/hr and  $W=0.3$  seconds. A square pulse could also be used, but it would change the demand abruptly.

The main difficulty with this modification is that the stage change must either be known in advance or be delayed by a time period equal to  $W$ . And since the demanded stage may be a function of the actual fuel flow, changing the demanded flow will change the actual flow, which may change the demanded and actual time of the stage change.

## Stability of the Linear Model

Nonlinear stability is often difficult or even intractable for problems with nonlinear blocks that have equations that change abruptly in time, as does the CPFN pressure regulator. Because of this, it was decided to determine the stability of linearized versions of the nonlinear system (at several operating points) and also to investigate the stability of the nonlinear system in the time domain with simulations.

To determine the stability, only the CPFN loop was included in the model. This loop consists of the CPFN regulator and the CPFN valve. The nonlinearities of this loop are in the equations for  $Q_{PSV}$  and  $K_{PSV}$ . The equations for these variables are functions of  $\sqrt{100/(P_1(k-1)-20)}$  or  $\sqrt{100/(P_S(k-1)-P_1(k-1))}$  depending on the direction of the main part of the flow of  $Q_{PSV}$ . The main part does not include the bias flow. For each of the three parameters: flow direction,  $P_1$ , and  $P_S$  there is a linear model. This linear model is the set of transfer functions given in the section "CPFN Transfer Functions". The manifold pressure is treated as a disturbance in these models and does not affect the stability.

The model was reparametrized to be a function of flow direction,  $P_1$ , and the difference between the pressures "dp" where  $dp=P_S-P_1$ . Ranges for  $P_1$  and dp were chosen and the stability was determined for the eight cases that are obtained when each parameter can be at one of its extremes. The extremes that were chosen for the stability analysis are 40 and 200 for  $P_1$ , 300 and 500 for dp, and forward or backward for the main part of the flow  $Q_{PSV}$ .

The linear models were analyzed in the frequency domain and with root locus. The roots were stable for all eight cases and the stability margins for a controller with  $K_P=2200$  and  $K_I=24$  were in the ranges listed below.

2.43 < Gain Margin < 2.44

7.74 < Gain Margin (db) < 7.75

41.7 < Phase Margin < 41.8 deg

The ranges are very tight, because the controller gain at these frequencies is mostly based on the proportional term, and the factor  $KP_{PSV}$  in this term nearly cancels out the effect of the changing gain from the TMC to the signal flow.

Typical gain and phase margin goals are 6 db and 30 deg. The calculated gain margin for this fuel system implies that the system would be stable for plant a uncertainty factor of 2.43. The phase and gain margins occur at frequencies of 15.4 and 30.3 rad/sec respectively. Therefore, this phase margin shows that the linear system will be stable at 2.45 hz with an unmodeled delay of 0.047 seconds.

The stability of the linear models was determined by the Matlab function in Appendix A.

## Results

### Position Control

Results of a simulation using the basic proportional plus integral position controller with gains  $KP=2200$  and  $KI=24$  are shown in Appendix B. Figure B-1a shows the demanded and actual CPFN piston position as a function of time. It changes from stage 1 to 2 to 3. Figure B-1b shows that the velocity becomes nonzero around 0.25 seconds. This is due to an increase in the pressure difference across the cylinder, which is due to an increase in manifold pressure that is caused by an increase in demanded fuel flow. The demanded fuel flow is a ramp function in this simulation. Similarly, the piston breaks loose around 1.05 and 1.7 seconds. Since the feedback signal to the controller is position, the best it can do is to react after the piston has moved. The next section will illustrate the performance of a controller, to be used when the piston is static, that senses a pressure difference and drives it towards zero to reduce the number of breakaways.

The model was received by Analex with the CPFN piston mass set equal to 1.0 lbm. Current specifications call for the mass to be 0.138 lbm. When the piston is still, the mass is irrelevant. When the piston is in motion, the pressure, spring, and frictional forces are much larger than the inertial force of the piston (because of its small mass) and a very good approximation to the transient response can be obtained by neglecting the inertial force. This was verified by performing three simulations in which the CPFN piston mass was set to the values of 0.138, 1.0, and 10 lbm. The plots were indistinguishable to the human eye. Since the EXCEL solver frequently had difficulty with a piston mass of 0.138, a value of 1.0 was used in the runs described in this paper.

### Position and Pressure Control

Results of a simulation using the position feedback controller while the piston is moving and a pressure feedback controller while the piston is static are shown in Appendix C. Figure C-1a shows that the piston moves from stages 1 to 6. Figure C-1b depicts the velocity. After the first stage transition the velocity does not reach zero so the static controller was not activated. It was activated after the 2<sup>nd</sup>, 3<sup>rd</sup>, and 4<sup>th</sup> transitions and it



prevented the piston from breaking loose. The breakaway that occurs after the 5<sup>th</sup> transition, happens before the static controller is turned on. For this simulation the static controller was not allowed to become active until a lowpassed velocity signal was within certain limits. The breakaway that occurs before the 1<sup>st</sup> transition is due to a change in the dynamics of the PSV flow. In the model, this is manifested as a change in the PSV flow equation. The static controller was not predicted to prevent a breakaway due to this change in dynamics which occurs infrequently. The actual value of the friction in the simulation (as opposed to the estimated value based on pressure transducers) is shown in Figure C-1c. It is seen that the static controller drives the friction to zero when it is active (zero velocity). It is also seen that the friction oscillates much more at higher stages. The oscillation can be greatly reduced by either reducing the gain at higher stages (gain scheduling) or by using pressure transducers with higher bandwidths. The pressure transducer had a cut-off frequency of 8 hz in this simulation.

Figure C-2a shows the value of the controller switch and the position error. When the switch is zero the dynamic controller is active, when it is one the static controller is active. Figure C-2b shows the proportional and integral outputs of the active controller, i.e., whichever controller is active at the time. The integral part is on top. The proportional part is not strictly a constant times the position when the dynamic controller is on due to limiting and hysteresis.

Figure C-3a shows the controller switch and the error signal used by the pressure controller. This error signal has a term due to the piston position and preload. This plot clearly shows how the error signal is driven to zero when the static controller is active. It also shows that the error signal is at a constant of  $FSL/A$  when the piston position is at stage two but moving slowly. This occurs between 0.8 and 1.0 seconds. This illustrates that the pressure controller error signal (and hence the static friction) does not move to or stay near zero without pressure feedback control. Figure C-4a depicts the FMV demanded fuel flow, the FMV flow, and the combustor flow (WF36). The demanded flow is constant until 0.1 seconds and then a ramp after that. The actual fuel flow has slight "bumps" (deviations from a straight line) due to the fact that the bypass filter does not keep the pressure drop across the FMV exactly at the target value during transients. The FMV flow is the highest trace at four seconds. The combustor flow has larger bumps than the FMV flow due to CPFN piston movements. Figure C-4b shows the error between the FMV demand and the combustor flow. By observing the portions between the transients, it is seen that the error is decreasing with time in a smooth and predictable fashion. Because of this, it seems appropriate to add a correction to the demand so that the actual flow is much closer to the demand. The piston movement for the transition from stage 2 to 3 causes a fuel flow error of about 900 lbm/hr. The next three transitions cause errors of about 800, 1000, and 1200 lbm/hr respectively. Modification of the demand to reduce these drops is covered in a later section. The last plot on this page, C-4c, shows the fuel nozzle pressure drop. It stays above the requirement of 20 psi.

Figure C-5a is a plot of the position error. It is seen again that the error is changing between the first and second transitions. The error for the next four stages is within

$\pm 0.005$  inches. Plot C-5b was made to determine the usefulness of the error signal that is the input to the pressure feedback controller. The error signal uses a measured value of  $P_1$ , which is the pressure of the output of the CPFN PSV, instead of the actual value of  $P_3$ , which is the signal pressure of the CPFN valve. If the error signal used was the actual value of  $P_3$ , then the trace in the figure would be zero when the piston is static. However, it is seen that for stage 6 (4.0 to 4.5 seconds) especially, the error oscillates about zero with a peak magnitude of about 20 psi and a frequency of about 10 hz. What can not be determined from this plot alone is how much of the deviation from zero is caused by pressure differences from  $P_1$  to  $P_3$  and how much of the deviation is caused by sensor or transducer errors. The transducer is modeled as a low pass filter. The cut-off frequency for this simulation is 8 hz. The next section contains results from a simulation in which the cut-off frequency is 48 hz.

The gains that were used for the static controller are  $K_p=0.5$  and  $K_i=0.1$ .

### Position and Pressure Control with a High Bandwidth Pressure Transducer

It was stated earlier that two methods could be employed to reduce the oscillations of the pressure feedback controller for stage six. The simulation described in this section uses a pressure transducer with a larger cut-off frequency, namely 48 hz. When the pressure feedback controller is active for stage six the oscillations of the static friction are seen in Figure D-1c to be much smaller than they were with the 8 hz transducer (compare to Figure C-1c). The controller switch and the error signal for this run are plotted in Figure D-3a.

As expected, the plots of Figure D-4 are quite similar to those of C-4. By comparing the controller switch of Figure D-3a with the plot of Figure D-5b, it is seen that when the static control is active, its feedback signal is quite good. Therefore, the feedback signal is good for the intervals:

0.2 to 0.4  
1.45 to 1.6  
2.1 to 2.75  
3.2 to 3.65  
3.95 to 4.7

This demonstrates that increasing the bandwidth of the pressure transducer is a very effective method to reduce the oscillation at high stages.

### Position Control with Decreasing Flow

This section describes a simulation in which the stages change from 6 to 1 using only the position feedback controller. The demanded and actual CPFN piston positions are shown in Figure E-1a. It is seen that the actual position overshoots the demanded position during the first and second transition. This did not happen going in the opposite direction, i.e. from stage 1 to stage 6. Figure E-1c shows that without the pressure feedback controller, the friction hits the static limit and the piston moves as shown in Figure E-1b at 1, 2.9, and 4.3 seconds. Figure E-2a shows that the controller was intentionally held at zero to illustrate the effectiveness of position only control going from stages 6 to 1. This figure also shows that the error is large for stage 4 (3.2 to 3.7 seconds). Figure E-2b shows that for this time period, the integral output is going down linearly and presumably would correct the position error if the demand for stage 5 did not occur.

Figure E-4a shows the demanded and actual FMV flows as well as the combustor flow. Figure E-4b shows the error. The fuel nozzle pressure drop is seen in Figure E-4c to stay above the requirement of 20 psi. The position error is shown in Figure E-5a.

### Position Control with Fuel Demand Modification

Results of a simulation in which the fuel demand was modified are shown in Appendix F. The demanded fuel flow was modified for the first stage change which is seen in Figure F-1a to occur at about 0.4 seconds, but it was not modified for the second stage change that occurred at about 1.2 seconds. The fuel demand modification shown in Figure F-5c is seen to be half a period of a sine wave as described in a previous section. The peak error for the transition is about 1400 lbm/hr for the stage change without the modification and about 900 lbm/hr with the modification (see Figure F-4b).

### Stage Change Position Errors

The distance between ports in the CPFN cylinder is 0.103 inches, so that the total error of the piston with all dispersions and control system transient errors needs to be less than half of this value or  $\pm 0.051$  inches. GE has conducted a preliminary study on the piston error due to dispersions such as variances in the spring constant, spring preload, orifice location, friction, and LVDT accuracy. The simulations described here only show the position errors due to the dynamics of the system with the controller and the nonlinear actuator.

Table 1 lists the position errors for the simulations of Appendices C and E. In Appendix C, the CPFN piston was successively stepped from stage 1 to stage 6. The position and pressure feedback controllers were both used in this appendix. For Appendix E, only the position feedback controller was used, but the position errors listed in the table were taken before the breakaways (see Figure E-1a and E-5a). In this appendix the CPFN piston was successively stepped from stage 6 to 1.

**Table 1                      Stage Change Position Errors**

Stage	Appendix C		Appendix E	
	Time	Position Error (0.001 inch)	Time	Position Error (0.001 inch)
1	N/A	N/A	5	-6.5
2	N/A	N/A	4	1.3
3	1.5	1.9	3.5	-16.1*
4	2.5	-3.1	2.5	-7.2
5	3.5	0.8	1.75	-7.8
6	4.5	4.1	N/A	N/A

\* This value would probably be changed by the integrator in time.

## Conclusion

The analysis here shows that the basic PI controller has good stability margins. It typically produces a single stage change in a time interval of 0.25 to 0.35 seconds. It was shown that the dips in the fuel flow due to the speed of the stage change can be reduced by modifying the demanded fuel flow. The position errors for a stage change were generally less than  $\pm 0.010$  inches. The fuel nozzle pressure drop stayed above the requirement of 20 psi in all of the runs. However, simulations of a complete set of operating points is needed to better determine whether the pressure requirement will always be met and this is beyond the scope of this work.

The only area of performance in which the basic controller did not perform well was with the uncommanded piston movements due to large changes in the manifold pressure during quiescent periods of the demanded fuel flow. For these uncommanded movements, a pressure feedback controller was proposed and tested with simulations. It was shown to be very effective in preventing these uncommanded movements.

## Issues for Further Study

Before the proposed control is used, a dispersion analysis should be performed and a decision should be made to determine which method should be used to reduce the oscillations for stage six. The dispersion analysis needs to determine how much effect the spring rate and preload will have on the controller performance. The oscillations of stage six can be reduced by using a pressure transducer with a bandwidth higher than 8 hz or by lowering the gain for stage six.

It is also recommended to derive a transfer function model of the CPFN and CPFN PSV loop when the piston is static. This model could then be used to generate frequency domain plots and root locus plots for the static controller. These could in turn be used to quickly design and evaluate a pressure feedback controller that may outperform the one given here.

```

function [stab,gmdb,pm,wgain,wphase]=cpfnstab(kp,ki,plotopt,printopt)
%      [stab,gmdb,pm,wgain,wphase]=cpfnstab(kp,ki,plotopt,printopt)
%
%      determines the stability margins of the CPFN loop
%      based on 2^n parameter combinations
%
%      parameters: P1, dp=(Ps-P1), Qpsveq
%
%      inputs:
%      kp = proportional gain
%      ki = integral gain
%      plotopt = 0 no plot
%              1 plot
%      printopt = 0 don't print plot file
%                1 print plot file
%
%      outputs:
%      stab = stability flag, value = stable or unstable
%      gmdb = gain margin in decibels
%      pm = phase margin
%      wgain = frequency at which the gain margin is obtained (rad/sec)
%      wphase = frequency at which the phase margin is obtained (rad/sec)
%
%      written by Rick Lalonde   written 8-31-98   revised 9-10-98
%      if (nargin < 1), kp=2200; end
%      if (nargin < 2), ki=24; end
%      if (nargin < 3), plotopt=0; end
%      if (nargin < 4), printopt=0; end
%
%      area=0.785;
%      h13=0.3935; h14=0.18; T=0.01;
%      f19=0.6065; h19=0.1804; i19=0.2131;
%
%      w=logspace(-1,2,300)';
%
%      initialize "stab" to stable, if unstable roots are found this is changed
%      stab='stable';
%
%-----
%      p1min=40; p1max=200;
%      dpmin=300; dpmax=500;
%      eqmin=1; eqmax=2;

```

```

%-----
case=0;
for ii=1:2
for jj=1:2
for kk=1:2
case=case+1;

if (ii==1), p1=p1min; else p1=p1max; end
if (jj==1), dp=dpmin; else dp=dpmax; end
if (kk==1), eq=eqmin; else eq=eqmax; end

ps=p1+dp;

% t.f. from CPFN velocity to position
n1=[0 T]; d1=[1 -1];

% sensor t.f.
n2=[0 h19+i19]; d2=[1 -f19];
num=conv(n1,n2); den=conv(d1,d2);

%
if (eq==1),
kppsv=sqrt(100/(p1-20));
gainpsv=1/kppsv;
end
if (eq==2),
kppsv=sqrt(100/(ps-p1));
gainpsv=1/kppsv;
end
%kppsv=1;

% controller t.f.
n3=[kp*kppsv ki*T-kp*kppsv]; d3=[1 -1];
num=conv(num,n3); den=conv(den,d3);

% t.f. from TMC4 to Qpsv
n4=gainpsv*[0 h13*h14]; d4=[1 -(1-h13)];
num=conv(num,n4); den=conv(den,d4);

% gain from Qpsv to velocity
n5=-1 / (30*area); d5=1;
num=n5*num;

% calculate closed loop t.f.
num=-num;

```

```

numcl=num; dencl=num+den;

% calculate roots
poles=roots(dencl);
if any((abs(poles) >= 1)), stab='unstable'; end

% plot Nichols chart
[m,ph]=dbode(num,den,T,w);
mdb=20*log10(m);

if (plotopt==1 | printopt==1),
    figure(case);
    plot(-180,0,'*',ph,mdb); grid;
    xlabel('PHASE (deg)'); ylabel('MAG (db)');
    title([' "cpfntab.m" p1= ',num2str(p1),' ps= ',num2str(ps), ...
        ' eq= ',num2str(eq),' case= ',num2str(case),' ',date]);
end

if (printopt==1),
    print -dps -append c:\cpfntab.ps
end

[gm,pm(case,1),wgain(case,1),wphase(case,1)]=margin(m,ph,w);
gmdb(case,1)=20*log10(gm);

p1vect(case,1)=p1; psvect(case,1)=ps; eqvect(case,1)=eq;
kpvect(case,1)=kp;

end % ii loop
end % jj loop
end % kk loop

disp('p1 ps eq KPpsv ');
[p1vect psvect eqvect kpvect]
%
%-----

```



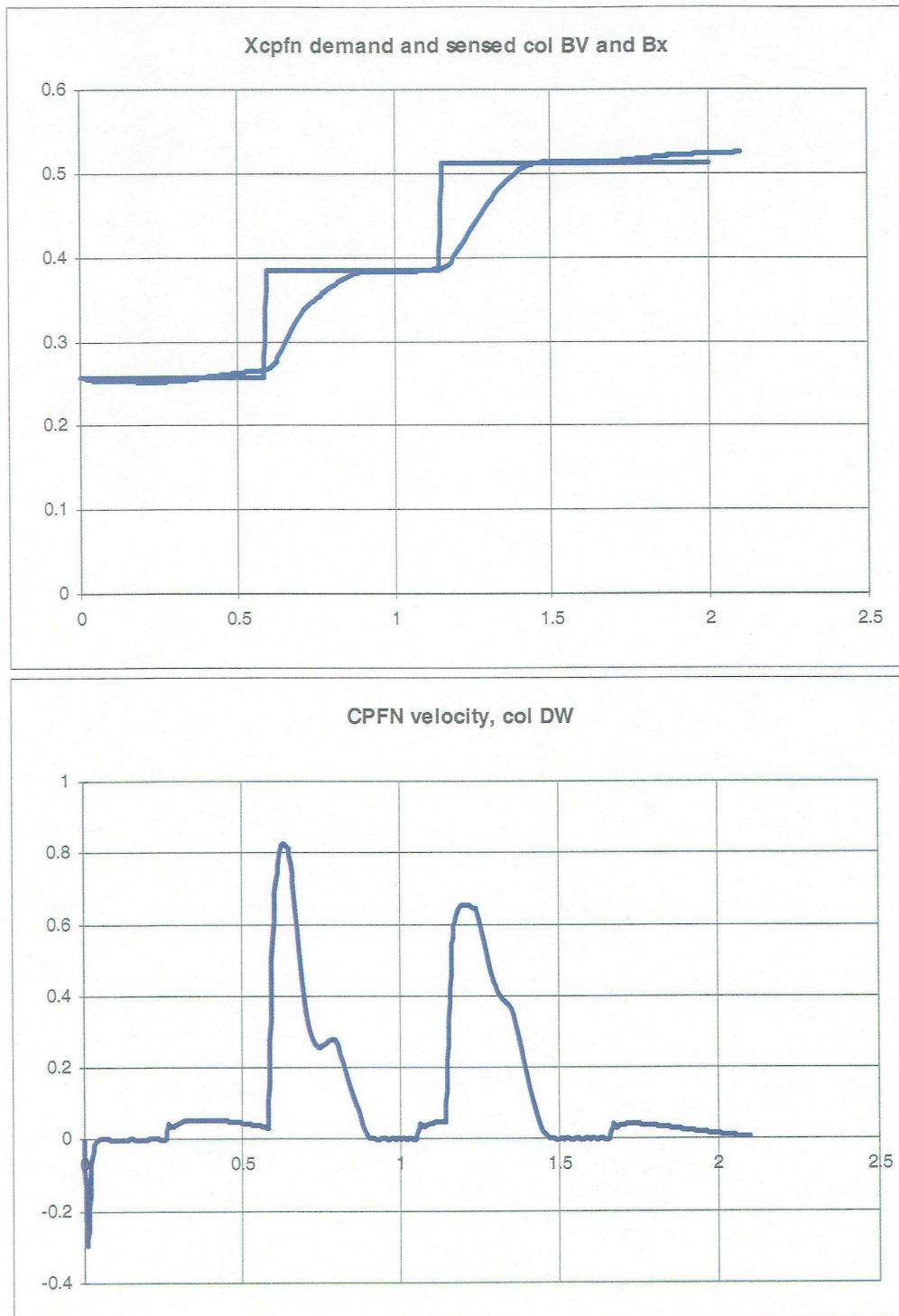


Figure B-1

Appendix B - Position Control with Breakaways, Stages 1 to 2

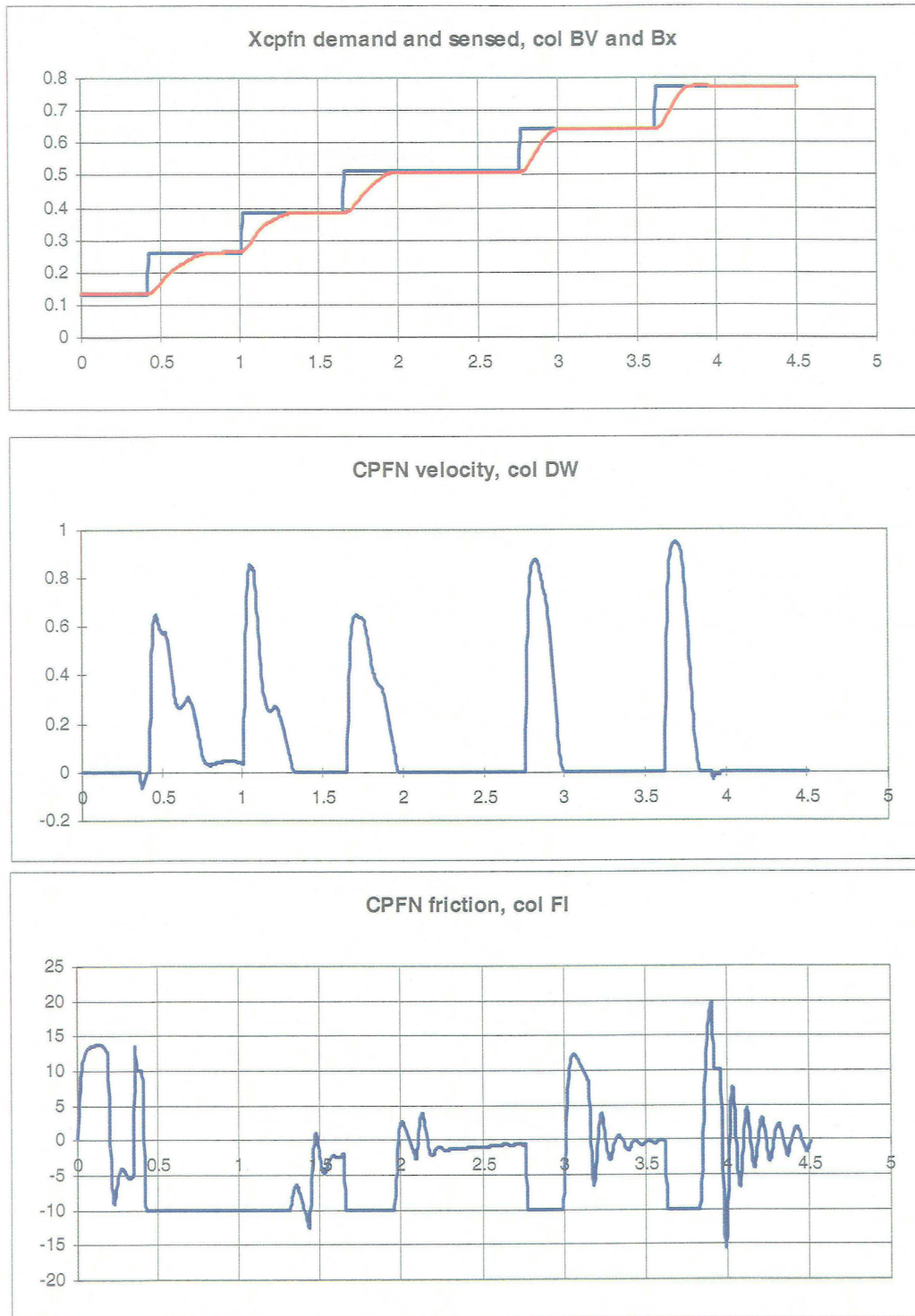


Figure C-1

Appendix C - Position and Pressure Control, Stages 1 to 6

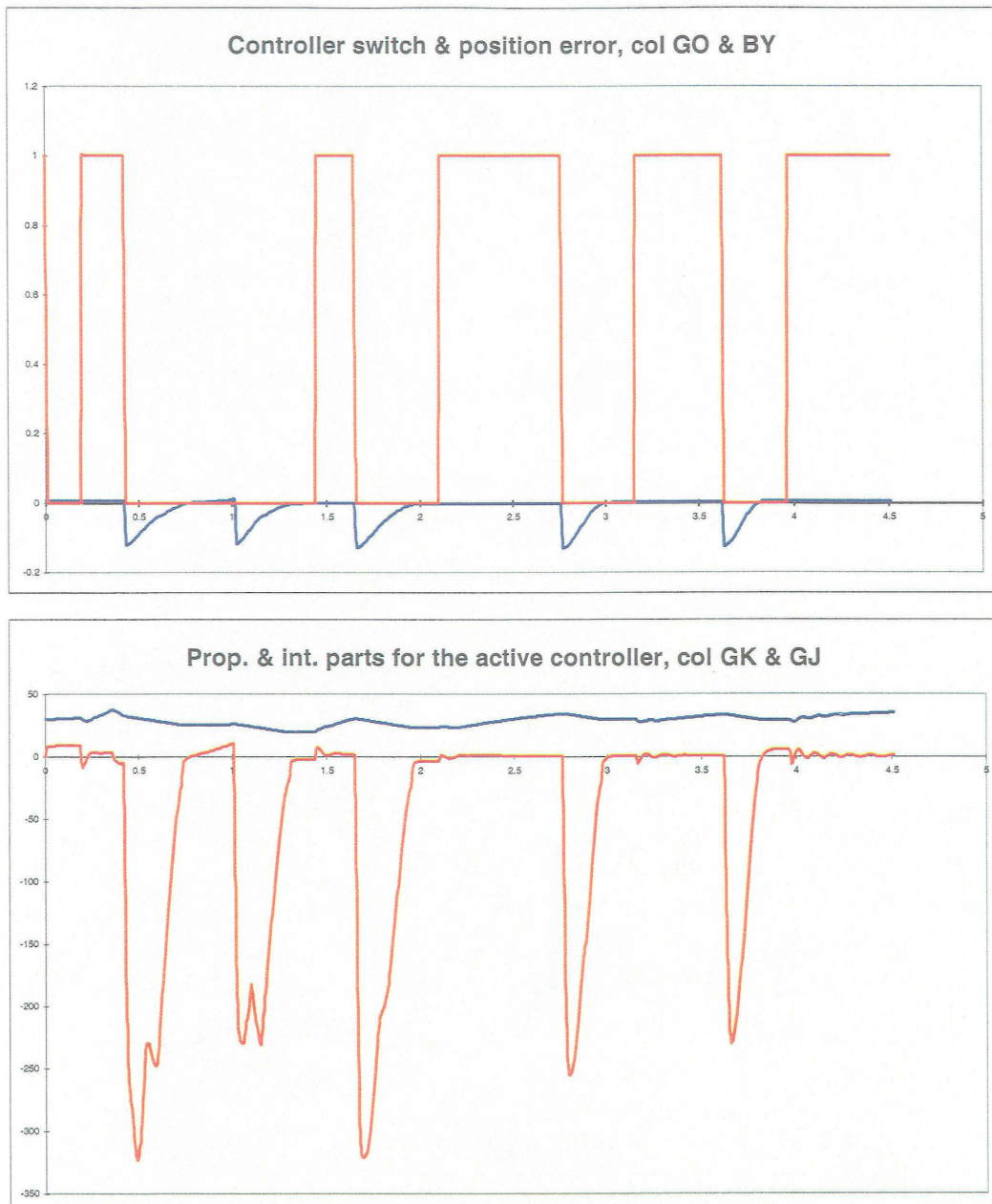


Figure C-2

Appendix C - Position and Pressure Control, Stages 1 to 6

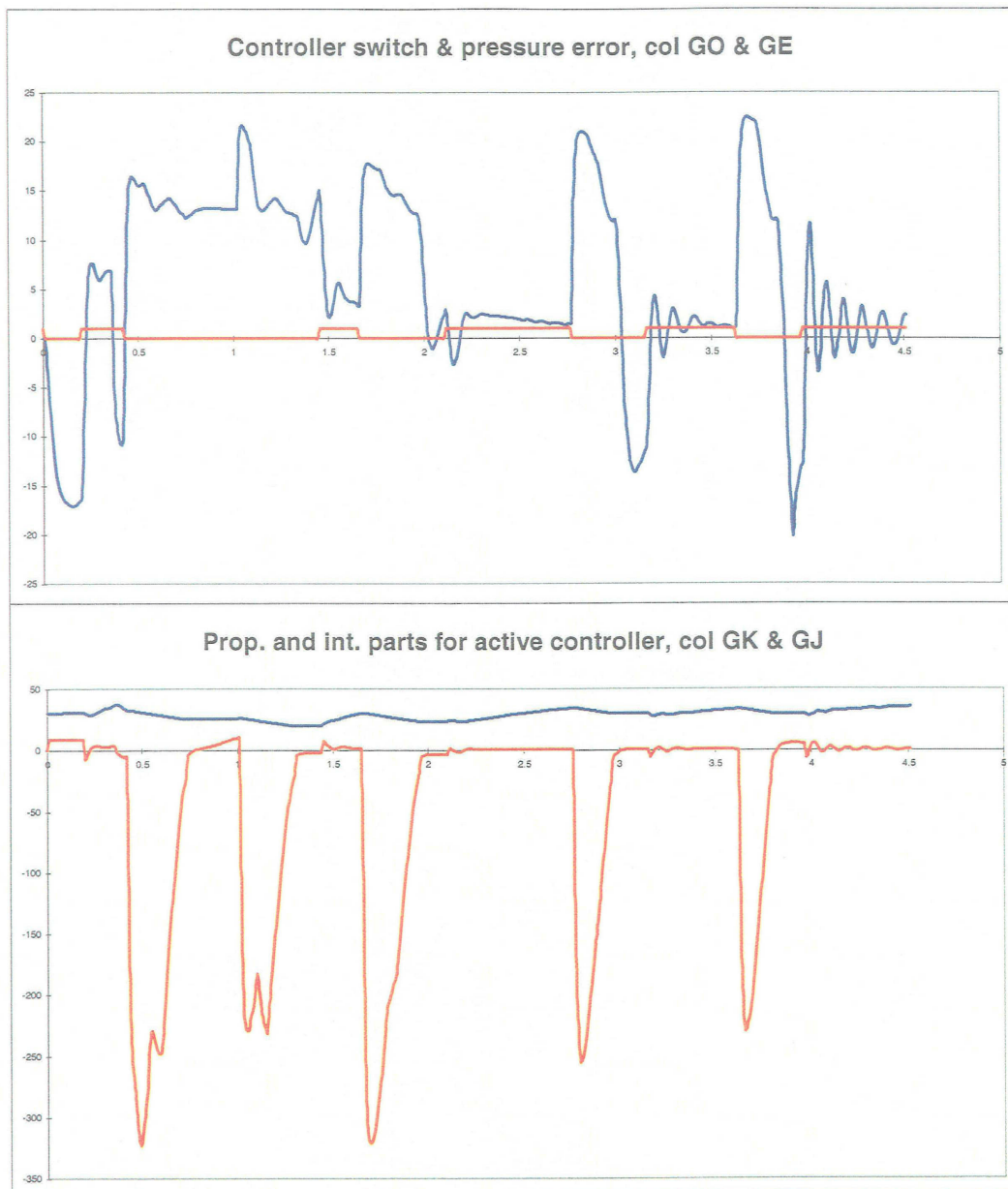


Figure C-3

Appendix C - Position and Pressure Control, Stages 1 to 6



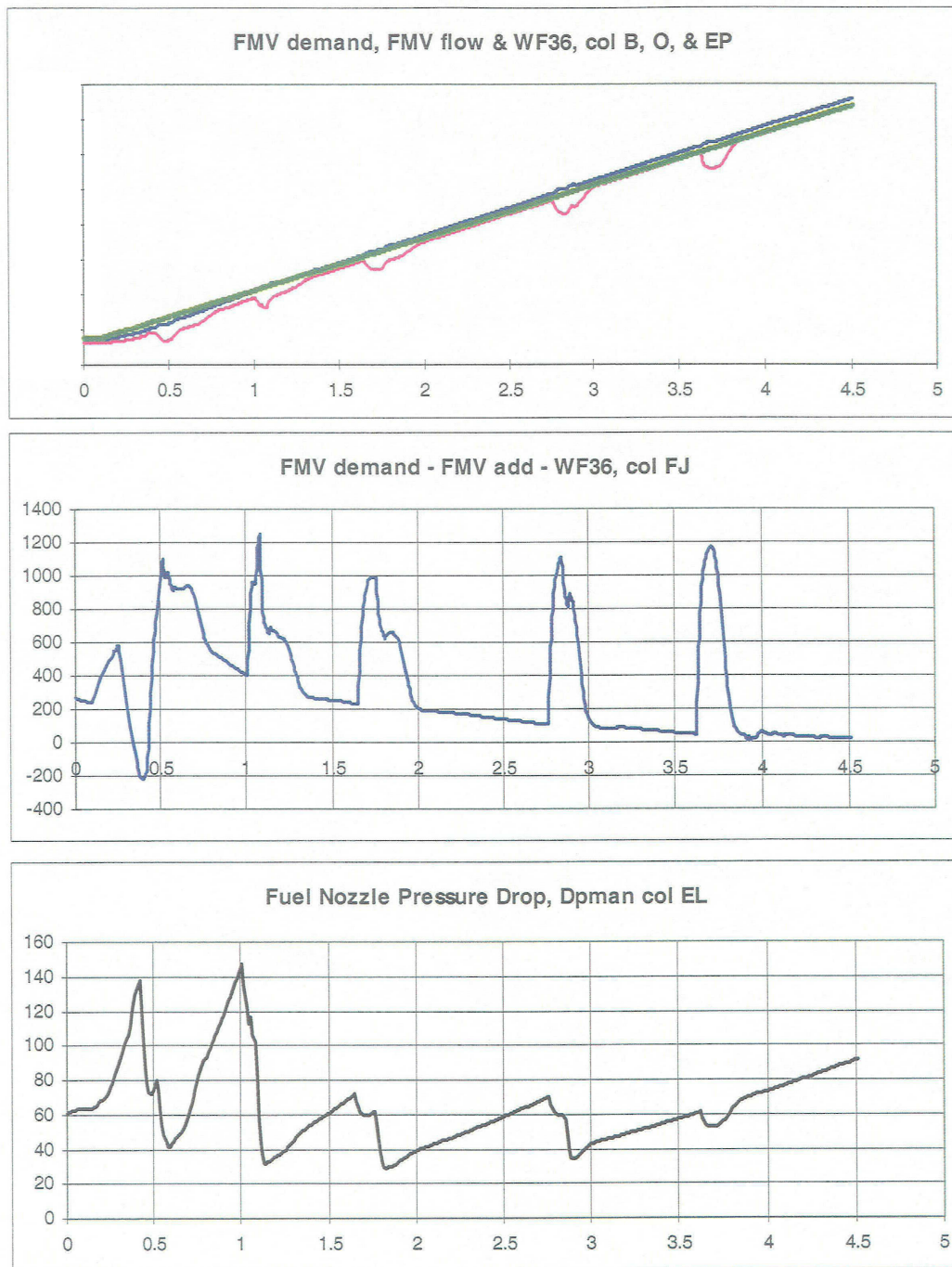


Figure C-4

Appendix C - Position and Pressure Control, Stages 1 to 6

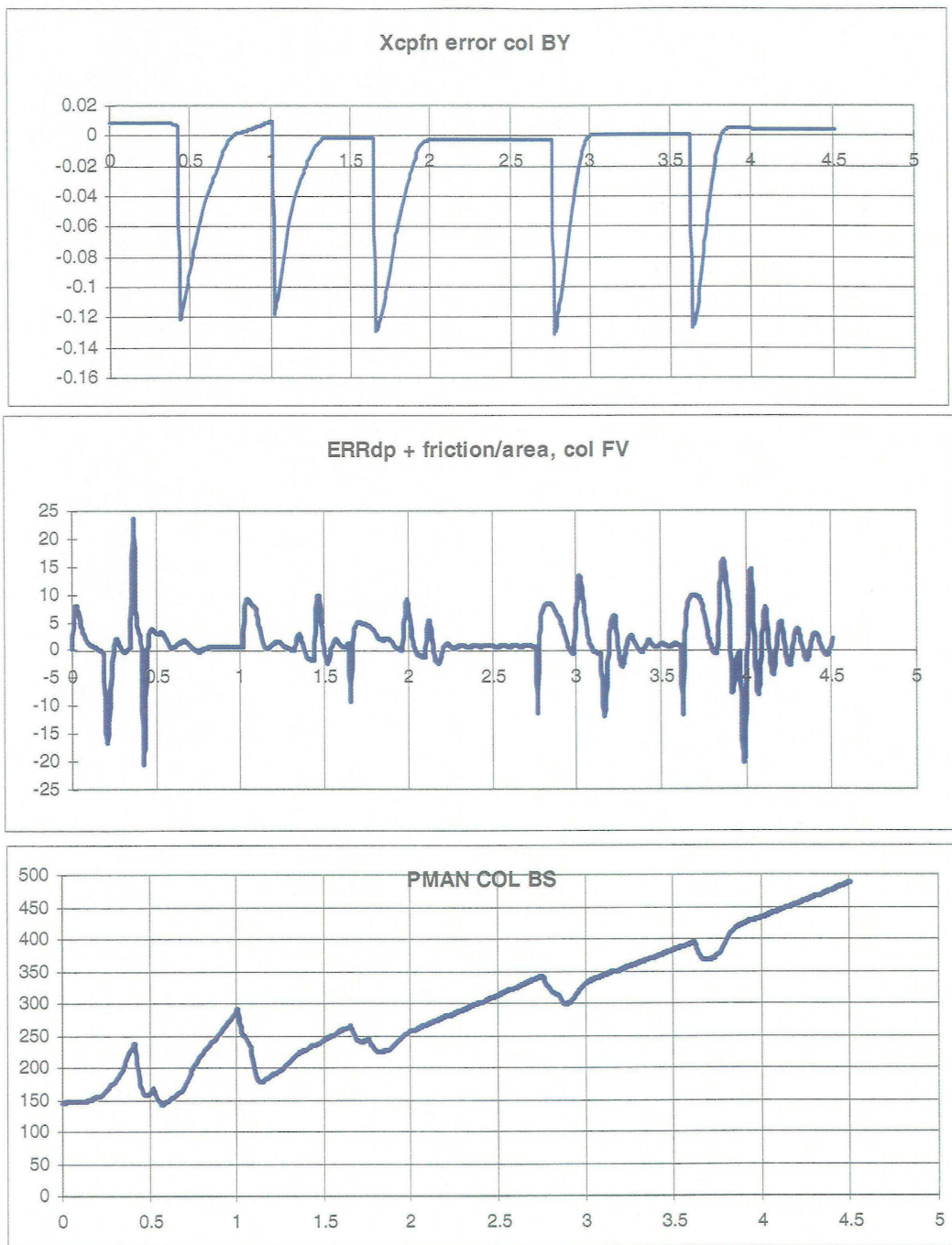


Figure C-5

Appendix C - Position and Pressure Control, Stages 1 to 6

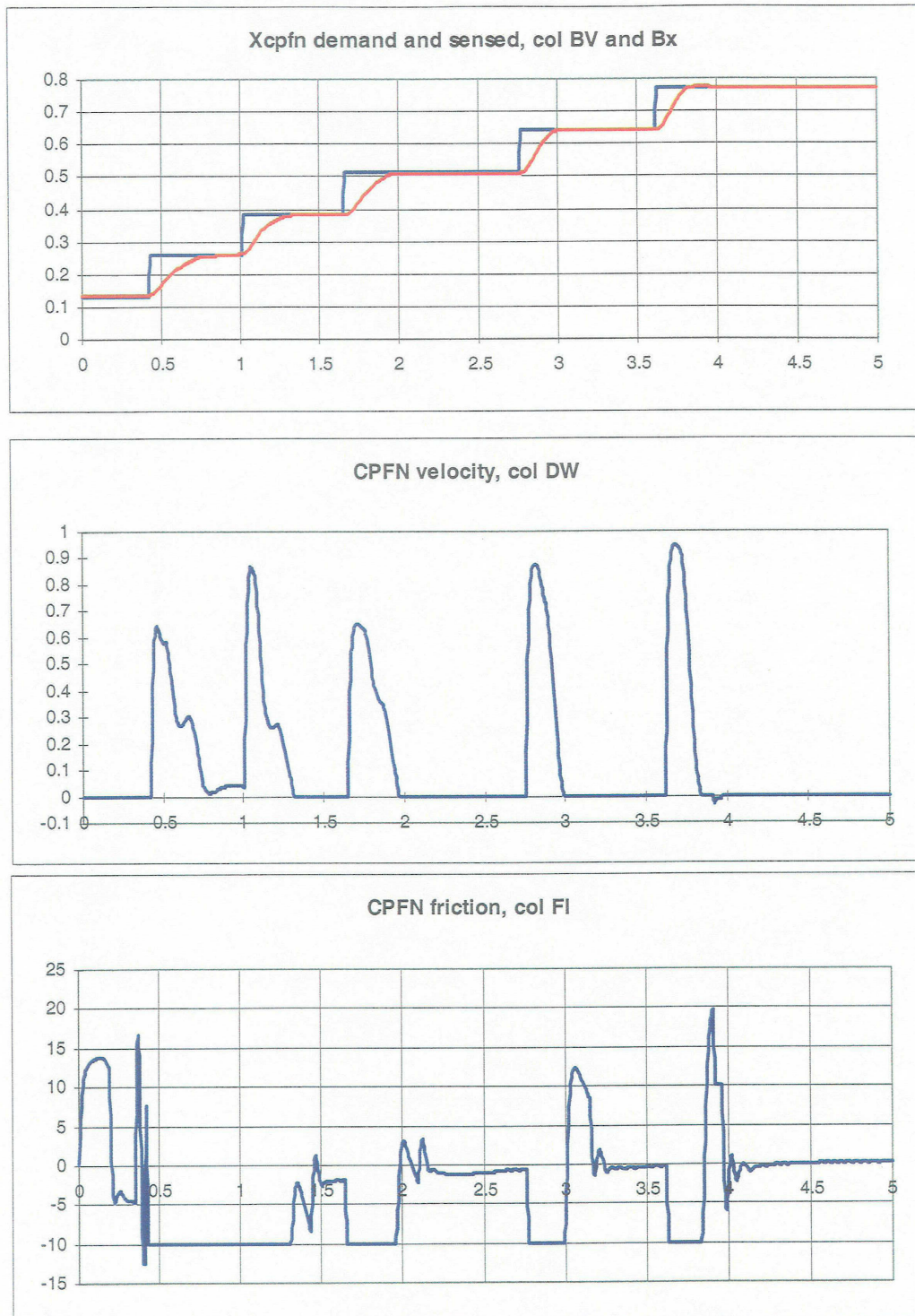


Figure D-1

Appendix D - Position and Pressure Control With High Bandwidth Pressure Transducer, Stages 1 to 6



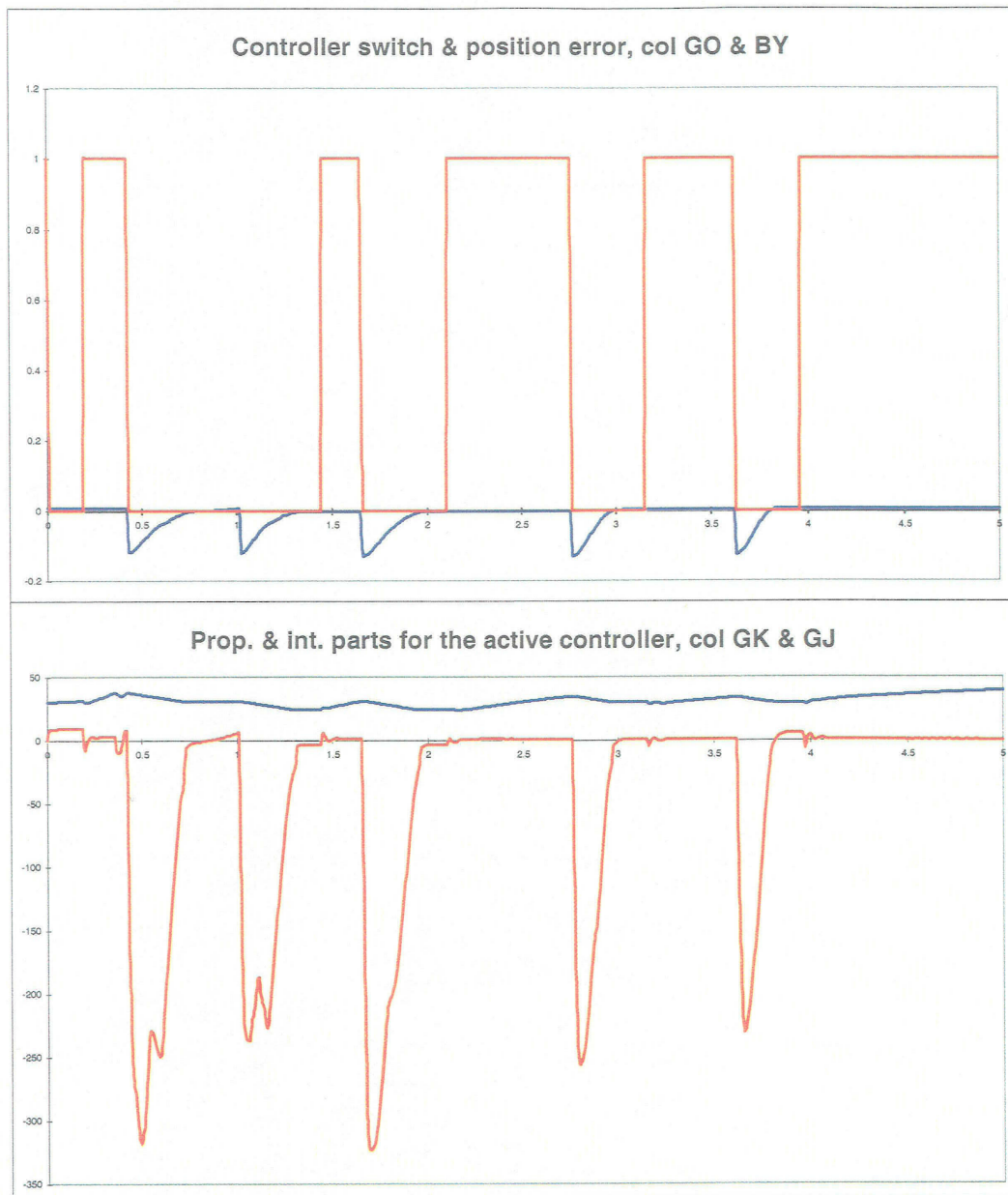


Figure D-2

Appendix D - Position and Pressure Control With High Bandwidth Pressure Transducer, Stages 1 to 6



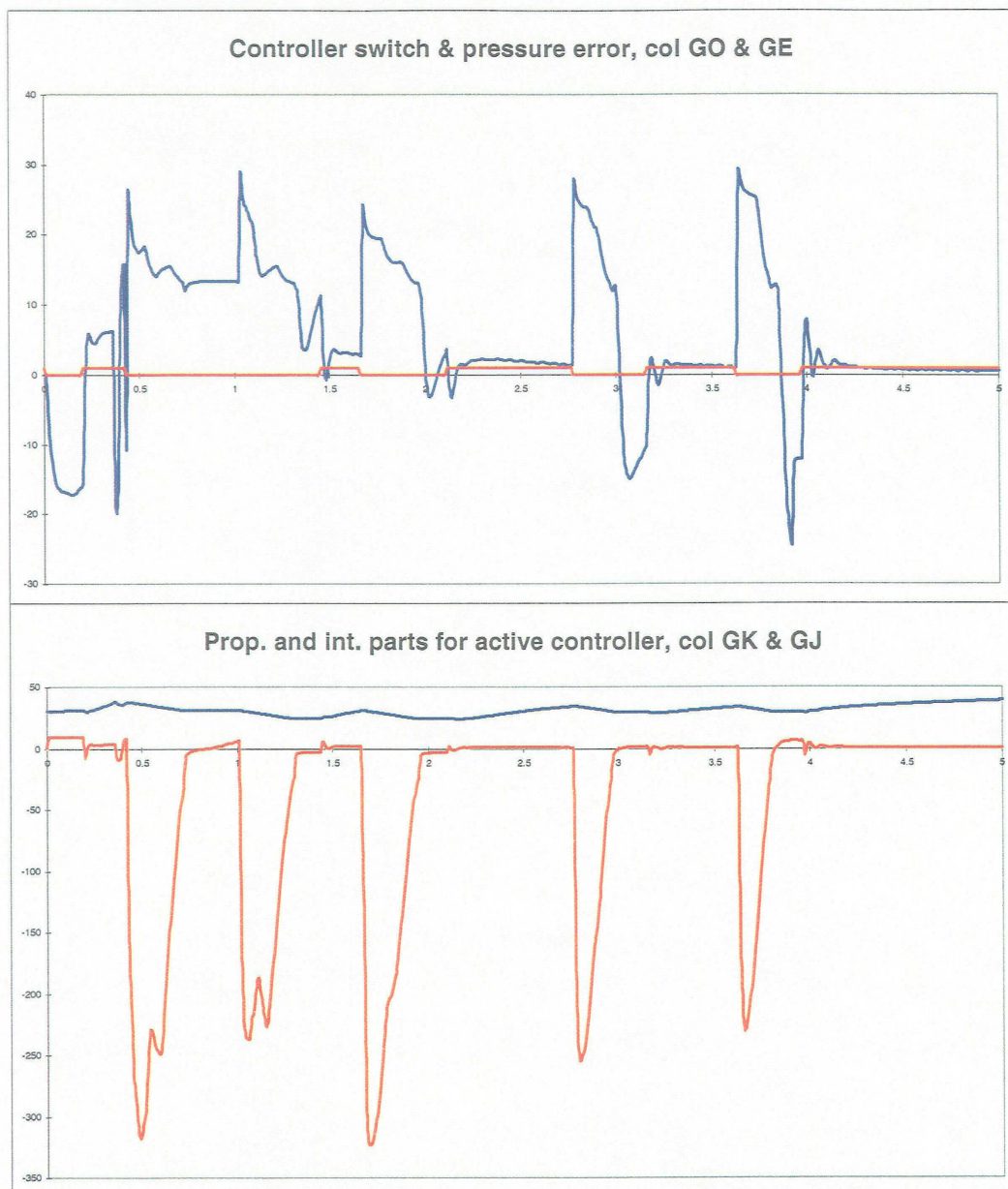


Figure D-3

Appendix D - Position and Pressure Control With High Bandwidth Pressure Transducer,  
Stages 1 to 6

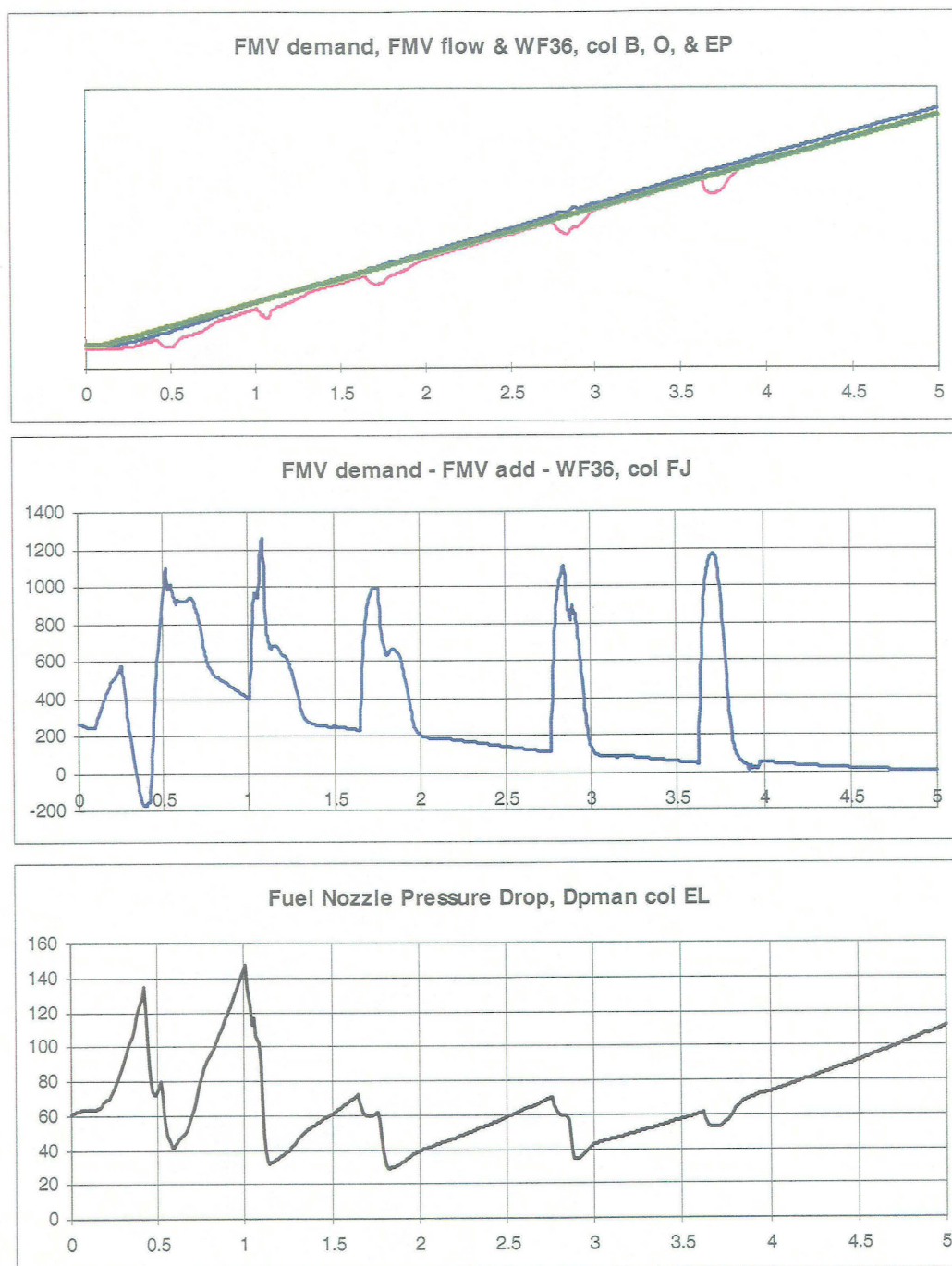


Figure D-4

Appendix D - Position and Pressure Control With High Bandwidth Pressure Transducer,  
Stages 1 to 6

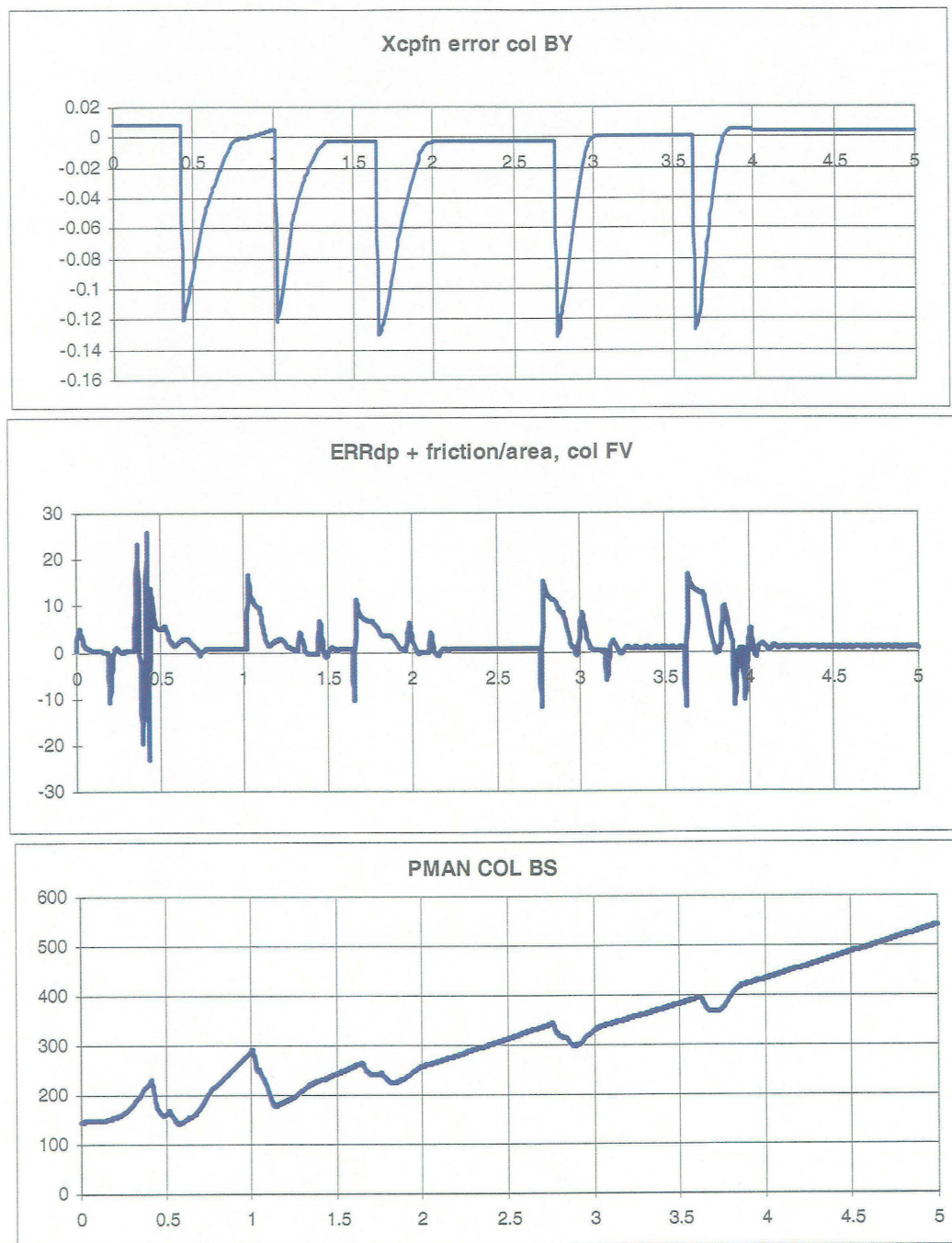


Figure D-5

Appendix D - Position and Pressure Control With High Bandwidth Pressure Transducer,  
Stages 1 to 6



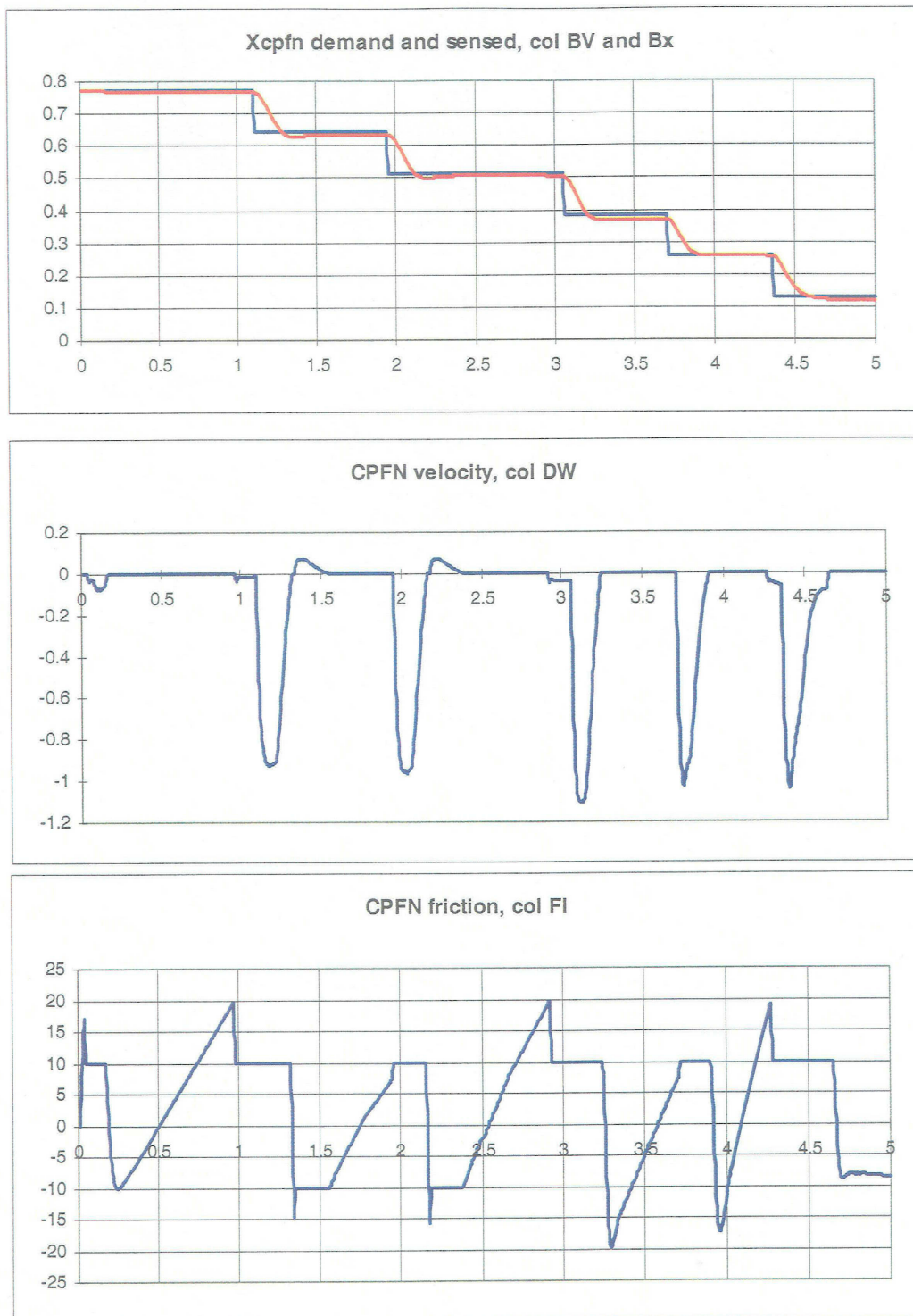


Figure E-1

Appendix E - Position Control With Decreasing Flow, Stages 6 to 1

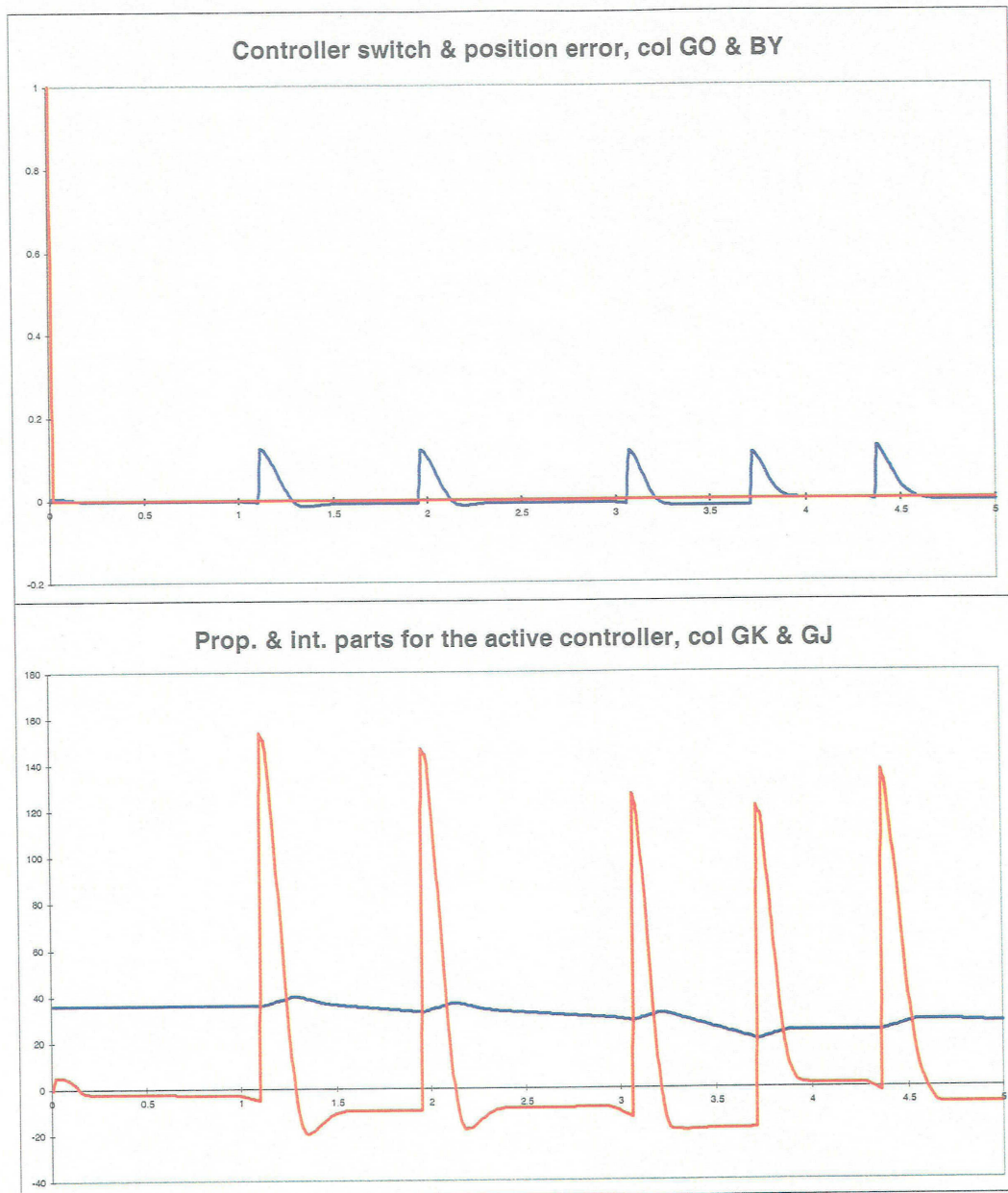


Figure E-2

Appendix E - Position Control With Decreasing Flow, Stages 6 to 1

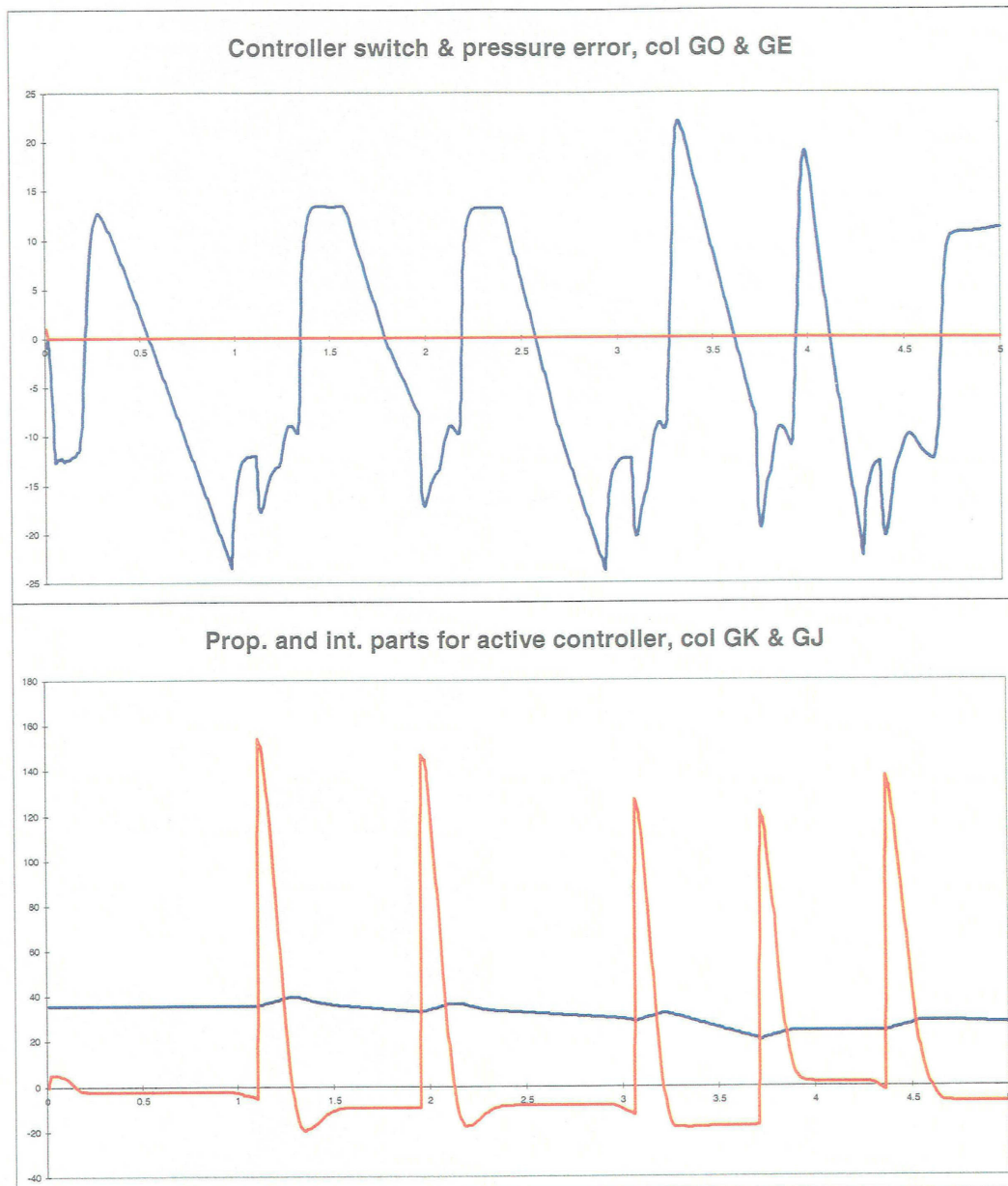


Figure E-3

Appendix E - Position Control With Decreasing Flow, Stages 6 to 1

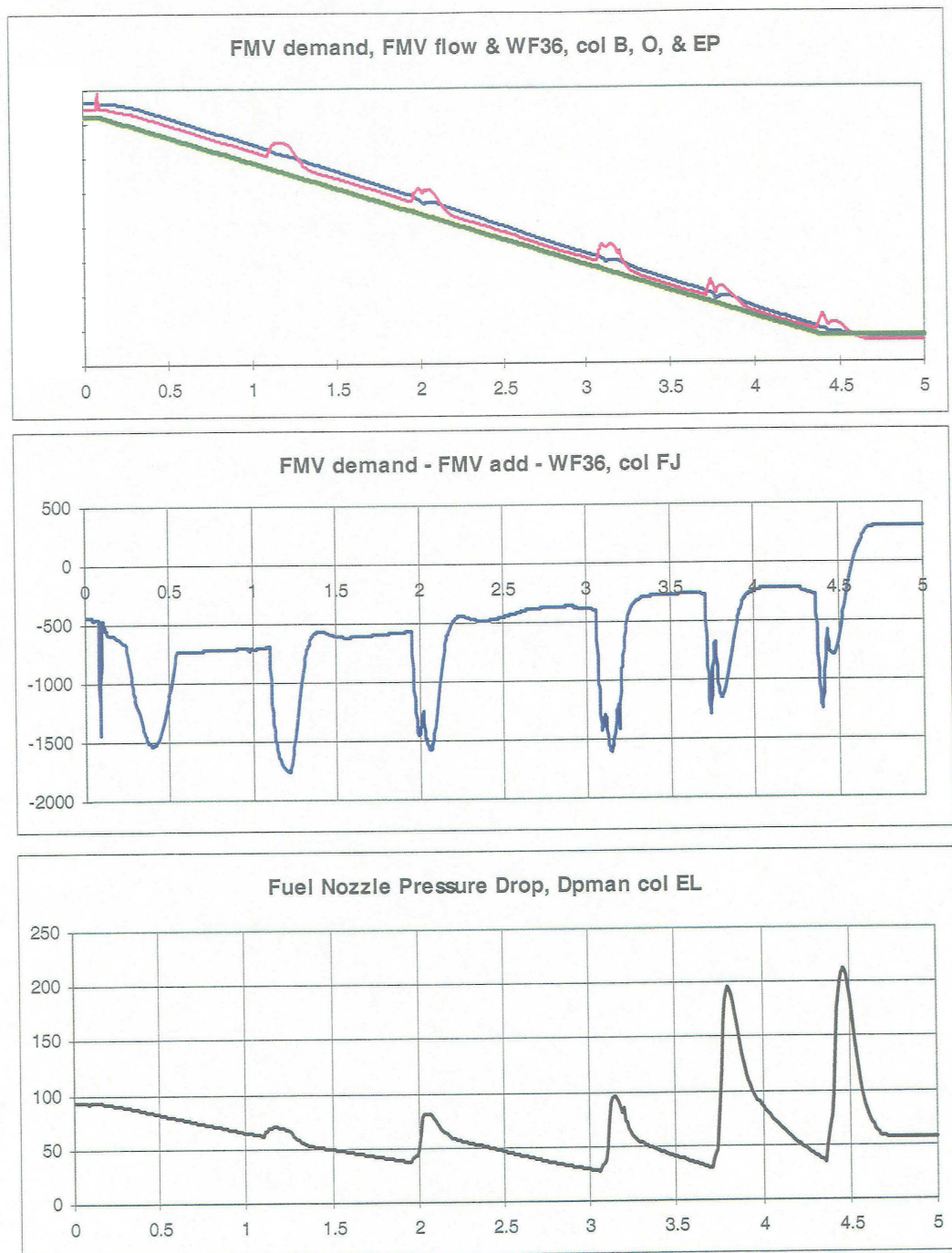


Figure E-4

Appendix E - Position Control With Decreasing Flow, Stages 6 to 1



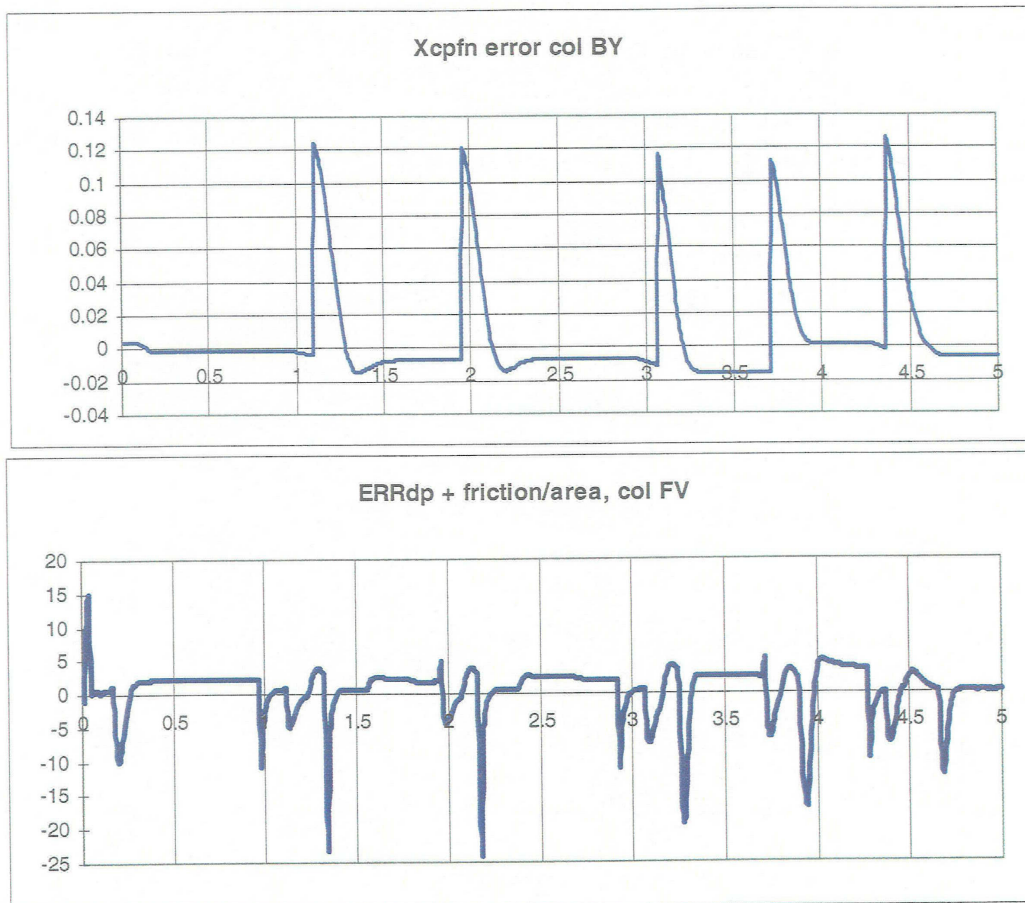


Figure E-5

Appendix E - Position Control With Decreasing Flow, Stages 6 to 1



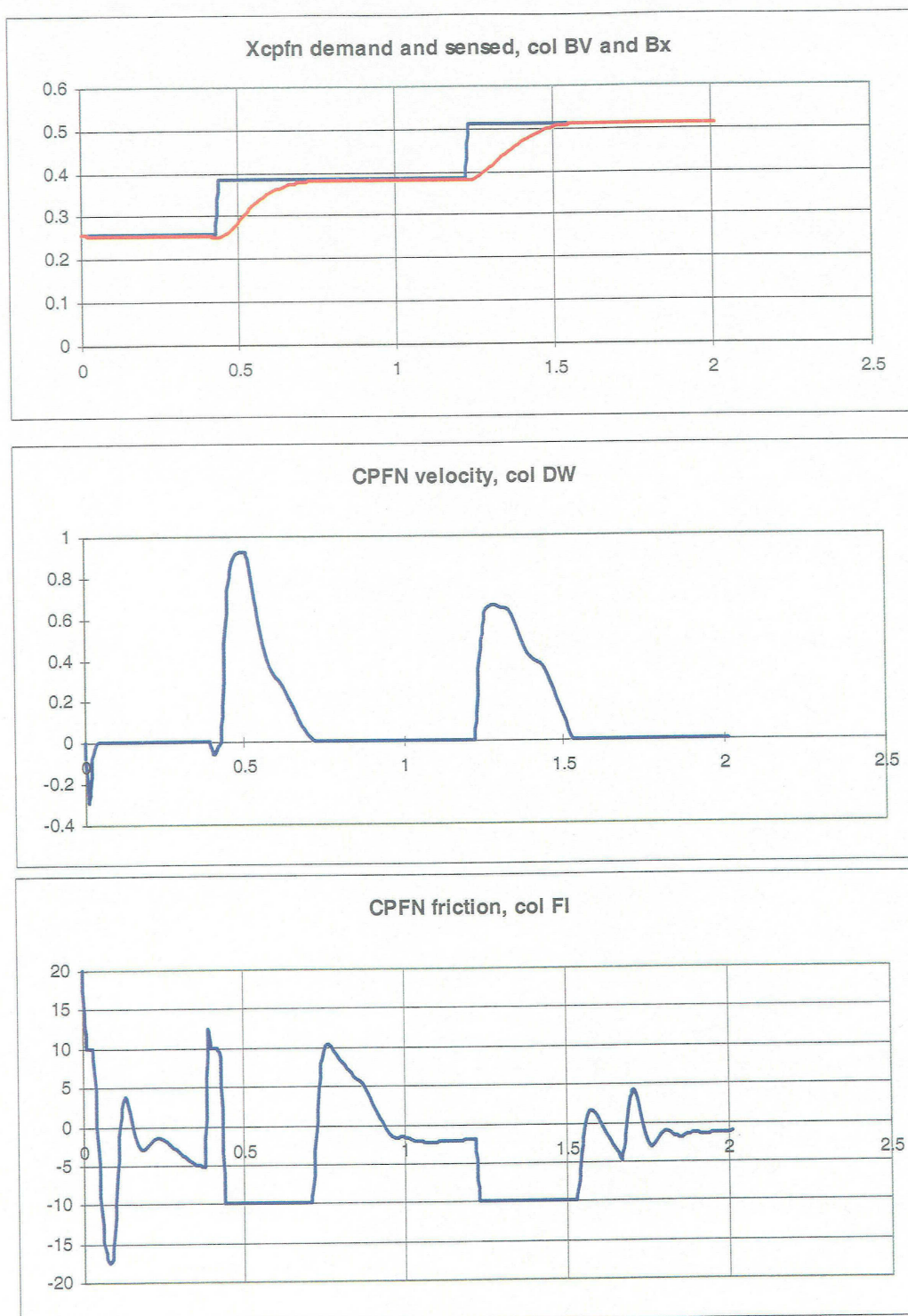


Figure F-1

Appendix F - Position Control With fuel Demand Modification, Stages 2 to 4

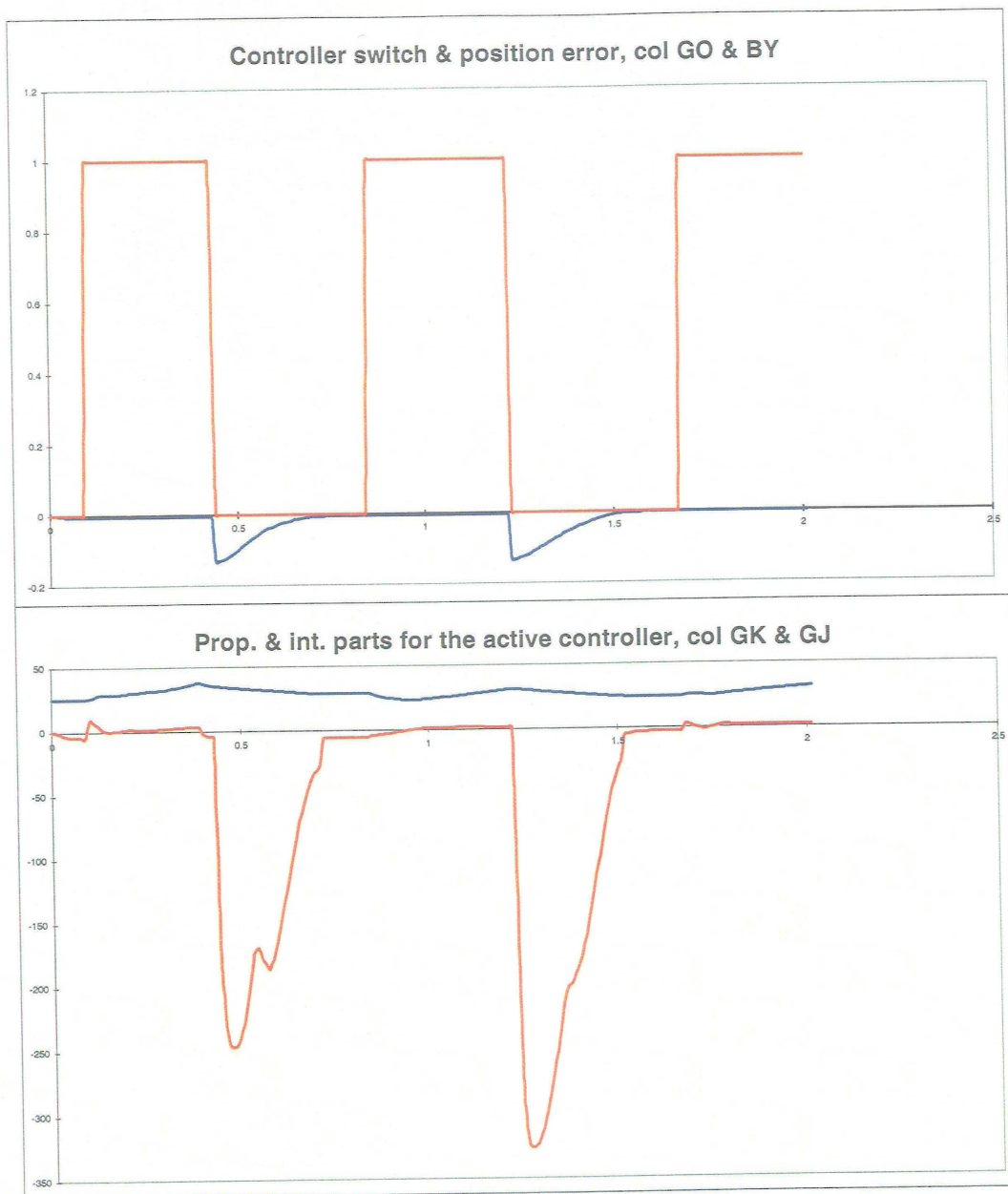


Figure F-2

Appendix F - Position Control With fuel Demand Modification, Stages 2 to 4

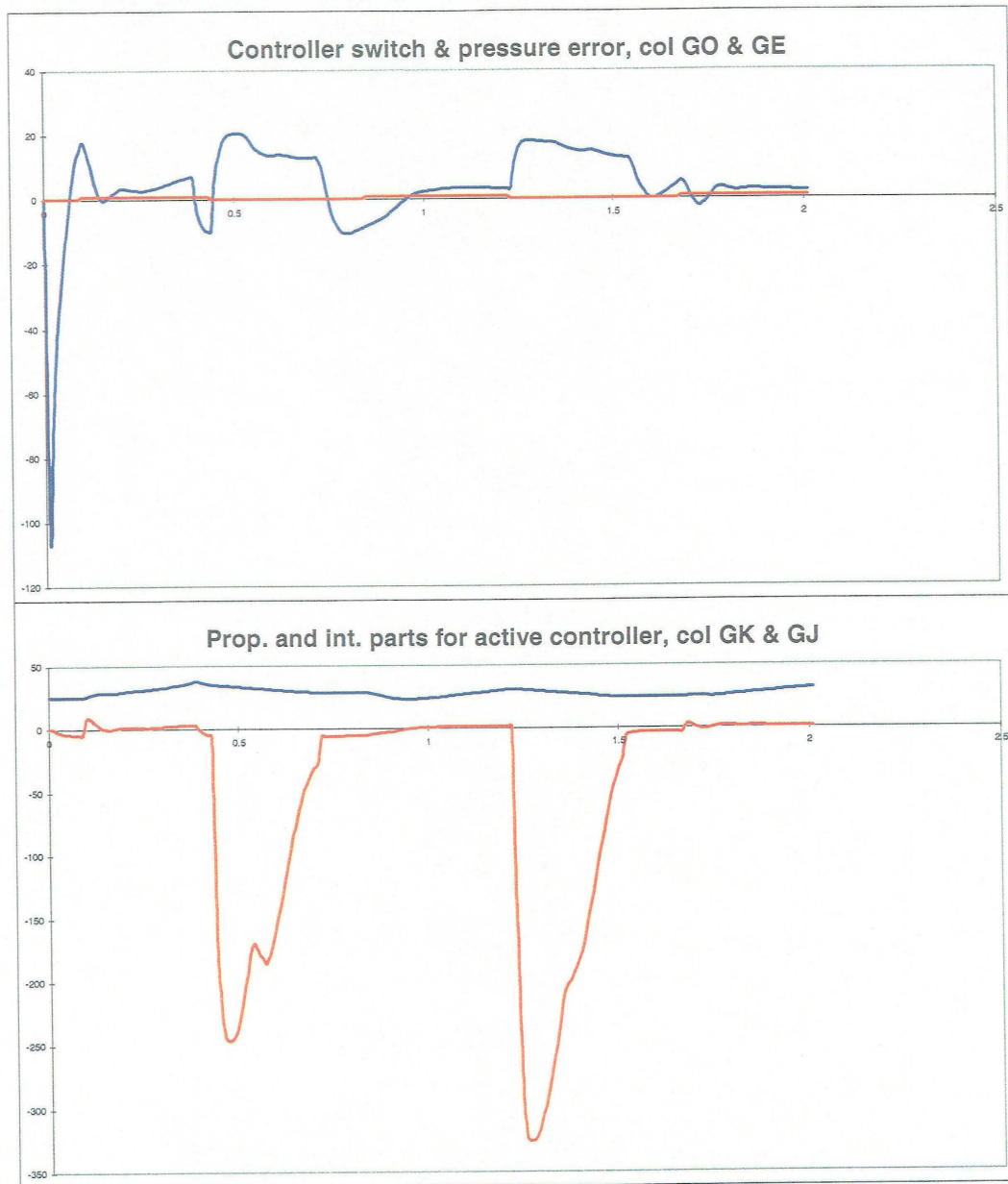


Figure F-3

Appendix F - Position Control With fuel Demand Modification, Stages 2 to 4

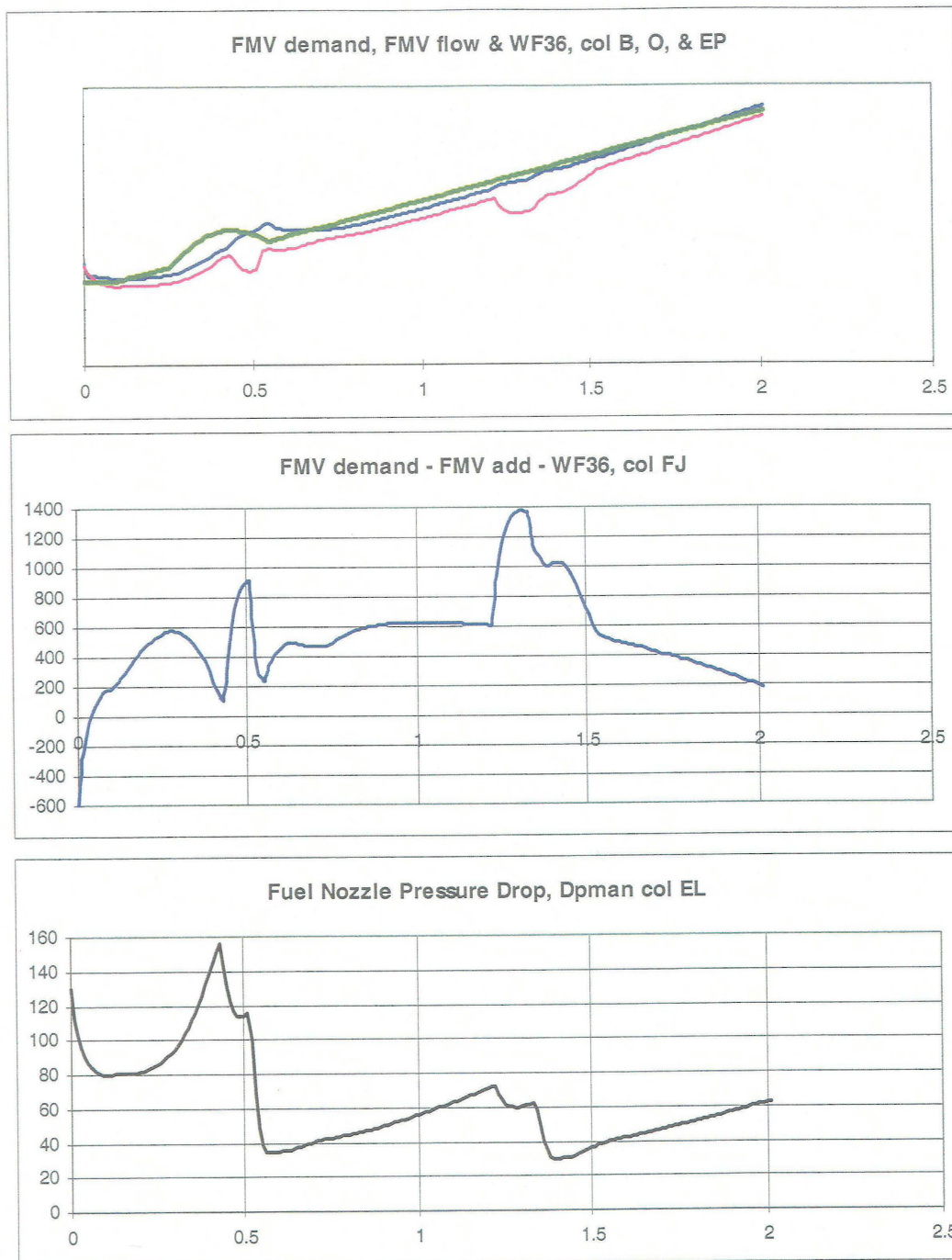


Figure F-4

Appendix F - Position Control With fuel Demand Modification, Stages 2 to 4



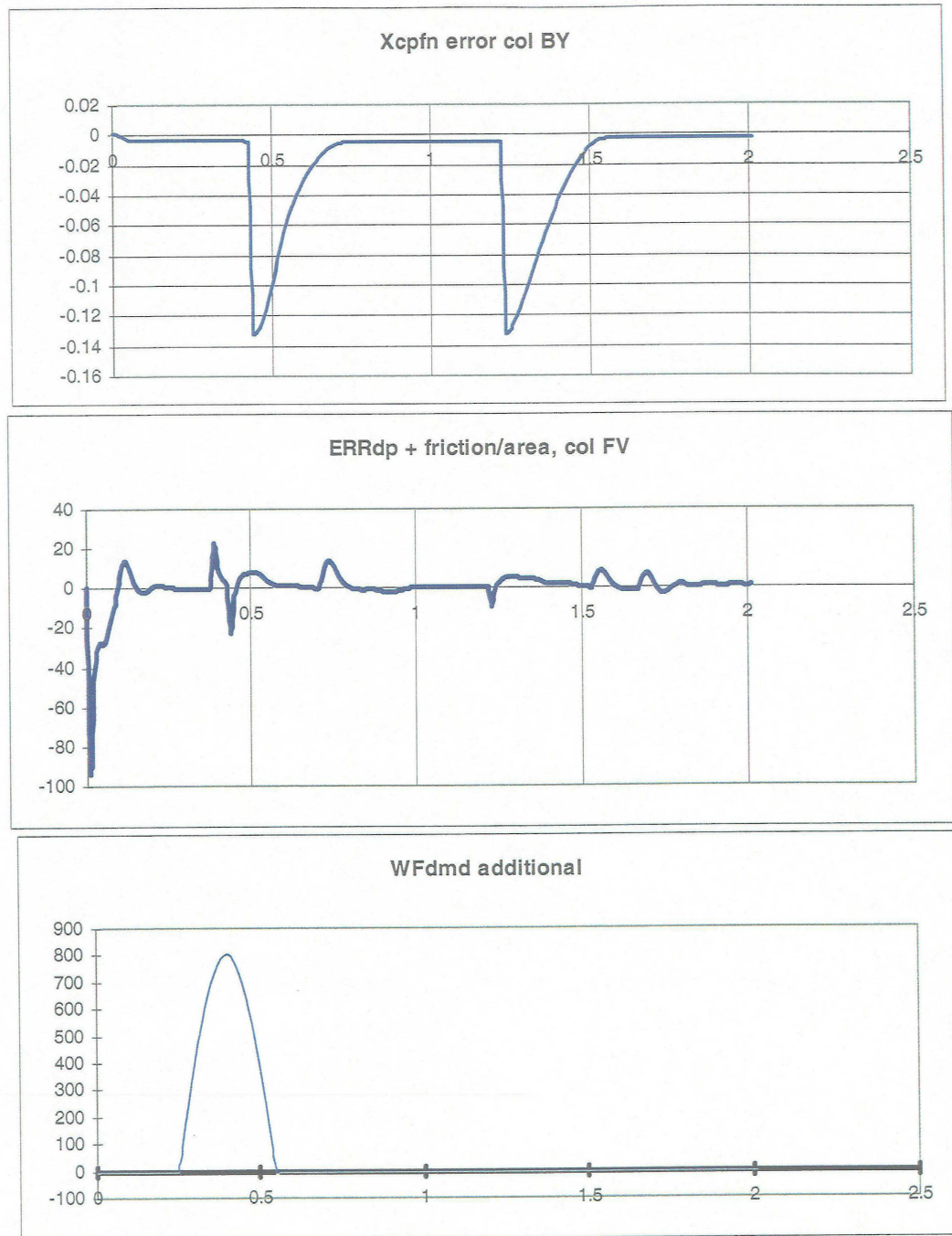


Figure F-5

Appendix F - Position Control With fuel Demand Modification, Stages 2 to 4

**Attachment III: Neural Networks for NO<sub>x</sub> Emission  
Prediction – Final Report**



# NEURAL NETWORKS FOR NO<sub>x</sub> EMISSION PREDICTION

May 26, 1999

**Prepared By:**

**Rick Lalonde  
Engineer  
Controls Group  
Analex Corporation**



## Introduction

The purpose of this work was to evaluate the efficacy of artificial neural networks (NN) for prediction of oxides of nitrogen produced by aeronautical or aeronautically derived turbine engines. The terminology “oxides of nitrogen” covers both nitric oxide (NO) and nitrous oxide (NO<sub>2</sub>) and is denoted by the formula NO<sub>x</sub> where x is a variable. The usefulness of the NNs should be determined mostly by their prediction error, however, complexity and ease of prediction are also important. The prediction of the NNs is compared here to the prediction errors of the previous prediction standard: empirically derived exponential models.

The data available for this phase of the work is from two engine tests of two different LM6000 engines fueled by natural gas. In each data set there are 36 inputs and 6 outputs. These are listed in Appendix A. The inputs are mostly temperatures, pressures, and flows. The outputs are the raw and adjusted values of NO<sub>x</sub>, carbon monoxide, and unburned hydrocarbons. The only output considered for this work is NOX15, the adjusted NO<sub>x</sub> value.

Goals of this work were to

- 1 Evaluate different NN structures and training methods and determine a structure and training method that will work well for predicting NOX emissions.
- 2 Determine how many neurons are needed to get good prediction results.
- 3 Determine how large the data set needs to be to train the network effectively.
- 4 Make the prediction error small.

The main goal is to generate one model that is good for all LM6000 engines that meet the design specifications. Therefore, the model should perform well on LM6000 engines that it has not been trained with. Good performance only on the engine used for training is not considered sufficient.

## NO<sub>x</sub> Measurement Error and Surface Roughness

The NN can not be expected to produce a model with an error smaller than the error of the output that was given to it during training. For this reason, it was desired to estimate the sensor measurement error. The error was estimated in the following manner.

The inputs were normalized and for each operating point in the data set, the point with the closest input vector was determined. A plot was then made of the change in the value of the output as a function of the distance between the input vectors. If two inputs exist that produce different outputs, then a pathology exists and maybe caused by one of the following: the input set does not contain all of the necessary inputs (that affect the output), or the actual outputs are the same and the sensor error causes the sensed outputs to be different. For data set 112, there were no pathological points when all of the inputs were used, see Figure B-1. In fact, in Figure B-2, a subset of six inputs is shown not to have any pathological points. For lack of a better name, these plots will be referred to

here as roughness plots as the variation of the points at a particular distance show the roughness of the output surface over the input.

When two straight lines are drawn to represent the top and bottom of the envelope of points on the roughness diagram, they become closer together as they move from right to left. The distance between the lines at the left is an estimate of the sensor measurement error. For data set 112 this error seems to be conservatively less than 0.5 PPM for NO<sub>x</sub>.

## Theoretical Equations for NO<sub>x</sub> Production

According to [1], oxides of nitrogen can be produced in gas turbine engines by at least four different mechanisms: Thermal NO, the Nitrous Oxide Mechanism, Prompt NO, and Fuel NO. Balanced chemical equations are listed in that reference. However, the amount of production of the oxides of nitrogen by these four mechanisms depends on the fuel, the type of fuel atomization, the droplet size, temperatures at various stages, pressures at various stages, the equivalence ratio, the residence time, etc. Because of all of these factors, the determination of a set of equations for the amount of NO<sub>x</sub> produced is currently, nearly intractable, even for a specific engine. To date, researchers have modeled the amount of NO<sub>x</sub> with equations using a subset of the above factors. The constants in the equations have been determined by curve fitting and regression techniques. This paper considers two classes of models. The first class consists of models in which the NO<sub>x</sub> is an exponential function of temperatures. The second class of models is artificial neural network models.

## Single Input Exponential NO<sub>x</sub> Model

NO<sub>x</sub> is plotted versus TFLPDF for data set 112 in Figure D-1. (This plot contains only the points for BRNDMD=15.) Since the data for a single combustion chamber is expected to be exponential, this plot was expected to have an exponential relationship with additive “noise” due to, at the least, the inner and outer flame temperatures. By inspection an exponential curve can be drawn through some of the data starting at about (3100,16) and ending at (3450,60). Points were chosen along this path every 50 degrees and then were curve fit to the equation

$$\text{NO}_x \cong e^{(a \cdot \text{temp} + b)}$$

The fit resulted in the values of  $a=0.004016$  and  $b=-9.7333$ .

## Three Input Exponential NO<sub>x</sub> Model

General Electric’s Aircraft Engine (GEAE) Division has a NO<sub>x</sub> prediction model for the LM6000 engine. The model is

$$\text{NO}_x \cong (1 / \sum(\text{wp}(i))) \sum \text{wp}(i) e^{(\text{cp}(i) \cdot (\text{tfl}(i) + \text{dtflp}(i)) + \text{mup}(i))}$$

where:

tfl(1) = outer flame temperature

tfl(2) = pilot flame temperature

tfl(3) = inner flame temperature

wp(i) = flow fraction for outer, pilot, and inner, respectively

## **Regularization and Enhancing Performance**

Neural nets are generally thought to be very capable of producing targets close to those of the training set. (The set of untrained inputs and outputs is often referred to as the complimentary set.) Unfortunately, this is no guarantee that the nets will produce good outputs in response to inputs they have not seen. This can be attributed to several causes. One is that the training set is not sufficiently large, so that the inputs in the complimentary set are more like extrapolations of the training set than interpolations. The second reason also has to do with training sets that are not large enough. If the number of parameters of the net is roughly the same size or larger than the number of inputs, then the network can “overfit”. Sometimes overfitting is so apparent that the error on the training set is practically zero, while the error on the complimentary set is very large because the model has severe fluctuations between the points in the training set.

A net is said to regularize well if the errors on the complimentary set are not much larger than those of the training set. Therefore, regularization is a property that is desired of most networks.

For this particular application (gas turbine engines), the training set could be data from one engine and the complimentary set could be data from the same engine. In this case, training of the NN could happen before the unit is sold. The training set could also be data from a test or reference engine and the complimentary set could be data from other engines. For either of these cases, the most important set to perform well on is the complimentary set. That is why this analysis focused heavily on reducing the prediction error of the complimentary set by reducing overfitting and by providing good generalization. Making the prediction error of the training set small, by itself, is of little value.

Early stopping and using a validation set are two ways to avoid or reduce overfitting. They will be described briefly below, followed by two techniques and a network architecture that were developed to provide good generalization. There are many papers in the literature on techniques for regularization and to avoid overfitting. The ones presented here are a subset of those that the author used for this task.

### **Early Stopping**

The most simplistic approach to avoid overfitting, other than to select a small number of neurons, is to train the network for a small number of epochs. (training for one epoch means to present the training set to the network only one time). The hope is that with just

a few epochs, the net will learn the input/output relationship relatively well, but will not fit the noise in the training set.

### Validation

Another common practice to avoid overfitting is to split the data into three sets: a training set, a validation, and a complimentary set. As the network is being trained, calculate the prediction errors for both the training and complimentary sets. The error of the training set will often be monotonically decreasing. When the error of the validation set starts to increase, then save the network parameters from when the validation set had the minimum error. The network is then tested on the complimentary set as usual.

### Training with Bayesian Regularization

Another way to avoid overtraining and improve generalization is Bayesian Regularization (BR). This training algorithm is a modified version of the Levenberg-Marquardt algorithm in which the error function has an added term which is the sum of the squares of the network parameters. This added term places a penalty on the parameters as well as the prediction error. Thus as the network is being trained there is a trade-off between error of the training set and the size of the parameters. This reduces the effective number of parameters (i.e. effective size) of the network, thereby reducing the probability of overfitting.

### Radial Basis Networks

There are two main types of radial basis networks: exact and inexact. The exact networks have exactly zero error on the training set because they have as many neurons in the input layer as data points in the training set. This is a severe drawback, but they generalize well do the architecture of their first layer. In the first layer, the input vector is compared to a vector stored in each neuron (these vectors comprise the radial basis). The distance between the input vector and the stored vector is computed. If the distance is zero, the output of the neuron is one, otherwise it is positive and less than one. Therefore, the neurons in the first layer only respond well to input vectors close to their stored vector. The second layer takes a weighted average of the targets of the first layer by using the outputs of the first layer as weights.

The inexact radial basis networks have the same architecture as the exact radial basis nets, but fewer neurons. This causes them to have non-zero error on the training set, but they generalize well again because of their first layer.

### Input Jitter

Another technique to produce a net that will generalize well is to add jitter to the inputs. This is done by taking each input of the training set and making “n” copies of the input each with additive (and independent) noise. For each artificial input use the exact same output that the real input had. The new training set will be (n+1) times the size of the original set. This will force the network to be relatively smooth around each of the inputs

in the training set, thereby providing better regularization. If several of the artificial inputs are very close together, then the network will generally produce an output for that region of input space that is close to the average of the outputs in that region. Since it is a goal to have many more data points than parameters in the net, these artificial points are often sufficient to meet the goal.

## **Generalization Techniques Applied to the LM6000 Engine Data**

All five techniques described in the previous section to reduce overfitting and improve generalization were used in moderately thorough tests with the available engine data. The best results were obtained using input jitter and the Bayesian Regularization training method together. Therefore, only results obtained by using these two methods will be presented in this report.

### **Calculated Pilot Ring Flame Temperature for Data Set 112**

The data set for engine serial number 112 has four burner demands: 0, 15, 25, and 40. Figure D-1 shows the adjusted NO<sub>x</sub>, NOX15, for a burner demand of 15. The raw data is plotted with asterisks. It is seen that much of the data can be fit reasonably well to a curved line. The curved line in the plot is  $NO_x \cong e^{(a \cdot \text{temp} + b)}$  with  $a=0.004016$  and  $b=-0.73333$ . Since the points in the upper left portion of the graph are not approximated well by the curved line, the validity of the calculation for the pilot temperature became a small concern. The calculated pilot flame temperature is not a measurement, but is an estimation, like the other calculated flame temperatures. They are based on the demanded inner and outer ring flame temperatures and other variables. Therefore the relationship between NOX15 and the pilot temperature is only as good as the calculation of the pilot temperature.

Figure D-2 shows the demanded and calculated inner ring flame temperatures for burner demands of 15 and 40. For burner demands of 15, it is seen that some of the predicted data points are far from the demand. This does not necessarily mean that the prediction is inaccurate. (Since the actual flame temperatures can not be measured in a practical manner, the accuracy of the calculation can only be inferred here and can not be determined.) To see the effect of this difference between the demanded and calculated data points, the calculated temperatures above the line in Figure D-2 were adjusted by 120 deg F, creating plots D-3 and D-4. Figure D-3 shows the demanded and calculated inner ring flame temperatures after this modification. Figure D-4 shows the values of NOX15 versus calculated pilot ring flame temperatures with the modification to them. They were shifted 120 deg in the opposite direction, thereby keeping the average (and sum) of the flame temperatures the same before and after modification. The plot of NOX15 versus pilot flame temperature is much more like an exponential curve now. The relationship between NOX15 and the pilot temperature seems to be exponential with corrections for factors other than the pilot temperature.

## Results for Data Set 112

As a baseline for determining the usefulness of the NNs, the standard deviations (SDs) and means of the errors for the exponential models were calculated for Data Set 112. These are listed in Tables 1 and 2 for the raw data set and in Tables 3 and 4 for the data set with the previously mentioned modification of the calculated flame temperatures. The parameters for the three input exponential model were based only on a burner demand of 40. This is why the table does not have entries for other burner demands for this model. The column labeled "ALL" designates all four values of the burner demand. It is seen that the modification of the calculated flame temperatures, for the burner demand value of 15, reduces the SDs of the error of both exponential models. This lends credibility to the modification.

Results using a feed-forward NN with input jitter and the Bayesian Regularization training method are shown in Appendix E. Figure E-1 shows the SDs of the error of the training and complimentary sets versus training size. To make this graph, Modified Data Set 112, which has 179 operating points, was randomly ordered. Then the first 20 points were used as a training set and the last 159 as the complimentary set. After this, the first 30 were used as the training set. Therefore, 20 of the operating points were the same as the previous run. This was then completed until 160 points were used for the training set, thereby leaving only 19 points in the complimentary set. It is thought that fewer than 19 points is not statistically significant. Figures E-2 through E-5 show the results with different initial random orderings. Finally, Figure E-6 is an average of the previous five graphs. The mean and standard deviation for the largest training set size, namely 160, is given at the top of the plot and in Table 2. The SD of the training set seems to be settling around 2.4, but the SD of the complimentary set still seems to be decreasing and appears like it would go further below 3.0 if the data set were large enough. The standard deviation of the neural network is 24% of the three input model and 55% of the one input model.

Forty epochs were used for all of the results. Since jitter increased the number of data points by a factor of five, the ratio of data points to NN parameters was five times higher and over training was not a problem.

Table 1 Standard deviations of the error for Data Set 112 without the modification.

BURNER DEMAND	0	15	25	40	ALL
Single Input Exp. Model	3.66	8.14	4.53	5.36	6.79
Three Input Exp. Model				4.98	11.65*
NN Model using Jitter					

Table 2 Standard deviations of the error for Data Set 112 with the modification.

BURNER DEMAND	0	15	25	40	ALL
Single Input Exp. Model	3.66	3.14	4.53	5.36	4.67
Three Input Exp. Model				4.98	10.67*
NN Model using Jitter					2.59

Table 3 Means of the error for Data Set 112 without the modification.

BURNER DEMAND	0	15	25	40	ALL
Single Input Exp. Model	-2.59	-4.47	3.04	0.10	-1.27
Three Input Exp. Model				2.42	4.67*
NN Model using Jitter					

Table 4 Means of the error for Data Set 112 with the modification.

BURNER DEMAND	0	15	25	40	ALL
Single Input Exp. Model	-2.59	0.49	3.04	0.10	0.42
Three Input Exp. Model				2.42	5.18*
NN Model using Jitter					-0.35

## Results for Data Set 118

Figures F-1 to F-5 show the results of five different initial random orderings of Data Set 118. Figure F-6 gives the average of the previous five plots. In these figures, it is seen that the SDs of the training set are smaller than those of Data Set 112, even for the same training set size. This is also true for the exponential models as can be seen by Tables 5 and 6. The reason for this is not known. The SD of the NN models is 57% of the three input exponential model 29% of the one input exponential model. These percentages are quite similar to those of Data Set 112, which are 55% and 24% respectively.

Table 5 Standard deviations of the error for Data Set 118.

BURNER DEMAND	0	15	25	40	ALL
Single Input Exp. Model	3.12	1.86	5.50	2.35	3.62
Three Input Exp. Model				1.13	7.19*
NN Model using Jitter					2.05

Table 6 Means of the error for Data Set 118.

BURNER DEMAND	0	15	25	40	ALL
Single Input Exp. Model	-1.36	-3.32	1.33	-2.47	-1.45
Three Input Exp. Model				3.43	-0.26*
NN Model using Jitter					0.06

\* The three input exponential model constants were only intended for a burner demand of 40.

## Results for Data Sets 112 & 118 Combined

Data Sets 112 and 118 were combined in two different ways for this work. The first way was to randomly order each set and then combine the sets to make the first 179 operating points of the new set to be those of 112 and to make the last 66 points to be those of 118. The second way is to merge the two sets and then to randomly order the combined set. The first way should present a more difficult test to the NN, because for small training set sizes, the training set will not have any of Data Set 118 in it, but the complimentary set will. In other words, the second way is easier because, the NN is trained on both sets and tested on both sets.

The results from combining the sets the first way is shown in Figures G-1 to G-6. The resulting mean is 0.03 and the SD is 2.77. Figure G-6 is quite important. It shows that when the training set size is 170 and the NN has been trained only on Data Set 112, that it performs as well on Data Set 118 as a NN trained only on Data Set 118 (compare to complementary set of Figure F-6). This shows that the underlying relationship between the inputs and outputs is quite similar with both LM6000 data sets, as it should be. The network is seen to generalize well; the SDs of the complimentary set are not much higher than those of the training set. The input set for all of the results presented in this paper is the set of variables [9 15 16 17 20 22] from page A-1.

The results from combining the data sets the second way are shown in Appendix H. The resulting mean is 0.19 and the SD is 2.65. Even though theoretically, the first way of combining the sets should pose a more difficult test, the results are relatively close. One has a lower mean, the other has lower SD. The SDs given here from the combined set are similar to the SDs for Data Set 112.

Table 7 compares the single input exponential model to the NN models. The three input exponential model of [2] is not compared here because it was only intended for one value of the burner demand and it has different coefficients for each engine. Therefore, it is much more limited.



Table 7 Results from combining Data Sets 112 & 118.

MODEL	MEAN	SD	SD RATIO
Single Input Exp. Model	-0.08	4.39	100%
NN randomization & merging of the data sets (App. G)	0.03	2.77	63%
NN merging & randomization of the data sets (App. H)	0.19	2.65	60%

It is seen from the table, that the SDs of the errors of the NN model are roughly 60% of those of the single input exponential model.

## Conclusion

The most important contribution of this work was to determine how to generate a NN that would generalize well, so that it could be trained on one engine and perform well on another. To keep this report concise, results from the different methods (listed in this report) to provide generalization and to enhance performance were not given here. Relatively thorough tests were conducted using the previously described methods: early stopping, validation, radial basis networks, training with Bayesian Regularization, and input jitter. It was determined that the last two work the best for this application and therefore only those results were shown.

This work has shown that by using input jitter and by training feed-forward networks of only 12 neurons using Bayesian Regularization, that NO<sub>x</sub> prediction errors of about 3.0 can be achieved for data sets that the NN has not been trained on. Furthermore, due to the use of input jitter and the BR training method, the relationships between the inputs and the output are smooth. This greatly reduces the probability of the NN providing a very poor NO<sub>x</sub> prediction on any input that can be considered as an interpolation of the training inputs. Since jitter increased the number of data points by a factor of five, the ratio of data points to NN parameters was five times higher and overfitting was not a problem.

It is always preferably to have many data sets to draw inferences from. However, it appears that if the two used for this study are typical, that a NN trained on one LM6000 engine (with 180 operating points or more) can provide good performance on other LM6000 engines when input jitter is used and the network is trained with Bayesian Regularization.

## References

- [1] Gas Turbine Combustion, A. H. Lefebvre, 1999
- [2] “Empirical Model for Engines 112 and 118”, Excel spreadsheet, General Electric Aircraft Engines
- [3] Neural Network Toolbox User’s Guide –Version 3, the Mathworks, July 1998

## Appendix A – Variable Description for Data Sets 112 & 118

1	esn	engine serial number	
2	rdg	Data point reading number	
3	tdate	Date	
4	brnreq	Burner configuration SS target	n/d
5	brndmd	Burner configuration demand	n/d
6	nggsel	Gas Generator speed	rpm
7	nggdot	Gas generator speed rate of change	rpm/sec
8	t2sel	Gas generator inlet temperature	deg F
9	t3est	Compressor Discharge Temperature	deg F
10	t54sel	Turbine discharge temperature	deg F
11	tflycs	Smoothed calculated bulk flame temperature	deg F
12	tfldmd	Bulk flame temperature demand	deg F
13	tfllrf	Inner ring flame temperature demand	deg F
14	tfllorf	Outer ring flame temperature demand	deg F
15	tfllidf	Calculated inner ring flame temperature	deg F
16	tfllpdf	Calculated pilot ring flame temperature	deg F
17	tfllodf	Calculated outer ring flame temperature	deg F
18	tfllpct	Bulk flame percent (min=0, max=100)	%
19	p2sel	Gas generator inlet pressure	psia
20	ps3sel	Compressor discharge pressure	psia
21	p54sel	Turbine Discharge pressure	psia
22	wf36dmd	Fuel flow demand	pph
23	wf1abc	Inner fuel flow reference per staging valve	pph
24	wfoabc	Outer fuel flow reference per staging valve	pph
25	wfinr	Calculated inner ring fuel flow	pph
26	wfpil	Calculated pilot ring fuel flow	pph
27	wfotr	Calculated outer ring fuel flow	pph
28	wfinrs	Smoothed calculated inner ring fuel flow	pph
29	wfpils	Smoothed calculated pilot ring fuel flow	pph
30	wfotrs	Smoothed calculated outer ring fuel flow	pph
31	fwa36	Tflame airflow at station 36	pps
32	wacfli	Inner airflow burned in combustion	pps
33	wacflo	Outer airflow burned in combustion	pps
34	wacflp	Pilot airflow burned in combustion	pps
35	wb26q	Eight stage fractional bleed flow demand	n/d
36	wb3q	CDP fractional bleed flow demand	n/d
37	dwb36	Total bleed flow demand reflected to sta 36	pps
38	st8sel	Eight stage bleed valve sensed position	% stroke
39	cdpsel	CDP bleed valve sensed position	% stroke
40	nox	Raw Nox level	ppm
41	nox15	Nox level corrected to 15% O2	ppm
42	co	Raw Co level	ppm
43	co15	Co level corrected to 15% O2	ppm
44	uhc	Raw unburned hydrocarbon level	ppm
45	uhc15	Unburned hydrocarbon level corrected to 15% O2	ppm
46	lhvsel	Fuel lower heating value	btu/lbm
47	sgsel	Fuel specific gravity	n/d

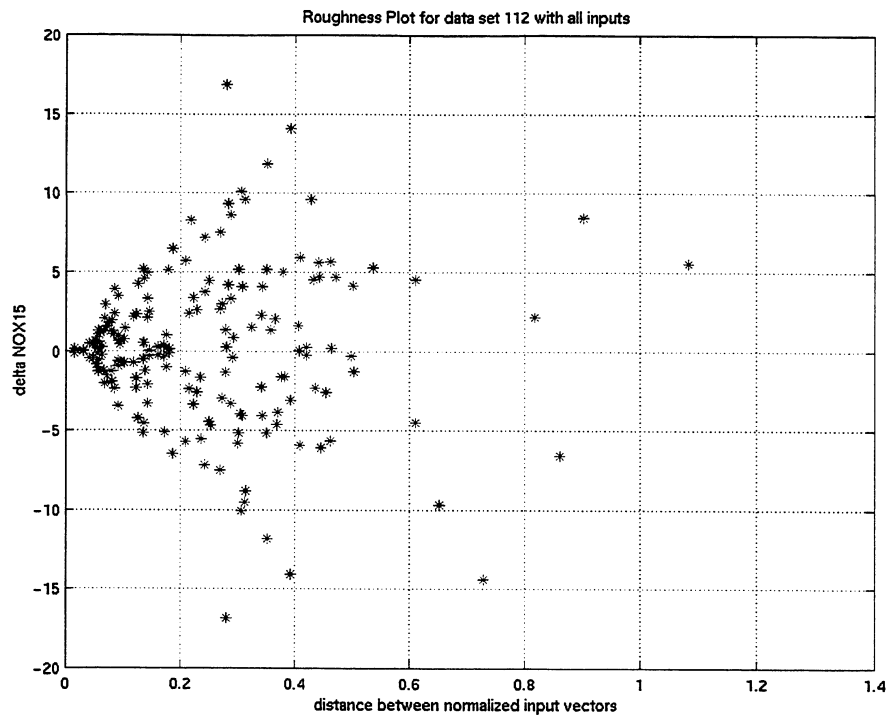


**Figure B-1** Roughness plot with all of the inputs.

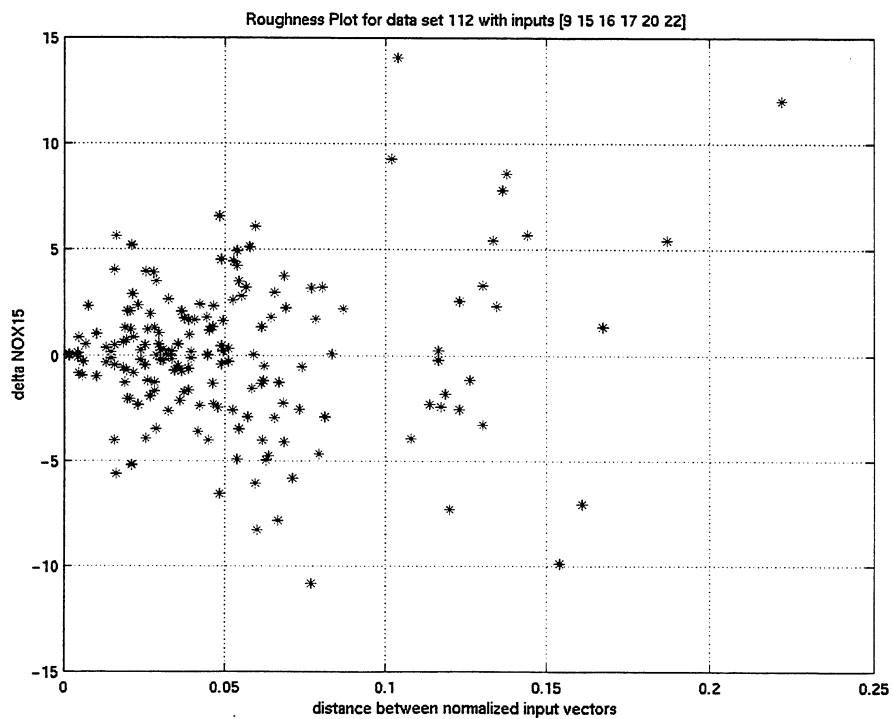


**Figure B-2** Roughness plot with inputs 9, 15, 16, 17, 20, & 22.

## Appendix C – Parameters for Three Input Exponential NOX Model

General Electric determined parameters for the three input exponential model for data sets 112 and 118. The Parameters are intended only for a burner demand (BRNDMD) of 40. The model equation is repeated below:

$$\text{NO}_x \cong (1 / \sum(\text{wp}(i))) \sum \text{wp}(i) e^{(\text{cp}(i) * (\text{tfl}(i) + \text{dtflp}(i)) + \text{mup}(i))}$$

The parameters are:

$$\begin{aligned} \text{dtflp112} &= [1.0795\text{e}2 \quad -2.2011\text{e}1 \quad 6.5252\text{e}1] \\ \text{dtflp118} &= [9.5405\text{e}1 \quad -3.5124\text{e}1 \quad -9.4431\text{e}1] \end{aligned}$$

$$\begin{aligned} \text{cp112} &= [1.2609\text{e}-2 \quad 5.6860\text{e}-3 \quad 5.6840\text{e}-3] \\ \text{cp118} &= [4.5500\text{e}-3 \quad 5.6860\text{e}-3 \quad 5.6840\text{e}-3] \end{aligned}$$

$$\begin{aligned} \text{mup112} &= [-4.2960\text{e}1 \quad -1.6926\text{e}1 \quad -1.6642\text{e}1] \\ \text{mup118} &= [-1.2581\text{e}1 \quad -1.6926\text{e}1 \quad -1.6642\text{e}1] \end{aligned}$$

$$\text{wp112} = \text{wp118} = [0.295 \quad 0.320 \quad 0.139]$$

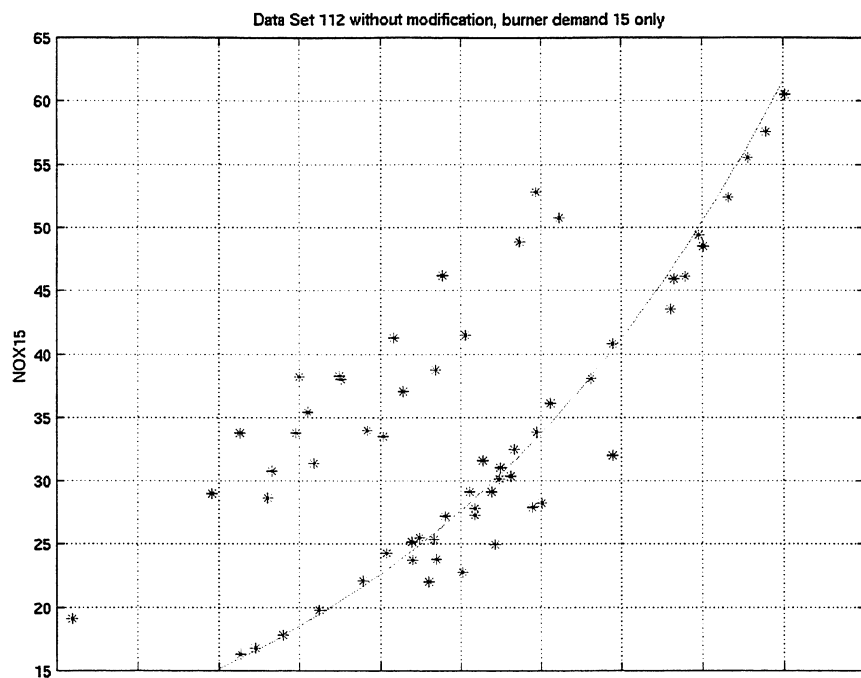


Figure D-1 NOX15 versus calculated pilot ring flame temperature for Data Set 112 without the modification

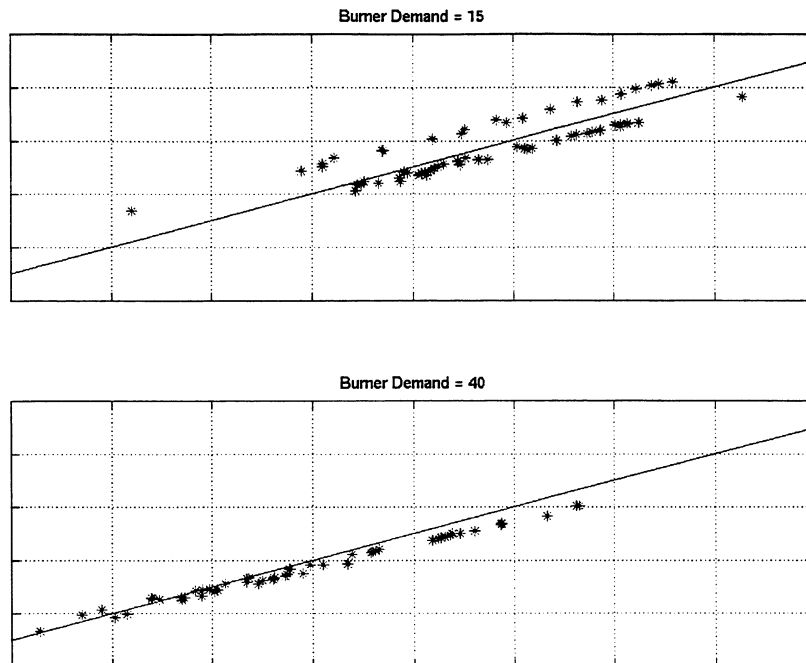


Figure D-2 Inner ring flame temperatures for Data Set 112 without the modification:  
calculated versus demanded temperature

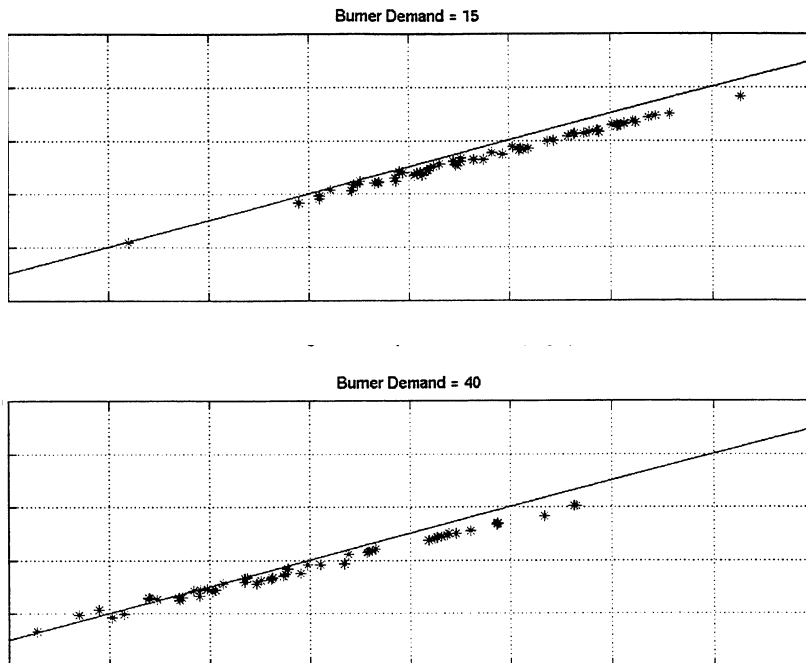


Figure D-3 Inner ring flame temperatures for Data Set 112 with the modification:  
calculated versus demanded temperature



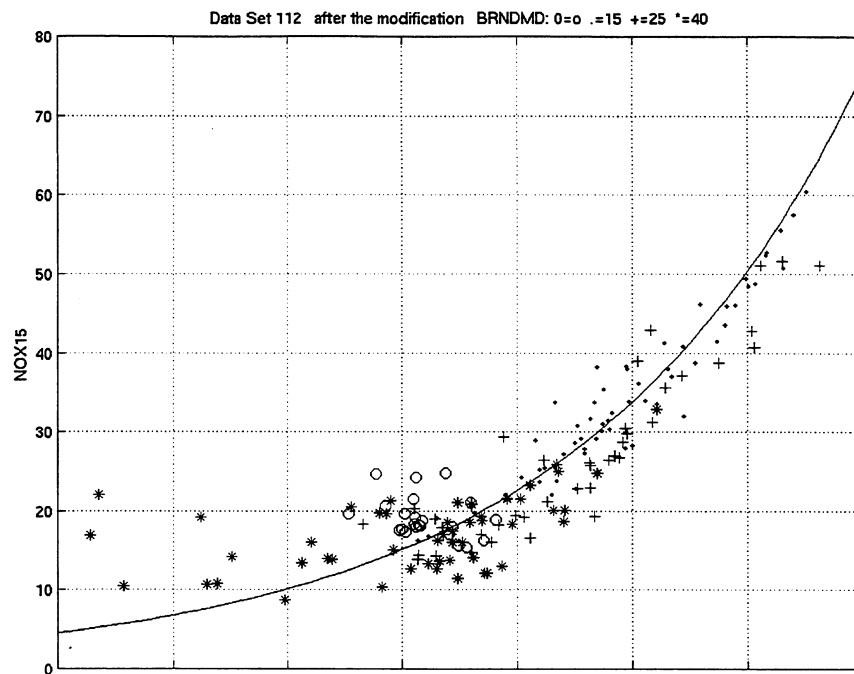


Figure D-4 NOX15 versus calculated pilot ring flame temperature for Data Set 112 with the modification

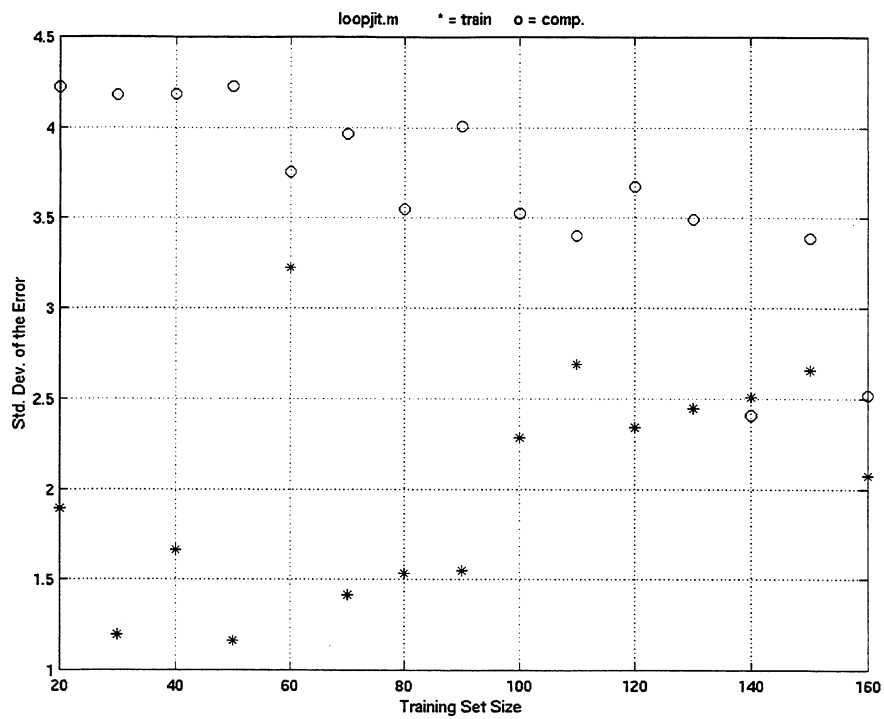


Figure E-1 Results of random ordering #1 of Data Set 112

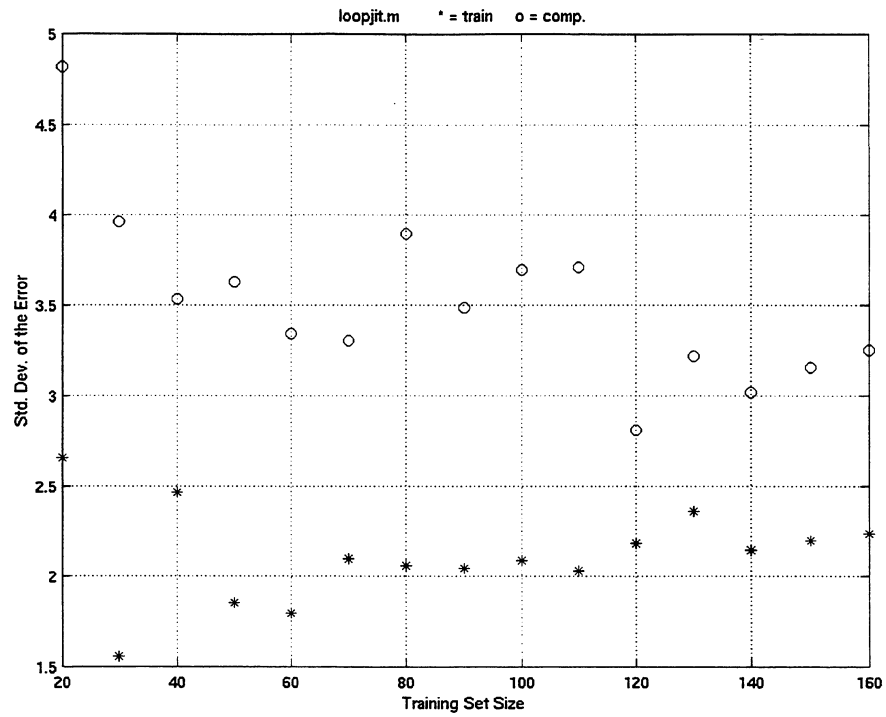


Figure E-2 Results of random ordering #2 of Data Set 112

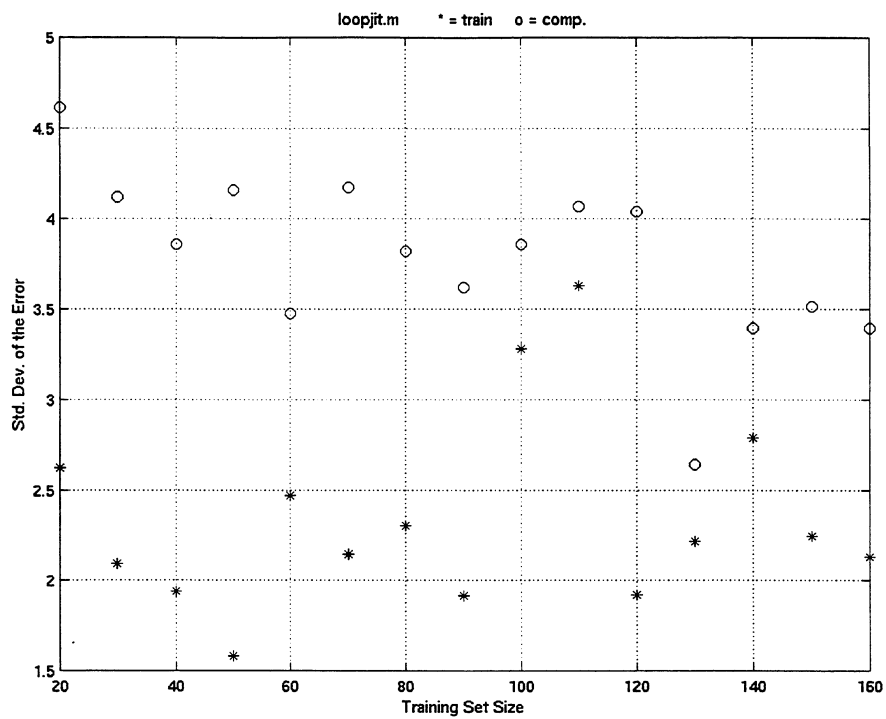


Figure E-3 Results of random ordering #3 of Data Set 112

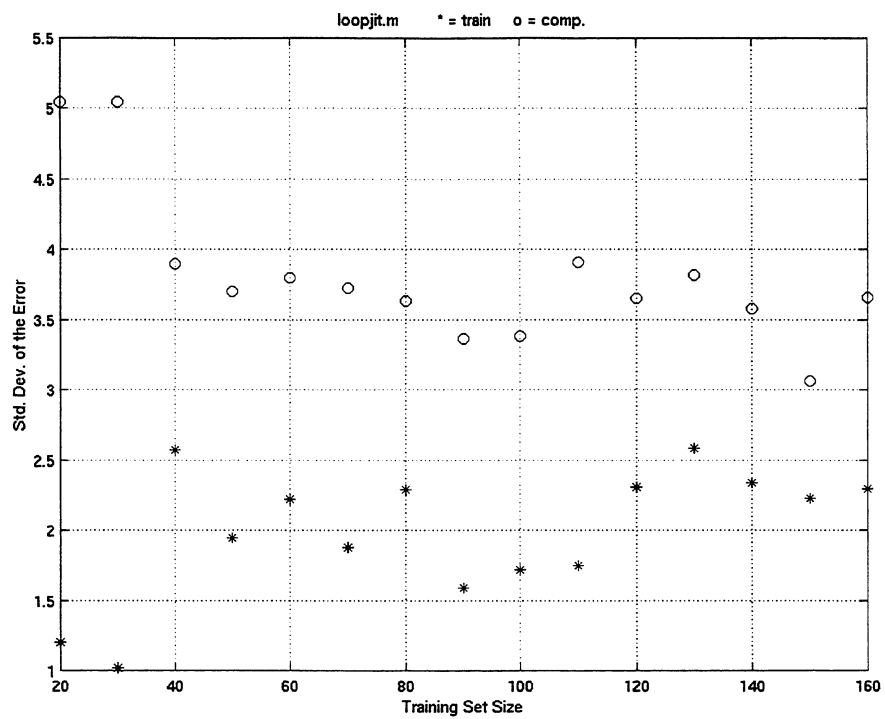


Figure E-4 Results of random ordering #4 of Data Set 112

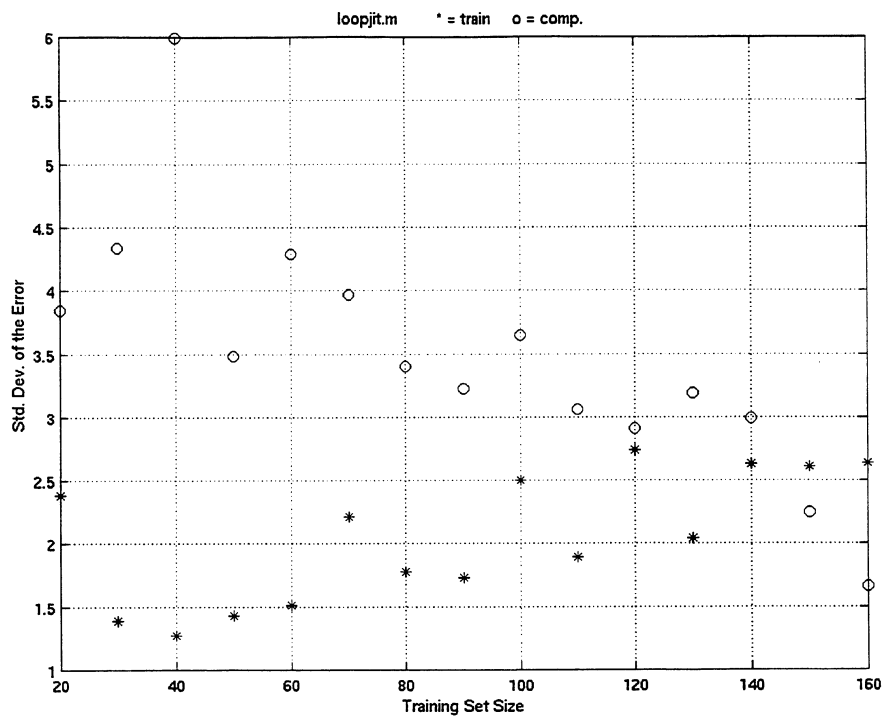


Figure E-5    Results of random ordering #5 of Data Set 112

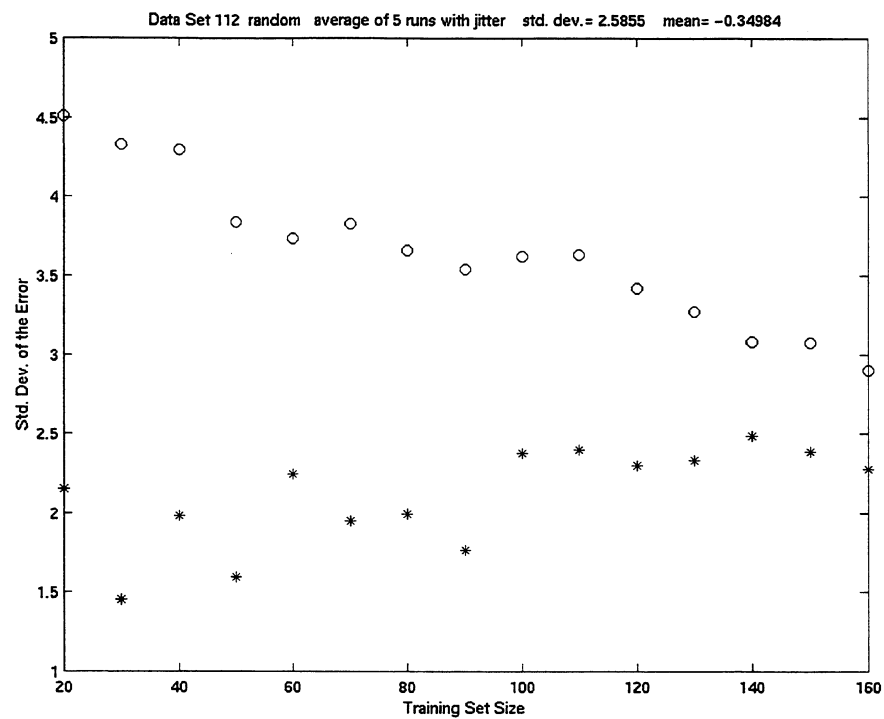


Figure E-6 Results of 5 random orderings of Data Set 112

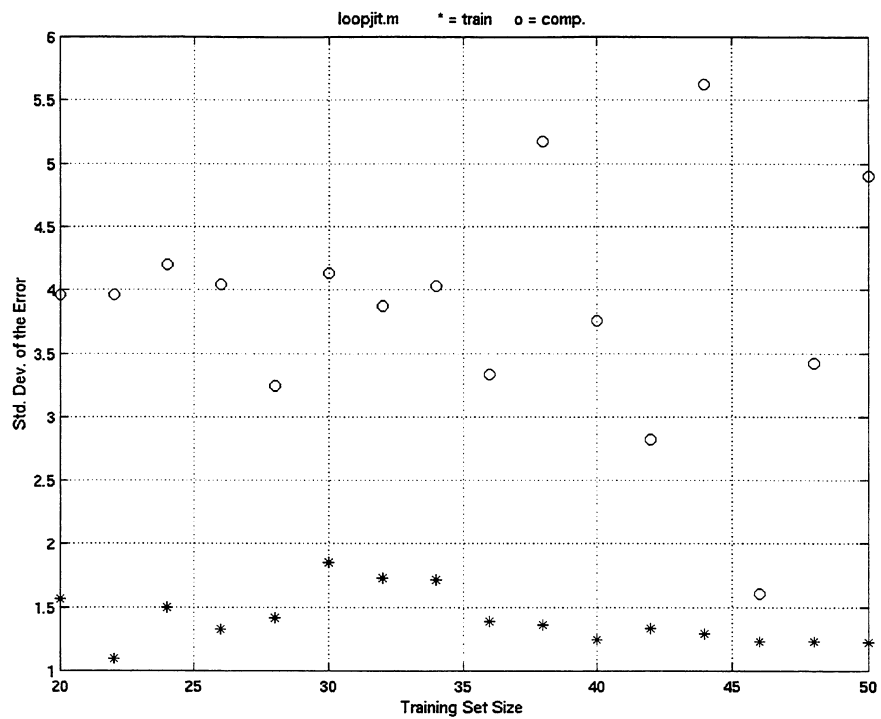


Figure F-1 Results of random ordering #1 of Data Set 118



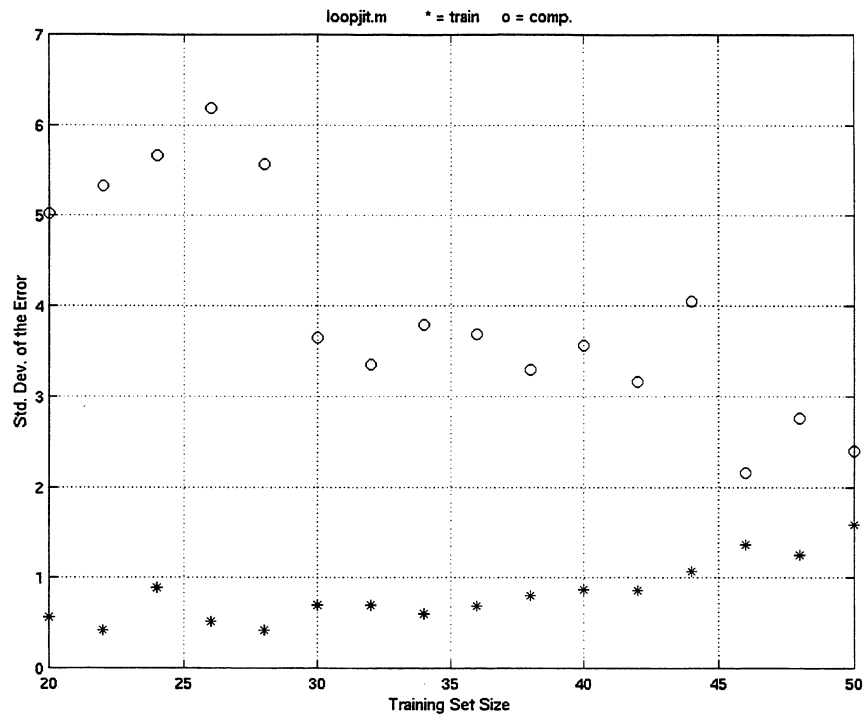


Figure F-2 Results of random ordering #2 of Data Set 118

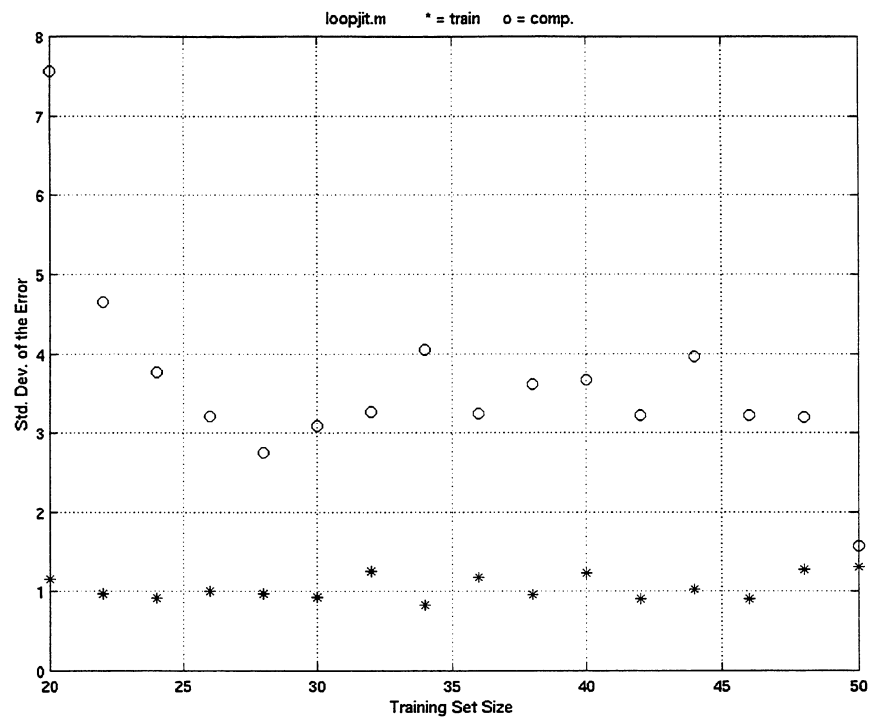


Figure F-3    Results of random ordering #3 of Data Set 118

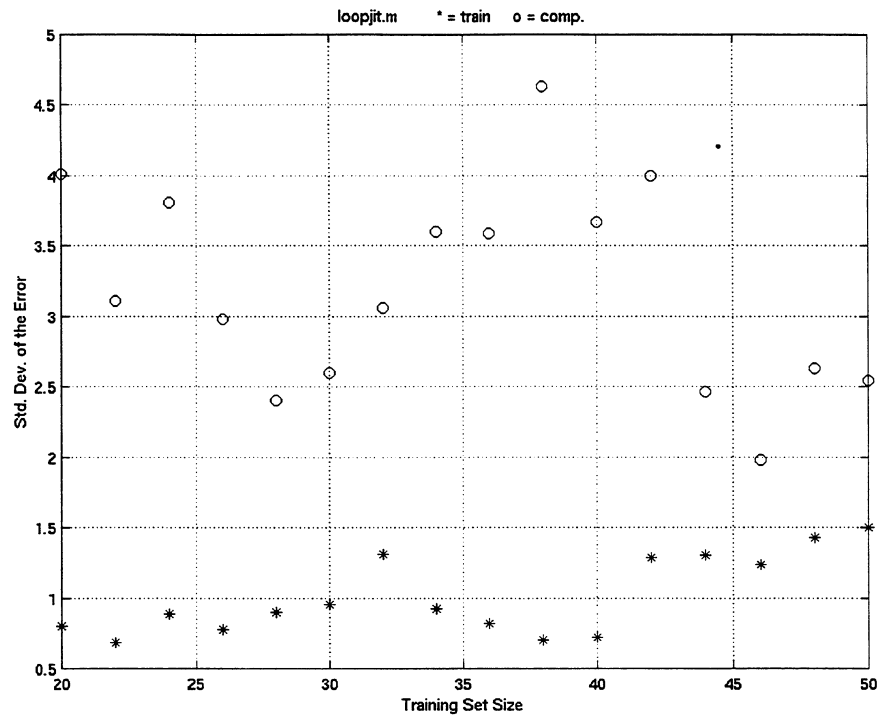


Figure F-4 Results of random ordering #4 of Data Set 118

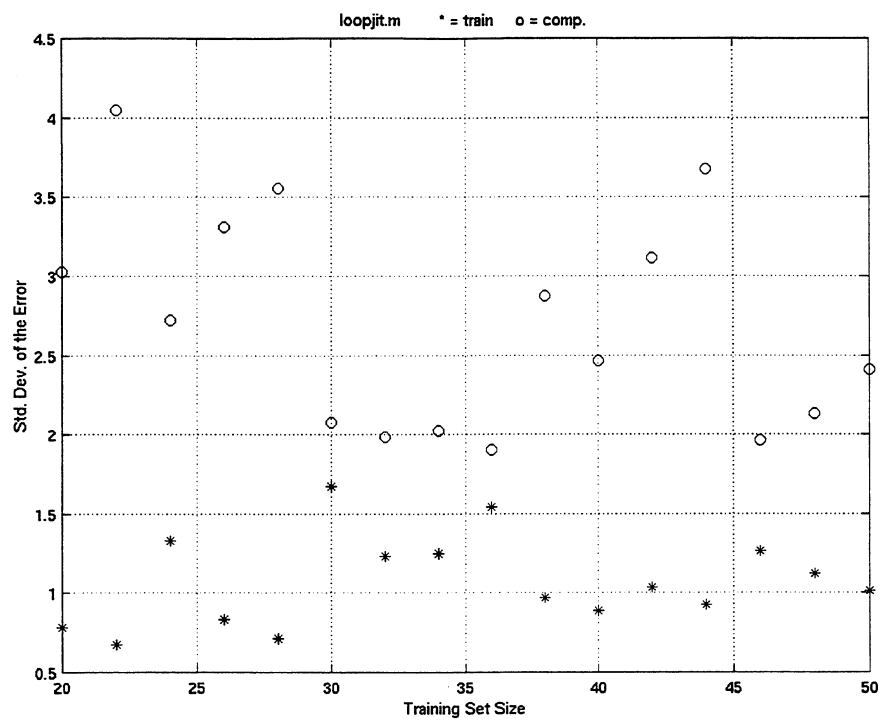


Figure F-5 Results of random ordering #5 of Data Set 118

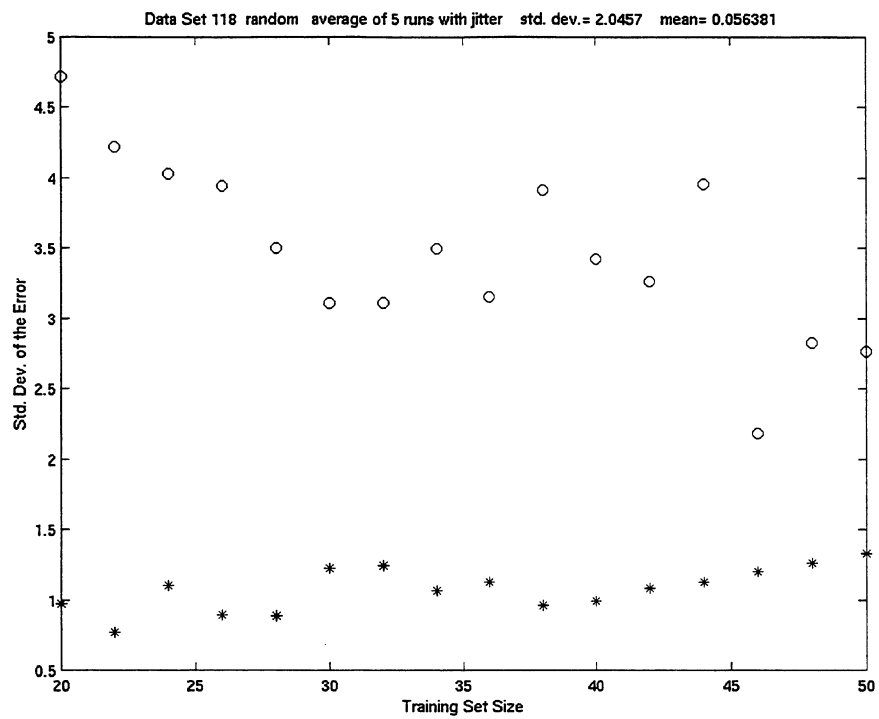


Figure F-6 Results of 5 random orderings of Data Set 118

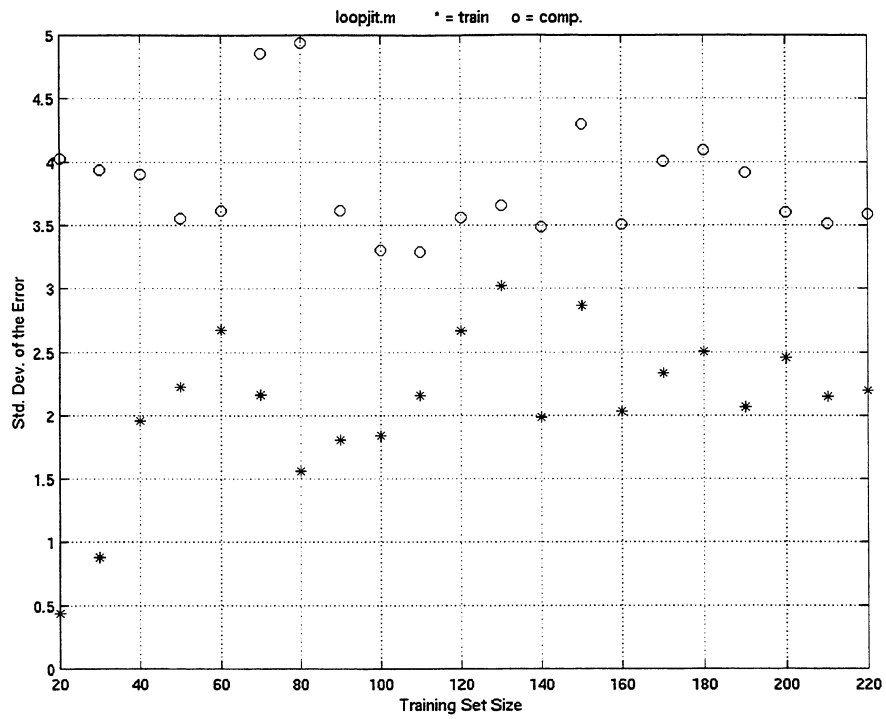


Figure G-1 Results of random ordering #1 of the separate Data Sets 112 & 118

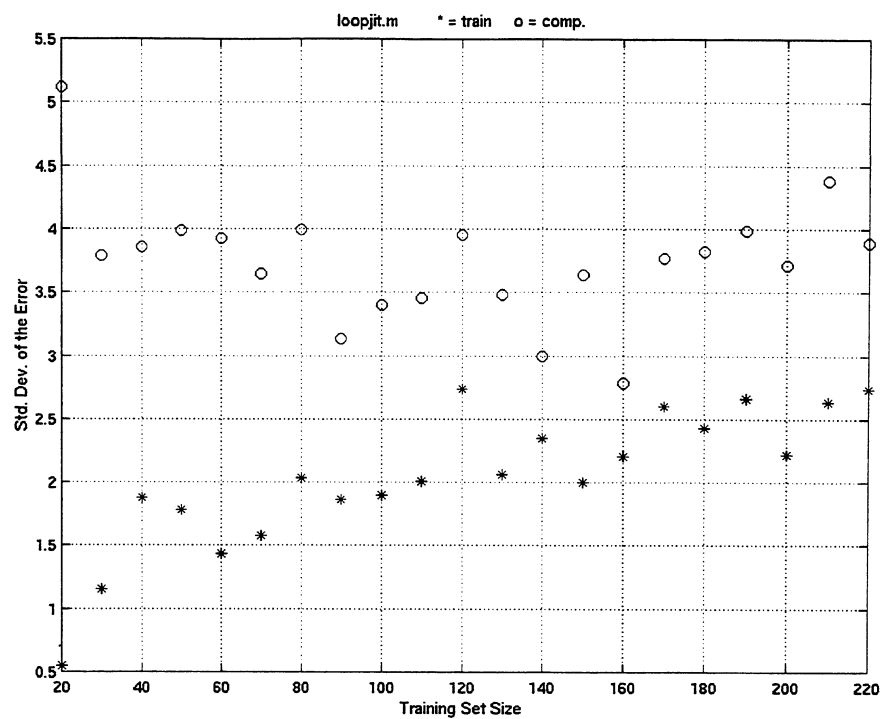


Figure G-2 Results of random ordering #2 of the separate Data Sets 112 & 118

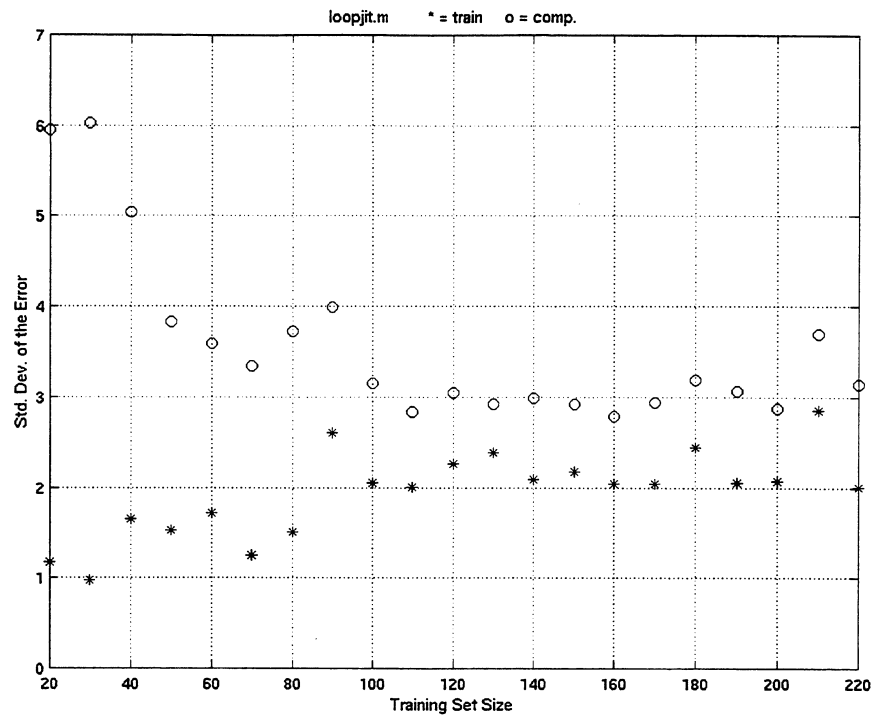


Figure G-3 Results of random ordering #3 of the separate Data Sets 112 & 118



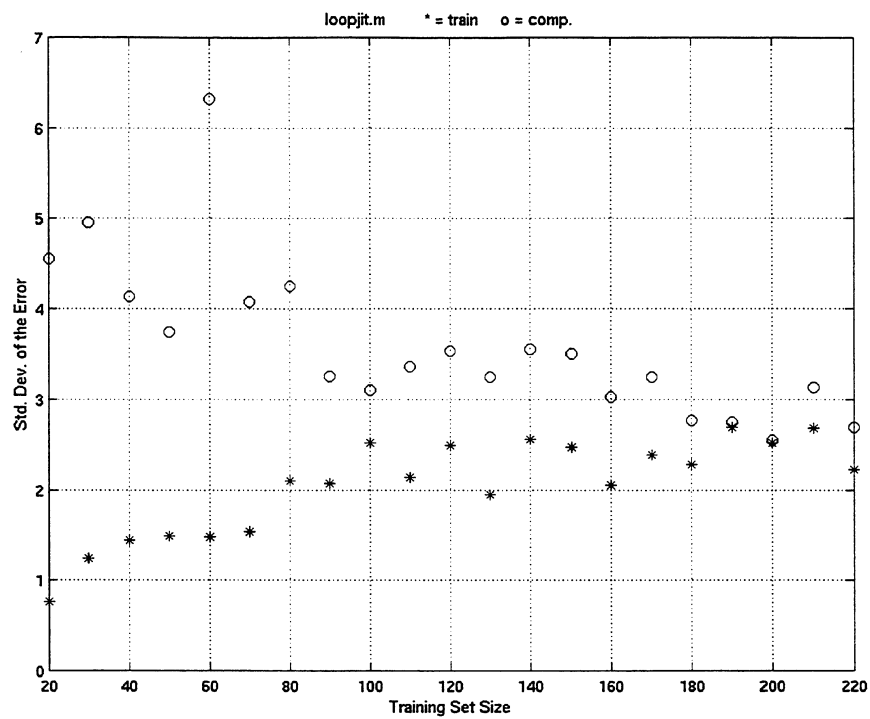


Figure G-4 Results of random ordering #4 of the separate Data Sets 112 & 118

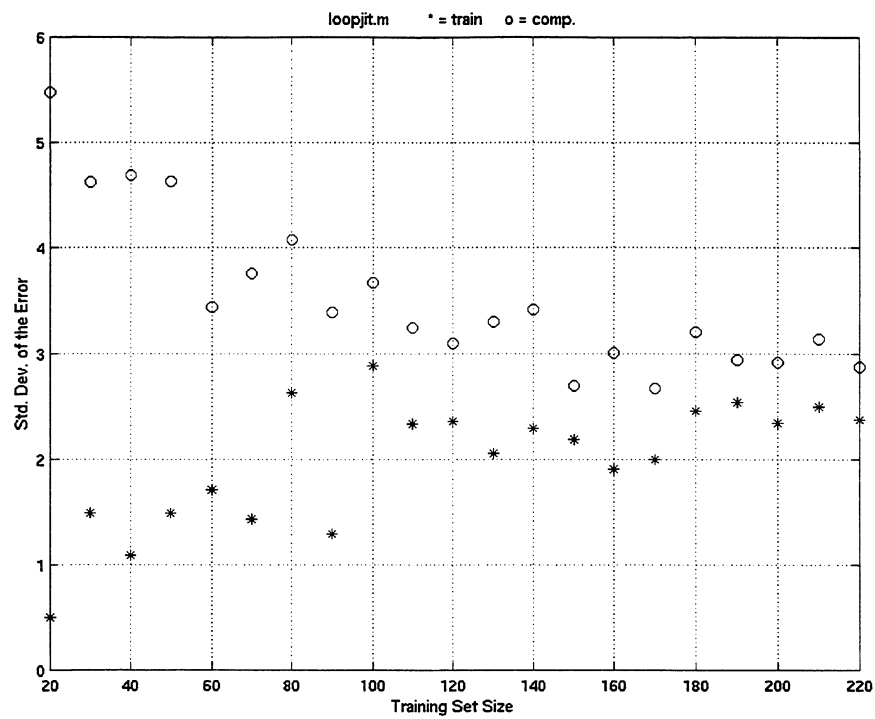


Figure G-5 Results of random ordering #5 of the separate Data Sets 112 & 118

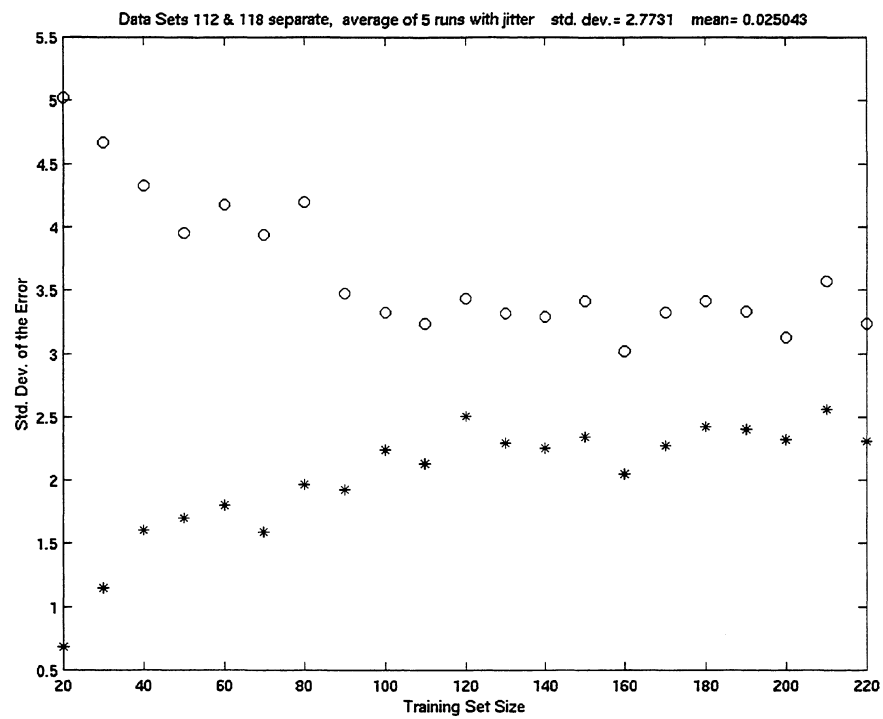


Figure G-6 Results of 5 random orderings of the separate Data Sets 112 & 118

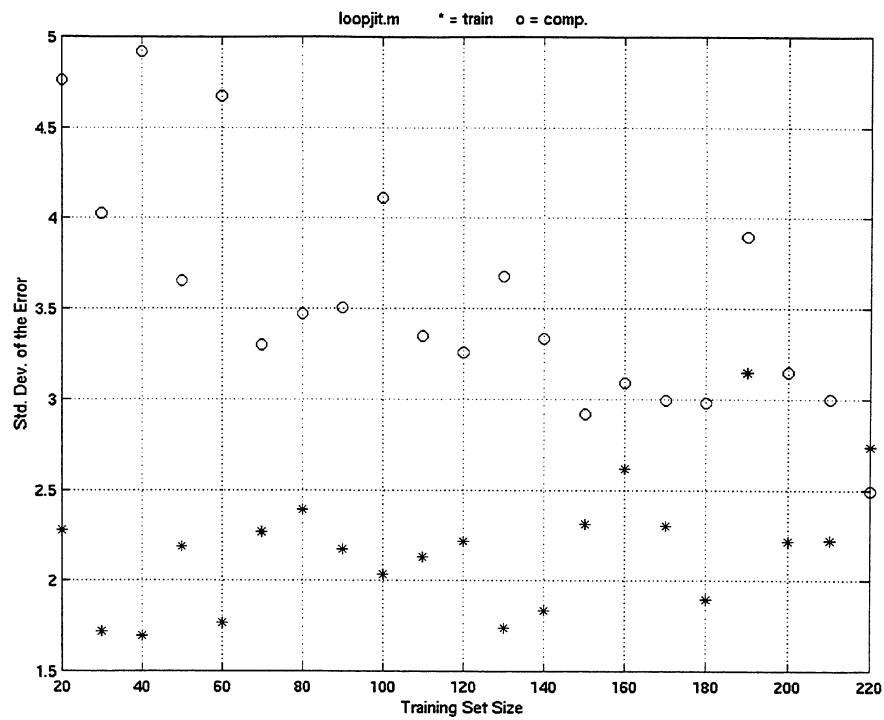


Figure H-1 Results of random ordering #1 of the combined Data Set 112 & 118

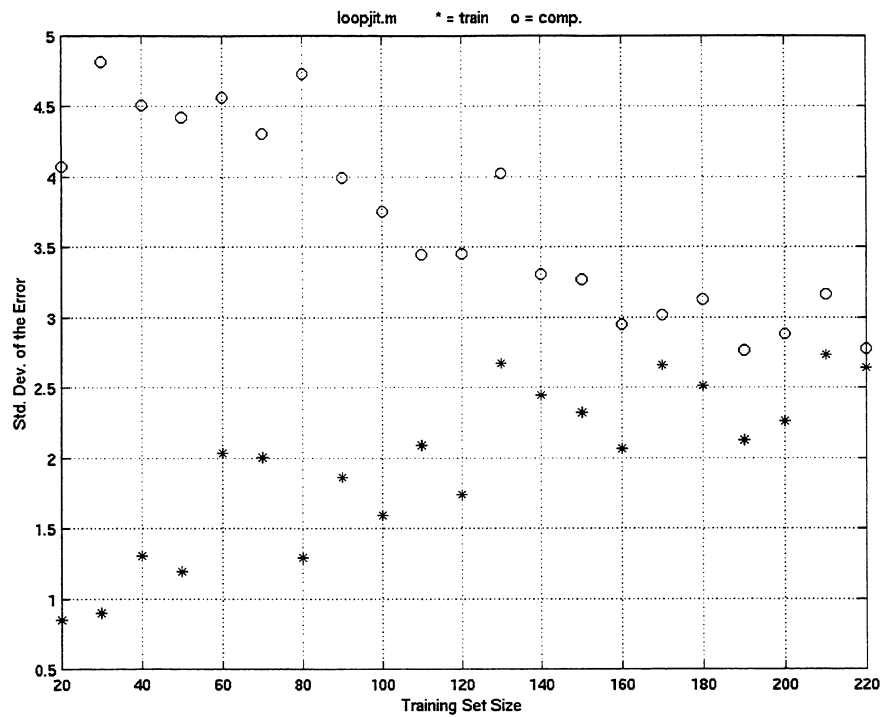


Figure H-2 Results of random ordering #2 of the combined Data Set 112 & 118

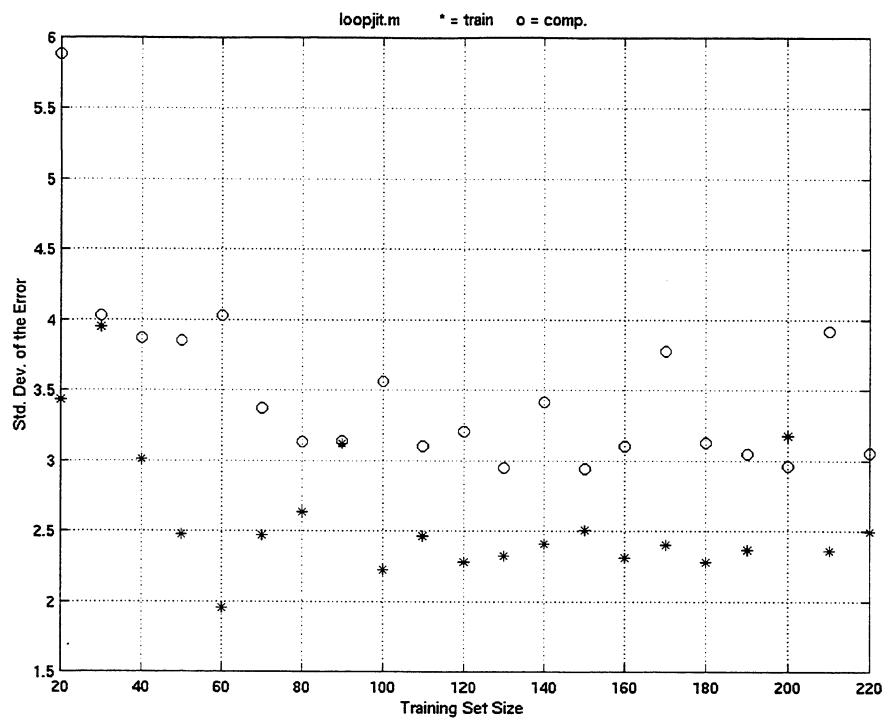


Figure H-3 Results of random ordering #3 of the combined Data Set 112 & 118

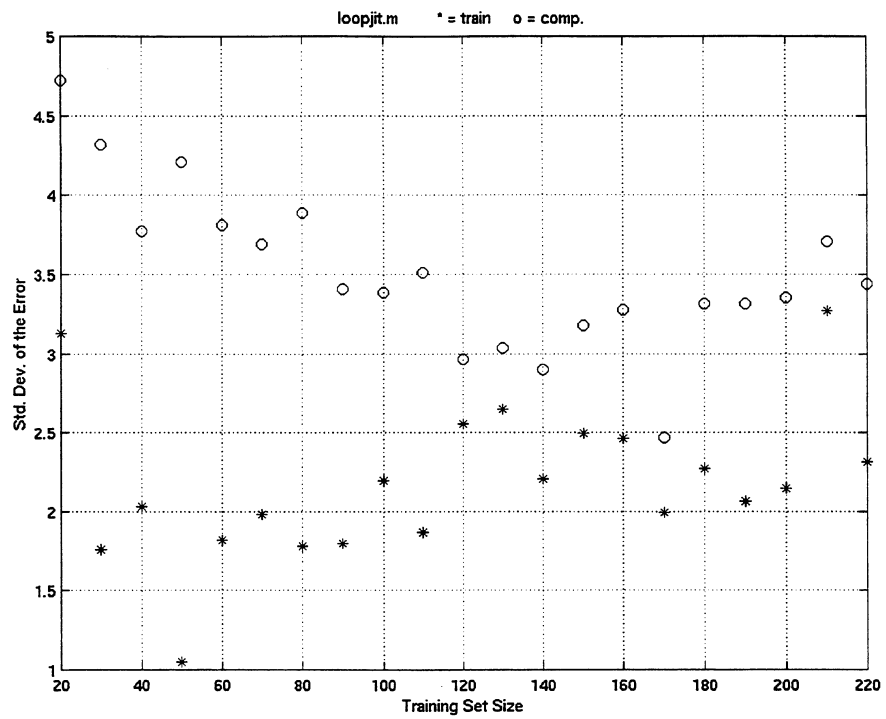


Figure H-4 Results of random ordering #4 of the combined Data Set 112 & 118

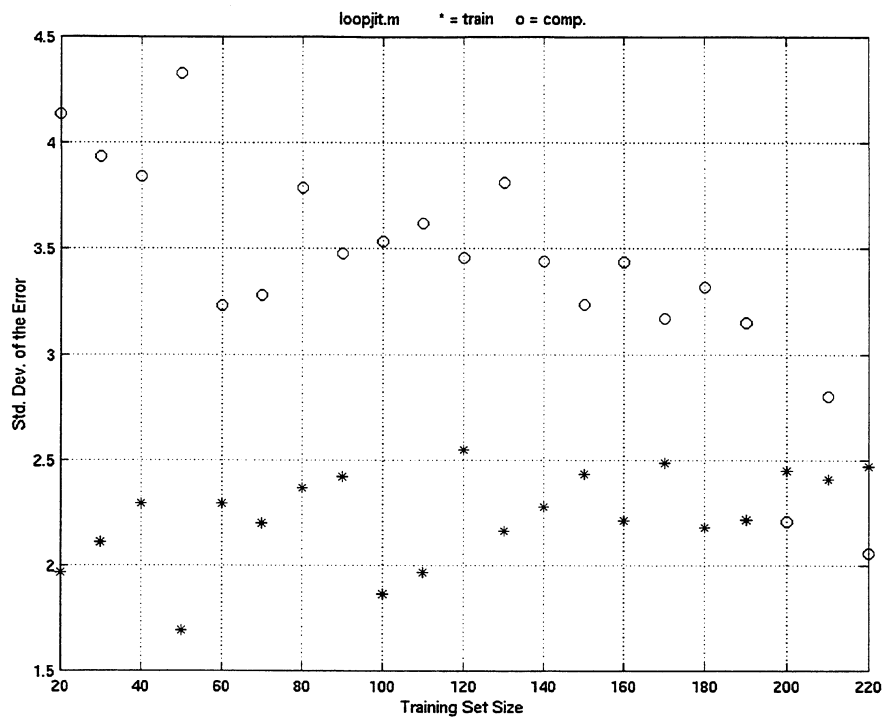


Figure H-5 Results of random ordering #5 of the combined Data Set 112 & 118



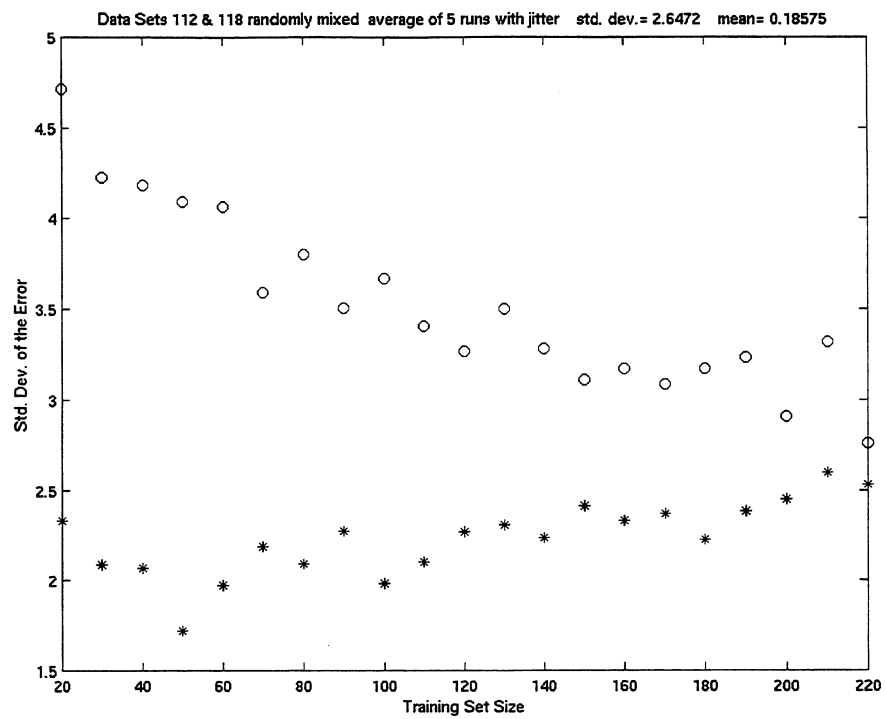


Figure H-6 Results of 5 random orderings of the combined Data Set 112 & 118

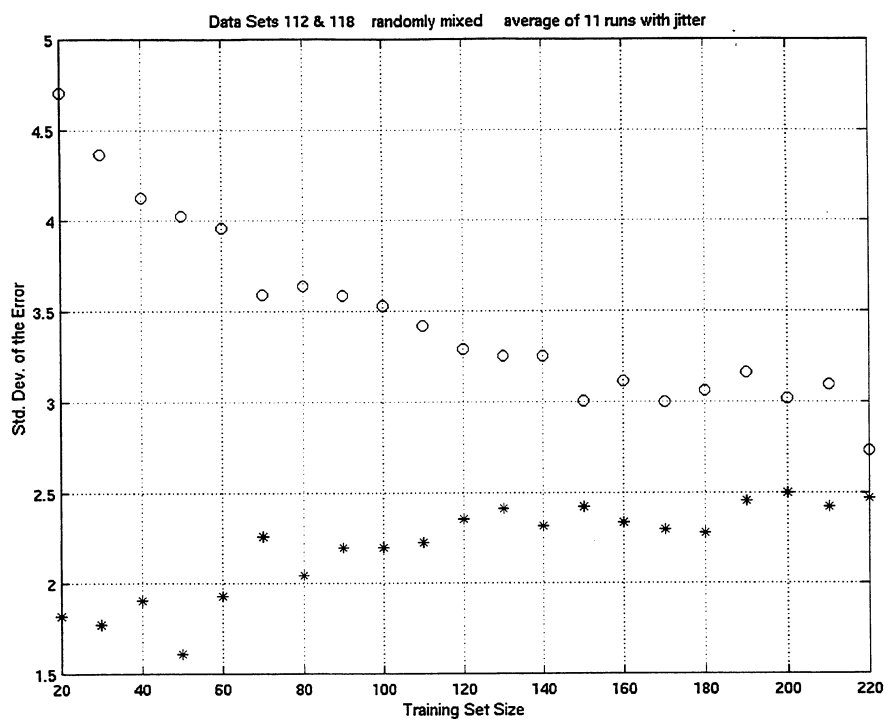


Figure H-7 Results of 11 random orderings of the combined Data Set 112 & 118

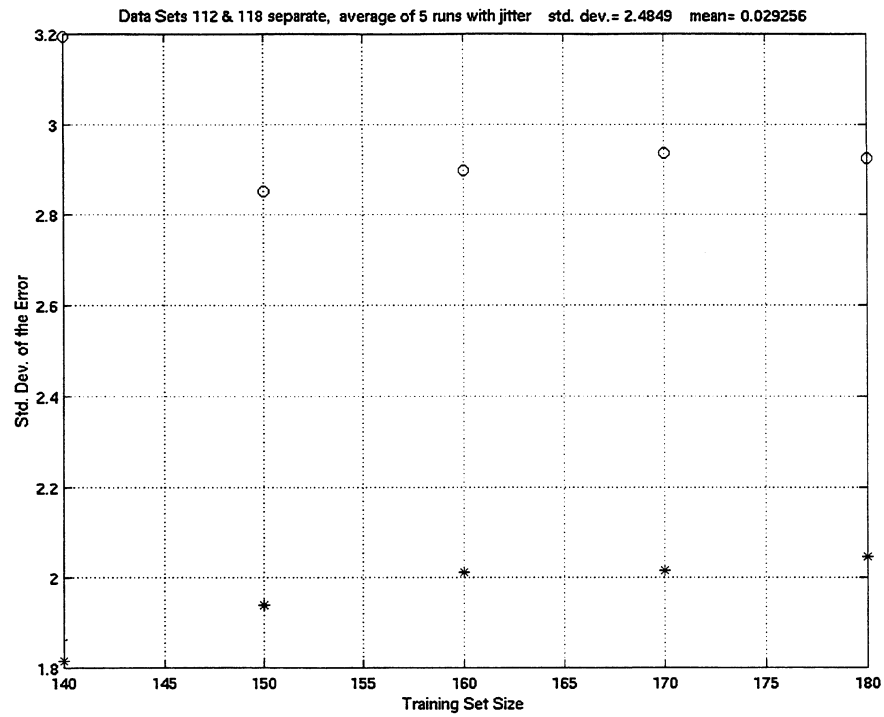


Figure I-1 Results of 5 random orderings of the separate Data Sets 112 & 118, 80 epochs

Table J-1      Matlab functions written for this neural network task.

DATE	*.M FILE	DESCRIPTION
10-2-98	nnsccater	output scatter plots with different colors and symbols
10-2-98	datacorr	correlation of vectors
12-1-98	expmodel	exponential model
12-1-98	identexp	identifies an exponential model
12-2-98	datadist	calculates distance apart of input vectors
12-3-98	datamod1	interpolate NN input data (input data conditioning)
12-3-98	sdcomp	calculates mean and SD of complimentary set
12-4-98	<b>nettest</b>	short (one page) & simple NN setup and training function
12-10-98	tempflow	divides three temps by flows
12-18-98	insccater	plots inputs with a color scatter
12-18-98	earlystp	implements "early stopping"
12-21-98	trainsiz	plots SD of error versus training set size
1-6-99	netsize	plots SD of error versus NN size
1-22-99	manymods	averages "n" NN models
1-26-99	radbtest	short and simple implementation of radial basis networks
1-26-99	sizegrnn	short and simple implementation of gen. regression NNs
1-27-99	<b>roughnes</b>	makes "roughness" plots
1-28-99	findexp	finds operating points that are near single input exp. model
2-1-99	regress	regression
2-2-99	geexpmod	GE's three input exponential model
2-3-99	<b>jitter</b>	adds jitter to the input data set
2-8-99	<b>loopjit</b>	calls jitter and nettest repeatedly to make plot versus size
2-11-99	sortdata	sorts based on burner demand and plots
2-11-99	<b>pilotemp</b>	modifies Data Set 112 pilot temperature

The most important functions are in boldface type.



**Attachment IV: FMUX Dynamic Modeling – Summary  
Memorandum**



Woodward Governor Company  
Rockford, Illinois

EN831562

SUBJECT: Addition of FMU to Active Combustor Control Model

PROJECT NUMBER: X83753

FROM: Daniel McLevige

DATE: August 28, 1998

TO: Bill Myers, GEAE

cc: Ted Hommema

### 1.0 ABSTRACT

The FMU and pump were added to the Active Combustor Control Simulink dynamic model to check for interactions between the two systems. No significant dynamic interactions were found, but a steady state total flow change of up to 1.5% was found due to bypass valve droop at 125% flow split.

### 2.0 CONCLUSIONS & RECOMMENDATIONS

a) The FMU and pump were added to the Active Combustor Control Simulink dynamic model and runs made stepping both total flow and flow split.

b) Flow split step behavior was essentially identical to previous runs of the model before the FMU was added.

c) No adverse dynamic interaction between the HMUX flow splitting function and FMU flow metering function was seen.

d) As flow was uptrimmed on one nozzle, the resultant increase in back pressure caused total flow drop because of bypass valve droop. Up to 1.5% total flow drop was seen at 125% nozzle flow uptrim. If this is deemed a concern, a closer look using a steady state model should be done, since the dynamic model is not optimized for precisely predicting steady state performance.

e) Since the simulation does not model all 30 nozzles individually, it was found to give improper response of flow split to total flow steps. To model all 30 nozzles in detail is beyond the capability of the hardware/software used.

### 3.0 DISCUSSION

The Simulink model of the active combustor control HMUX has been used to predict dynamic behavior. Model runs involving step response in requested flow split between nozzles have been presented at the October 9, 1997 and May 27, 1998 design reviews at GEAE - Evendale.

Representative model run plots were included in the hand-out books for the two reviews. At the last review, GEAE requested that the FMU be added to the model to look for interaction between the flow splitting function of the HMUX and the fuel metering function of the FMU. This was done and selected runs of the combined model made.



### 3.1 Model Summary

Components included in the FMU model are as follows (see schematic Figure 1):

- a) Bypass valve - mass, damping, spring rate, damping orifices, nonlinear flow equation and flow force equation at all ports
- b) Pressurizing valve - mass, damping, spring rate, friction, damping orifice, non linear flow equation and flow force equation
- c) Boost pump - pressure as function of speed and flow
- d) Gear pump - flow as function of speed with internal leakage proportional to pressure rise
- e) FMU internal leakage - proportional to square root of  $P_s - P_b$
- f) Fuel valve - port flow equation only
- g) P1, P2, and P22 volumes compressibility

The active combustor control HMUX model was essentially the same as described in the previous design reviews, and included the following components (see schematic Figure 2):

- a) One HMUX only
- b) Force motor & first stage pilot valve
- c) Rotating sleeve (2 ports in detail, rest simplified)
- d) Hydraulic turbine - speed follows  $P_s - P_b$  with a time constant
- e) Pressure transducer
- f) Throttle valves (2 in detail, other 28 lumped together and simplified)
- g) Nozzles (2 in detail, other 28 lumped together and simplified, with option for turning nozzles off at low flows to maintain minimum nozzle delta P)
- h)  $P_c$  regulator - not used for runs made for this report (Assumed  $P_s$  supply to impulse turbine and HMUX first and seconds stages)
- i) Digital controller (2 nozzles plus delta P in detail, other 28 nozzles lumped together)
- j) Fluid compressibility and inertia in selected locations

### 3.2 Model Runs

Model runs were done at three total flows: 4,500 pph, 21,000 pph, and 29,000 pph. Similar cases were run as had previously been done with the model without FMU. One minor difference was that for the combined model runs, nozzles were shut off to maintain 30 psid nozzle delta P for the 75% flow split case. The previous work had set the minimum nozzle delta P at 30 psid for the nominal 100% flow split case, meaning that delta P became excessively low for the downtrim cases. This change affected the 4,500 pph point only.

Three cases were looked at for each flow level: 10% p-p flow split steps, +/-25% large flow split steps, and 10% p-p total flow steps. The flow split steps were compared to earlier model runs without the FMU and found to be essentially identical for the 21,000 pph and 29,000 pph cases. The 4,500 pph case was a little different because of the difference in the nozzle delta P. In all cases, no adverse dynamic interaction between the FMU flow metering and HMUX flow splitting functions was seen.

However, a steady state effect was seen. As flow split changed, it changed the back pressure on the bypass valve for the cases off the pressurizing valve. Since the bypass valve does not contain

an integrator, this causes some delta P droop and flow error. While the model is optimized for showing dynamic rather than steady state performance, the bypass valve model is detailed enough that it should be close for steady state also.

Model runs both with and without HMUX Pc regulator were done, but for brevity only plots from runs without Pc regulator are presented in this report. The runs with Pc regulator were similar.

Plots of representative runs are attached as follows:

a) Figure 3: 10% Flow Split Steps at 21,000 pph; Nozzles 1 & 2 Opposite Directions

This shows a split time constant of about 3/4 seconds causing about 0.3% p-p total flow disturbances.

b) Figure 4: +/- 25% Full Range Flow Split Steps at 21,000 pph, Nozzles 1 & 2 Opposite Directions

This is a very unrealistic case, and is run only to prove that the system is stable with any conceivable step size. It shows total flow effects of 1.5% p-p. This is a steady state droop effect caused by the increased back pressure affecting the proportional bypass valve.

c) Figure 5: 10% p-p Total Flow Steps from 21,000 pph

This shows the total flow steps causing about a 1.5% temporary error in flow split. This is believed to be a model anomaly that is not expected to occur in the real system. In the model, only two nozzle channels were modeled in detail; the other 28 were lumped together and simplified. In the real system, all nozzle channels are identical, and a common mode effect such as stepping total flow should affect all equally. Therefore, for the case of all channels at 100% split, no significant change in flow split should occur during a total flow transient.

d) Figure 6: 10% p-p Total Flow Steps from 4,500 pph

This shows the total flow steps causing about a 3% temporary error in flow split. Again, this is believed to be an artifact of the model and should not happen in the real system.

e) Figure 7: 10% p-p Total Flow Steps from 29,000 pph

This shows the same effect, in this case about a 4% temporary flow split error, which again should not be real.

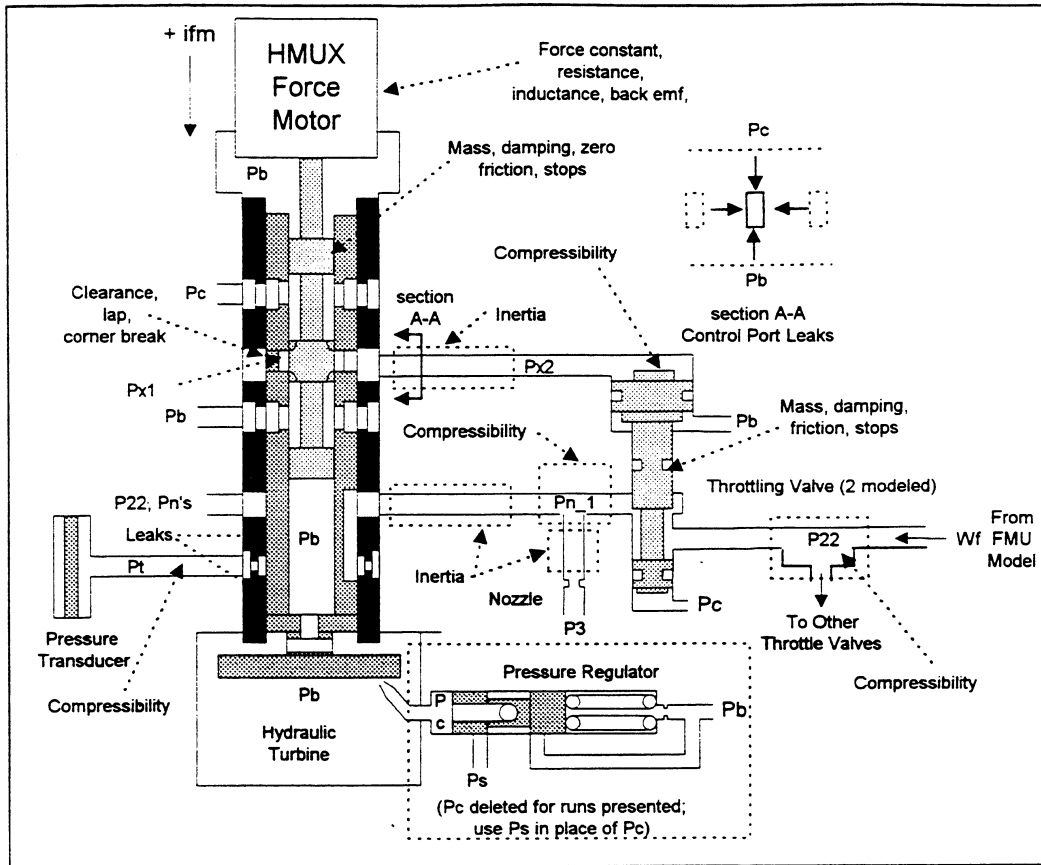


Figure 1 HMUX Model Schematic

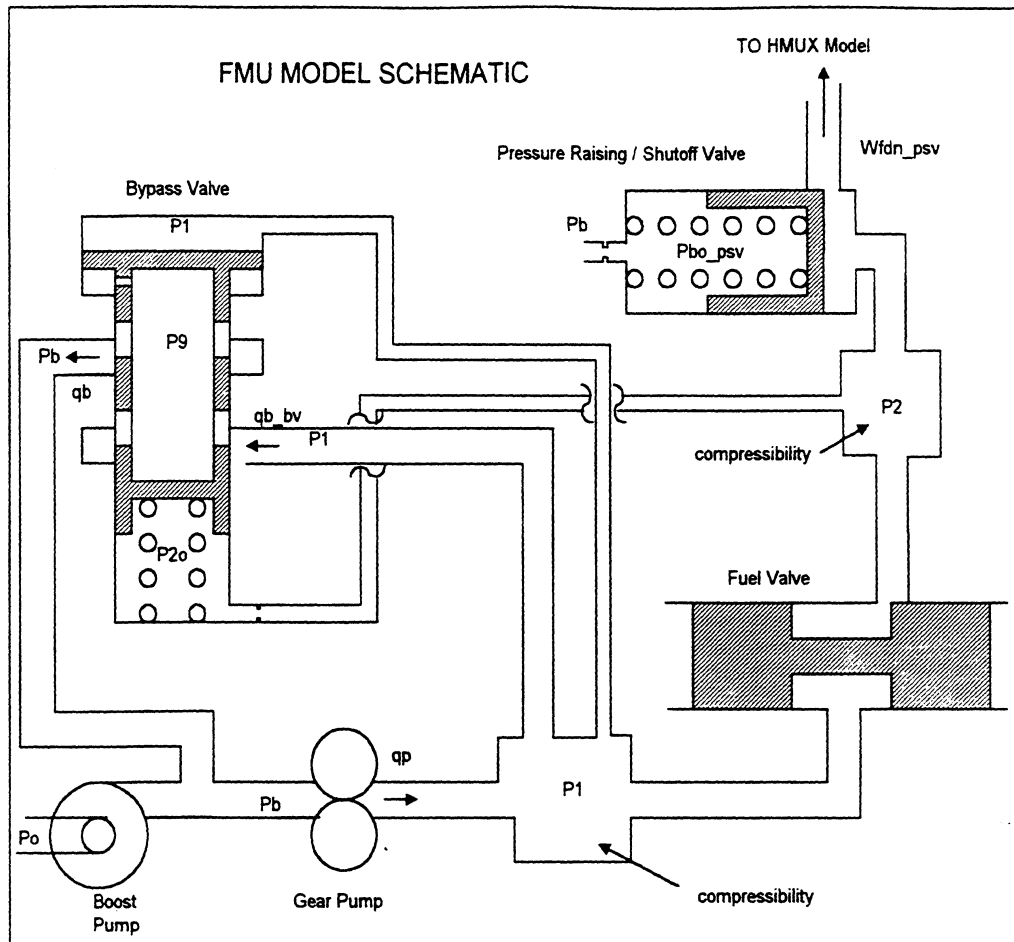


Figure 2 FMU Model Schematic

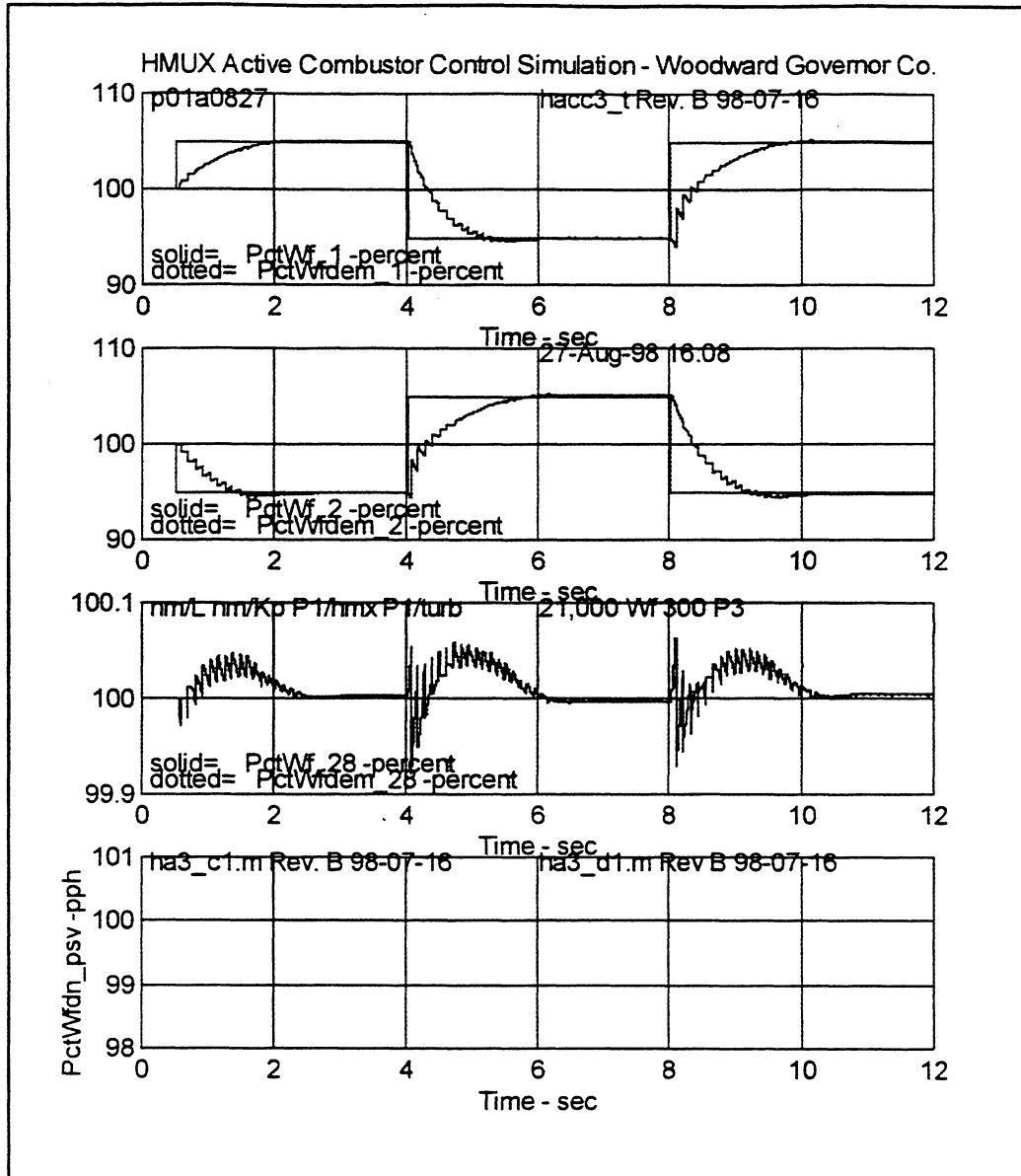


Figure 3 Flow Split Steps at 21,000 pph  
10% Steps Nozzles 1 & 2 Opposite Directions

Variables vs. time:

- 1) Percent flow split - channel #1
- 2) Percent flow split - channel #2
- 3) Percent flow split - channels #3-30 lumped together
- 4) Total flow at pressurizing valve discharge - percent

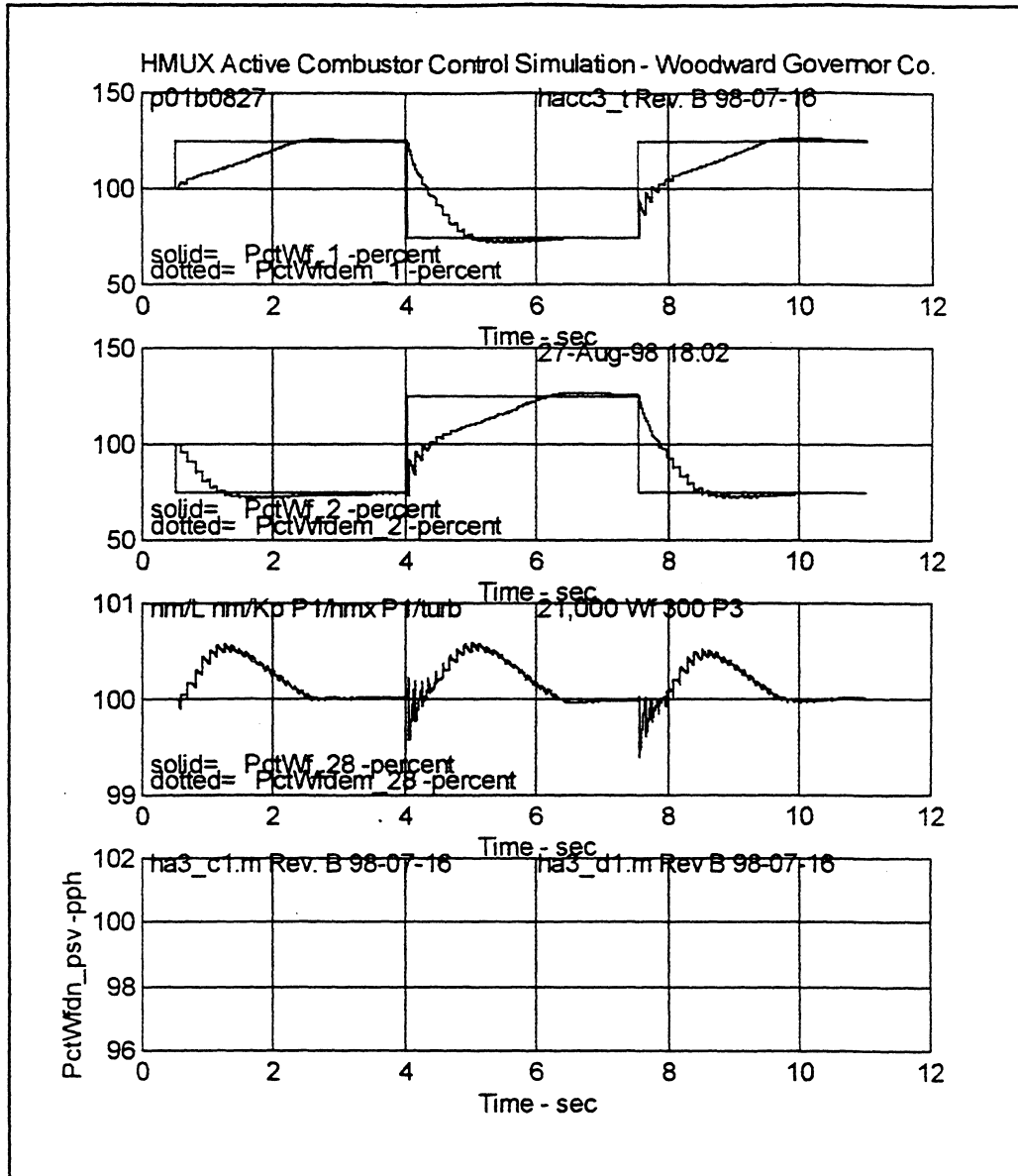


Figure 4 Full Range Flow Split Steps at 21,000 pph  
+/- 25% Steps, Nozzles 1 & 2 Opposite Directions

Variables vs. time:

- 1) Percent flow split - nozzle #1
- 2) Percent flow split - nozzle #2
- 3) Percent flow split - nozzles #3-30 lumped together
- 4) Total flow at pressurizing valve discharge - percent

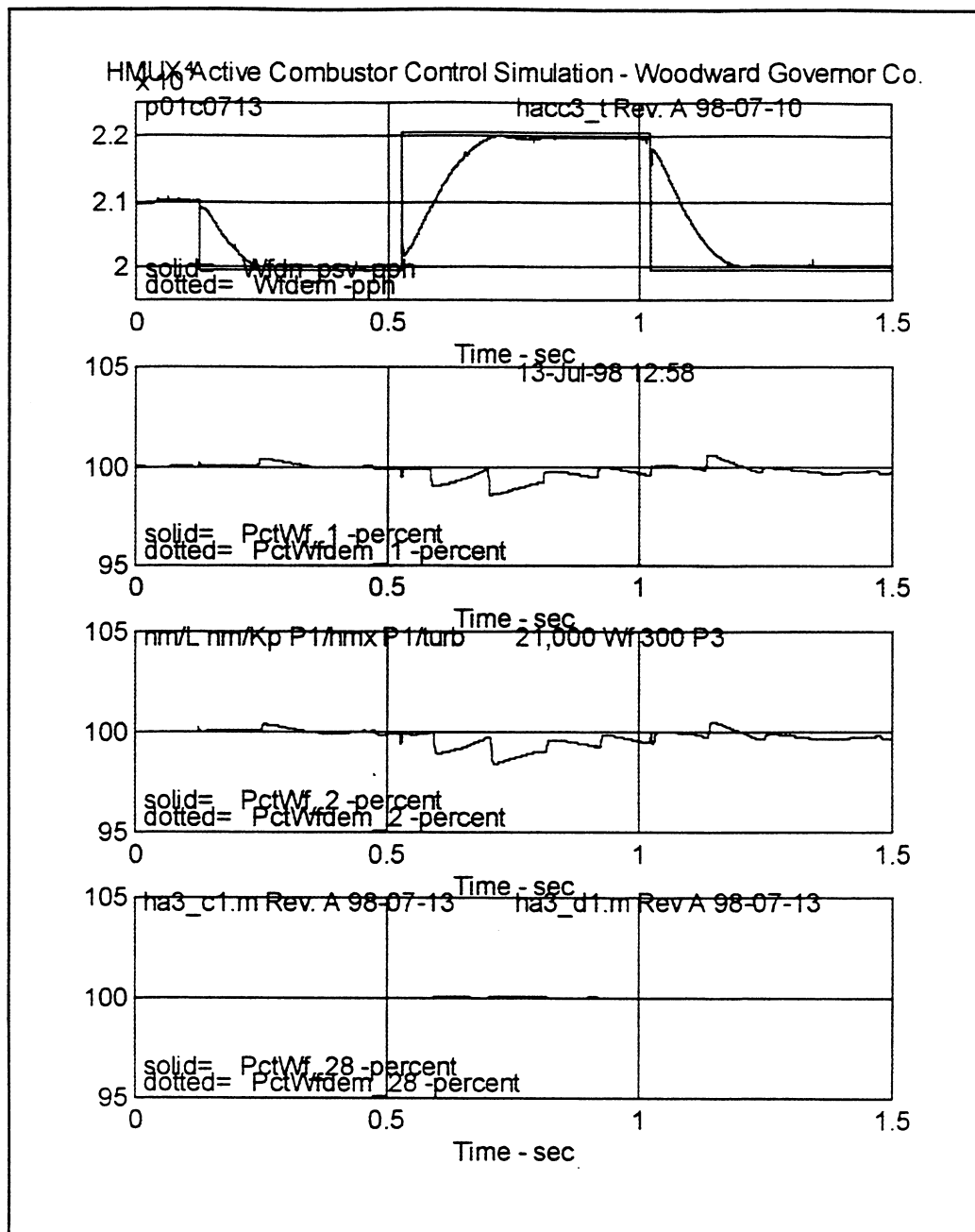


Figure 5 Total Flow Steps from 21,000 pph  
10% p-p Steps  
Variables vs. time:  
1) Total flow at pressurizing valve discharge - percent  
2) Percent flow split - nozzle #1  
3) Percent flow split - nozzle #2  
4) Percent flow split - nozzles #3-30 lumped together

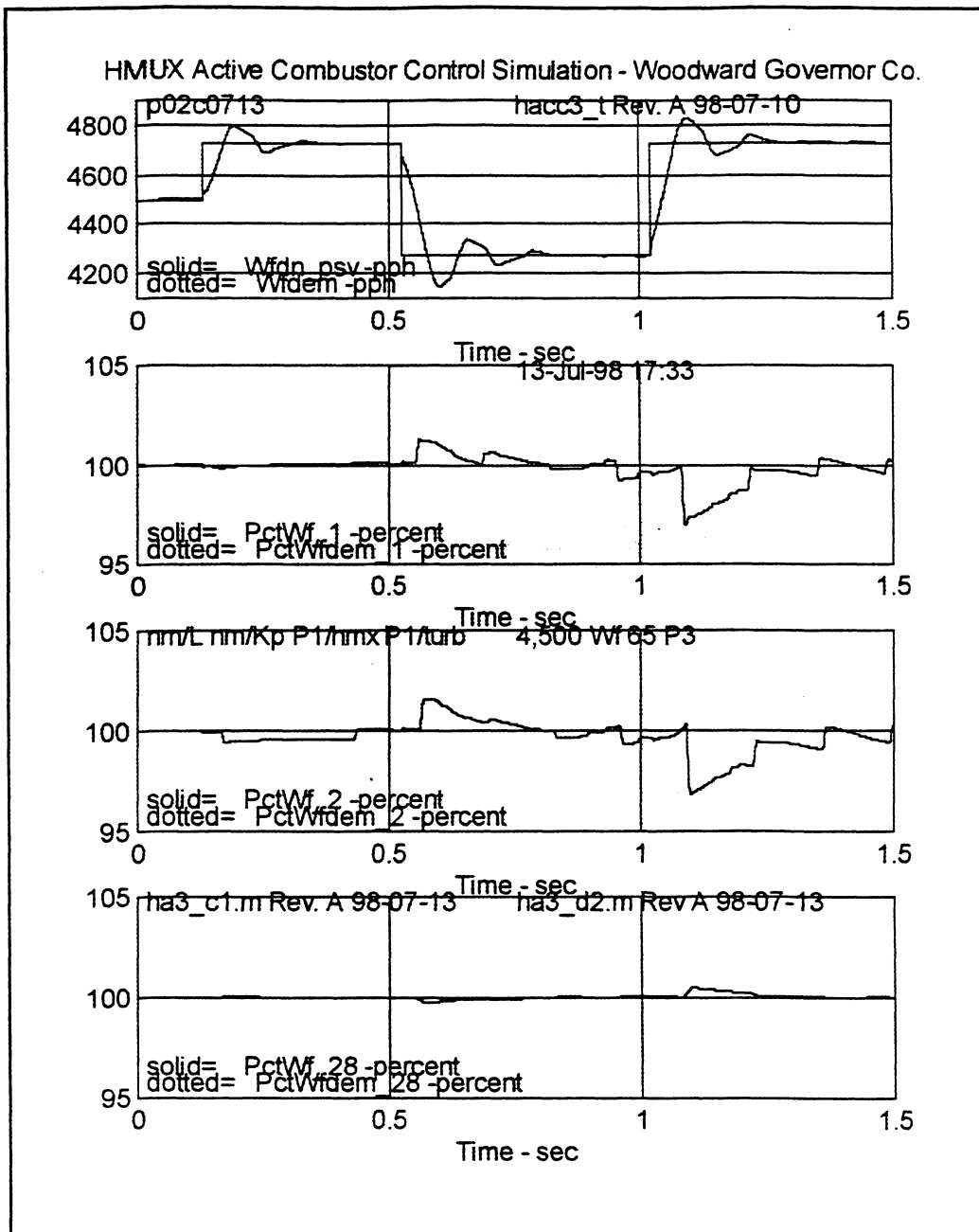


Figure 6 Total Flow Steps from 4,500 pph

10% p-p Steps

Variables vs. time:

- 1) Total flow at pressurizing valve discharge - percent
- 2) Percent flow split - nozzle #1
- 3) Percent flow split - nozzle #2
- 4) Percent flow split - nozzles #3-14 lumped together (other 16 nozzles closed off)



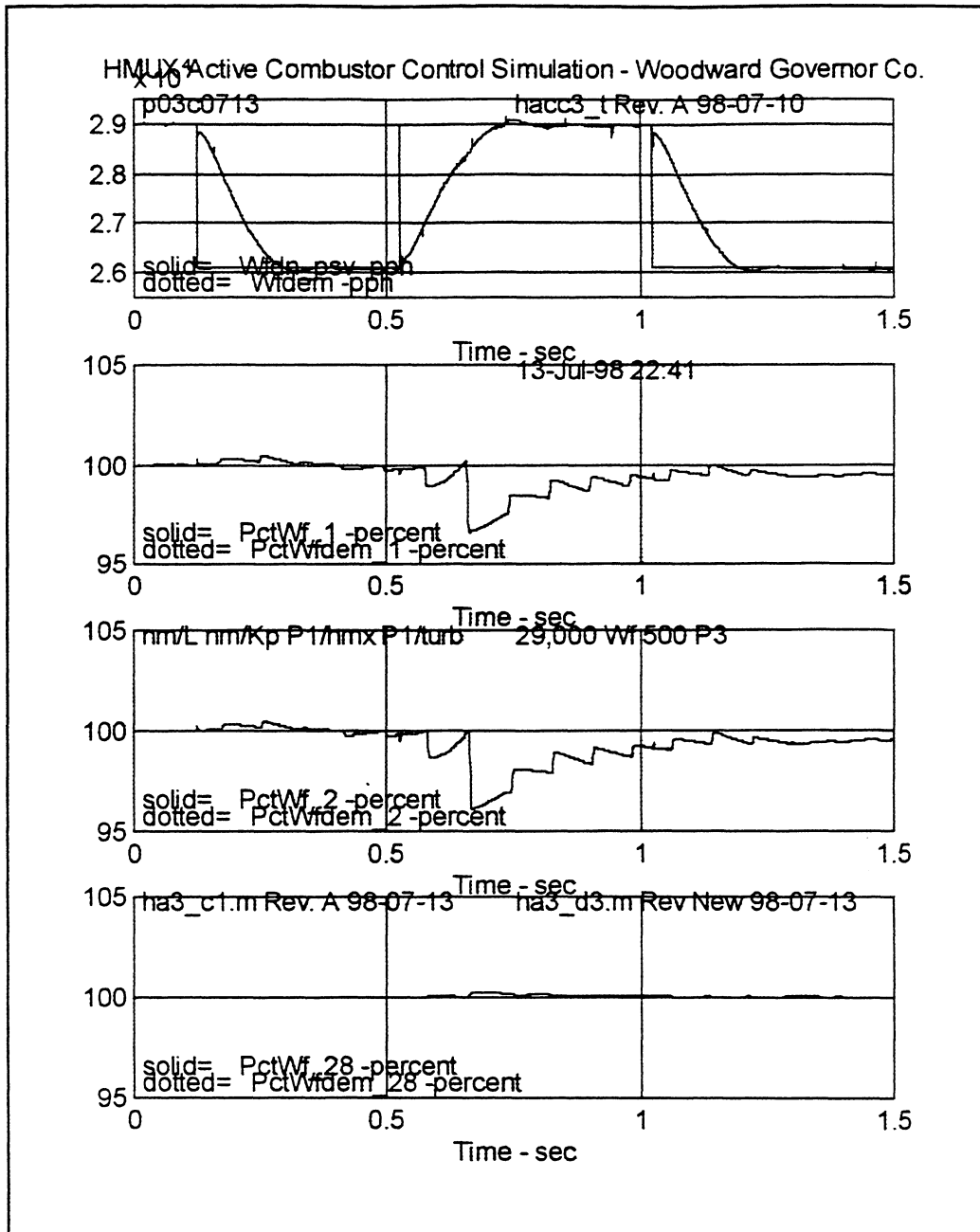


Figure 7 Total Flow Steps from 29,000 pph  
10% p-p Steps  
Variables vs. time:  
1) Total flow at pressurizing valve discharge - percent  
2) Percent flow split - nozzle #1  
3) Percent flow split - nozzle #2  
4) Percent flow split - nozzles #3-30 lumped together

REPORT DOCUMENTATION PAGE			Form Approved OMB No. 0704-0188	
Public reporting burden for this collection of information is estimated to average 1 hour per response, including the time for reviewing instructions, searching existing data sources, gathering and maintaining the data needed, and completing and reviewing the collection of information. Send comments regarding this burden estimate or any other aspect of this collection of information, including suggestions for reducing this burden, to Washington Headquarters Services, Directorate for Information Operations and Reports, 1215 Jefferson Davis Highway, Suite 1204, Arlington, VA 22202-4302, and to the Office of Management and Budget, Paperwork Reduction Project (0704-0188), Washington, DC 20503.				
1. AGENCY USE ONLY (Leave blank)		2. REPORT DATE June 2006		3. REPORT TYPE AND DATES COVERED Final Contractor Report
4. TITLE AND SUBTITLE AST Critical Propulsion and Noise Reduction Technologies for Future Commercial Subsonic Engines Area of Interest 1.0: Reliable and Affordable Control Systems			5. FUNDING NUMBERS  WBS-22-714-20-20 NAS3-27720	
6. AUTHOR(S)  William Myers and Steve Winter				
7. PERFORMING ORGANIZATION NAME(S) AND ADDRESS(ES)  General Electric Aircraft Engines One Neumann Way Cincinnati, Ohio 45215			8. PERFORMING ORGANIZATION REPORT NUMBER  E-15489	
9. SPONSORING/MONITORING AGENCY NAME(S) AND ADDRESS(ES)  National Aeronautics and Space Administration Washington, DC 20546-0001			10. SPONSORING/MONITORING AGENCY REPORT NUMBER  NASA CR-2006-214244	
11. SUPPLEMENTARY NOTES  This research was originally published internally as AST037 in July 2000. Project Manager, John DeLaat, Instrumentation and Controls Division, NASA Glenn Research Center, organization code RIC, 216-433-3744.				
12a. DISTRIBUTION/AVAILABILITY STATEMENT  Unclassified - Unlimited Subject Categories: 01, 02, and 07  Available electronically at <a href="http://gltrs.grc.nasa.gov">http://gltrs.grc.nasa.gov</a>  This publication is available from the NASA Center for AeroSpace Information, 301-621-0390.			12b. DISTRIBUTION CODE	
13. ABSTRACT (Maximum 200 words)  The General Electric Reliable and Affordable Controls effort under the NASA Advanced Subsonic Technology (AST) Program has designed, fabricated, and tested advanced controls hardware and software to reduce emissions and improve engine safety and reliability. The original effort consisted of four elements: 1) a Hydraulic Multiplexer; 2) Active Combustor Control; 3) a Variable Displacement Vane Pump (VDVP); and 4) Intelligent Engine Control. The VDVP and Intelligent Engine Control elements were cancelled due to funding constraints and are reported here only to the state they progressed. The Hydraulic Multiplexing element developed and tested a prototype which improves reliability by combining the functionality of up to 16 solenoids and servo-valves into one component with a single electrically powered force motor. The Active Combustor Control element developed intelligent staging and control strategies for low emission combustors. This included development and tests of a Controlled Pressure Fuel Nozzle for fuel sequencing, a Fuel Multiplexer for individual fuel cup metering, and model-based control logic. Both the Hydraulic Multiplexer and Controlled Pressure Fuel Nozzle system were cleared for engine test. The Fuel Multiplexer was cleared for combustor rig test which must be followed by an engine test to achieve full maturation.				
14. SUBJECT TERMS  Aircraft engines; Engine control; Combustion control; Combustion stability; Control			15. NUMBER OF PAGES 347	
			16. PRICE CODE	
17. SECURITY CLASSIFICATION OF REPORT Unclassified	18. SECURITY CLASSIFICATION OF THIS PAGE Unclassified	19. SECURITY CLASSIFICATION OF ABSTRACT Unclassified	20. LIMITATION OF ABSTRACT	



